Carbon-free Bifunctional Gas Diffusion Electrode for Alkaline Energy Converter

Dissertation

zur Erlangung des akademischen Grades

DOKTOR-INGENIEUR

(Dr.-Ing.)

Vorgelegt dem Rat der Chemisch-Geowissenschaftlichen Fakultät der

Friedrich-Schiller-Universität Jena

Von M. Sc. Artur Bekisch

Geboren am 10.06.1991 in Woschodskoje (Kasachstan)

Gutachter:

1. Prof. Dr. Micheal Stelter

2. Prof. Dr. Andrea Balducci

Tag der Verteidigung: 16.11.2022

Danksagung

Unser Leben ist das, wozu unser Denken es macht.
Mark Aurel

Ich möchte mich bei einigen Menschen bedanken, die einen unterstützenden Beitrag zum Gelingen dieser Arbeit hatten.

Als erstes möchte ich mich bei Prof. Dr. Michael Stelter bedanken, dass ich unter seiner Leitung diese Doktorarbeit anfertigen durfte. Des Weiteren bin ich für den gegebenen Entfaltungsfreiraum und für die fachliche Unterstützung dankbar.

Prof. Dr. Andrea Balducci danke ich für sein Interesse an meiner Arbeit und für die Bereitschaft als Zweitgutachter.

Ich bedanke mich sehr bei der Reiner Lemoine Stiftung und dem Stiftungsgremium für das gesetzte Vertrauen, mich und diese Arbeit mit einem Stipendium zu unterstützen. Besonders hervor heben möchte ich, dass durch das Ausrichten der Stipendiaten-Tage ist es einem möglich gewesen Dr. Annegret Jatzkeweitz, Dr. Paul Grunow, Alexander Steinke, Dr. Anja Lemoine, Busso von Bismarck, Eberhard Holstein, Clemens Triebel, Stipendiaten und ehemalige Stipendiaten persönlich in einer familiären Umgebung kennenzulernen und sich auszutauschen. Weiterhin möchte ich mich bei Lutz Plöttner für seine organisatorische Unterstützung bei den Anmelde- und jährliche Berichtsprozessen bedanken.

Dr. Roland Weidl und Dr. Matthias Schulz danke ich für die Aufnahme in die Abteilung 450 und in die Gruppe 454.
In der Gruppe 454 herrschte immer eine familiäre Stimmung, wo ich mich wohl gefühlt habe und ich zu jeder Zeit auf jeden zu gehen konnte.
Womit auch ein großer Dank an die gesamte neue und alte 454 geht, insbesondere an Hannes Bauer, Benjamin Schüßler, Martin Hofacker, Martin Becher, Cornelius Dirksen, Micha Fertig, Dr. Matthias Schulz und Dr. Karl Skadell.

Dr. Karl Skadell danke ich besonders für seine große Hilfe nicht nur bei der Antragstellung für ein Stipendium, sondern auch für die thematische Begleitung und Weiterentwicklung der Doktorarbeit, für die Diskussionen und Erleuchtungen und für dein kritisches Auge.

Erfahrung ist nicht das, was einem zustößt.
Erfahrung ist das, was man aus dem macht,
was einem zustößt.
Aldous Huxley

Table of Contents

Contents

List of Abbreviations

Abbreviation	Meaning
AEM	anion exchange membrane
AEMEL	anion exchange membrane electrolyzer
AEMFC	anion exchange membrane fuel cell
AFC	alkaline fuel cell
Ag/AgCl	silver / silver chloride electrode
APS	atmospheric plasma spraying
BET	Brunauer-Emmet-Teller
Capex	capital expenditure
CF-GDE	carbon-free gas diffusion electrode
CL	catalyst layer
CNTs	carbon nano tubes
CO2RR	CO2 reduction reaction
CPE	constant phase element
DFT	density functional theory
DPB	double-phase-boundary
DPBgl	double-phase-boundary gas-liquid
DPBls	double-phase-boundary liquid-solid
ECR	electrochemical CO2 reduction
EL	electrolyzer
FC	fuel cell
FEP	fluorinated ethylene propylene
FESEM	field emission scanning electron microscopy
FFT	fast Fourier transformation
Fle	fleece
Fo	foam
Fop	pressed foam
GDE	gas diffusion electrode
GDEref	commercially acquired carbon-based gas diffusion electrode
GDL	gas diffusion layer
gff	glass fiber fleece
HCD-Zone	high current density zone
HER	hydrogen evolution reaction
Hg/HgO	mercury / mercury oxide electrode

Abbreviations

HiFew	high scan rate few cycles
HiMny	high scan rate many cycles
HOR	hydrogen oxidation reaction
KF-GDE	Kohlenstoff freie Gasdiffusionselektrode
L	large pores
LDH	layered double hydroxide
LoFew	low scan rate few cycles
LoMny	low scan rate many cycles
M	medium pores
MAB	metal-air battery
MD	molecular dynamic
MPL	microporous layer
MPS	macroporous substrate
ODC	oxygen depolarized cathode
OER	oxygen evolution reaction
ORR	oxygen reduction reaction
PAFC	phosphoric acid fuel cell
PEM	proton exchange membrane
PEMEL	proton exchange membrane electrolyzer
PEMFC	proton exchange membrane fuel cell
PTFE	polytetrafluorethylene
PVDF	polyvinylidene
RHE	reversible hydrogen electrode
S	small pores
SCE	saturated calomel electrode
SHE	saturated hydrogen electrode
SOEC	solid oxide electrolysis cell
SOFC	solid oxide fuel cell
ss	stainless steel
TEM	transmission electron microscopy
TPB	three-phase-boundary
UR-AEMFC	unitized reversible anion exchange membrane fuel cell
URFC	unitized regenerative fuel cell
UR-PEMFC	unitized reversible proton exchange membrane fuel cell
UV	ultraviolet
W	Warburg

XPS	X-ray photoelectron spectroscopy
XRD	X-ray diffraction

List of Physical Quantities

Quantity	Symbol	Unit
Actual surface area	A_{actual}	m^2
Amount of Substance	n	mol
Angular Degree	θ	°
Angular Velocity	ω	s^{-1}
BET specific surface area	S_{BET}	$m^2\,g^{-1}$
Capacitance	C	F
Charge passage current density	j_{cp}	$mA\,cm^{-2}$
Charge passage overpotential	η_{cp}	V
Charge passage resistance	R_{cp}	Ω
Charge Transfer Coefficient	α	unitless
Charge transfer resistance	R_{ct}	Ω
Concentration	c	$mol\,l^{-1}$
Conductivity	λ	S
Constant	$c_{=1,2,\dots}$	/
Constant Phase Element Value	Q_0	$F\,s^{(\alpha_{CPE}-1)}$
Contact angle	CA	°
Contact angle Cassie and Baxter	$\theta_{C\&B}$	°
Contact angle Wenzel	θ_W	°
CPE Exponent	α_{CPE}	unitless
Current Density	j	$mA\,cm^{-2}$
Current Density Mass	jmass	$mA\,mg^{-1}$
Diffusion Coefficient	D	$m2\,s^{-1}$
Diffusion Flux	j	$mol\,m^{-2}\,s^{-1}$
Double Layer Capacitance	C_{dl}	$F\,g^{-1}$
Dynamic scan rate	r_{scan}	$mV\,s^{-1}$
Electric Current	I	A
Electric Overpotential	η	V
Electric Potential	φ	V
Enthalpy	G	$J\,kg^{-1}$
Exchange current density	j_0	$mA\,cm^{-2}$

Abbreviations

Faraday Constant	F	C mol^{-1}
Gas Constant	R	J K^{-1} mol^{-1}
Geometric surface area	A_{geo}	m²
Imaginary Part Resistance	Z''	Ω
Length	x	m
Mass	m	g
Ohmic resistance	R_{ohm}	Ω
Overpotential-window	$\eta_{OER} + |\eta_{ORR}|$	V
Oxygen evolution reaction overpotential	η_{OER}	V
Oxygen reduction reaction overpotential	η_{ORR}	V
Polarization resistance	R_p	Ω
Pressure	p	Pa
Ratio	q	%
Real Part Resistance	Z'	Ω
Real part resistance new value	Z'_n	Ω
Real part resistance value	Z'_x	Ω
Real part resistance x-axis intersection	$Z'_{intersec}$	Ω
Resistance	R	Ω
Roughness factor	r	/
Standard Potential	φ_{00}	V
Surface Area	A	m²
Surface Tension	γ	kg s^{-2}
Surface tension liquid-gas	γ_{lg}	kg s^{-2}
Surface tension solid-gas	γ_{sg}	kg s^{-2}
Surface tension solid-liquid	γ_{sl}	kg s^{-2}
Temperature	T	°C
Time	t	s
Volume	V	l
Warburg Coefficient	$\sigma_{Warburg}$	Ω s$^{-1/2}$

1 Introduction

The paradigm shift towards 100% environmentally friendly electricity consumption is the major goal worldwide and especially in Europe. To achieve this goal, technologies for the generation and conversion of electricity from renewable energy sources are needed. However, challenges such as fluctuating wind and solar power generation and electricity consumption patterns result in a surplus of wind and solar power. Increasingly, this surplus can neither be consumed nor fully stored. In addition, the frequency fluctuations of the transmission grid must be reduced to ensure stable 50 Hz and prevent damage to the entire grid or potential electricity blackouts. As a result, responsive energy conversion technologies such as fuel cells, electrolyzers, and batteries are of great importance to store this excess energy through electrochemical processes. The stored excess energy can then be used to meet power demand and stabilize frequency, thereby better protecting the power grid from blackouts.

Electrolyzers, batteries and fuel cells are increasingly becoming the focus of industry and research institutes in order to meet European CO_2 emission targets. The main basic components of these electrochemical systems, such as electrolyte, separator and electrodes (anode and cathode), are similar to each other and are constantly being optimized. One class of electrodes is the gas diffusion electrode (GDE), which electrochemically catalyzes the reactions at the interface between solid, gas and liquid phases. GDEs are used in:

- - Fuel cells based on proton exchange membranes (PEMFC), anion exchange membranes (AEMFC), alkaline media (AFC) or in a unitized regenerative mode (URFC).
- - Metal-air batteries such as Zn-Air and Fe-Air batteries (MAB).
- - Certain water electrolyzers with open anodes or cathodes based on proton exchange membranes (PEMEL) or anion exchange membranes (AEMEL).
- - Chlorine production by chlore-alkali electrolysis with oxygen depolarized cathodes (ODC).
- - Electrochemical CO2 reduction (ECR) applications.

The combination of a catalyst, PTFE as a binder, and porous carbon is a fundamental method for producing state-of-the-art GDEs. These GDEs are used for various reaction combinations such as:

- oxygen evolution | oxygen reduction reactions (OER | ORR)
- chloride evolution | ORR
- hydrogen evolution | OER
- carbon dioxide reduction | OER

Some of these applications such as MAB and URFC use GDEs that must be capable of two opposite electrochemical reactions such as OER and ORR. These are bifunctional GDEs. There are

quite a number of studies showing new bifunctional catalysts, their combinations with different elements, materials, architectures of surface structures and crystal planes to develop low cost and noble metal free GDEs.[1] [2] [3].

However, bifunctional carbon-based GDEs exhibit carbon corrosion in alkaline media, leading to technology malfunction. Therefore, new carbon-free (CF-)GDEs [4] [5] [6] [7] [8] are being developed to avoid carbon corrosion and its unstable behavior during OER /ORR [2] [9] [10] [11]. In general, carbon is oxidized by the attack of reactive species (peroxide) generated during ORR. This leads to higher overpotentials on OER, which cause direct oxidation of carbon. This carbon corrosion leads to mechanical destabilization, reduction in conductivity, loss of catalyst, and eventually a collapse in electrochemical performance. Therefore, the durability of state-of-the-art GDEs is limited. However, there is an opportunity to develop CF-GDE designs that could have higher durability than state-of-the-art GDE designs. One way to replace carbon is to use a porous metal as a current collector, which is then coated with an electrocatalyst [7] [8].

1.1 Objective and Research Strategy

The goal of this work is to propose a novel, long-term stable, bifunctional, carbon-free (CF-)GDE design for alkaline energy converters.

This is achieved by understanding how the electrochemical activity of GDEs is affected by the pore size and the surface properties (hydrophobic and hydrophilic) of the electrode.

In addition, combinations of different pore sizes and surface properties (hydrophobic and hydrophilic) and their influence on electrochemical activity will also be investigated.

It is also necessary to understand the difference between the designed CF-GDE and the state-of-the-art carbon-based GDE_{ref}.

To accomplish this, I used the following research strategy.

Alternatives for carbon in GDEs for alkaline applications are porous metal substrates. Therefore, nickel and/or stainless-steel alloys are used as substrates because they are stable in the applied electrochemical environment. It is also of great importance to use metal substrates with a large coatable specific surface area, such as metal foams or fleeces. Thus, metal substrates with three different pore sizes ($500 - 600$ μm, $20 < x \leq 200$ μm and 20 μm) are used. They serve as electrode bodies, which are electrochemically coated with MnO_x as electrocatalyst, which is also electrochemically stable in an alkaline medium.

The MnO_x is electrodeposited on the metal substrates using an electrochemical setup similar to that of *Tsai at el*. [12]. The electrodeposition setup is a combination of potentiostatic and potentiodynamic deposition. The difference with *Tsai at el*. [12] is that the setup of the potentiodynamic deposition is varied by the cycle number and dynamic scan rate (r_{scan}) to obtain the most suitable electrodeposition setup for the OER and ORR activity. Therefore, the deposited MnO_x is analyzed by X-ray diffraction (XRD) and transmission electron microscopy (TEM) to determine the crystal phase.

Then, some of the MnO_x-coated metal substrates are hydrophobized with PTFE to obtain a hydrophobic surface property.

In general, the different pore sizes and surface properties (hydrophobic and hydrophilic) of the considered metal substrates affect the electrochemical activity. Therefore, these differences need to be compared with each other and with the carbon-based GDE to determine at which pore size, surface properties and their combinations a high electrochemical activity is obtained. Therefore, all metal substrates coated with MnO_x and PTFE as GDE_{ref} will be analyzed with different surface measurement methods to investigate their surface structure (field emission scanning electron microscopy - FEREM), pore structure (X-ray tomography), specific surface area (nitrogen sorption - Brunauer-Emmet-Teller - BET) and hydrophobicity (contact angle - CA).

Then, they are electrochemically characterized by electrochemical impedance spectroscopy, galvanostatic and potentiostatic measurements with a half-cell setup.

Impedance spectroscopy characterizes the individual parameters (charge transfer resistance, ohmic resistance of electrolyte and membrane, Warburg diffusion coefficient and electrochemically active surface area) that determine the electrical response and indicate the electrochemical activity. Consequently, it is possible to understand which parameter or electrochemical process is more dominant.

In addition, GDEs are also tested at higher electrical loads to determine their electrochemical behavior in near-application environments. For a given current density, the galvanostatic measurement indicates the total cell potential, from which the overpotential is calculated for OER and ORR. This is because the overpotential is an indirectly proportional parameter value for electrochemical activity. The potentiostatic measurement works similarly to the galvanostatic measurement, but is used for long-term stability measurements to determine the degradation of the GDE at specific electrical potentials for OER and ORR.

Based on the individual CF-GDE surface and electrochemical results, hydrophobic and non-hydrophobic MnO_x-coated metal substrates are combined to design a layered CF-GDE with a specific pore size gradient and a hydrophilic/hydrophobic transition. They are also electrochemically analyzed to describe the influence of the pore size gradient and hydrophilic/hydrophobic transitions on OER and ORR activity.

All the above measurement methods and their results are used to highlight and understand the differences between GDEs and to explore their interrelationships. Based on this, a novel CF-GDE design can be proposed that can potentially compete with the state-of-the-art carbon-based GDE_{ref}.

The approach of this work is divided into three parts:

The first part is the determination of a coating method for the preparation of a catalyst that can be applied in a standardized manner to various metal substrates (nickel foam, pressed nickel foam, and stainless-steel fleece).

The second part is the study of different substrates with specific macropore sizes coated with MnO_x and the influence of PTFE on them.

The third part is the design of layered bifunctional carbon-free GDEs. It is necessary to design a hydrophilic/hydrophobic porosity gradient by combining several MnO_x and PTFE coated substrates with different macropore sizes.

2 Literature

2.1 Gas Diffusion Electrodes

2.1.1 Applications

Electrochemical applications such as proton exchange membrane (PEMFC)[13], anion exchange membrane (AEMFC)[14] and alkaline (AFC)[14] [15] [16] fuel cells, metal-air batteries (MAB)[17], zero gap, membrane electrode assembly (MEA) or AEM electrolyzers[18] [19] (AEMEL) and electrochemical CO_2 reduction (ECR) systems[20] use GDEs or GDE-related electrodes[21]. The starting point of alkaline GDE applications is the *Bacon* fuel cell, developed by *Francis Thomas Bacon* in the late 1930s[22]. All of the above applications are similar in design. They consist of an anode, a cathode, an electrolyte and a separator. Their electrodes require contact with a gas phase and an aqueous phase. For this reason, the electrodes are commonly referred to as GDEs[23]. Some of them, such as PEMFC, AEMFC, and AEMEL, have a polymer electrolyte membrane that is proton or anion conductive and therefore does not require an aqueous electrolyte and separator. These polymer membranes are wetted by supplying H_2O to provide OH^- or H^+ transport during operation of the specific applications. The schematic depictions of the above technologies and their GDEs can be seen below in Figure 1, with the exception of the *Bacon* fuel cell.
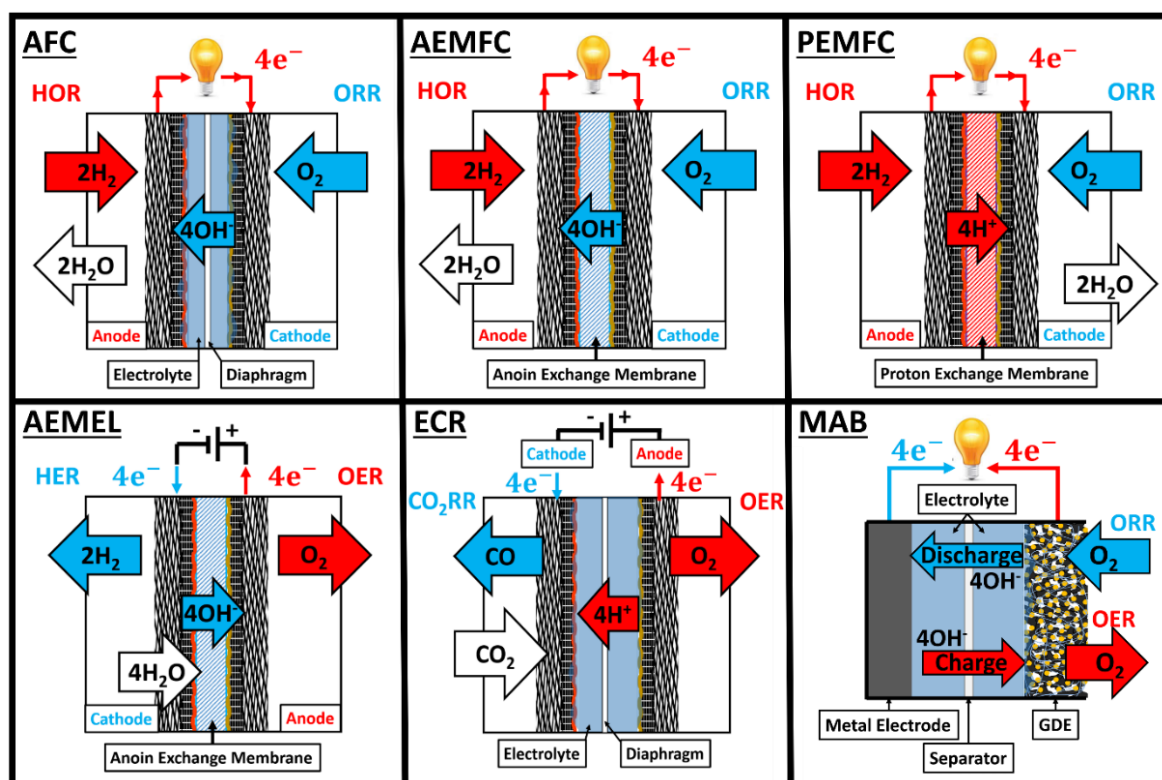
Figure 1. Schematic depiction of different gas diffusion electrode applications (ALFC: alkaline fuel cell; AEMFC: anion exchange membrane fuel cell; PEMFC: proton exchange membrane fuel cell; ECR: electrochemical CO_2 reduction system; AEMEL: anion exchange membrane electrolyzer; MAB: metal-air-battery).

2 Literature

There are even more applications than those shown in Figure 1 that use a GDE or GDE-related electrodes, such as solid oxide fuel cells (SOFC[24]), phosphoric acid fuel cells (PAFC[25]), or proton exchange membrane electrolyzers (PEMEL[26]). In general, they are similar in design to the other applications shown (Figure 1), but with different separators and/or GDEs, resulting in different operating principles. Nevertheless, the selection shown in Figure 1 will be introduced. All applications shown schematically (Figure 1) have a GDE on the anode and cathode side, with the exception of MAB, which has a GDE on only one side.

Fuel cell applications (AFC, AEMFC and PEMFC) are supplied with hydrogen (H_2) and oxygen (O_2) to generate electricity. H_2 is electrochemically oxidized at the anode, while O_2 is reduced at the cathode, resulting in the production of H_2O. The chemical reactions used are hydrogen oxidation (HOR) and oxygen reduction reaction (ORR). AFC and AEMFC show the same reaction and due to their alkaline environment (E 1 and E 2), have different membranes. The AFC has a porous hydrophilic membrane that is permeable to liquid electrolytes, while the AEMFC has an anion exchange membrane that is conductive only to anions. The PEMFC, on the other hand, has a proton exchange membrane and is more similar to the AEMFC than the AFC because the PEM is permeable only to protons (H^+). In addition, the PEMFC also has HOR and ORR, which are different from the reactions of the AFC because they occur in an acidic environment (E 4 and E 5). The reactions are shown for both environments in the following chemical equations.

Alkaline:

Anode / positive electrode:

$$2\ H_2 + 4\ OH^- \leftrightharpoons 4\ H_2O + 4\ e^- \qquad\qquad E\ 1$$

Cathode / negative electrode:

$$O_2 + 2\ H_2O + 4\ e^- \leftrightharpoons 4\ OH^- \qquad\qquad E\ 2$$

Cell-reaction:

$$2\ H_2 + O_2 \leftrightharpoons 2\ H_2O \qquad\qquad E\ 3$$

Acidic:

Anode / positive electrode:

$$2\ H_2 + 4\ H_2O \leftrightharpoons 4\ H_3O^+ + 4\ e^- \qquad\qquad E\ 4$$

Cathode / negative electrode:

$$O_2 + 4\ H_3O^+ + 4\ e^- \leftrightharpoons 6\ H_2O \qquad\qquad E\ 5$$

Cell-reaction:

$$2\ H_2 + O_2 \leftrightharpoons 2\ H_2O \qquad\qquad E\ 6$$
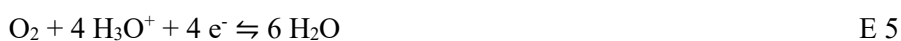
These reactions on the electrodes take place at the respective catalyst layer on the GDEs. However, the catalysts differ depending on the alkaline or acidic environment of a FC and the electrolyzer[19] [27]. The principle and design of GDEs are explained in more detail in the next chapter.

Furthermore, different ion conducting media lead to different transport mechanisms. In the alkaline environment, anions (OH^-) transport the charge from the cathode to the anode. Consequently, the electrolyte in alkaline aqueous applications is usually a 5 to 7 M (25 - 30 %) KOH solution (FC and EL) because it has the highest ionic conductivity compared to other alkaline electrolytes[28] [19].

In AFCs, both sides (anode and cathode) are separated by a diaphragm[14]. Zirfon® is often used as state-of-the-art diaphragm[19]. It consists of ceramic powder (zirconia) and a polymer matrix (polysulfone)[29]. The electrolyte fills the mesopores of the diaphragm and provides ionic conductivity between the anode and cathode. This description of the electrolyte and diaphragm provides the framework for the design of AFC and alkaline water electrolysis. In alkaline water electrolysis, the reverse reaction occurs as in AFC, but with electrodes derived from GDEs. This is because the electrodes are fully immersed in the electrolyte.

The difference between AFC and AEMFC is their ion transport medium. The AEMFC has an AEM (anion exchange membrane) that replaces the electrolyte and diaphragm of the AFC. Generally, the AEM contains a polymer backbone to which cationic functional groups are attached to provide anion conductivity. But AEMs still have low chemical stability under alkaline conditions, which has been intensively researched[30] [31] [32]. The occurrence of chemical degradation is caused by the chemical instability of cationic functional groups and polymer backbone[33] [34]. However, cationic functional groups such as quaternary ammonium[35], imidazolium[36] and some phosphonium[37] groups and aliphatic or mixed aromatic/aliphatic polymer backbones[34] are promising to improve the chemical stability of AEMs[38]. Therefore, they are currently being developed for applications such as AEMFC and AEMEL, as these were originally optimized for less aggressive environments (desalination, electrode ionization, electrodialysis)[30].

On the other hand, PEMFC is fully commercialized and works with Nafion©, the state-of-the-art proton exchange membrane polymer[13]. Proton conductivity is provided by functionalized sulfonic acid groups on the tetrafluoroethylene (PTFE) polymer backbone[39].

GDE-derived electrodes are used in electrolyzers[21], such as AEMEL, AEL or PEMEL, to produce H_2 and O_2 by water splitting. The corresponding electrochemical reactions are oxygen evolution (OER) and hydrogen evolution reaction (HER), which are the reverse reactions of an AFC and AEMFC, respectively (E 1 and E 2). There is also the PEM water electrolysis (PEMEL), which has the reverse electrochemical reactions of a PEMFC (E 4 and E 5). Accordingly, the FC is potentially capable of electrolyzing water through its reverse operation. The reverse operation of HOR and ORR is HER and OER and leads to the unitized regenerative (UR-)PEMFC[40] technology, which focuses on water electrolysis and FC operation by bifunctional GDEs. Bifunctional GDEs

have catalysts suitable for both processes. However, the efficiency of UR-PEMFC is lower compared to a single PEM water electrolyzer or a single PEMFC due to the slow kinetic rate of the ORR and the limitations in mass transport of the gaseous reactants to the reaction sites[41].

In addition, there is also an application of GDEs that enables electrochemical CO_2 reduction (ECR) to produce hydrocarbon fuels and feedstocks[42] [20]. This ECR system is under development and is used in three common configurations:

I.   Microfluidic cell: as shown in Figure 1 (ECR), but with an electrolyte flow channel[43].

II.   Hybrid cell: same design as MAB but the GDE (cathode) is gassed with CO_2[44].

III.   Zero-gap cell: same design as AEM or PEM electrolyzer cells[45] [46].

The ECR system operates in neutral or alkaline electrolytes (KOH) and the electrochemical reactions for CO evolution are as follows:

<div align="center">Anode / positive electrode:</div>

$$4\ OH^- \leftrightharpoons O_2 + 2\ H_2O + 4\ e^- \hspace{4cm} \text{E 7}$$

<div align="center">Cathode / negative electrode:</div>

$$2\ CO_2 + 2\ H_2O + 4\ e^- \leftrightharpoons 2\ CO + 4\ OH^- \hspace{3cm} \text{E 8}$$

<div align="center">Cell-reaction:</div>

$$2\ CO_2 \leftrightharpoons 2\ CO + O_2 \hspace{5cm} \text{E 9}$$

As mentioned above, it is also possible to produce other carbon products such as CH_4, C_2H_4 or HCOOH[47]. The electrochemical reactions take place at the catalyst layer on the respective GDE. OH^- is split into oxygen and recombines at the anode to form H_2O. The H_2O diffuses through the membrane and reaches the cathode. CO_2 and water are reduced to CO and hydroxide ions at the cathode, and the hydroxide ions diffuse to the anode. The separator of an ECR system can consist of different ion exchange membranes[45] [48] [49]. It depends on the media conditions whether a bipolar-membrane, a cation exchange membrane or an anion exchange membrane is used[20] [45] [49]. The ECR system is still under development due to problems with stability and product selectivity[20] [47] [48] [50] [51]. Stability is affected by poisoning mechanisms due to metal impurities in the electrolyte. These impurities reduce the active surface area of the catalyst and consequently affect the product selectivity[52] [53]. Selectivity is also affected by pH variations and the occurrence of HER, which must be suppressed to maintain selectivity[50] [54].

The solid oxide electrolysis cell (SOEC) is a highly efficient approach for the co-electrolysis of CO_2 and H_2O to syngas (H_2 and CO) at high temperatures[55]. However, SOEC is beyond the scope of this work.

The last GDE application presented is MAB (Figure 1). It consists of a metal anode, an aqueous, non-aqueous or solid electrolyte, a separator and a GDE. There are various metals that can be used as anode, such as Zn, Mg, Si, Fe, Al, Li, K, or Na[17] [56] [57]. However, Zn was the first researched anode for MAB applications and is state-of-the-art (e.g., primary battery for hearing aids)[58]. For highly active metals such as Li, K, and Na, non-aqueous aprotic electrolytes such as ether-, sulfoxide-, or amide-based solvents[59] [60] with an anode-specific metal salt (such as $LiCF_3SO_3$, LiTFSI, or $LiPF_6$ [61]) are needed. For the other metals such as Zn, Mg, Si, Fe, and Al, an alkaline or neutral aqueous electrolyte such as KOH[56] [58] or chloride-based electrolytes[17] are used. There are also combinations of ionic liquids with aqueous and non-aqueous electrolytes due to their wide potential window, low volatility, high ionic conductivity and non-flammability[58] [62].

Furthermore, solid-state electrolytes are divided into three different types: Gel-polymer, solid polymer and ceramic electrolyte[58]. Gel-polymer electrolytes are very flexible and have slightly lower ionic conductivity than aqueous electrolytes. This is because they are a combination of a 3D polymer skeleton and a liquid electrolyte[63] [64]. A solid polymer electrolyte, on the other hand, has an ion-conducting polymer matrix but no liquid solvent. As a result, the ionic conductivity is lower compared to a gel-polymer[65]. In addition, there are also ceramic electrolytes, for example, of the NASICON, garnet, sulfide, or perovskite type[65] [66]. These electrolytes have high mechanical strength but low conductivity. For this reason, research is focused on increasing ionic conductivity and electrochemical stability[66]. The interface between electrolyte and electrode plays an important role. Based on the many different types of electrolytes and anodes, it is possible to develop a wide variety of MABs.

Some of them require a separator between the electrodes to avoid their contact and to control dendrite growth. In general, the separator must be ionically conductive, electronically insulating, mechanically and dimensionally stable, chemically resistant, migration inhibiting, and wettable by the electrolyte[67]. Therefore, there are different types and materials of separators depending on the MAB electrolyte and anode. Fibers, polymer films, and solid ionic conductors are materials that are used[67].

The last component of the MAB is a GDE that makes the air electrochemically available. The electrochemical reactions are initiated by a catalyst. However, MABs are distinguished between aqueous and non-aqueous, as these two types have different GDE reactions[57] [58]. In the following, only the aqueous GDE type will be discussed (E 10 – E 12). Compared to the other GDEs presented, which are electrochemically active for only one reaction, the GDE of a MAB must be electrochemically active for ORR and OER, such as UR-PEMFC. Therefore, it is referred to as a

bifunctional GDE. These bifunctional GDEs are used in secondary batteries. They are discharged by ORR and charged by OER. The corresponding reactions are shown below in the discharge direction.

GDE / ORR / cathode /negative electrode:

$$O_2 + 2\ H_2O + 4\ e^- \leftrightharpoons 4\ OH^- \hspace{4cm} E\ 10$$

Zinc metal electrode / anode / positive electrode:

$$2\ Zn + 4\ OH^- \leftrightharpoons 2\ ZnO + 2\ H_2O + 4\ e^- \hspace{3cm} E\ 11$$

Cell-reaction:

$$O_2 + 2\ Zn \leftrightharpoons 2\ ZnO \hspace{5cm} E\ 12$$

These exemplary reactions of a Zn-air-battery are reversible. The other metal anodes mentioned (Mg, Si, Fe, Al, Li, K or Na) are also reversible or theoretically reversible. However, the secondary MABs are still under development to increase the durability and bifunctional electrochemical activity and avoid capacity degradation[17]. In highly simplified terms, the capacitance is determined by the metal electrode, the OER/ORR activity is affected by the GDE, and the durability depends on both electrodes. In this context, there are three main problems: Passivation[57] of the metal anode, dendrite growth[58] of the metal anode and carbon corrosion[9] of the GDE[17]. Based on the above components, there are a variety of MABs, all of which are under development. Nevertheless, there are already commercial primary Zn-air-batteries for hearing aids[4].

2.1.2 Working Principle

In the previous chapter, various applications were shown that use a GDE. In this chapter, the basic principles and operation of the GDE are described. In the following, only the alkaline environment will be considered. In general, a GDE can be defined as follows:

A GDE has an interface between the solid, gaseous, and liquid phases, at which it electrochemically catalyzes the reactions between the liquid and gaseous phases through the electrically conductive solid phase of the catalyst.

Therefore, a GDE is designed to provide a large electrolyte surface area to allow the gas to dissolve in the liquid phase and then diffuse to the electrochemically active site for its reaction.

Generally, the largest possible electrolyte surface area for dissolving the gas is achieved by combining materials that have certain properties: a large specific surface area and hydrophilic/hydrophobic behavior. Their combination forms an electrolyte wetting film inside the GDE in which the gas can dissolve without the electrolyte leaking. Thus, if the wetting film is large, the amount of dissolved gas in the electrolyte is also large. In the following, two different standard designs of GDE are presented, which are shown schematically in Figure 2.
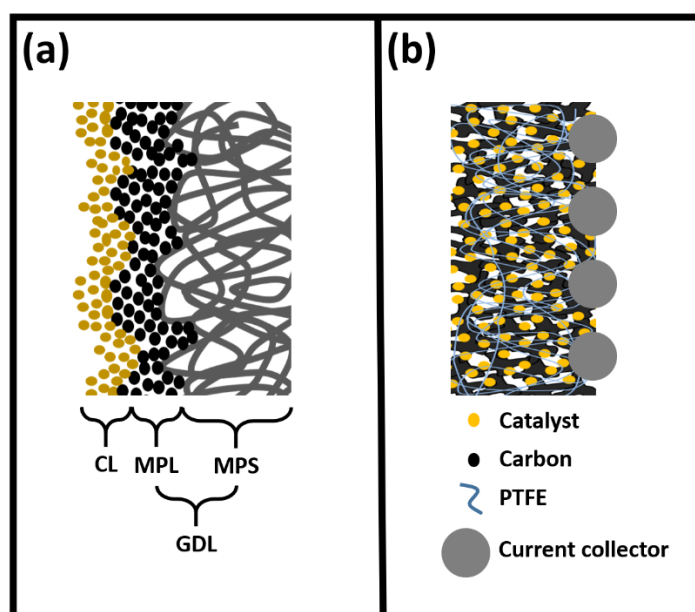
Figure 2. Schematic depiction of GDE designs: (a) a layered electrode GDE: combination of gas diffusion layer (GDL) (macro porous substrate (MPS) & micro porous layer (MPL)) with catalyst layer (CL); (b) a porous electrode GDE: mixture of carbon, catalyst and PTFE[15] [20] [68] [69].

The layered electrode GDE design in Figure 2 (a) consists of two main layers, a gas diffusion layer (GDL) and a catalyst (CL). The GDL provides gas transport toward CL and serves as a physical carrier. In general, the GDL is hydrophobic to prevent electrolyte leakage and flooding of the GDL-pores. Therefore, the GDL is mixed or coated with a hydrophobic additive such as PTFE[51]. In addition, there are two different types of GDL. A single-layer GDL, which consists of only a

macroporous substrate (MPS), and a double-layer GDL, which also has a microporous layer (MPL)[20]. Thus, the electrolyte wetting film is formed between CL and GDL. The thickness of the GDL affects the gas supply and the sensitivity of liquid water accumulation[70] [71]. It has been shown that an additional microporous layer is beneficial for higher performance[70]. However, there are competing trends when the thickness of the diffusion layer is varied. Thicker GDLs are less sensitive to liquid water accumulation, but the extended transport channels contribute to mass transfer limitations and *vice versa*[70]. These GDLs are composed of porous carbon materials such as carbon fibers (MPS) and/or compressed activated carbon powder (MPL).

In contrast, the porous electrode GDE (Figure 2 (b)) consists of a GDL completely covered with catalyst particles bound by a hydrophobic additive[23] [72]. Accordingly, the porous electrode GDE is a combination of a PTFE-bound GDL and CL, resulting in a hydrophobic/hydrophilic all-in-one approach. The electrolyte wetting film forms near the bulk electrolyte side at the hydrophobic/hydrophilic pore system of the porous electrode. Generally, the GDL is a percolation system of electrically conductive powder such as carbon, silver or nickel[22] [72] [73]. It depends on the application of the GDE whether an additional catalyst is needed, which is then applied to the GDL surface. Therefore, it is possible to fabricate a carbon-free bifunctional porous electrode GDE with this design by using only catalyst powder and PTFE that is stable in alkaline electrolytes[74].

The GDE design with two main layers (GDL and CL, Figure 2 (a)) is usually the most commonly used, especially in FCs, MABs, and electrolyzers. This is because of the low catalyst mass of CL, which is only a few micrometers thick layer on the hydrophobized carbon GDL. As a result, expensive catalysts such as Pt, Ru, or Ir are affordable when this design is used. One way to replace noble metal catalysts with non-noble metals is to increase the mass of the non-noble metal catalysts to compensate the total electrochemical activity[2]. For this reason, the porous electrode is a well-suited option for this purpose. The nickel GDE of *Bacon*-FC is a good example[22]. However, there are also special applications such as oxygen depolarized cathodes (ODCs) for alkaline chlorine production, where the design of hydrophobic porous electrode is used (Figure 2 (b))[72] [75]. As indicated above, a commercial ODC consist of a mixture of silver powder and PTFE pressed onto a metal mesh current collector[76] [77]. In addition to the ODC, the most state-of-the-art GDEs have a carbon-based GDL, which is known for its carbon corrosion during OER/ORR operation in alkaline medium[2] [9] [10] [11]. Therefore, novel GDE designs and/or carbon-free material combinations have been investigated and are presented below.

The goal of various research groups is to develop a GDE that has high electrochemical activity and is electrochemically stable over the long term. These GDE designs (Figure 3) are carbon-free and carbon-based for OER/ORR and OER/CO_2RR applications. In general, they can still be broken

down to the single functional layer of CL and GDL. Figure 3 shows examples of novel GDEs. The first of the GDEs shown (Figure 3 (a)) was developed for Zn-Air-Batteries[7]. *Ke Xu et al*. used a hydrothermal method to grow MnO_2 nanospheres directly on nickel foam (MnO_2/Ni). CNTs and a PTFE emulsion were used to prepare a GDL that was fitted on the MnO_2/Ni and then also attached to a Teflon membrane. In general, the coated nickel foam is actually a CL on a GDL, similar to the porous electrode described (Figure 2 (b)). The PTFE/CNT is a hydrophobic/hydrophilic transition region between MnO_2/Ni and PTFE membrane, which provides the largest possible electrolyte surface area for O_2 solvation. They presented the positive effect of the hydrophobic agent (PTFE), which modified the pore structure and contributed to the large wetting film and efficient gas transport. As a result, this GDE achieved a discharge voltage of 0.8 V at 100 mA cm^{-2} and exhibited a completely stable discharge for four hours at 20 mA cm^{-2}.
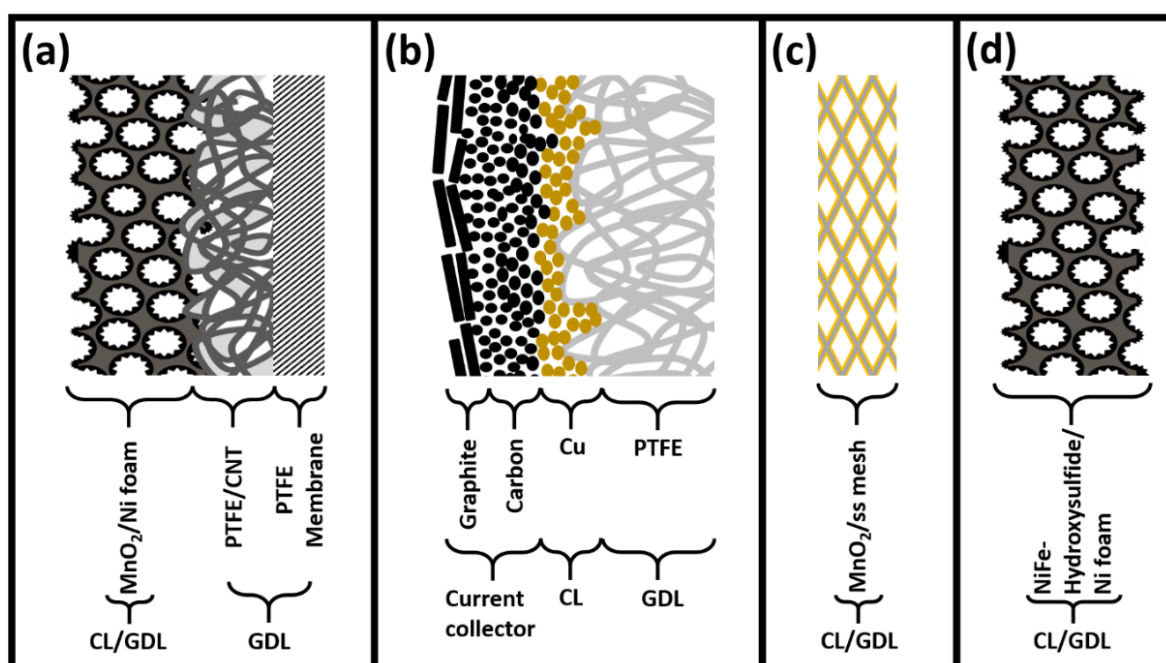
Figure 3. Schematic depiction of different GDE designs: (a) MnO₂/nickel foam/carbon nanotubes (CNT)/PTFE/PTFE membrane GDE[7]; (b) graphite/carbon nanoparticles/Cu/PTFE GDE[44]; (c) MnO₂/stainless steel mesh (ss)[8]; (d) NiFe-Hydroxysulfide/nickel foam GDE[6].

In Figure 3 (b), the second GDE is used for the electrochemical reduction of CO_2 (ECR) to ethylene[44]. *Dinh et al*. sputtered a Cu catalyst onto a porous PTFE membrane. They then spray-coated carbon black nanoparticles on top to make electrical contact with CL and achieve uniform distribution of current density. The graphite layer serves as the overall support and current collector. The direct connection of CL with the electrically non-conducting GDL (porous PTFE) leads to the formation of the electrolyte wetting film at their interface. Accordingly, this design has very short transport distances for the dissolved CO_2 to its reaction site since there is no hydrophilic/hydrophobic carbon between CL and PTFE. In this design, the porous carbon layer is used only as a current

collector that is fully immersed in the alkaline aqueous electrolyte. Moreover, the carbon-based current collector layer was not consumed during the CO_2 reduction reaction (CO_2RR). This ECR GDE had an average current density of 110 mA cm^{-2} at an applied voltage of 2.4 V for one hour. In addition, the ethylene selectivity indicated no loss for 150 hours at current densities between 75 – 100 mA cm^{-2}.

In Figure 3 (c), the third GDE is a simple design and was used as an O_2 electrode in a MEA operated in an UR-AEMFC (unitized regenerative – anion exchange membrane – fuel cell)[8]. *Ng et al*. electrodeposited MnO_x on stainless steel (ss) mesh and then annealed it at 480 °C. Thus, the CL (MnO_x coating) covers the inside and outside of the GDL (ss mesh), which has similar short transport distances for O_2 as the previously mentioned ECR GDE. However, the catalyst-coated ss mesh is not hydrophobic and thus requires a hydrophobic GDL for electrochemical systems with aqueous electrolytes. Nevertheless, this GDE exhibited stable electrochemical activity during OER and ORR alternating operation for 100 cycles in 0.1 M KOH, measured with a rotating disk electrode assembly. Subsequently, the coated mesh was used in a MEA setup in an UR-AEMFC that exhibited a current density of 60 mA cm^{-2} at 1.75 V in electrolyzer mode and a current density between 43 and 57 mA cm^{-2} at 0.45 V in FC mode.

The last GDE (Figure 3 (d)) was used in a Zn-Air-Battery (OER/ORR) and as a water-splitting electrode (HER/OER)[6]. *Wang et al*. electrodeposited $Ni_{2.3}Fe(OH)_{7.6}$ on a nickel foam and then immersed it in a Na_2S solution at 25 °C for one hour. This resulted in a conversion of $Ni_{2.3}Fe(OH)_{7.6}$ to $Ni_{1.9}FeS_{1.09}(OH)_{4.6}$ on the nickel foam. All in all, this is a similar approach as the coated ss mesh, but with a potentially larger coatable surface area due to the 3D pore structure of the nickel foam. For this reason, the transport distances for dissolved O_2 are also short and the GDE is also not hydrophobic. Nevertheless, the CL has uniform electrical contact due to the electrically conductive GDL (Ni foam). The coated nickel foam GDE exhibited stable charge (1.8 V) and discharge (0.77 V) voltage at 2 mA cm^{-2} in a flexible solid-state rechargeable Zn-Air-Battery using an alkaline gel electrolyte. In addition, it exhibited excellent long-term stability after a test of 25 hours for 75 charge and discharge cycles. Moreover, it achieved an overpotential of 266 mV at 10 mA cm^{-2} during OER in 1.0 M KOH, which outperformed the Ir/C setup. Lastly, it exhibited a water splitting voltage of 1.62 V at 10 mA cm^{-2} when used on both sides (anode and cathode).

In general, all novel GDE designs (Figure 3) have their own advantages over the state-of-the-art due to their different arrangement of functional layers and different materials. These advantages can be summarized as follows:

- shorter transport distances for dissolved gasses
- more uniform and direct electrical conductivity of CL
- carbon-free materials to avoid carbon corrosion

To understand these advantages, it is necessary to take a closer look at the GDE, where the three phases, solid, liquid and gas, are in contact with each other. The three phases are:

Solid: CL (typically consisting of a catalyst and an electron conducting material)

Liquid: Electrolyte

Gas: Oxygen

It is known that the gas reduction reaction (ORR or CO_2RR) occurs at the three-phase-boundary (TPB). The three phases meet at a point on the catalyst in the GDE. This and the oxygen transport through the gas-solid double-phase-boundary (DPB_{gs}) to the TPB is shown schematically in Figure 4. The oxygen adsorbs on the catalyst surface. It then dissociates and travels by interfacial diffusion to the TPB, where the reduction reaction takes place.
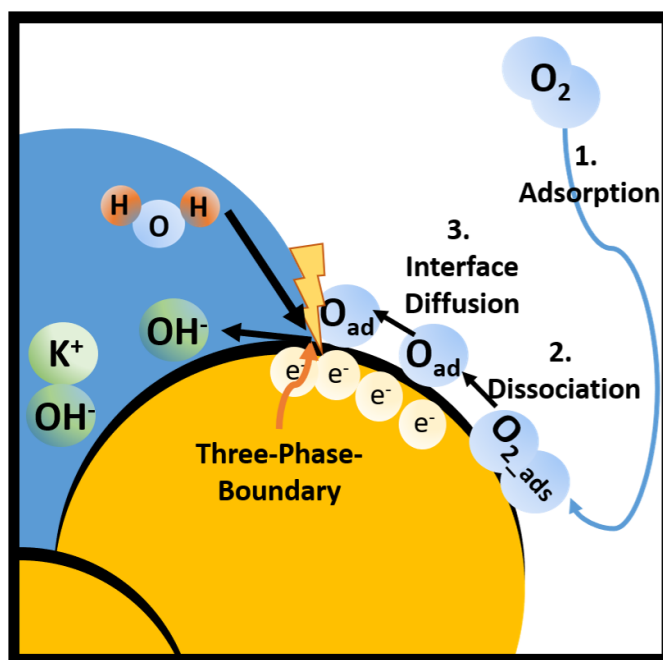
Figure 4. Schematic depiction of a gas-solid oxygen mass transport to the three-phase-boundary (TPB)[78].
Blue: electrolyte; yellow: catalyst

However, *Nesbitt et al.*[79] have shown that the liquid-solid DPB (DPB_{ls}) dominates the gas reduction reaction activity due to higher diffusion rates than at the gas-solid (DPB_{gs}) interface[80] [81]. This higher diffusion rate of oxygen to the active site at the liquid-solid interface (DPB_{ls}) occurs only in the electrolyte thin film. However, the diffusion rate depends on the thickness of the electrolyte film, which will be discussed below. In addition, this DPB_{ls} region has a larger active surface area than the TPB because the micro- and nanometer pore structure of CL is flooded by an electrolyte thin film[82]. Consequently, the DPB_{ls} region contributes more to the electrochemical activity than the

TPB region. These facts are consistent with the high current densities in an ORR or CO_2RR GDE that they observed.

Bekisch et al.[83] experimentally confirmed a DPB_{ls} GDE (schematically shown in Figure 3 (c)). They electrochemically coated a nickel mesh with MnO_x and electrochemically characterized the coated mesh in a symmetric cell in which the GDE was completely wetted with an electrolyte thin film.

Moreover, *Bockris* and *Cahan*[84] displayed different current distributions along a Pt surface in contact with a H_2SO_4 electrolyte meniscus (finite contact angle of $\sim 3\,°$ at the tip, Figure 5). The Pt surface exhibited currents within a few micrometers of the meniscus tip depending on the applied electrical potential. Lower potentials (0.39 V vs RHE) resulted in extension of the current contributing Pt surface within the meniscus to as much as 6 μm. Therefore, the thickness of the meniscus electrolyte film ranged from 3 to ~ 300 nm on the current contributing Pt surface[84] [79].

In addition, *Röhe et al.*[75] presented a model of water activity for an oxygen depolarized cathode (ODC), which is a state-of-the-art porous electrode design (Figure 2 (b)) consisting of silver particles and PTFE. They described the DPB_{ls} region as a thin-film region with a thickness of 80 nm and displayed oxygen concentration profiles for different current densities under a convective electrolyte flow and a stagnant electrolyte. In the thin-film region (80 nm thick), the initial concentration and the slope of the concentration profile depend on the applied current density. At higher current densities, the initial concentration decreases, and the slope becomes more negative. Convective electrolyte flow has a positive effect on the profiles. This confirms that water activity at low local electrolyte viscosity favors the solubility of O_2 and its rapid diffusion. However, the oxygen concentration profile decreases with increasing film thickness.

These results by *Bekisch et al.* [83], *Bockris et al.* [84] and *Röhe et al.* [75] support the findings of *Nesbitt et al.* [79] that liquid-solid DPB dominates the gas reduction reaction activity.

On this basis, a schematic representation of an electrode surface in contact with an electrolyte meniscus is shown in Figure 5 on the left. The contact surfaces are divided into a "flooded zone" at the oxygen- and electrolyte-bulk and a "high current density zone" where the electrolyte film thickness is thin. The high current density zone is represented by the dashed rectangular box. The arrows symbolize the processes described in the enlargement of the dashed box on the right.
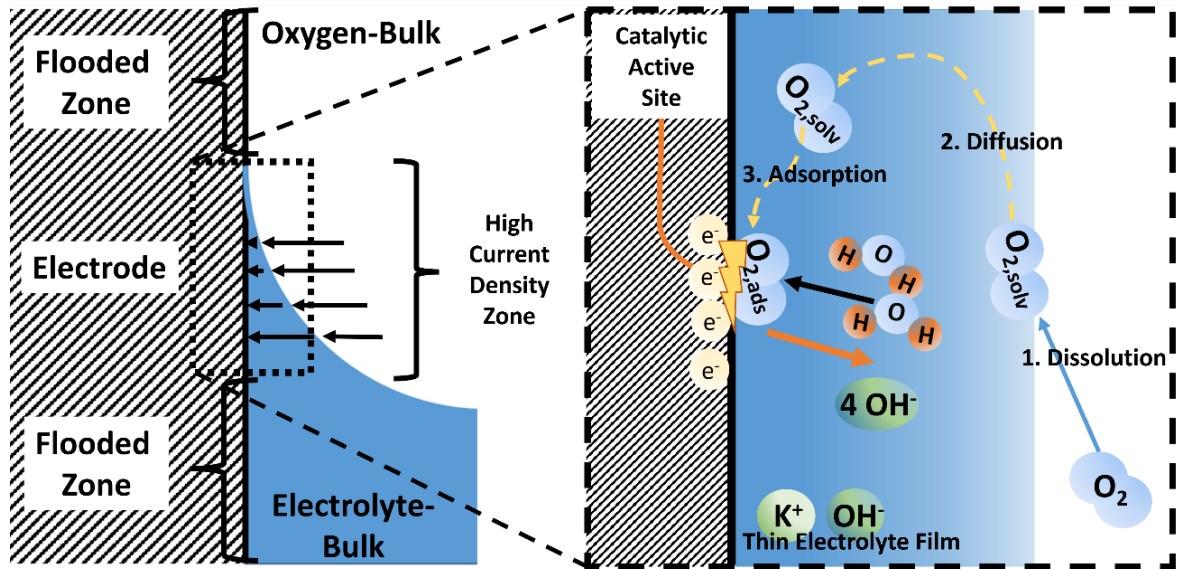
Figure 5. Schematic depiction of the three-phase zone at a meniscus and the processes for the oxygen reduction reaction at the gas-liquid and liquid-solid double-phase-boundaries (DPB$_{lg}$ and DPB$_{ls}$)[68] [79].

In the magnification, the individual process steps show the path of the oxygen molecule from the DPB$_{gl}$ (gas-electrolyte) to the DPB$_{ls}$ (electrolyte-CL). First, the oxygen molecule diffuses near the electrolyte film (DPB$_{gl}$), then dissolves there and is transported by diffusion near the CL surface (DPB$_{ls}$) [79]. There it adsorbs at the catalytically active site and subsequently the oxygen is reduced to a hydroxide ion[68].

Dissolution of CO_2 in an electrolyte film, for example, occurs by the formation of a thin CO_2 film on the electrolyte. The CO_2 molecules lose their kinetic energy from the gas phase and then dissolve in the electrolyte. This has been described by DFT and molecular dynamic (MD) simulations, and density measurements have shown that the density of the electrolyte decreases at the interface, confirming this[79] [85]. These simulations resulted in a CO_2 film of about 0.5 nm thickness on the electrolyte[79]. In addition, *Nesbitt et al.*[79] concluded that the transfer of CO_2 between phases (gas to liquid) is faster than CO_2 diffusion through the liquid phase to the catalyst site.

The dissolution of oxygen in an electrolyte thin film is expected to be similar to the dissolution of CO_2. This is because the similarity of the energy profiles and the reduced electrolyte density[79] [85] [86] indicate that the thickness of the oxygen film is comparable.

Moreover, comparison of the results of *Somasundaram et al.* [85] and *Vácha et al.* [86] shows that the free solvation energy of oxygen is lower than that of CO_2. This suggests that the dissolution of oxygen is faster than that of CO_2. The transition from the thin O_2 film to the electrolyte is symbolized by the light blue color of the electrolyte in Figure 5 on the right. In general, thin electrolyte films are advantageous for oxygen mass transport because the transport distances to the active site are shorter.

However, water activity and thus ionic conductivity play an important role in the solubility and diffusivity of O_2[75] [79] [87]. Hydration of ions (e.g., K^+ and OH^-), i.e., the binding of ions to water molecules, reduces water activity[75] [88]. The water covering capacity is inversely dependent on the electrolyte concentration[89]. The solubility of oxygen decreases with increasing electrolyte concentration[87], as ions occupy excess water molecules[75] [88]. For this reason, fewer water molecules are available for the hydration shell of an oxygen molecule, which requires six water molecules for solvation[90]. In addition, low water activity of an electrolyte leads to low diffusivity of oxygen[87] and thus slower reaction rates[91]. For this reason, very thin electrolyte films (about 3 nm or less) potentially have comparatively low water activity[84].

Consequently, the cation concentration (K^+) on the wetted CL is expected to increase locally with increasing current density. This was confirmed by *Weng et al.*[92], which also supports the previously mentioned results of *Röhe et al.*[75]. Therefore, due to the higher water activity and lower ion accumulation, the local reaction zones on CL are generally closer to the electrolyte bulk in DPB_{gl} (gas-liquid interface) than in TPB[79]. This is also supported by the fact that the ionic resistance increases at the thin tips of the electrolyte meniscus of porous electrodes ((Figure 2 (b))[93].

In summary, most of the electrochemical reactions occur in the high current density zone[68] (Figure 5). The DPB concept contributes the most to the high current density zone compared to the TPB concept due to the faster oxygen diffusivity in the electrolyte and the larger available electrochemically active surface area (DPB_{gl} → DPB_{ls}). This is illustrated by *Nesbitt et al.*[79] for CO_2 reduction (Figure 6).
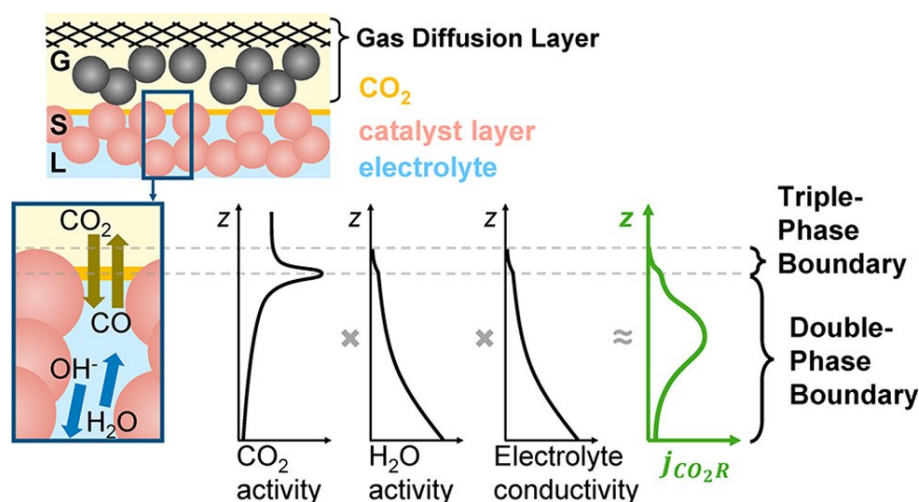
Figure 6. Comparison of the contribution of the TPB and DPB to the current density of CO_2 reduction. Reprinted with permission from Nesbitt et al.[79] Copyright © 2020, American Chemical Society.

The contributions of TPB and DPB (DPB_{gl} + DPB_{ls}) to the current density are affected by the conductivity of the electrolyte, the gas activity, and the water activity, as shown in the plots in Figure

6. As a function of distance, gas activity peaks at the gas film and decreases with increasing distance from the gas bulk. In contrast, water activity and electrolyte conductivity increase with increasing proximity to the electrolyte bulk. These variables affect the current density of the reduction reaction (green graph in Figure 6). The TPB contributes mainly in the region of the gas film, leading to the first increase in the reduction current density. After the region of the gas film, the current density increases much more in the region of the electrolyte thin film or DPB$_{ls}$, respectively. The reason for this is the increase in water activity and conductivity of the electrolyte.

Moreover, the reduction reaction takes place under the electrolyte film with a film thickness of several nanometers to one micrometer[79]. This reaction depth depends on the water activity, as it affects the solubility or dissolution of O_2 in the electrolyte. Accordingly, the water activity also affects the oxygen concentration and its diffusivity. Therefore, high electrolyte concentrations should be avoided to maintain high water activity. This will ensure that the external convection of the electrolyte will compensate for the local increase in ions, thus maintaining sufficient water activity. Nevertheless, thin electrolyte films on an electrochemically active surface should not become too thick so that the transport distance (diffusion length) of the active substances is short to maintain high current densities[72] [94].

As shown, the high current density zone – also called the "thin-film-zone" – is essential for the GDE. This is because the supply of electric current is ensured by the electrochemical reactions that take place in each pore with a thin-film-zone. This zone is influenced by the porosity of the CL, the hydrophobicity of the CL or the GDL (depending on the GDE design), the electrolyte- and gas-pressure. It is also necessary to achieve a balance between the flooded, thin-film and gas zones in the GDE by using a hydrophobic additive such as PTFE. This is because the capillary pressure of the electrolyte in the pores must be controlled to prevent flooding of the pores. However, the gas- or electrolyte-pressure must not be too high, otherwise the electrolyte will be forced out of the pores, or the pores will be completely flooded.

Figure 7 shows a schematic depiction of a state-of-the-art GDE with the corresponding mass-transport processes in the gas bulk, in the thin-film-zone and in the electrolyte bulk.
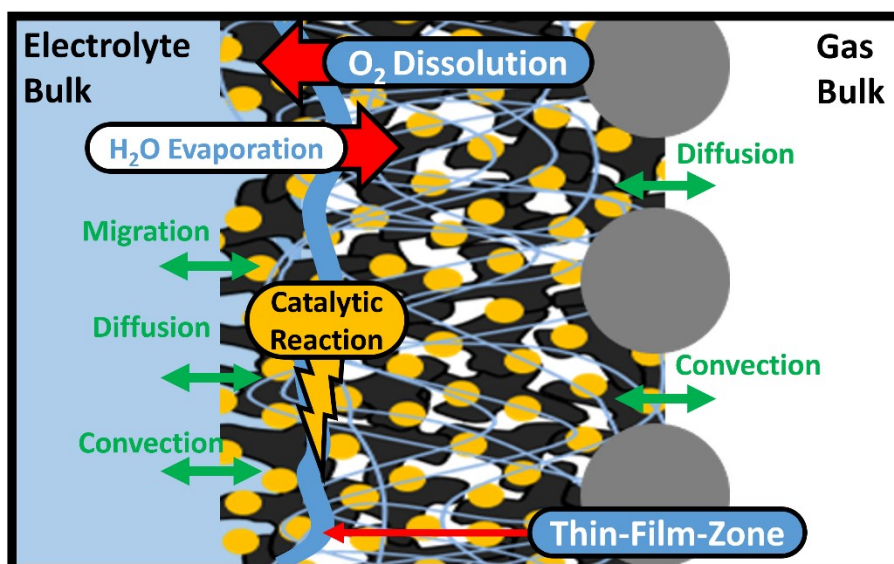
Figure 7. Schematic depiction of a state-of-the-art porous electrode GDE and the mass-transport processes during operation.

Mass transport of oxygen begins in the gas bulk during ORR (battery discharging):

Oxygen is transported through the gas pores of the electrode to the hydrophobic electrode surface, mainly by *Knudsen*-diffusion[95] or sometimes by convection[23]. Oxygen dissolves up to 10^{-3} mol l^{-1} at aqueous electrolyte concentrations between $0.1 - 1$ mol l^{-1}, at a temperature of 293 K and atmospheric pressure[87] in the thin-film-zone, which is schematically shown in Figure 5. In the DPB_{gl} (thin-film-zone), a concentration equilibrium between gaseous and dissolved oxygen is targeted during ORR operation (discharge of MAB, Figure 1). Consequently, oxygen consumption by the GDE leads to further oxygen dissolution to maintain the concentration equilibrium[95]. Evaporation of the electrolyte is driven in the same way[23]. Dissolved O_2 diffuses through the pores into the Helmholtz double layer. It adsorbs at the catalyst reaction site and the ORR takes place. The position of the thin-film-zone is influenced by the capillary pressure of the electrolyte, which is affected by wetting properties of the electrode and the hydrostatic pressure of the gas- and liquid-phases[23].

Mass transport of hydroxide ions begins in the electrolyte bulk during OER (battery charging):

Mass transport of hydroxide ions occurs by convection and migration from the electrolyte-bulk to the vicinity of the electrode surface[23] [72]. At this point, the *Nernst* diffusion layer is reached, and the ions are transported to the *Helmholtz* double layer by diffusion only. Then they adsorb on the catalyst active site by losing their hydration shell, and the OER takes place. For this diffusion through the Helmholtz double layer, an activation energy or charge transfer potential, respectively, is required. The energy for diffusion through the double layer depends on the active species, the electrolyte and its concentration and the properties of the electrode/catalyst.

These transport processes lead to spatial gradients in electrolyte concentration (hydroxide ions and dissolved oxygen) and electric potential[23]. The mass transport resistance for the particular electrochemical reaction (OER or ORR) is the sum of all individual transport processes involved in the reduction or oxidation of oxygen. Ohmic losses are determined by the conduction of e⁻ in the electrode and the conduction of ions in the electrolyte and membrane. Their influence on the total cell voltage in dependence of current density is shown schematically in the following Figure 8.
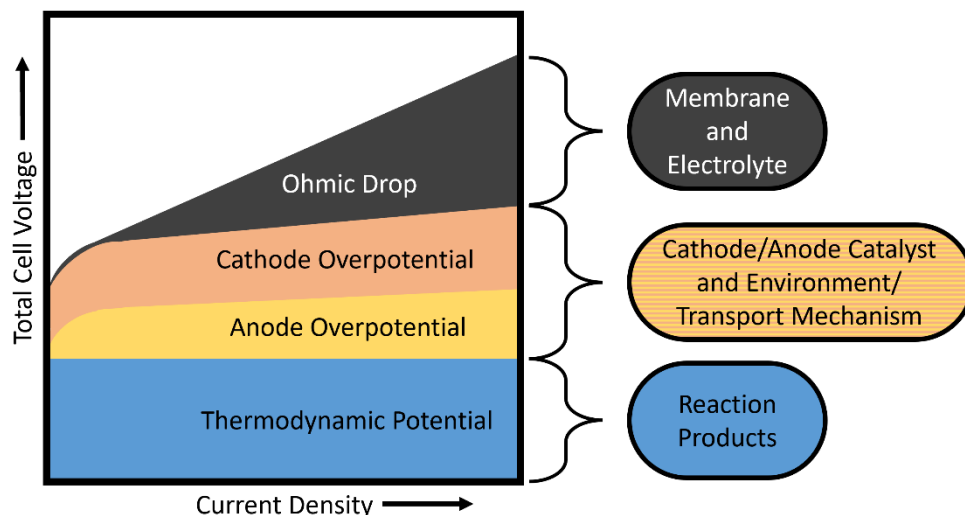
Figure 8. Current density as a function of the voltage divided into the single factors involved and their corresponding cause.

The thermodynamic potential is a constant value for the reaction, but the overpotential of the anode and cathode varies depending on their electrochemical activity, the electrochemical environment used, and the transport mechanisms at the applied current density. In addition, the limited ionic and electron conductivity of important parts of the cell, such as the membrane and electrolyte, the current collector, and – possibly – the cell´s housing plates, results in ohmic resistance, also known as ohmic drop. This contributes to the fact that the total voltage of the cell increases with increasing current density.

The group of *Krewer*[23] [72] and *Turek*[96] [97] summarized some modeling options for various GDE applications. However, the most critical point of a GDE is its electrolyte thin film. Accordingly, mass transport plays a key role. The mass transport of oxygen during ORR is the rate-determining step, since the active reactant (OH⁻) is already dissolved during OER and is available in large amounts near the catalyst sites. Since the oxygen must first be dissolved in the electrolyte thin film before diffusing to the active site, where it is finally adsorbed on the catalyst site during ORR. The mass transport of oxygen and OH⁻ have been studied in a model-based manner to understand their critical influence and limitations and to find possible improvement potential of the GDE[94] [97] [98] [99].

2.1.3 Hydrophobicity

Hydrophobicity is required in GDEs for the GDL, which provides gas transport but inhibits aqueous fluid transport or evaporation[100]. The GDL is critical for the thin electrolyte film that affects the electrochemical performance of the entire GDE. To understand the GDL, the fundamentals of hydrophobicity are important. In general, hydrophobic surfaces increase the corrosion resistance of exposed surfaces in the environment and maintain their long-term chemical stability. One measure of hydrophobicity is the contact angle of the liquid on the solid surface, described as wettability. Figure 9 shows three schematic examples of possible contact angles.
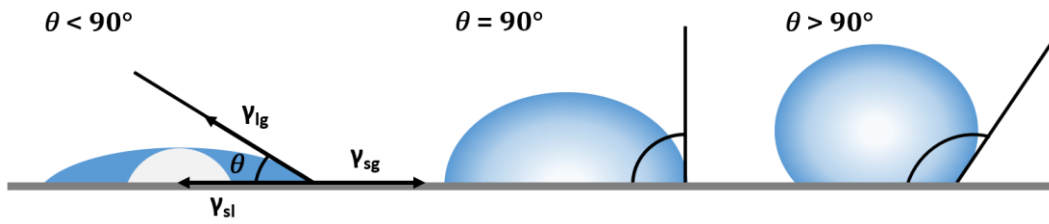
Figure 9. Schematic depiction of sessile liquid drops on a smooth homogeneous solid surface and their corresponding formed contact angles (γ_{lg}: liquid-gas interface tension; γ_{sg}: solid-gas interface tension, γ_{sl}: solid-liquid interface tension). Yuan and Lee, 2013[101]. Added with permission of Barati Darband, G. et al., 2018[102]. CC BY-NC-ND license (http://creativecommons.org/licenses/by-nc-nd/4.0/).

Solid surfaces with a contact angle of about 90 ° are hydrophobic, greater than 90 ° are superhydrophobic, and less than 90 ° are hydrophilic. The contact angle is affected by the surface energy, surface roughness, and surface tension of the liquid. The surface energy can be lowered, for example, by using silane groups, which increases the electrical resistance[102]. Surface tension is the derivative of free enthalpy (G) as a function of surface area (A) at constant temperature and pressure. This is shown in the following equation:

$$\gamma = \left(\frac{dG}{dA}\right)_{T,p} \qquad \text{m. Eq. 1}$$

The interfacial tensions between phases (γ_{sg}: solid-gas; γ_{sl}: solid-liquid; γ_{lg}:liquid-gas) determine the contact angle of a liquid droplet on an ideal flat surface. Therefore, *Young´*s equation is used (mathematical equation 2 (m. Eq. 2))[102]:

$$\cos\theta = \frac{\gamma_{sg} - \gamma_{sl}}{\gamma_{lg}} \qquad \text{m. Eq. 2}$$

However, surface roughness is not considered in *Young's* equation. Therefore, *Wenzel* introduced an equation (m. Eq. 4) in which the surface roughness is taken into account by the roughness factor "r" (m. Eq. 3) [103]:

$$r = \left(\frac{A_{actual}}{A_{geo}}\right) \qquad\qquad \text{m. Eq. 3}$$

$$r * (\gamma_{sg} - \gamma_{sl}) = \gamma_{lg} \cos \theta_W \qquad\qquad \text{m. Eq. 4}$$

This equation represents the change in wettability as a function of the surface property. Surface roughness increases the contact angle of a flat surface when the contact angle is greater than 90 °. If it is smaller than 90 °, the contact angle is decreased due to the increase in surface roughness[104]. Consequently, the *Wenzel* model is applicable only for homogeneous surfaces and not for heterogeneous surfaces[102] [104].

This model is helpful to understand that rough surfaces of a GDL or CL behave completely differently when they are in contact with the aqueous electrolyte and their roughness increases. In general, both have homogeneous surface structure but different contact angles. GDL is hydrophobic and for this reason higher roughness increases the contact angle. However, the contact angle of the CL becomes smaller as the roughness increases. Since the CL should be hydrophilic to ensure a large contact area with the electrolyte.

The heterogeneous rough surfaces are assumed to be heterogeneous solid surfaces with air pockets. Therefore, *Cassie and Baxter*[105] defined the contact angle with the following equation (m. Eq. 5):

$$\cos \theta_{C\&B} = f_{s1} * \cos \theta_{s1} + f_{s2} * \cos \theta_{s2} \qquad\qquad \text{m. Eq. 5}$$

The cosine of the contact angle of a liquid droplet on a heterogeneous surface is equal to the sum of the cosines of the contact angles on two different homogeneous surfaces of the respective materials, each multiplied by its surface area (f_{s1} and f_{s2}). The contact angle of the air-surface is assumed to be 180° and thus the equation is (m. Eq. 6)[105]:

$$\cos \theta_{C\&B} = f_s * (\cos \theta_s + 1) - 1 \qquad\qquad \text{m. Eq. 6}$$

Figure 10 shows schematically the three wetting models mentioned. It must be emphasized that a hydrophobic rough heterogeneous surface in contact with a liquid has air pockets (*Cassie and Baxter* model). For example, a heterogeneous rough surface has nanometer-scale structures overlying

micrometer-scale structures[106] [107]. They are therefore also referred to as hierarchical surface structures (Figure 11).
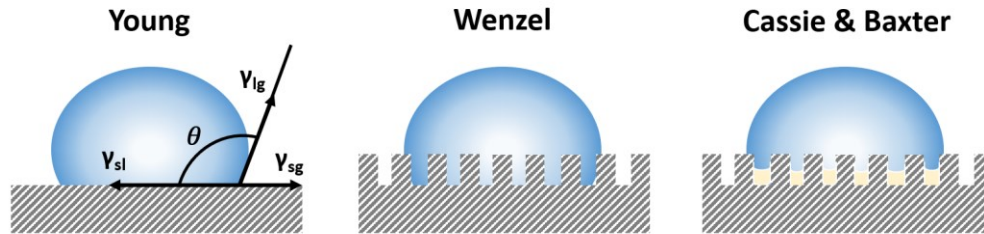
Figure 10. Schematic depiction of the three different mathematical wetting models. Added with permission from Barati Darband, G. et al., 2018 [102]. CC BY-NC-ND license (http://creativecommons.org/licenses/by-nc-nd/4.0/).
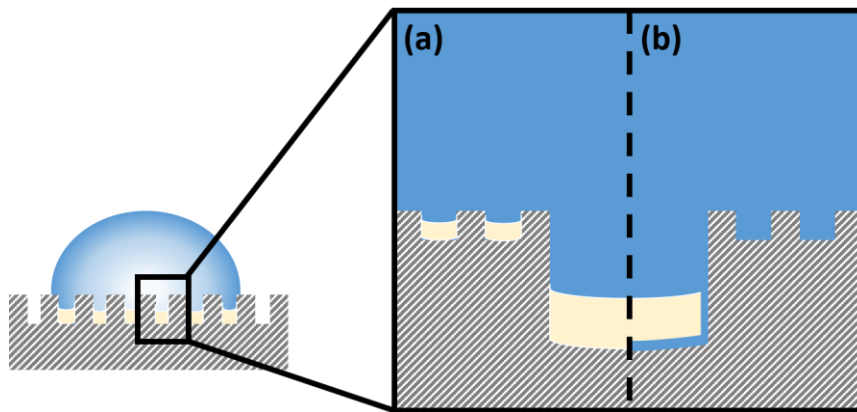
Figure 11. Schematic depiction of a hierarchical surface structure with a droplet exhibiting trapped air pockets ((a) hydrophobic[106]; (b) hydrophilic[107]).

In Figure 11 (a), hydrophobic hierarchical structures show nano- and micrometer-scale air entrapment, as described by *Nagayama and Zhang*[107]. In contrast, the hydrophilic hierarchical structure (Figure 11 (b)) shows filled capillaries in nanometer-scale structures and partially filled micrometer-scale structures with an entrapped air pocket, as described by *Bormashenko and Starov*[106]. This helps to understand the wetting behavior of the aqueous electrolyte of a CL and GDL in terms of hierarchical structures.

In nature, there are even combinations of hydrophobic and hydrophilic surfaces such as the leaf of the *Salvinia* plant, which has a superhydrophobic surface (Figure 12)[108]. This superhydrophobic plant leaf exhibits a stable air-film under water due to the hydrophilic tip of the plant hairs. The hydrophilic properties of the hair-tips are shown in Figure 12 (b).

2 Literature
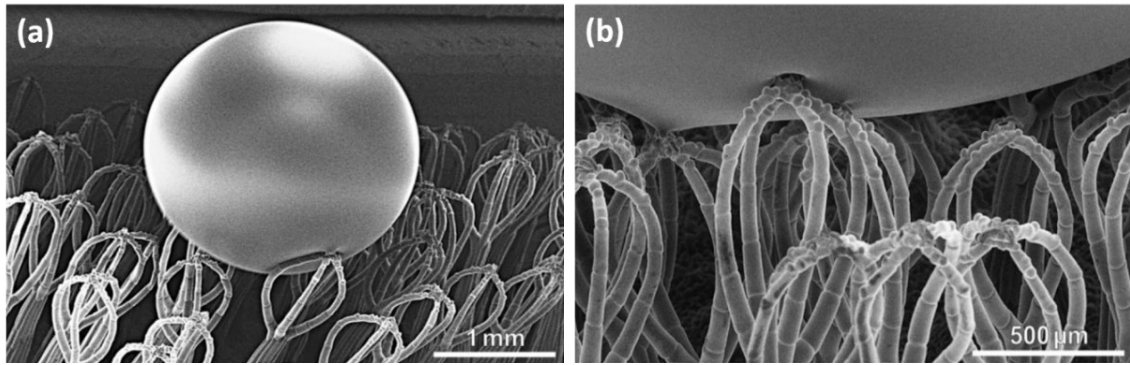
Figure 12. SEM image of Salvinia leaf and their hairs with a droplet of a water-glycerol solution in (a) 1 mm and (b) 500 μm range. Barthlott et al., 2010; Reproduced with permission. All rights reserved[108].

This combination of completely different surface properties inherently helped the leaf to create a large DPB surface area between gas- and liquid-phase. A similar combination approach could be applied to the GDE to increase the surface area of the electrolyte thin film. Since the electrolyte thin film on the CL, as mentioned earlier, is the main factor for the ORR on a GDE.

In general, the CL should be in good contact with the electrolyte (wetted) for the electrochemical reactions, i.e., it should be hydrophilic. The hydrophobic GDL restricts the passage of the electrolyte to ensure gas transport. The GDLs are made of carbon-[15] [20] [68] [69], PTFE-[44], or metal-based [109] [110] [111]. Carbon materials coated with polytetrafluoroethylene (PTFE - Figure 13 (a)) are most commonly used[20] [47] [51] [112]. There are also other additives such as polyvinylidene fluoride (PVDF - Figure 13 (b)) and fluorinated ethylene propylene (FEP - Figure 13 (c)) that are used as hydrophobic additives for the GDL[20] [113]. Their chemical structures are shown in Figure 13.

There are several methods to apply the hydrophobic additive into the GDL. Dipping, spraying, or brushing, with dipping being the most commonly used method[20].
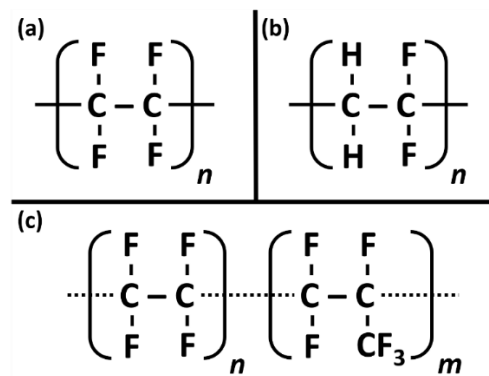
Figure 13. Chemical structures of (a) polytetrafluoroethylene (PTFE), (b) polyvinylidene fluoride (PVDF) and (c) fluorinated ethylene propylene (FEP).

The hydrophobicity is regulated by the applied mass of the hydrophobic additive. *Chan and Wang[113]* developed a carbon paper with a FEP mass fraction of 10 % that served as a GDL. This

displayed the highest current densities at different operating temperatures. It was mentioned that a higher FEP mass fraction tends to clog the pores and therefore reduces reactant transport and product removal. For this reason, the proper amount of hydrophobic additive is also critical to the electrochemical performance of a GDE.

In general, the hydrophobicity in the GDE or GDL is controlled by the amount of PTFE compared to the total mass of the GDE and by its surface structure.

2.1.4 Bifunctionality

Certain GDE applications must be electrochemically capable of the back-and-forth reaction such as OER and ORR or HER and HOR. These are bifunctional GDEs used, for example, in UR-PEMFCs and MABs (chapter 2.1.1). Regenerative fuel cells, such as the UR-PEMFC, have two different bifunctional GDEs to enable an electrolyzer working mode to produce H_2 (HER) and O_2 (OER) and a fuel cell working mode to consume H_2 (HOR) and O_2 (ORR) to produce electricity. The MAB has only a bifunctional GDE that charges the MAB through OER and discharges through ORR. This bifunctionality is achieved by the using bifunctional catalysts or combining individual catalysts for each reaction in the CL. The catalysts should be suitable for the particular environment (alkaline or acidic) to enable the reaction.

The specific reactions of UR-PEMFC in an acidic environment require mainly noble metals such as Pt, Ir, and Ru to achieve high current densities[40]. This is because these noble metals are thermodynamically stable in this environment[19]. However, there are several research approaches for catalysts based on non-precious metals for UR-PEMFCs, such as N-doped carbon (N-BCE3)[114] or copper/manganese oxide ($Cu_{1.5}Mn_{1.5}O_4$)[115]. In general, Pt has the highest activity for the ORR[116] in the FC mode. However, it oxidizes and this leads to stability problems in the electrolyzer mode[40]. Therefore, Ir-based catalysts are used for the OER[117] despite their low ORR activity[118]. On the other electrode side, the HOR and HER take place, which are also supported by Pt and Ir with minor mass transport limitations[119] [40]. However, the stability of HER is limited by impurities in the supplied water, chemical decomposition, and thermomechanical deformation[19]. A comparison of the hydrogen and oxygen electrode sides shows that the bottleneck of UR-PEMFC is on the oxygen side. Attempts are being made to overcome this bottleneck with noble metals. In general, noble metals such as platinum or iridium oxide on a carbon support are the most common and commercially used catalysts for acidic reaction environments because they are thermodynamically stable[10] [120] [121].

As mentioned earlier, the MAB has only a bifunctional GDE for the OER and ORR. For these reactions in alkaline environment, the same noble metals are used as in UR-PEMFC. These noble metal catalysts (Pt, Ru or Ir) can be alloyed[122] [123] and hybridized[124] [125] with transition metals to increase the bifunctional activity and stability and reduce the cost[17]. However, there are more alternatives to noble metal catalysts in alkaline media than in acidic media. Non-noble metals such as nickel, manganese, and cobalt and their oxides are thermodynamically stable above the OER and below the ORR electrical potentials at high pH[19]. With great effort, the same methods (alloying and hybridization with transition metals) are applied to non-noble metal catalysts to increase their activity and durability. Their lower cost compared to noble metals makes them attractive. Consequently, various perovskites, spinels and oxides and their combinations are used as bifunctional catalysts to overcome the dependence on noble metals[126] [127] [128]. The different types of catalysts are categorized

into carbon-based and non-noble metal-based catalysts [1] [2] [3] [10] [128]. These categories can also be divided into several subcategories, which are shown in Figure 14.
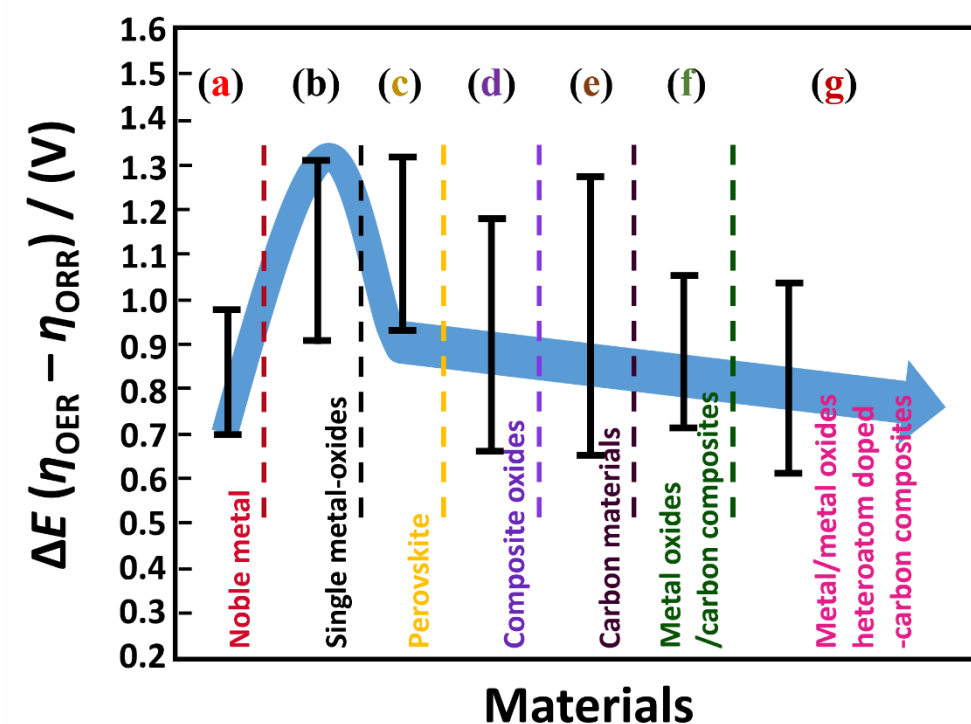
Figure 14. Overview of bifunctional catalyst materials and their cumulative overpotentials ΔE at 10 mA cm⁻²
for OER and 3 mA cm⁻² for ORR. (cumulative overpotential: sum of η$_{OER}$ and η$_{ORR}$; (a): Noble metal; (b): Single
metal-oxides; (c): Perovskites; (d): Composite oxides; (e): carbon materials; (f): Metal oxides/carbon
composites; (g): Metal/metal oxides heteroatom doped-carbon composites). <u>Wu et al., 2020</u>;slightly
redesigned; Reproduced with permission.

In Figure 14, *Wu et al.* [128] summarized bifunctional catalysts and their cumulative overpotentials (sum of η$_{OER}$ and η$_{ORR}$) of composite oxides (d), carbon materials (e), metal oxides/carbon composites (f), and metal/metal oxides heteroatom doped-carbon composites (g). These cumulative overpotentials are similarly low or even lower than the overpotentials of the noble metal category. Thus, there are many alternatives to noble metal catalysts. Single metal-oxides and perovskites have higher cumulative overpotentials than noble metals. However, they overlap and therefore it is possible to use single metal-oxides and perovskites that can compete with noble metals by using more non-noble metal catalyst mass[2].

Transition metals such as nickel, manganese, iron, cobalt, and the corresponding oxides are discussed in more detail below. *Dresp* and *Strasser*[2] have presented some non-noble metal oxides as bifunctional catalysts and compared them with the commercial catalysts (Pt and Ir). The results are summarized in Figure 15.
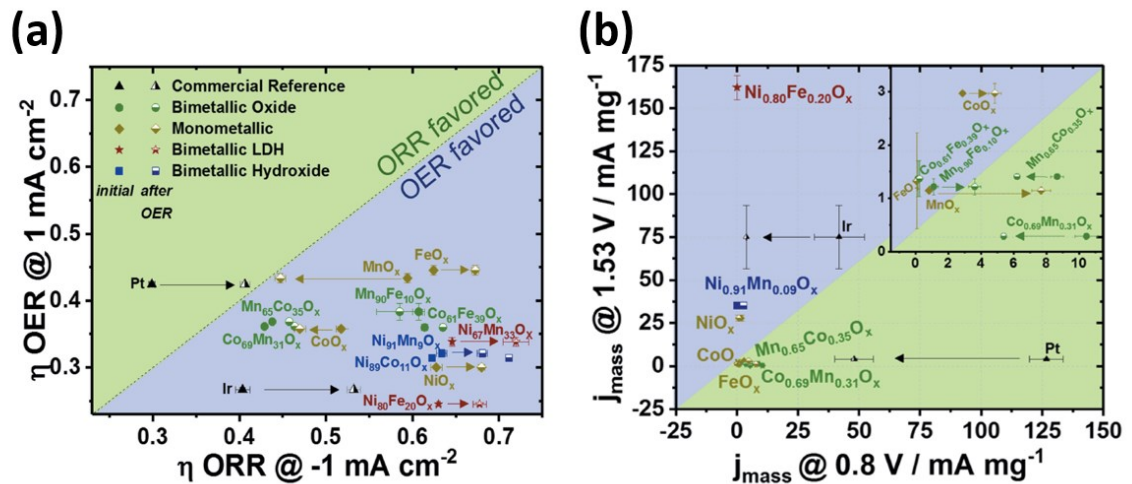
Figure 15. (a) Diagram of catalyst materials at -1 mA cm^{-2} (ORR) and 1 mA cm^{-2} (OER). (b) Elemental metal mass activities for different catalysts at 1.53 V (OER) and 0.8 V (ORR) vs. RHE. (LDH: layered double hydroxide). Dresp and Strasser, 2018; Reproduced with permission. All rights reserved[2]

Monometallic and bimetallic catalysts were studied and categorized as ORR- or OER-favored at different workloads. In general, many characterized catalysts are OER-favored at $\pm$ 1 mA cm^{-2}. Some of the non-noble metal catalysts were approximately in the same overpotential range as the noble metals at this galvanostatic workload (Figure 15 (a)). However, the elemental metal mass activities show the superiority of Pt and Ir (Figure 15 (b)). This can be compensated by higher masses of non-noble metal catalysts. NiO_x, CoO_x, and FeO_x tend to favor OER and MnO_x tends to favor ORR in the elemental metal mass activity analysis (Figure 15 (b)). These single metal- or monometallic-oxides have a relatively low synthesis effort. Therefore, these catalysts are a good way to get a first look at a novel GDE design by using these materials as catalysts. In general, the following orders of single metal-oxides show which of them have lower overpotentials at OER and ORR [128]:

OER: $NiO_x > CoO_x > FeO_x > MnO_x$

ORR: $MnO_x > CoO_x > FeO_x > NiO_x$

NiO_x at OER and MnO_x at ORR are good complementary catalysts, when combined with each other.

There are several approaches to combine these materials and several methods to apply a catalyst (MnO_x) to the surface of an electrically conductive, carbon-free support (nickel or nickel alloy). For example, there is atmospheric plasma spraying (APS)[129] [130], sputtering[44] [47], hydrothermal synthesis[131] [132], and electrochemical deposition [8] [133] [134] [12].

Electrochemical deposition is discussed in more detail below. Electrochemical deposition can be used to apply catalyst coatings with different properties by varying various factors:

- electrical potential/current

- potentio-/galvanostatic/ or potentio-/galvanodynamic mode

- deposition time

- temperature

- concentration of the deposition-electrolyte

Chou et al.[133] electrochemically deposited thin films of starfruit-like (carambola-like) γ-MnO_2 nanoflakes with a thickness of 20 nm on nickel sheets. They combined potentiostatic and cyclic voltametric electrodeposition techniques. Electrochemical measurements have shown a high potential plateau of about 1 V vs. Zn in a primary Zn/MnO_2 cell at 500 mA g^{-1} and a high specific capacitance of 240 F g^{-1} at 1 mA cm^{-2}.

Cao et al.[134] deposited hierarchical radial nickel phosphide (Ni_xP) nanospheres on nickel foam by potentiostatic electrodeposition. This bifunctional Ni_xP/Ni foam electrode exhibited an overpotential of 63 mV at 10 mA cm^{-2} in 1 M KOH. Moreover, this electrode exhibited a high specific capacitance of 382.7 F g^{-1} at 2 mA cm^{-2}.

Tsai et al.[12] deposited meso-macroporous structures of pyrolusite MnO_2 on nickel foam by combinations of potentiostatic and potentiodynamic electrodeposition techniques. In addition, an asymmetric supercapacitor was fabricated by combining MnO_2/Ni foam as the positive electrode and activated carbon as the negative electrode. It provided 7.7 Wh kg^{-1} at 600 W kg^{-1} and exhibited a retention ratio of 98 % of the original capacity after 10,000 cycles.

Ng et al.[8] coated MnO_x on stainless steel mesh by cyclovoltammetry and calcined it at 480 °C in air for 10 hours. This electrode exhibited high oxygen reduction and water oxidation activity in a rotating disk electrode assembly. It also exhibited stable OER and ORR current densities for 100 cycles.

These four examples of electrodeposited coatings show that they are suitable for MABs and URFCs. It is also possible to control the applied surface structure, thickness and mass of the catalyst.

2.1.5 Durability

One possible definition of the durability of a GDE is the electrochemically stable performance over a certain time or over a certain number of cycles, understood here as alternating sequences of OER and ORR. The electrochemically stable performance depends on the electrochemical and chemical stability of CL and GDL. The mechanisms behind the stability losses of CL and GDL are described below.

There are chemical and physical changes of CL, which reduce the electrochemical activity. In general, it is necessary to use catalysts that are stable in the electrolyte and the electrical potential range in which it is used. The thermodynamic diagrams of *Pourbaix[135]* show certain regions of stability, passivation, and corrosion for different materials. Nevertheless, there are still some negative mechanisms that reduce the electrocatalytic activity of CL (Figure 16).

1. Catalyst poisoning by adsorption of metallic impurities of the electrolyte[136] [51] [19]. This can be reversed by a reoxidation step that desorbs the adsorbed species[137].

2. Pulverization of the catalyst layer[51] due to the incorporation of hydrogen into the catalyst lattice, leading to catalyst fracture. This was shown by *Wu et al.*[138].

3. *Ostwald* ripening leads to agglomeration of electrocatalysts by dissolution and redeposition on larger catalyst particles[19] [139] [140] [141]. This leads to a reduction in the electrocatalytically active surface area and *ergo* to a lower electrochemical activity of the GDE.

4. Chemical degradation of the catalyst binder (e.g., Nafion®) due to anion attack on the fluorinated structures causing molecular changes. This leads to depolymerization or alteration of the side chains resulting in loss of catalyst particles[51] [142].

5. Detachment of the catalyst from the substrate (GDL) due to changes in the passivation layer and/or corrosion of the catalyst or carbon substrate[19] [140] [141].
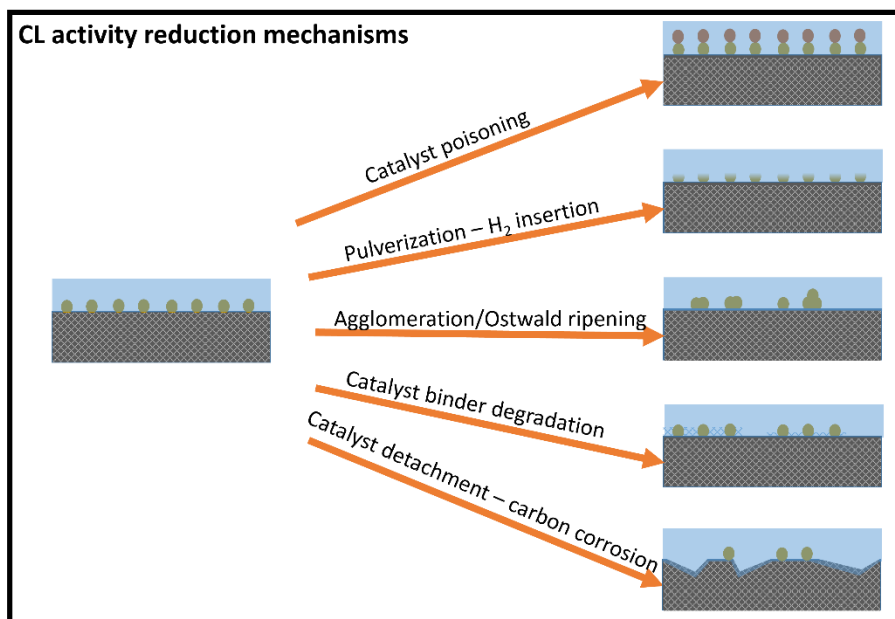
Figure 16. Schematic depiction of various CL activity reduction mechanisms.

In addition to these problems of CL, there is the problem of GDL flooding caused by the reduction of hydrophobicity. The result is a decrease in performance due to the reduction of gas channels. GDL flooding can result from several mechanisms, which are described below (Figure 17).

1. Electrowetting is controlled by the applied electric potential as it affects the surface tension of the liquid-solid phase[112] [143] [144]. *Yang et al.*[112] pointed out that electrowetting in the carbon-based GDL occurred at – 0.68 V and the flooding rate actually increased with increasing negative potential (– 0.83 V vs. RHE). However, no flooding occurred at – 0.60 V vs. RHE. Therefore, they recommend the use of highly active catalysts that exhibit low overpotentials.

2. Flooding is caused by a local increase in the concentration of OH$^-$ during ORR[15] [144] [145]. *Hull et al.* [145] have shown that the ORR zone moves or narrows, respectively, due to the local increase in OH$^-$ concentration through the electrode. Since these ions must be hydrated by water molecules, which result in a movement of water from the electrolyte bulk toward the high ion concentration. This leads to flooding of the GDE.

3. Precipitation of K_2CO_3 due to CO_2 in the air[15] [51] [144] [146]. First, the dissolution of CO_2 leads to a slow exchange of OH$^-$ with CO_3^{2-}, which causes a decrease in ionic conductivity. Then, K_2CO_3 particles form in the pore structure, leading to a decrease in hydrophobicity, and the GDE is slowly flooded. Moreover, these salt particles also block the surface of CL, and their solubility is low in CO_3^{2-} saturated electrolyte.

4. Pressure difference between the liquid and gas sides[15] [143] [147]. It is important to control the pressure on both sides. Otherwise, the electrolyte will be forced out on the

gas side and the number of gas channels will be reduced, or the gas will be forced out on the electrolyte side and the gas bubbles will reduce the contact surface area between CL and the electrolyte. Both scenarios lead to a reduction in electrochemical performance.

5. Corrosion of carbon by peroxide. It slowly oxidizes the edges of exposed carbon to C-O bonds and converts them to CO_2 in the reduction reaction of GDE. This leads to hydrophilic surfaces due to the oxygen bonds on the carbon surface and loss of carbon material due to corrosion. Therefore, the flooding of carbon-based GDLs is slowly increasing. Moreover, anodization of carbon to CO_2 also occurs at high electrical potentials due to low OER electrochemical activity. As a result, anodization intensifies the flooding mechanism. There are several studies that conclude this[15] [44] [51] [144] [146].

6. Chemical alteration of PTFE by high electrochemical potentials. *Shapoval et al.*[148] pointed out that PTFE decomposes at – 2 V vs. SCE, *Yang et al.*[112] displayed that decomposition of PTFE can occur at less negative potentials. *Schulze et al.*[149] and *Yang et al.*[112] described the decomposition mechanism of PTFE-bonded GDEs by XPS measurements. The C-F bonds of PTFE break during decomposition and C=C and/or C-O bonds are formed, which are hydrophilic. This mechanism contributes to the flooding of the GDL, but only to a small extent. This is because other mechanisms are faster (electrowetting) and more destructive (carbon corrosion)[51] [112].
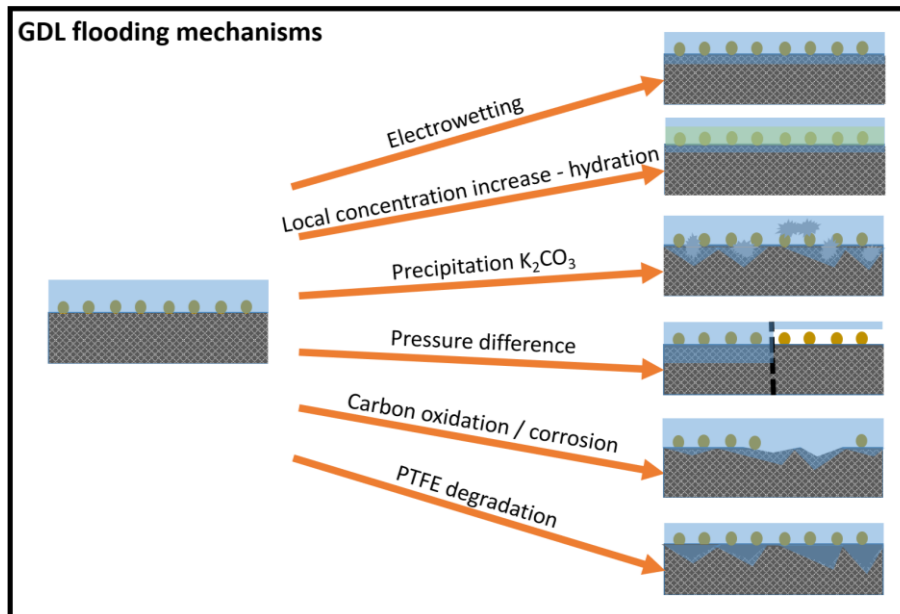
Figure 17. Schematic depiction of various GDL flooding mechanisms.

All in all, some of the negative mechanisms described are slower than others and become noticeable only after a certain long period of operation, such as the chemical stability of PTFE and Nafion®. In addition, the material limits are known. Therefore, the operating environment can be kept within these limits by adjusting the electrolyte concentration and using highly active electrocatalysts to achieve low electrical potentials.

Otherwise, other electrolytes or materials are used to replace those that are harmful or unstable. For example, the replacement of carbon materials as substrates or GDLs is necessary to prevent the influence of carbon corrosion. This eliminates two negative mechanisms that lead to flooding and loss of catalysts. It is important to look at the electrode reactions of oxygen in alkaline environments to understand OER and ORR and why carbon corrosion is caused.

2.2 Electrochemical Reactions in the Gas Diffusion Electrode

2.2.1 Alkaline Oxygen Evolution and Reduction Reaction

The oxygen evolution reaction (OER) and the oxygen reduction reaction (ORR) are the key reactions for applications such as electrolyzers, fuel cells or metal-air batteries. For example, in metal-air batteries (Figure 18), the charging process is the evolution of oxygen (OER) and the discharging process is the consumption of oxygen (ORR).
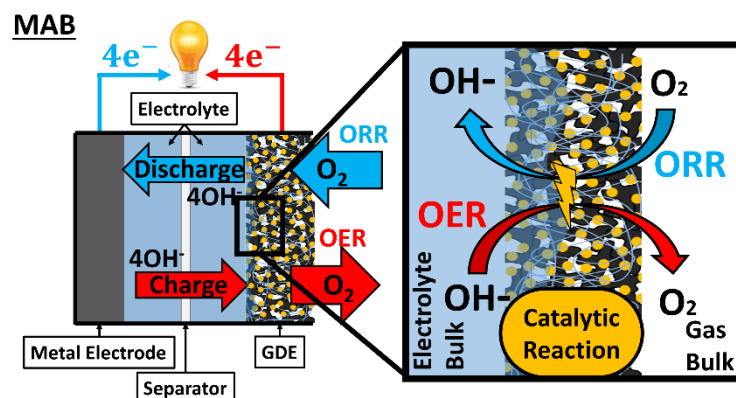
Figure 18. Schematic depiction of a metal-air battery and its reactions.

In OER the reactants are OH^- in alkaline and H_2O in acidic electrolytes. The steps for the alkaline OER are shown in the following general reaction pathway (S is an active catalyst site)[150]:

$$OH^- + S \leftrightharpoons SOH + e^- \qquad\qquad\qquad\qquad\qquad \text{E 13}$$

$$SOH + OH^- \leftrightharpoons SO + H_2O + e^- \qquad\qquad\qquad \text{E 14}$$

$$2\,SO \leftrightharpoons O_2 + 2\,S \qquad\qquad\qquad\qquad\qquad\qquad \text{E 15}$$
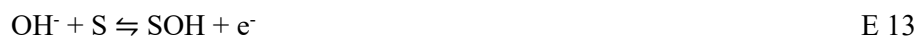
However, there are four other possible OER paths, each with several intermediate steps in the alkaline electrolyte, summarized by *Matsumoto* and *Sato*[151]. The indicated reaction pathway (E 13 – E 15) is assumed to have also a hydrogen peroxide and a peroxide path[150]. The different electrochemical paths were summarized by *Giordano et al.*[152], which are shown below in dependence of the pH environment (Figure 19).
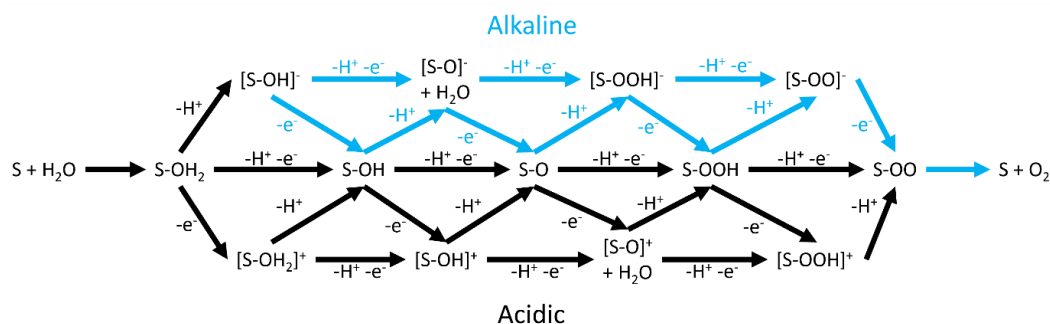
Figure 19. Schematic depiction of OER pathway for alkaline and acidic regime. Added with permission from Giordano et al., 2016 [152]. Copyright © 2015 Elsevier B.V. All rights reserved.

Figure 19 shows schematically the complex OER pathway through the blue arrows for alkaline electrolytes, where each intermediate represents an electron step. It begins with the adsorption of water at the active site and continues with one-electron steps leading to a peroxide ion intermediate in the third step. Peroxide is known to be reactive and can attack the carbon in the GDE, leading to carbon corrosion[4] [153]. However, the peroxide usually reacts with a hydroxide ion in the final step to form water and molecular oxygen at the catalyst site. However, the reaction path also depends on the crystal structure and oxidation state of the catalyst. For example, RuO_2 has two or four electron paths without the intermediate step of peroxide[152].

The *Pourbaix[135]* diagram of oxygen is calculated thermodynamically as a function of pH and electric potential (Figure 20).

This diagram shows that as pH increases, the electrical potential for oxygen evolution and reduction decreases. The alkaline regime is so attractive for OER and ORR systems because more non-noble metal catalysts are available that are stable in this alkaline regime and at these electrical potentials (chapter 2.1.4). The light blue area marks an alkaline regime between a pH of 12 and 13. The different colored bars within the long bar show the calculated equilibrium of all oxidation and reduction reactions of oxygen. In general, the production of O_3 and H_2O_2 or HO_2^- should be avoided due to their highly reactive properties.

This thermodynamically derived *Pourbaix[135]* diagram is only an orientation for the particular electrochemical setup, which helps to estimate the reaction product at a given electric potential and pH. The electrochemical kinetics play an important role in the formation of products, which can be controlled by the proper use of catalysts.

Figure 20. Potential-pH equilibrium diagram of the oxygen – water system at 25 °C. Diagram slightly changed. Added with permission from Pourbaix [135]. Rightsholder: AMPP GLOBAL CENTER, INC All rights reserved.

On the other hand, there is the alkaline ORR. The four-electron or so called "direct" pathway is as follows:

$$O_2 + 2\ H_2O + 4\ e^- \leftrightharpoons 4\ OH^- \qquad\qquad\text{E 16}$$

It is generally assumed that the OER corresponds to the back reaction of E 16. However, there is an additional two-electron reaction or indirect pathway, respectively, that runs parallel to the four-electron reaction[68]:

$$O_2 + H_2O + 2\ e^- \leftrightharpoons HO_2^- + OH^- \qquad\qquad\text{E 17}$$
$$HO_2^- + H_2O + 2\ e^- \leftrightharpoons 3\ OH^- \qquad\qquad\text{E 18}$$
$$O_2 + 2\ H_2O + 2\ e^- \leftrightharpoons H_2O_2 + 2\ OH^- \qquad\qquad\text{E 19}$$

Equation E 17 shows the reduction of oxygen to a peroxide ion. It is further reduced to three hydroxide ions (E 18). Equation E 19 is another competitive oxygen reduction reaction, producing

hydrogen peroxide. The electric potentials at a given pH for these reactions can be estimated from the *Pourbaix*[135] diagram of oxygen (Figure 20). It is well known that the ORR and OER have a sluggish four-electron charge transfer kinetic[1] [2]. This leads to high overpotentials and consequently large inefficiencies. In general, these reaction pathways occur on an electrochemically active surface area of a catalyst via various adsorption mechanisms. Adsorption at one end of the oxygen molecule (Figure 21 (a)) leads to the two-electron ORR pathway due to a relatively undiminished bond.
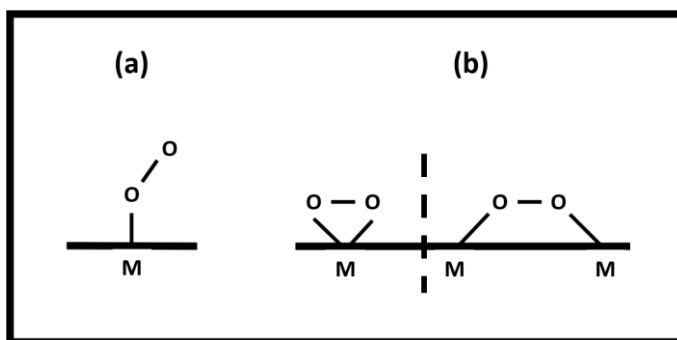
Figure 21. Schematic depiction of (a) one- and (b) both-end adsorption mechanisms of oxygen on a catalyst surface[68].

The both-end adsorption at one site and at two sites (bridge form) of a catalyst surface is shown schematically in Figure 21 (b). In contrast to one-end adsorption, it reduces the second bond and enables the four-electron ORR.

In general, the electrochemical catalyst should have low overpotentials at high current densities. This is possible if there are no parallel reactions such as the two-electron pathway shown, which leads to higher overpotentials. This is because all of the intermediate steps in the two-electron pathway have a higher total energy consumption than the four-electron pathway. In addition, these intermediate steps generate highly reactive species such as peroxide or hydroperoxide that can attack the components of the electrode, resulting in a shorter durability[4] of a GDE.

2.2.2 Carbon Corrosion

In carbon-based GDEs, carbon corrosion occurs, which is triggered by the aforementioned peroxide evolution (two-electron ORR pathway) and the subsequent purely chemical reactions as well as the electrochemical oxidation reaction of the carbon surface (E 20).

$$C + 2\,H_2O \rightarrow CO_2 + 4\,H^+ + 4\,e^- \hspace{4cm} \text{E 20}$$

Carbon oxidation also leads to hydrogen evolution. The standard potential of this carbon oxidation reaction as a function of pH, is shown in Figure 22 below.
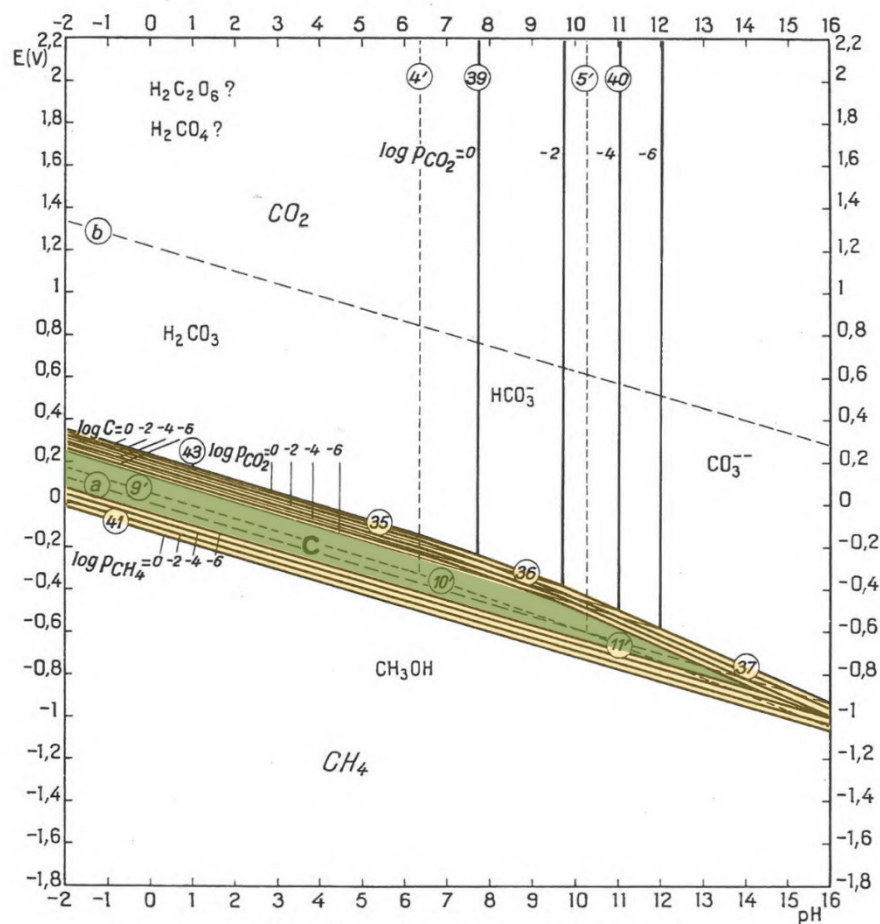
Figure 22. Potential-pH equilibrium diagram of the carbon – water system at 25 °C (considering carbon in the form of graphite). Diagram slightly changed. Added with permission from Pourbaix [135]. Rightsholder: AMPP GLOBAL CENTER, INC All rights reserved.

In this diagram, the green colored area shows the electric potential as a function of pH, at which carbon is stable. However, when the electrode potential is higher than the family of lines (35), (36) and (37), carbon is oxidized to CO_2, H_2CO_3, HCO_3^-, and CO_3^{2-}. In addition, carbon is reduced when the electric potential is lower than the family of lines (41), resulting in the formation of

methane, methyl alcohol, and other organics. These lines (35, 36, 37, and 41) are colored yellow and indicate the limit at which carbon is oxidized and reduced as a function of pH and electric potential.

As mentioned earlier, this diagram helps to estimate the stability of the material under certain conditions. *Pourbaix[135]* states that these reactions of carbon do not occur below 25 °C at atmospheric pressure. However, it is known that the thermodynamic oxidation of carbon occurs at 0.207 V vs. SHE in acidic environments[10] [154]. Consequently, carbon corrosion is inevitable at high anodic potentials. This is also evident in Figure 22. However, under experimental conditions, carbon oxidation starts above 0.207 V vs. SHE due to the slow reaction kinetics and intrinsic properties of the electrode materials and electrolyte.

For this reason, *Yi et al.*[154] studied the electrochemical corrosion of glassy carbon in acidic, neutral, and alkaline media and indicated that the carbon begins to oxidize or corrode, respectively, at 1.2 V vs. SHE. Their linear sweep measurement also indicated that when the electric potential of OER is reached (above 1.5 V vs. SHE), the carbon surface undergoes a greater change than at 1.2 V vs. SHE.

Yi et al.[154] described that in alkaline media, carbon oxidation is stronger than in acidic or neutral media. This is because the dissolution process of carbon occurs only in alkaline media through the formation of hydroxide radicals. The alkyl site chains at the edges of the graphitic domains are attacked by the radicals. The layer becomes more and more hydrophilic due to the formation of C=O bonds until the π–π interaction between flakes and glassy carbon weakens and finally dissolves in the electrolyte[154]. After that, a raw carbon surface remains for the next attack.

They also observed a brown discoloration of the electrolyte during the experiment in alkaline media. Their UV-vis measurement of the electrolyte showed peaks at 220-300 nm representing polycyclic aromatic hydrocarbons. There also detected a brownish substance that turned out to be small carbon nanoparticles with an average diameter of less than 10 nm. This led to the conclusion that exfoliation of carbon also occurs during OER.

The use of highly active catalysts can reduce the total cell voltage (see Figure 8, Figure 14, and Figure 15), and consequently carbon corrosion is slowed. But corrosion cannot be completely avoided in the long run. This is shown by the reports of carbon-based GDEs in metal-air batteries, electrolyzers, and fuel cells that are not stable at OER[4] [9] [11] [20] [120] [121]. Even with noble metal catalysts such as Pt, carbon corrosion takes place in a fuel cell, as shown by *Meier et al.*[140]. Nevertheless, catalyst development for OER and ORR continues to achieve low overpotentials with earth-abundant and non-noble metals or metal-free materials such as carbon. These carbon-based catalysts exhibit higher corrosion resistance due to incorporated structural defects and/or heteroatoms[3] [10].

However, the carbon-based GDLs do not have protective structural defects and/or heteroatoms, and therefore, the carbon-based GDLs corrode as mentioned earlier.

This leads to:

1. increase in hydrophilic surface area
2. decrease in conductivity
3. loss of electrochemically active surface area
4. detachment of catalyst particles from the support
5. eventual collapse of the carbon-based GDE

Trogadas et al.[10] have summarized some specific criteria where carbon corrosion is very pronounced in GDEs. They base this on the PEMFC study by *Maass et al.*[155], where carbon-based cathode substrate corrosion has been demonstrated in the acidic regime.

One of the criteria is that the corrosion rate is higher at varying electric potentials than at constant potential. This is because, the duration of the applied high electric potentials is not sufficient to produce irreversible oxide layers[10]. Therefore, this criterion should be applied when studying the electrochemical stability of novel GDEs.

In general, it must be emphasized that carbon corrosion is much more pronounced in alkaline media than in acidic or neutral media. Moreover, carbon corrosion also occurs in acidic environments despite the use of Pt as a catalyst. Therefore, carbon corrosion in alkaline media is avoided by replacing the carbon with other electrically conductive materials such as metals.

2.3 Electrochemical Deposition of MnO_x on a Metal Substrate

In general, it is possible to obtain specific electrochemically active coatings with high specific surface area by certain electrodeposition settings. Starting from the deposited metal, it is necessary to know at what pH of the aqueous electrolyte and at what electric potential the specific coating is deposited. *Pourbaix*[135] has summarized a large number of electrochemical equilibria of elements in aqueous solutions. One of these is manganese and is shown in Figure 23. Below are three examples of the electrochemical deposition of manganese oxide for specific settings and further treatments.
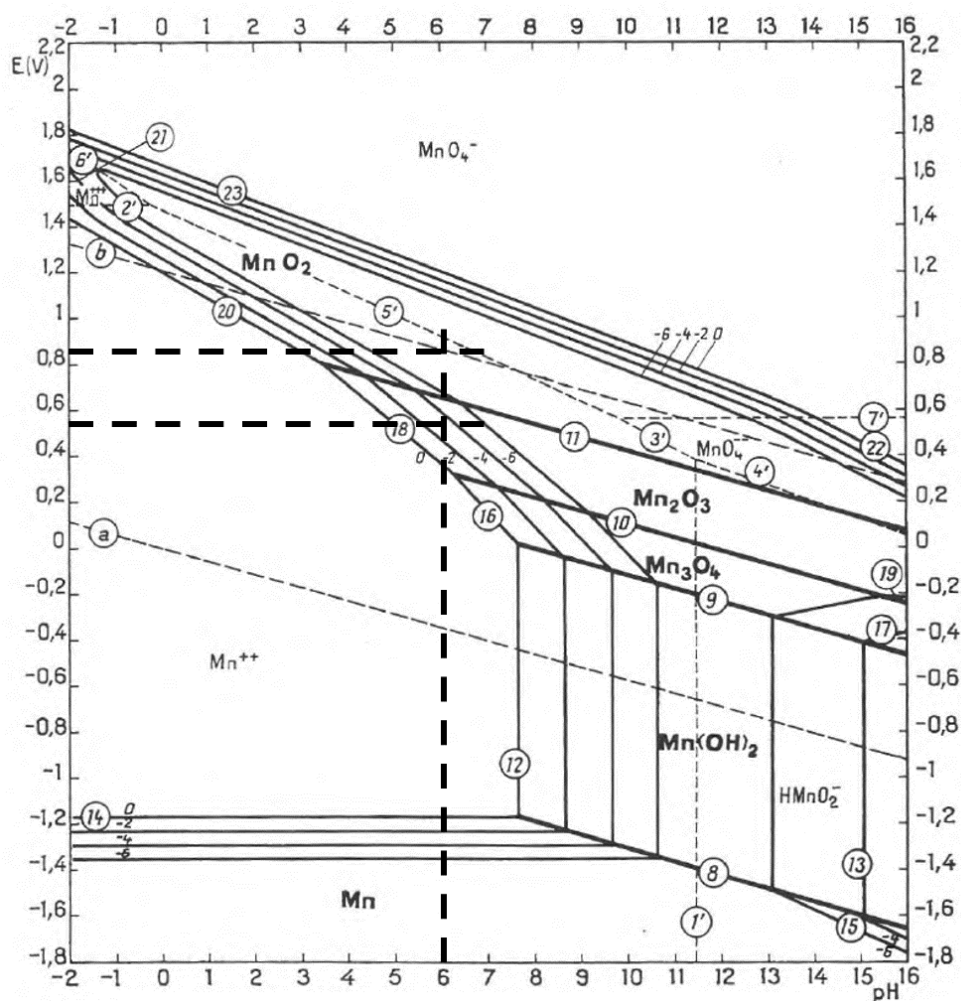
Figure 23. Potential-pH equilibrium diagram of the manganese-water system at 25 °C with dotted lines at 0.54 V and 0.84 V vs. SHE and at a pH-value of 6.0. Diagram slightly changed. Added with permission from Pourbaix [135]. Rightsholder: AMPP GLOBAL CENTER, INC All rights reserved.

Chou et al.[133] used an electrolyte of 0.1 M Na_2SO_4 (sodium sulfate) and 0.1 M $Mn(CH_3COO)_2$ (manganese acetate) and had an electrolyte pH of 6. For electrodeposition, they applied potentiostatically 0.6 V vs. SCE for 15 minutes to produce a thin MnO_2 film. Then, a cyclic voltametric method was applied in the potential range of 0.3 V and 0.6 V vs. SCE at a rate of 250 mV s^{-1} for 30 seconds, and then the potentiostatic method was used at 0.6 V for 1.5 minutes to

synthesize MnO_2 nanoflakes. With this combination, they obtained γ-MnO_2 in starfruit like form (called carambola) on a nickel sheet. This coating exhibited a large specific capacitance of 240 F g^{-1} at 1 mA cm^{-2}, indicating a large electrochemically active specific surface area.

Ng et al.[8] used only 0.1 M manganese acetate as electrolyte and electrodeposited at a potential range of 0.00 V and 0.60 V vs. Ag/AgCl with a sweep rate of 20 mV s^{-1} for 150 cycles. One cycle is a complete sequence from 0.00 V to 0.60 V and from 0.60 V back to 0.00 V vs. Ag/AgCl. The stainless-steel mesh coated with MnO_x was then calcined in air at 480 °C for 10 hours. Mn_2O_3 was formed during this treatment. The Mn_2O_3 coated stainless-steel mesh exhibited stable OER and ORR performance.

In this last example, *Tsai*[12] *et al.* used the same electrolyte as *Chou et al.*[133] (0.1 M Na_2SO_4 and 0.1 M $Mn(CH_3COO)_2$) and also applied the potentiostatic method at 0.60 V vs. SCE for 15 minutes. They additionally applied a potentiodynamic method at a potential range of 0.30 V to 0.60 V vs. SCE with a scan rate of 25 mV s^{-1} for 800 cycles. After the coating was deposited on a nickel foam substrate, it was annealed in air at 300 °C for two hours. Structural analysis displayed that pyrolusite MnO_2 was obtained. This electrochemically active coating on nickel foam exhibited a high specific surface area and was studied as an asymmetric supercapacitor.

Accordingly, in addition to the electrolyte concentration and pH, the working mode (potentiostatic, cyclic voltametric or potentiodynamic, respectively) and conditions such as potential value, duration, number of cycles and scan rate are also important. With these setting options it is possible to obtain specific coatings.

Based on the settings used by *Chou et al.*[133] and *Tsai*[12] *et al.* and the *Pourbaix*[135] diagram of manganese (Figure 23), one can estimate which manganese oxide species were deposited at different potentiostatic and cyclovoltametric (or potentiodynamic) modes. The electric potential of these working groups must be adjusted by the standard saturated calomel electrode (SCE) potential $\varphi_{00} = 0.24$ V for comparison with the *Pourbaix*[135] diagram. As a result, the potentials 0.60 V and 0.30 V vs. SCE change to 0.84 V and 0.54 V vs. standard hydrogen electrode (SHE). MnO_2 phases formed in both potentiostatic mode at 0.84 V vs. SHE and potentiodynamic mode in a potential range of 0.54 V and 0.84 V vs. SHE. However, the potentiodynamic mode was also in the region of dissolved oxides. Therefore, the results presented by them (γ-MnO_2 and pyrolusite MnO_2) are consistent based on the *Pourbaix*[135] diagram.

3   Experimental

The materials, sample preparation, and characterization methods were selected based on the literature presented.

3.1   Materiel List

- Nickel foam (1500 g m^{-2}) was purchased from (*INCOFOAM*) *Vale S.A.*, Brazil.
- Stainless-steel (alloy 1.4404) fleece (20 μm pore size) was purchased from *Reichelt Chemietechnik GmbH + Co*, Germany.
- Potassium hydroxide was purchased from *Merck KGaA*, Germany.
- Hydrochloric acid was purchased from *VWR International*, LLC, USA.
- Manganese (II) acetate tetra hydrate and sodium sulfate were purchased from *Carl Roth GmbH + Co. KG*, Germany.
- Teflon^{TM} PTFE DISP 30 water emulsion was purchased from *QuinTech Brennstoffzellen Technologie*, Germany.
- Commercial GDE (product name: MOC: pore size: 0.1 – 6.0 μm) and half-cell assembly FlexCell (Figure 25) were purchased from *Gaskatel Gesellschaft für Gassysteme durch Katalyse und Elektrochemie mbH*, Germany. The electrocatalyst of the commercial GDE is MnO_x.
- A hydrophilic Zirfon® membrane was supportably provided by *Agfa-Gevaert N.V.*
- Glass fiber fleece (Promaglav-HTI 1250 Papier 125 lfm) was purchased from *Etex Building Performance Gmbh*, Germany.

All reagents were of analytical grade and used as received without further purification.

3.2   Sample Preparation

Pretreatment

Samples of nickel foam and stainless steel fleece (24 mm diameter) were ultrasonically cleaned in acetone for 30 minutes and air dried. The cleaned samples were etched in 2 M HCl for 45 minutes, washed in deionized water, and then dried again. Finally, the samples were annealed in air at 350 °C for 20 minutes. Some nickel foam samples were pressed with pliers to reduce their thickness from 1.95 mm to 0.74 mm before etching.

Electrodeposition Protocol

The electrodeposition protocol is based on Chou et al.[133] and *Tsai[12] et al*. and was extended by my own specific adaptations. MnO_x was electrodeposited onto a pretreated nickel foam or stainless steel fleece, respectively. The composition of the aqueous deposition electrolyte was 0.1 M manganese (II) acetate tetrahydrate and 0.1 M sodium sulfate solution. The samples were

ultrasonicated in the deposition electrolyte for 10 minutes to ensure that there were no air bubbles on the metal surface before the electrochemical plating process began.

The deposition was carried out in a beaker at a temperature of 30 °C. Nickel foam or stainless steel fleece served as working electrode, a platinum electrode as the counter electrode, and an Ag/AgCl (3 M NaCl) electrode as the reference electrode. The electrical contact of the working electrode was established by clamping with a nickel wire connected to the potentiostat via an alligator clip. Therefore, the working electrode could be completely immersed in the electrolyte.

The reference electrode has a standard potential value of $\varphi 00 = 0.20$ V. Consequently, the potentials 0.60 V and 0.30 V vs. Ag/AgCl (3 M NaCl) change to 0.80 V and 0.50 V vs. standard hydrogen electrode (SHE). According to the *Pourbaix* diagram of manganese[135] (Figure 23) , the electrochemical settings were adjusted to obtain MnO_x with oxidation number 4 (MnO_2).

The electrodeposition process consisted of two steps. Starting with potentiostatic deposition at 0.60 V for 15 minutes, followed by potentiodynamic deposition between 0.30 V and 0.60 V at a specific scan rate (r_{scan}) (25 mV s^{-1} or 50 mV s^{-1}) for 500 or 800 cycles. A cycle is a complete sequence of 0.30 V → 0.60 V → 0.30 V. The process is shown schematically in Figure 24. After electrodeposition, the samples were dried in a drying oven at 120 °C and then annealed in air at 300 °C for two hours.
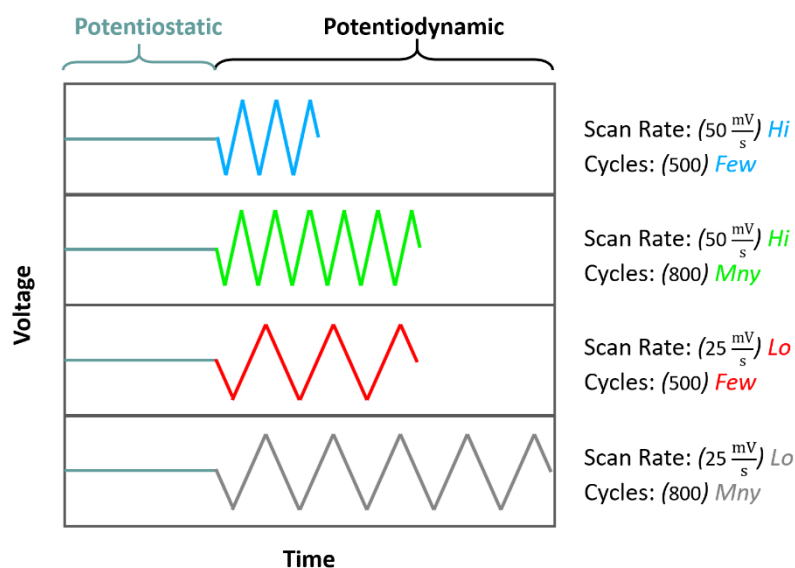
Figure 24. Schematic depiction of the deposition process (HiFew: 50 mV s^{-1} for 500 cycles; HiMny: 50 mV s^{-1} for 800 cycles; LoFew: 25 mV s^{-1} for 500 cycles; LoMny: 25 mV s^{-1} for 800 cycles).

In Figure 24, all electrochemical setups used for electrochemical deposition are shown schematically with their specific names. According to the diagram of *Pourbaix*[135] for manganese, the electrodeposited MnO_x species is not affected by the variation of the electrodeposition r_{scan} or the number of cycles. This is because the species is affected by the applied electric potential and pH. For this reason, the electrodeposited MnO_x species is the same for each setting (HiFew, HiMny, LoFew, and LoMny). Since the applied potential range for potentiodynamic deposition and the potential for potentiostatic deposition is constant for each sample.

Hydrophobization.

The coated samples were hydrophobized by dip coating. They were immersed in Teflon™ PTFE DISP 30 water emulsion for 10 seconds. Then they were rinsed in ethanol to remove the excess emulsion and dried in a drying oven at 120 °C to remove ethanol and water. They were then annealed at 305 °C for 30 minutes to remove the wetting agent.

Combination.

Coated substrates (nickel foam (foam: Fo), pressed nickel foam (pressed foam: Fop), and stainless- steel fleece (fleece: Fle)) were layered on top of each other in different order to create multiple macropore system gradients.

All samples were prepared in duplicate and their characteristics are listed in Table 1, Table 2 and Table 3.

Table 1. Sample overview of chapter 4.1 (nickel foam (foam)).

Sample Name	Electrode body	Coating setup	PTFE-coated
HiFew[1]	Foam	HiFew[1]	No
HiMny[2]	Foam	HiMny[2]	No
LoFew[3]	Foam	LoFew[3]	No
LoMny[4]	Foam	LoMny[4]	No

High scan rate, **Few** cycles[1]; **Hi**gh scan rate, **Many** cycles[2]; **Lo**w scan rate, **Few** cycles[3]; **Lo**w scan rate, **Many** cycles[4]

*Table 2. Sample overview of chapter 4.2 (nickel foam (Foam), pressed nickel foam (Fop.) and stainless-steel fleece (Fleece); * hydrophobic).*

Sample Name	Electrode body	Coating setup	PTFE-coated
Fo$_{Few}$	Foam	HiFew[1]	No
Fop$_{Few}$	pressed Foam	HiFew[1]	No
Fop$_{Mny}$	pressed Foam	HiMny[2]	No
Fle$_{Few}$	Fleece	HiFew[1]	No
Fle$_{Mny}$	Fleece	HiMny[2]	No
Fle*	Fleece	HiMny[2]	Yes
Fop*	pressed Foam	HiFew[1]	Yes

High scan rate, **Few** cycles[1]; **Hi**gh scan rate, **Many** cycles[2]; **Lo**w scan rate, **Few** cycles[3]; **Lo**w scan rate, **Many** cycles[4]

Table 3. Sample overview of chapter 4.3 (L: Foam with large-sized pores; M: Pressed Foam with medium-sized pores; S: Fleece with small-sized pores; □ non hydrophobic; ■ hydrophobic; nickel foam (Foam), pressed nickel foam (pressed Fo.) and stainless-steel fleece (Fleece)).

Sample Name	Electrode body	Coating setup	PTFE-coated
L□|M□|S■	Foam|pressed Fo.|Fleece	HiFew[1]|HiFew[1]|HiMny[2]	S
L□|M■|S■	Foam|pressed Fo.|Fleece	HiFew[1]|HiFew[1]|HiMny[2]	M and S
M□|M■|S■	pressed Fo.|pressed Fo.|Fleece	HiFew[1]|HiFew[1]|HiMny[2]	M and S
M□|S□|S■	pressed Fo.|Fleece|Fleece	HiFew[1]|HiMny[2]|HiMny[2]	S
S□|M■|S■	Fleece|pressed Fo.|Fleece	HiMny[2]|HiFew[1]|HiMny[2]	M and S

High scan rate, **Few** cycles[1]; **Hi**gh scan rate, **Many** cycles[2]; **Lo**w scan rate, **Few** cycles[3]; **Lo**w scan rate, **Many** cycles[4]

3.3 Characterization

3.3.1 Material Characterization Methods

Scanning Electron Microscopy

Field emission scanning electron microscopy (FESEM) ULTRA PLUS from *Carl Zeiss Microscopy GmbH* was used to investigate the morphology of the electrodes. An extra high voltage (EHT) beam of 10.0 kV (100 µm – 1 µm) and 2.0 kV (1 µm – 200 nm), a gun-to-sample distance of 3 to 4 mm, and Signal A = SE2 (100 µm – 10 µm), = InLens (1 µm – 200 nm), and = AsB (100 µm – 1 µm) were used for the measurements.

PTFE-coated samples were coated with carbon (vapor deposition) to increase the e⁻ conductivity of PTFE. For this reason, the structure of PTFE can be measured with SEM by using Signal A = angle selective backscatter (AsB).

X-Ray Diffraction

X-ray diffraction (XRD) analysis was performed using a D8 Advance Bruker and a Cu-K$_\alpha$ radiation from *Bruker Corporation*. Based on the electrodeposition protocol, MnO$_x$ was electrochemically deposited on a nickel plate at a r_{scan} of 12.5 mV s^{-1} to obtain as much mass as possible and then scraped off the nickel surface. This MnO$_x$ was measured from 5 ° to 90 ° 2Θ at a rate of 0.01 ° per 57.6 seconds.

Transmission Electron Microscopy

Transmission electron microscopy (TEM) was performed using a *Jeol* JEM2100Plus at a high voltage of 200 kV. The MnOx samples were prepared in the same way as described for the XRD samples. The synthesized samples were ground in ethanol for two minutes using a mortar. After 10 minutes of segregation, a droplet was placed on a carbon TEM grid. The lattice constants (or interplanar distance d, respectively) were calculated from the measured XRD pattern reflexes (2 Θ) using *Bragg´s* law, which is presented below:

$$n\lambda = 2\ d\ sin\ (\Theta) \hspace{4cm} \text{m. Eq. 7}$$

In m. Eq. 7, n is a positive integer and λ is the wavelength of the incident wave (Cu-k$_\alpha$ radiation).

X-Ray Tomography

X-ray tomography measurements were performed using the ZEISS Xradia Versa 620 3D x - ray microscope from *Carl Zeiss Microscopy GmbH*.

The electrodeposited nickel foam sample was analyzed in the z-axis direction with an optical magnification of 4x, at 50 kV, 89.93 µA, an exposer time of 12.0 s, a source-sample distance of - 7.160 mm, a detector-sample distance of 19.673 mm, and a source filter: LE5.

The electrodeposited pressed nickel foam sample was analyzed in the z-axis direction with an optical magnification of 4x, at 40 kV, 74.95 µA, an exposer time of 6.0 s, a source-sample distance of - 7.008 mm, detector-sample distance of 21.545 mm, and a source filter: LE5.

The electrodeposited stainless-steel sample was analyzed in the z-axis direction with an optical magnification of 4x, at 40 kV, 75.04 µA, an exposer time of 27.68 s, source-sample distance of – 10.385 mm, detector-sample distance of 59.884 mm, and a source filter: LE3.

Contact Angle

To determine the hydrophobicity of samples, contact angle measurements were performed using the Contact Angle System OCAH200 from *DataPhysics Instrument GmbH*. Droplets of 5 µl of deionized water were placed on the sample surface and after 3 to 5 seconds a camera of the Contact Angle System OCAH200 took a digital photo. This procedure was performed on three different locations of the same sample. The pre-installed program of the Contact Angle System OCAH200 (SCA20 version 2) analyzed the formed contact angle of the droplet.

Nitrogen Sorption (Brunauer-Emmet-Teller - BET)

The specific surface area study was determined by the nitrogen sorption method or the Brunauer-Emmet-Teller (BET) measurement, respectively, using the ASAP2020 from Micromeritics GmbH. The adsorption or desorption of nitrogen was initiated by the steady increase or decrease of nitrogen pressure. Meanwhile, the amount of adsorbed or desorbed nitrogen was measured. The Brunauer-Emmet-Teller model was used to calculate the specific surface area from the measured adsorption and desorption data.

3.3.2 Electrochemical Characterization Methods

A potentiostat SP-240 from *Bio-Logic Science Instruments* and a half-cell assembly from *Gaskatel Gesellschaft für Gassysteme durch Katalyse und Elektrochemie mbH* were used to characterize the electrode which is shown in Figure 25.
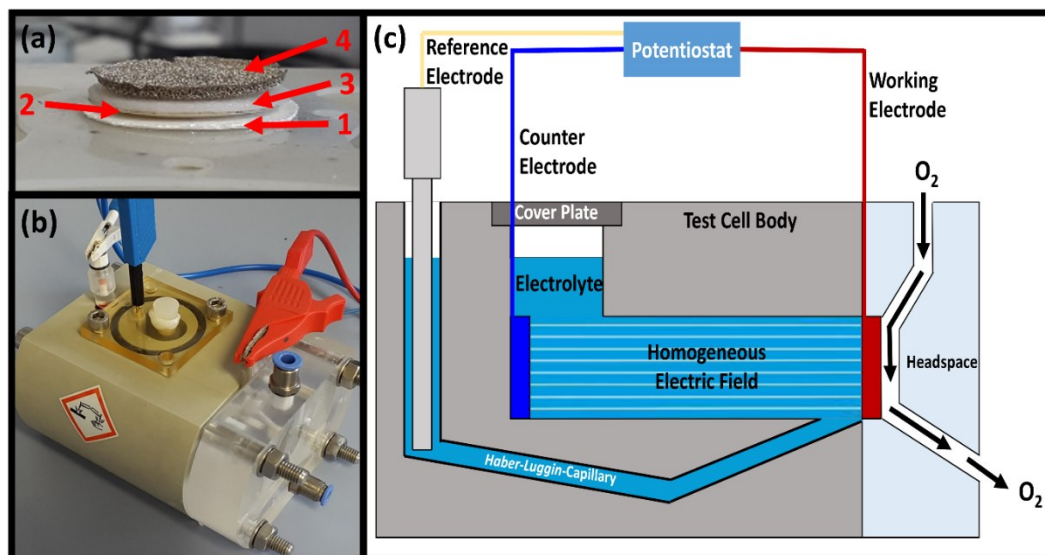
Figure 25. (a) the assembly of the individual parts (1. Zirfon® membran; 2. o-ring space holder; 3. glas-fiber-fleece soaked in KOH and 4. working electrode/GDE sample), (b) depiction of the connected Gaskatel FlexCell and (c) its schematic depiction of the cross-section.

For all measurements, the respective GDE sample served as the working electrode, a coiled platinum wire was used as the counter electrode, and a Hg/HgO (1 M NaOH) electrode was used as the reference electrode. The electrolyte was 0.1 M KOH (pH: 12.6), resulting in an O_2/ OH^- standard potential ($\varphi0$) of 0.37 V vs. Hg/HgO 1 M NaOH ($\varphi0 = 0.49$ V vs. SHE).

An oxygen supply of ~ 1 Nl min^{-1} was connected to the half-cell during all electrochemical measurements.

The GDE samples (working electrode) were prepared for measurement as shown in Figure 25 (a). The hydrophilic Zirfon® membrane (1.) is in direct contact with the electrolyte and reduces the electrolyte pressure on the GDE samples. The glass- fiber- fleece (3.) was soaked in KOH before assembly and it also reduced the electrolyte pressure on the GDE in the half-cell. The O-ring (2.) ensured that the Zirfon® membrane and the glass-fiber-fleece could be separated again after the measurement. The uncoated nickel foam (4.) represented the GDE samples, which were electrically connected by a nickel mesh. Then, all electrodes (working, counter and reference electrode) were connected to the potentiostat SP -240 as shown in Figure 25 (b). The schematic depiction (Figure 25 (c)) shows that the reference electrode was in close contact with the working electrode through the *Haber-Luggin-* capillary.

The measurements of the combined electrode bodies (for example: L□|M■|S■; (Table 3)) were assembled in the same way as shown in Figure 25 (a). Note that the first electrode body of the combination (L□|M■|S■) was in contact with the **electrolyte side** and the last electrode body of the combination (L□|M■|S■) was in contact with the **air side**.

The electrochemical behavior was studied by a galvanostatic method, electrochemical impedance spectroscopy and a potentiostatic method.

Galvanostatic Measurement

The galvanostatic method was performed at different current densities ($\pm$ 5 and $\pm$ 10 mA cm^{-2}) for at least three cycles, each cycle lasting 1 minute. A cycle is defined here as a completed sequence of OER and ORR. These results were averaged and subtracted with $\varphi_0 = 0.37$ V vs. Hg/HgO 1 M NaOH to obtain the overpotential for the ORR and OER. The following schematic diagram illustrates the calculation of the overpotential. Figure 26 shows the relationship between the potential response, φ_0 and the overpotential of an ORR and OER galvanostatic measurement.
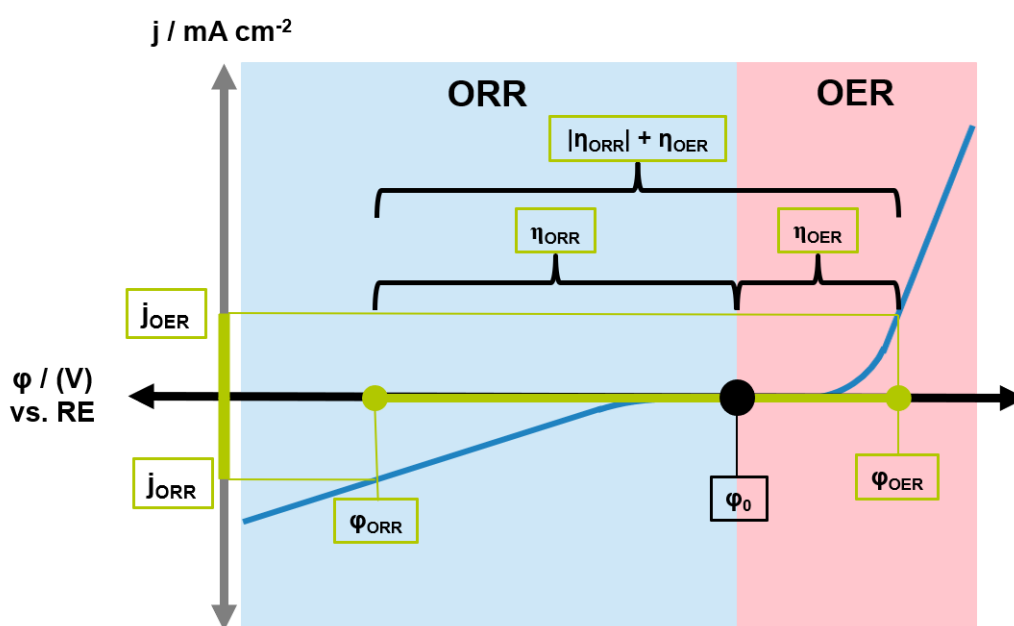
Figure 26. Schematic depiction of a current density – electric potential curve for ORR and OER.

In general, the individual overpotentials (η_{ORR} and η_{OER}) describe the electrochemical activity for ORR and OER. Small overpotentials are preferred because this indicates high electrochemical activity. Consequently, the sum of the overpotentials or the cumulative overpotential ($|\eta_{ORR}|+\eta_{OER}$), respectively, presents an overview of the GDE activity.

Moreover, these overpotentials (η_{ORR} and η_{OER}) are the sum of all individual overpotentials such as charge passage/transfer, diffusion, reaction (inhibition by chemical reaction), and adsorption (adsorption-desorption of the active species at the active site). These individual overpotentials

interact with each other in the environment of an electrochemical cell, resulting in a high degree of complexity. However, it is possible to quantitatively distinguish some of the individual contributions to inhibition, such as the charge passage-/transfer- and diffusion-overpotential, by electrochemical impedance spectroscopy.

Electrochemical Impedance Spectroscopy

Electrochemical impedance spectroscopy was measured from 100 kHz to 100 mHz at $\varphi_0 = 0.37$ V vs. Hg/HgO 1 M NaOH. Analysis was performed using EC-Lab software from *Bio-Logic Science Instruments* to determine charge passage/transfer resistance or polarization resistance, respectively, *Warbrug* diffusion coefficient and double layer capacitance.

The impedance spectroscopy Z` results were shifted in the *Nyquist* plots for visualization purposes by the following equation (Z`$_{intersec}$: x-axis intersection; Z`$_x$: Z` values; $c_{=1, 2, ...}$: Constant $= 1, 2, 3, 4$ or $5...$):

$$Z`_n = |Z`_x - Z`_{intersec}| + 0.5 * c_{=1,2,...}$$ m. Eq. 8

The first graph was set to $x_{intersection} = 0.50$ Ω, the second to $x_{intersection} = 1.00$ Ω and continuing in 0.5 Ω steps until the last graph, unless otherwise stated.

For the impedance measurement, the entire cell was analyzed, consisting of current collectors, alkaline electrolyte, a Zirfon® membrane, glass- fiber- fleece (gff) and the sample under investigation (Figure 25). The measured ohmic resistance includes the individual resistances of the individual cell components. Since the Zirfon® membrane was reused several times for the impedance spectroscopy measurements, slight changes during cleaning resulted in different ohmic cell resistances.

Therefore, the specific ohmic resistance of each GDE was not determined. This requires conductivity measurements through the DC plane, which were not performed.

However, the ohmic resistance is independent of the electrocatalytic activity of the MnO_x coated CF-GDEs. Thus, the characteristic impedance shape of each sample was not affected by the membrane.

In general, the *Nyquist* plot of porous electrodes is structured by three regimes [156]:

1. A 45 ° line in the high frequency range corresponding to ion migration and electron transport.

2. A semicircle in the mid-frequency range corresponding to the charge transfer reaction and the double layer capacitance at the electrode-electrolyte interface.

3. A diffusion regime in the low frequency range corresponding to electrolyte- and/or solid-phase diffusion. Depending on the electrochemical system under study.

These three regimes are exemplified in Figure 27 below. All three regimes are influenced by the pore shape, pore size, and porosity.
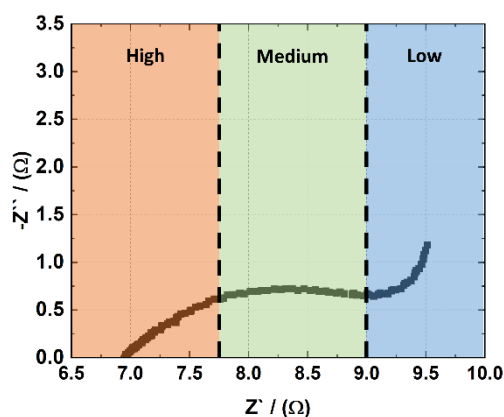
Figure 27. Nyquist plot of a porous electrode and its three frequency regimes (nickel foam coated with MnO_x
(HiFew)).

The following equivalent circuit (Figure 28) was used for the regression analysis of all *Nyquist* plots.
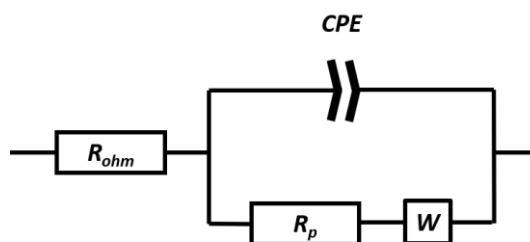
Figure 28. Depiction of the equivalent circuit for the potentiostatic electrochemical impedance spectroscopy
measurements (R_{ohm}: ohmic resistance; R_p: polarization resistance; W: Warburg element; CPE: constant phase
element).

Some CF-GDEs show for low frequencies the finite space *Warburg* diffusion[157] indicated by an asymptotic line course to a 90° line (Figure 27). For medium-low frequencies or in the transition range of the asymptotic course, respectively, the classical Warburg diffusion (straight 45° line) can

be observed. In order to obtain consistent results and to compare all samples with the same boundary conditions, the diffusion part was modeled by the classical Warburg diffusion. This classical Warburg diffusion only serves the purpose of comparing the samples with each other. Since other complex models are required for a more realistic approximation of the diffusion impedance in porous electrodes[158] this is beyond the scope of this work. Due to the porous surface structure and the complex composition of MnO_x and carbon (GDE_{ref})[159] [160] [161], a constant phase element was used.

R_{ohm} quantifies the electrolyte resistance, the Zirfon® membrane used, and the KOH-impregnated glass fiber fleece. R_p stands for the charge transfer resistance or charge passage resistance, respectively. The charge passage current density (j^{cp}) can be calculated by the Butler-Volmer-equation:

$$j^{cp} = j_0 \left\{ exp(\frac{\alpha nF}{RT}\eta_{cp}) - exp\left(-\frac{(1-\alpha)nF}{RT}\eta_{cp}\right)\right\} \qquad \text{m. Eq. 9}$$

For small charge passage overpotentials (η_{cp}) the following principle applies:

$$exp\, x = 1 + x \qquad \text{m. Eq. 10}$$

Thus, the Butler-Volmer-equation can be written as:

$$j^{cp} = j_0 \left\{1 + \frac{\alpha nF}{RT}\eta_{cp} - 1 + \frac{(1-\alpha)nF}{RT}\eta_{cp}\right\} \qquad \text{m. Eq. 11}$$

By further calculation it is possible to get the charge passage resistance (R_{cp}):

$$R_{cp} = \frac{\eta_{cp}}{j^{cp}} = \frac{RT}{nFj_0} \qquad \text{m. Eq. 12}$$

This R_{cp} is represented by the charge transfer or polarization resistance, respectively, (R_{ct} = R_p), which is determined by impedance spectroscopy. However, this is only valid for small charge passage/transfer overpotentials or excitation potentials. Therefore, the O_2/OH^- standard potential φ_0 = 0.37 V vs. Hg/HgO 1 M NaOH was chosen.

In addition, diffusive mass transport is described by the *Warburg* element. It is quantified by the *Warburg* diffusion coefficient ($\sigma_{Warburg}$). The *Warburg* impedance is written as follows[162]:

$$Z_W = R_W = \left(\frac{2}{\omega}\right)^{1/2}\sigma \qquad \text{m. Eq. 13}$$

$\sigma_{Warburg}$ can be calculated by the constants of the experiment (A = geometric surface area):

$$\sigma_{Warburg} = \frac{RT}{n^2 F^2 A\sqrt{2}} \left(\frac{1}{D_O^{1/2} C_O^{Bulk}} + \frac{1}{D_R^{1/2} C_R^{Bulk}} \right) \qquad \text{m. Eq. 14}$$

Further simplification shows the following relationship of $\sigma_{Warburg}$ and the diffusion coefficient D:

$$\frac{1}{\sigma_{Warburg}^2} = \frac{1}{k^2} \left(C_O^{Bulk\,2} D_O + C_R^{Bulk\,2} D_R \right) \qquad \text{m. Eq. 15}$$

It can be seen that $\sigma_{Warburg}$ is quadratic indirect proportional to D. The diffusion flux (J) of an electrochemical system is described by the *Fick's* first law:

$$J = -D \frac{dc}{dx} \qquad \text{m. Eq. 16}$$

All in all, it can be said that D becomes smaller at high $\sigma_{Warburg}$, which leads to a lower diffusion flux or slower mass transport, respectively. Consequently, small $\sigma_{Warburg}$ are preferred because diffusive mass transport is then fast.

The constant phase element (CPE) is used for electrochemical systems with inhomogeneous physical properties such as varying layer thicknesses[159], rough topography[160] and/or varying reaction rates[161]. The CPE quantifies the influence of the physical properties by the α_{CPE} exponent with the following mathematical equation:

$$Z_{CPE} = \frac{1}{Q_0} (i\omega)^{\alpha_{CPE}} \qquad \text{m. Eq. 17}$$

When $\alpha_{CPE} = 1$, the CPE behaves like the equivalent circuit of a capacitor and its phase angle is 90 °. However, when the influence of the mentioned physical properties is large, the value of α_{CPE} decreases and the phase angle is less than 90 °. Based on the SEM images (Figure 31) the CPE is used for all impedance spectroscopy measurements.

The double layer capacitance (C_{dl}) is calculated using the following equation[163] (C_{dl}: double layer capacitance [mF]; Q_0: CPE value (constant phase element) [F s$^{(\alpha-1)}$]; R_p: polarization Resistance [Ω]; α: CPE exponent):

$$C_{dl} = \frac{(Q_0 \, R_p)^{(1/\alpha)}}{R_p} * 1000 \qquad\qquad \text{m. Eq. 18}$$

Long-term Stability Measurement

Long-term electrochemical stability was measured in potentiostatic mode at 1.50 V (OER) and - 0.75 V (ORR) vs. Hg/HgO 1 M NaOH for 2100 cycles. Each selected electric potential was constant for 20 seconds, and a cycle is a completed sequence of OER and ORR. This measurement setup simulates rapid aging of the electrode due to the relatively high OER electric potential and the relatively rapid change of the working mode between OER and ORR for a large number of cycles. Based on the results of *Yi et al.*[154], the OER potential of 1.50 V induces moderate carbon corrosion. A program was also written in *Python* programming language to evaluate the results. The code can be found in the appendix (Appendix 1).

The performance of CF-GDEs was evaluated by comparing potential ratios. It was calculated by the following equation (*q*: ratio [%]; η_{GDEref}: overpotential of GDE$_{ref}$ [V]; η_{CFGDE}: overpotential of CF-GDEs [V]):

$$q = \left(\frac{\eta_{GDEref}}{\eta_{CF-GDE}} - 1 \right) * 100 \qquad\qquad \text{m. Eq. 19}$$

The results of the electrochemical stability measurement were calculated by the following equation (j_1: current density of the first cycle [mA cm^{-2}]; j_x: current density of the subsequent cycles [mA cm^{-2}]):

$$j_{norm} = \frac{j_1}{j_x} \qquad\qquad \text{m. Eq. 20}$$

4 Results and Discussion

As mentioned earlier, the aim of this work is to develop a carbon-free (CF-) gas diffusion electrode (GDE) for alkaline energy converters. Since carbon based GDEs are not stable in alkaline media due to carbon corrosion. The CF-GDEs consist of a porous metal substrate coated with an electrocatalyst.

Therefore, an electrochemical deposition method with variable setting parameters is determined in chapter 4.1 to establish a bifunctional MnO_x that can be applied to different substrates in a standardized manner.

In chapter 4.2, different substrates such as nickel foam (Fo), pressed nickel foam (Fop), and stainless-steel fleece (Fle) are coated with the bifunctional catalyst and PTFE. Their different pore sizes, hydrophobic PTFE coating, and influence on the electrochemical activity are investigated.

In chapter 4.3, individual hydrophilic and hydrophobic CF-GDEs from chapter 4.2 are combined to design layered bifunctional CF-GDEs with different porosity gradients. Therefore, it is necessary to analyze the hydrophilic/hydrophobic porosity gradient and its influence on oxygen evolution and oxygen reduction reaction activity.

4.1 Determination of the Electrodeposition Settings

Electrodeposition of catalysts is a relatively simple method and can be easily applied to the metal substrate or electrode body. Therefore, different electrodeposition parameters were used to determine the most suitable setup. Four different electrodeposition settings (see chapter 3.2) were used: HiFew (r_{scan}: 50 mV s^{-1} and 500 cycles), HiMny (r_{scan}: 50 mV s^{-1} and 800 cycles), LoFew (r_{scan}: 25 mV s^{-1} and 500 cycles), and LoMny (r_{scan}: 25 mV s^{-1} and 800 cycles). Based on the surface characteristics and electrocatalytic properties, it will be shown which electrodeposition settings exhibit the preferred electrochemical activities and surface properties. In addition, long-term stability measurements will be performed to analyze any degradation of the electrodeposited MnO_x. All CF-GDE results will be compared with the commercial carbon-based GDE (GDE$_{ref}$). Furthermore, only nickel foam was used as electrode body in this first approach.

4.1.1 Material Characterization

X-Ray Diffraction

The XRD patterns of electrodeposited MnO_x in unannealed (a) and annealed (300 °C) form (b) are shown in Figure 29. The XRD pattern of the unannealed MnO_x can be assigned to the Mn_2O_3-bixbyite-c (JCPDS #00-041-1442). It exhibits the following reflections: $2\theta = 23.2$ °, 33.0 °, 38.3 °, 45.3 °, 49.3 °, 55.2 °, and 65.8 ° [83]. Similar XRD patterns for annealed Mn_2O_3 were shown by

Pudukudy et al.[164] and *Menezes et al.*[165]. In general, there are still two small reflections associated with other structures such as sodium manganese sulfate hydrate ($Na_2Mn(SO_4)_2$ H_2O, JCPDS #00-020-1127). Note that only the large diffraction reflections ($2\theta = 26.7$ ° and 29.8 °) of the unannealed MnO_x can be assigned due to the large background noise. The second main peak of $Na_2Mn(SO_4)_2$ H_2O lies within the background noise. However, the reflex at $2\theta = 50.2$ ° could not be properly assigned due to the background noise, indicating a large amount of X-ray amorphous substances. These results were published in a peer-reviewed paper[83].

Annealing at 300 °C converted Mn_2O_3 to pyrolusite MnO_2 (Figure 29 (b), JCPDS #00-004-0779). Its reflections are approx. at $2\theta = 31.6$ °, 37.1 °, 42.3 °, 56.2 °, 58.3 °, and 65.8 °. A similar XRD pattern for pyrolusite MnO_2 was also obtained by *Tsai et al.*[12] who used similar potentiostatic and potentiodynamic deposition settings. However, the set number of cycles and the dynamic scan rate (r_{scan}) differed. Nevertheless, almost identical XRD diffraction peaks were obtained since the same potential-window and annealing treatment were used.

(a) **(b)**
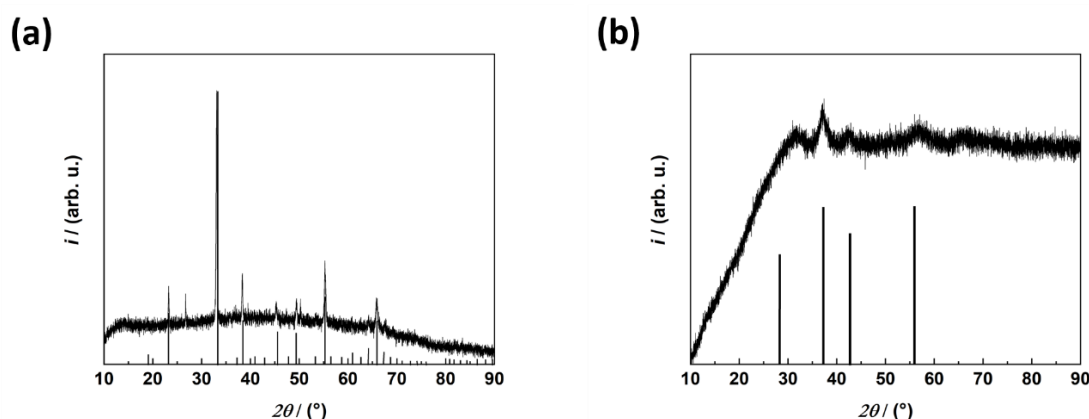
Figure 29. XRD-patterns of electrodeposited MnO_x ((a): non-annealed MnO_x (Mn_2O_3-bixbyited-c, JCPDS #00-041-1442; Reprinted with permission from <u>Bekisch et al. 2020</u>[83]*. All rights reserved <u>CC BY License</u>, https://creativecommons.org/licenses/by/4.0/deed.de); (b) annealed MnO_x at 300 °C (pyrolusite MnO_2, JCPDS #00-004-0779)).*

The XRD-patterns (Figure 29) show that the annealing treatment resulted in the conversion of Mn_2O_3 to pyrolusite MnO_2. It is assumed that the pH increased locally during electrodeposition, leading to the partial formation of Mn_2O_3. The annealing process oxidized these structures to Mn^{4+}. However, both exhibit strong background noise, indicating dominant amount of X-ray amorphousness. This could be due to strong phase heterogeneity, a larger number of defects, or simply that the crystallites are in the nm-range (compare MnO_x particle in Figure 30). The increase in the noise-to-signal ratio of the annealed sample associated with the phase change indicates an increase in defects or material heterogeneity, while the oxidation number of the manganese is increased (Mn^{3+} → Mn^{4+}). Since pyrolusite MnO_2 has been detected. This pyrolusite MnO_2 is known

to be highly OER/ORR bifunctionally active[166] and electrochemically stable for high cycle numbers[12] [166].

Transmission Electron Microscopy

In addition, TEM images of the unannealed MnO_x (Figure 29 (a)) were taken to examine the electrodeposited coating in more detail. For this purpose, the lattice plane and reflections were analyzed using the fast *Fourier* transformation (FFT). This is shown in Figure 30. These images show different morphologies and high polycrystallinity due to the differently oriented lattice planes on the right side of Figure 30, which is in good agreement with the XRD results. The FFT shows only weak reflections, which further emphasizes the amorphous nature of the unannealed MnO_x. However, the specific lattice constants or interplanar distances, respectively, are determined by the FFT of the respective TEM images.

These values can be compared with the distances calculated from the XRD. Briefly, the reflections at $2\theta = 33°$, $49.3°/50.2°$, and $55.2°$ show the highest agreement, which is shown in the appendix of the peer-reviewed paper[83]. The determination of the reflex signifiers at $2\theta = 49.3°$ and $50.2°$ was inconclusive due to their small interplanar distances. It is also possible that these reflex signals are only one signal. Based on these results, the electrodeposited material is largely amorphous MnO_x, except for minor domains of measurable crystallinity (Mn_2O_3 in Figure 29 (a)). These results were published in the same peer-reviewed publication[83] as mentioned above.
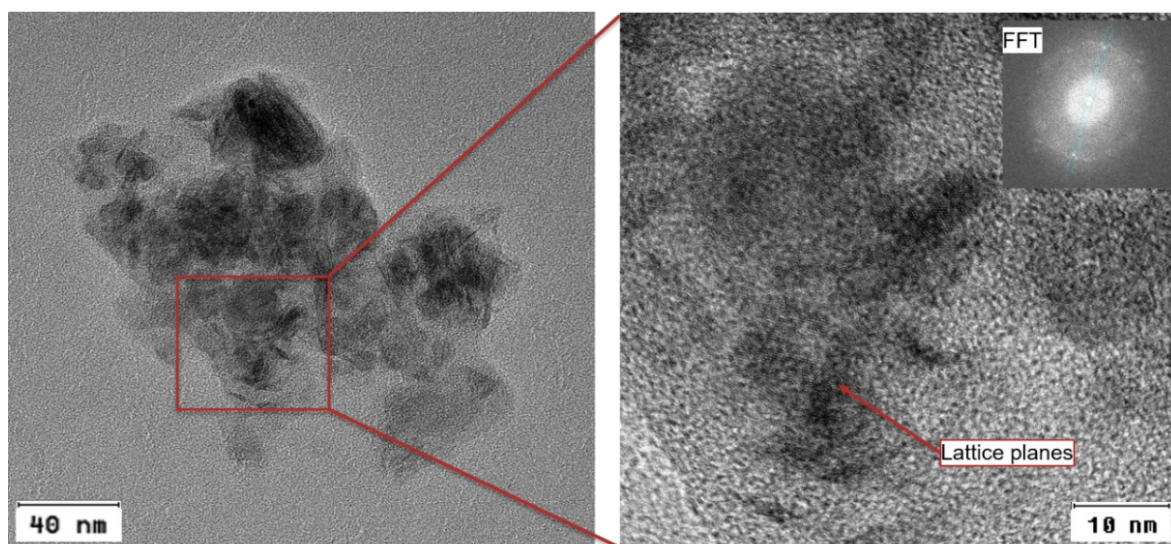
Figure 30. TEM images of electrodeposited non-annealed MnO_x particles at different orders of magnitude and fast Fourier *transformation (FFT). Reprinted with permission from Bekisch et al. 2020[83]. All rights resverd CC BY License, https://creativecommons.org/licenses/by/4.0/deed.de.*

Scanning Electron Microscopy

Figure 31 shows the CF-GDEs with different electrodeposition setups (HiFew, HiMny, LoFew, and LoMny) and the corresponding microstructures at two different magnifications. It is difficult to see any difference between the samples shown. However, a slight deviation of the starfruit structure can be seen compared to *Chou et al.*[133]. It can be taken into account that the dynamic deposition scan rate (r_{scan}), which acts as the electrodeposition rate, affects the surface structure and its appearance due to the potential-window and the time required for one cycle (Figure 24). In general, a higher r_{scan} leads to a faster completion of a cycle and thus to smaller structures. For this reason, a higher specific surface area of the active sites is obtained and *vice versa*.
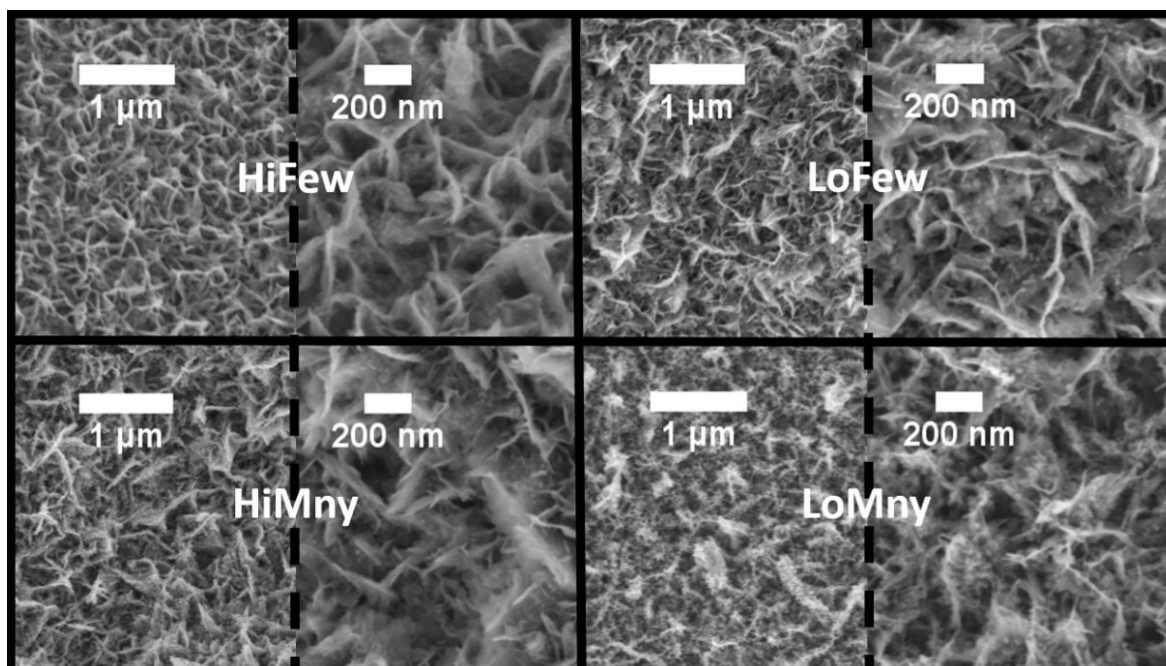
Figure 31. SEM images of carbon-free samples in 1 μm and 200 nm (HiFew: 50 mV s^{-1} & 500 cycles; HiMny: 50 mV s^{-1} & 800 cycles; LoFew: 25 mV s^{-1} & 500 cycles; LoMny: 25 mV s^{-1} & 800 cycles).

The SEM images of the deposited structures (Figure 31) show no difference between the electrodeposition settings applied. They all have a starfruit-like shape, similar to the deposited structure of *Chou et al.*[133]. The surface structures indicate a large number of active sites and are therefore beneficial for electrochemical activity.

Nitrogen Sorption & Deposited MnO$_x$ Mass

The specific surface area (S_{BET}) (a) and electrodeposited MnO$_x$ mass (b) results are shown in Figure 32. The BET results show a large difference between the CF-GDEs coated at 25 mV s^{-1} (LoFew and LoMny) and 50 mV s^{-1} (HiFew and HiMny). At high dynamic deposition scan rates (r_{scan}), twice the S_{BET} (200 m^2 g^{-1}) is obtained compared to low r_{scan} (about 100 m^2 g^{-1}). This is due to

the faster deposition of MnO$_x$, as the higher r_{scan} covers the potential difference between 0.30 V and 0.60 V faster than the lower r_{scan} (Figure 24).

The results of the SEM images do not show much difference in the surface structure between the CF-GDEs. Therefore, the effect of r_{scan} on the surface is not observed, indicating that the internal porosity of the deposited MnO$_x$ coatings must be different. Based on this assumption, there must be more pores in the samples (HiFew and HiMny) with higher dynamic deposition r_{scan}. The formation of more pores is possibly caused by a distorted layer formation with each electrodeposited thin layer per cycle due to the high dynamic deposition r_{scan}. Moreover, the effect of cycle number on S_{BET} is small. However, the S_{BET} increases slightly at high cycle numbers. In general, S_{BET} is mainly increased by high dynamic electrodeposition r_{scan} rather than by cycle number. The reason for the high S_{BET} (230 m^2 s^{-1}) of the commercial GDE$_{ref}$ is the use of porous carbon as an electrically conductive support for the catalyst.
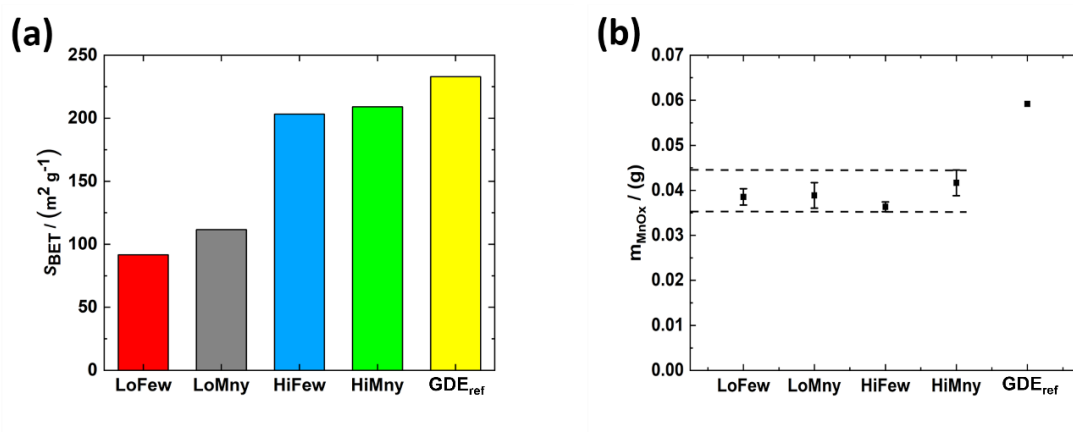
Figure 32. (a) Specific surface area of the samples measured with the Brunauer-Emmett-Teller (BET) method. (b) MnO$_x$ mass of carbon-free GDEs and GDE$_{ref}$. (HiFew: 50 mV s^{-1} & 500 cycles; HiMny: 50 mV s^{-1} & 800 cycles; LoFew: 25 mV s^{-1} & 500 cycles; LoMny: 25 mV s^{-1} & 800 cycles).

Figure 32 (b) shows the electrodeposited MnO$_x$ mass of CF-GDEs and the used MnO$_x$ mass in GDE$_{ref}$. A strong influence of r_{scan} and cycle number on the deposited mass is not observed, but only a slight tendency that more MnO$_x$ mass is deposited at high cycle number (HiFew vs. HiMny) or low r_{scan} (LoFew vs. HiFew). However, it was expected that the different setups would result in a more pronounced mass difference. This expectation discrepancy could be due to the experimental setup. The electrical connection to the nickel foam during electrodeposition was realized by a nickel wire clamped to the nickel foam. This results in a variation of sufficient conductivity that affects the degree of mass loading observed in the current-time diagram (Appendix *2* and Appendix 3) during electrodeposition. These variations in electrical contact are the limitations of the experimental setup used for electrodeposition. Nevertheless, a sufficient mass of about 0.04 g of MnO$_x$ is electrodeposited at each selected setting to fulfill the purpose of electrocatalysis.

Contact Angle

Figure 33 shows the contact angle (CA) for each treatment step applied to the nickel foam. These treatment steps are described in chapter 3.2.

The vertical dashed line separates the coated (annealed and non-annealed) from the uncoated samples. After cleaning in acetone, the electrode body (nickel foam) is still hydrophobic. Etching in HCl leads to a slight increase of the contact angle. However, temperature treatment (350 °C for 20 minutes) changes the surface property from hydrophobic to hydrophilic.
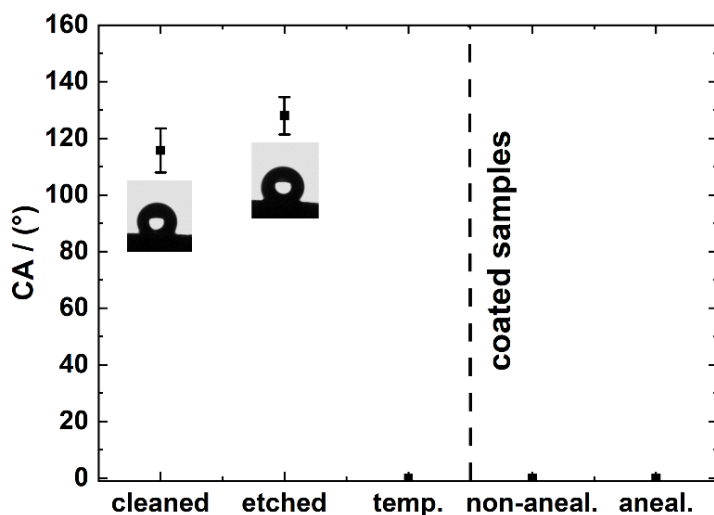
Figure 33. Individual contact angle of each treatment step.

This hydrophilic property is retained after electrodeposition of MnO_x and an annealing treatment. In aqueous electrodeposition, it is advantageous to use a hydrophilic surface to obtain a sample that is completely in contact with the deposition electrolyte. In this way, an uncoated surface can be avoided[83].

4.1.2   Electrochemical Characterization

The electrodeposited MnO_x coatings were further investigated using electrochemical impedance spectroscopy to determine which parameters are affected by dynamic electrodeposition r_{scan} and cycle number. Parameters such as ohmic resistance (R_{ohm}), specific double layer capacitance (C_{dl}), charge transfer resistance or polarization resistance, respectively, ($R_{ct} = R_p$) and *Warburg* diffusion coefficient ($\sigma_{Warburg}$) quantitatively describe the electrochemical processes and properties. This allows CF-GDEs to be compared with each other and with commercial GDEs (GDE$_{ref}$), representing the state of the art. In this way, the influence of different electrodeposition parameters can be understood.

Electrochemical Impedance Spectroscopy

An impedance measurement at the O_2/OH^- standard potential (0.37 V vs. Hg/HgO in 1 M NaOH) was performed to show the behavior of the electrochemical system and to determine R_p, $\sigma_{Warburg}$, and C_{dl} at small charge passage overpotentials. The *Nyquist* plots and corresponding frequencies of all samples are shown in Figure 34. The Z' measurement results were shifted for visualization purposes using equation m. Eq. 8 (see chapter 3.3.2).

The individual CF-GDEs can be clearly identified by their characteristic half circle shape and straight line upward, which can be interpreted as polarization or charge transfer, respectively, and diffusion (Figure 34). All CF-GDEs coated with different settings show a 45 ° line in the high frequency range, indicating porous electrode behavior [156]. However, the CF-GDEs show little different half circles in the medium frequency range. Large half circle sizes indicate reduced diffusion of O_2 [158]. This suggests a difference in MnO_x deposition because the substrate of these CF-GDEs is the same nickel foam.
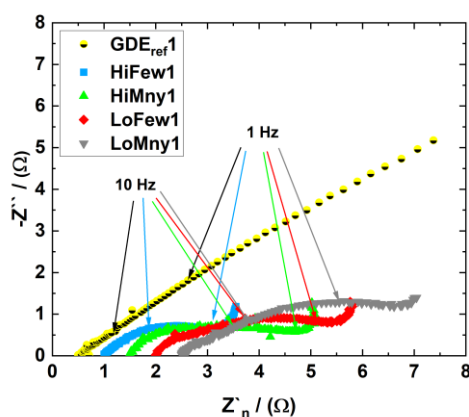
Figure 34. Nyquist plots of all nickel foam samples and GDE$_{ref}$ at a frequency range of approx. 3 kHz – 0.1 Hz (last point) at $\varphi_0 = 0.37$ V vs. Hg/HgO 1 M NaOH. The remaining measurements are at the Appendix 4.

The GDE$_{ref}$ has as porous electrode a 45 ° line in the high frequency range. In the medium frequency range, the line transitions to a smaller degree indicating a small half circle. After that, the course of the line towards the low frequency range has the 45 ° again and decreases again and remains below 45 ° in the low frequency range. The low visibility of the half circle or its small size, respectively, indicates a high reactant conductivity. Thus, GDE$_{ref}$ exhibits high ion migration and high diffusion of O$_2$ [156] [158].

At low frequencies, the line of CF-GDEs has a larger slope than 45 °, which looks like a capacitor element, but is interpreted as finite space *Warburg* diffusion[167] [168]. In general, the finite space Warburg diffusion means that an electrochemically active reactant is transport limited (depletion near the catalyst) or the transport of this active reactant is too slow[169] [170] [171] [172]. Moreover, the line also approaches 90 ° at low frequencies when the pore end is blocked[167]. In the case of CF-GDEs, it is assumed that the 10 – 1000 nm electrolyte thin film is the finite space and the pores of MnO$_x$ are blocking pores. This is shown schematically in Figure 35.
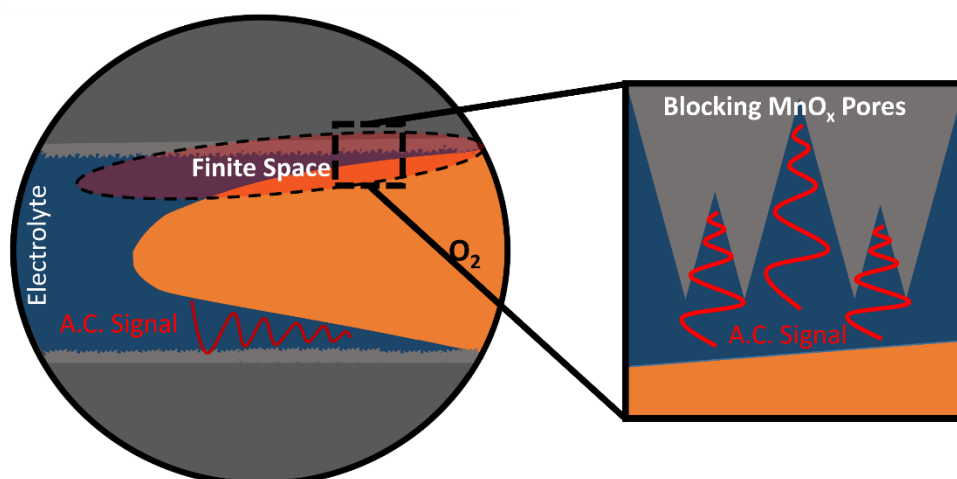
Figure 35. Schematic depiction of coated nickel foam pore with electrolyte meniscus which forms a thin film on MnO$_x$ coating (a. c. signal: alternative current signal induced by impedance measurement).

Dissolved O$_2$ has a lower concentration than OH$^-$ in the electrolyte thin film. Both act mainly as active reactants in this electrochemical system due to the applied equilibrium potential (0.37 V vs. Hg/HgO in 1 M NaOH). Consequently, the active reactant, dissolved O$_2$, diffuses from the thin electrolyte film to the catalyst. This leads to a kind of depletion of dissolved O$_2$ in the thin electrolyte film due to the lower concentration. Therefore, the resistance limits of dissolution of gaseous O$_2$ (transport limitation) are approached and the finite space *Warburg* diffusion is formed. Moreover, the a. c. signal approaches the blocking MnO$_x$ pores, which also contributes to this asymptotic progression toward 90 °. The comparison of GDE$_{ref}$ and CF-GDEs shows that GDE$_{ref}$ has a larger electrolyte thin film surface area than CF-GDEs. Therefore, a larger amount of dissolved oxygen is available for the catalytic reaction. Since GDE$_{ref}$ does not exhibit finite space *Warburg* diffusion.

Regression Analysis

The results of the regression analysis of impedance spectroscopy at 0.37 V vs. Hg/HgO 1 M NaOH (Figure 34) are shown in Figure 36. The α_{CPE} values of the constant phase element can be found in Appendix 5.
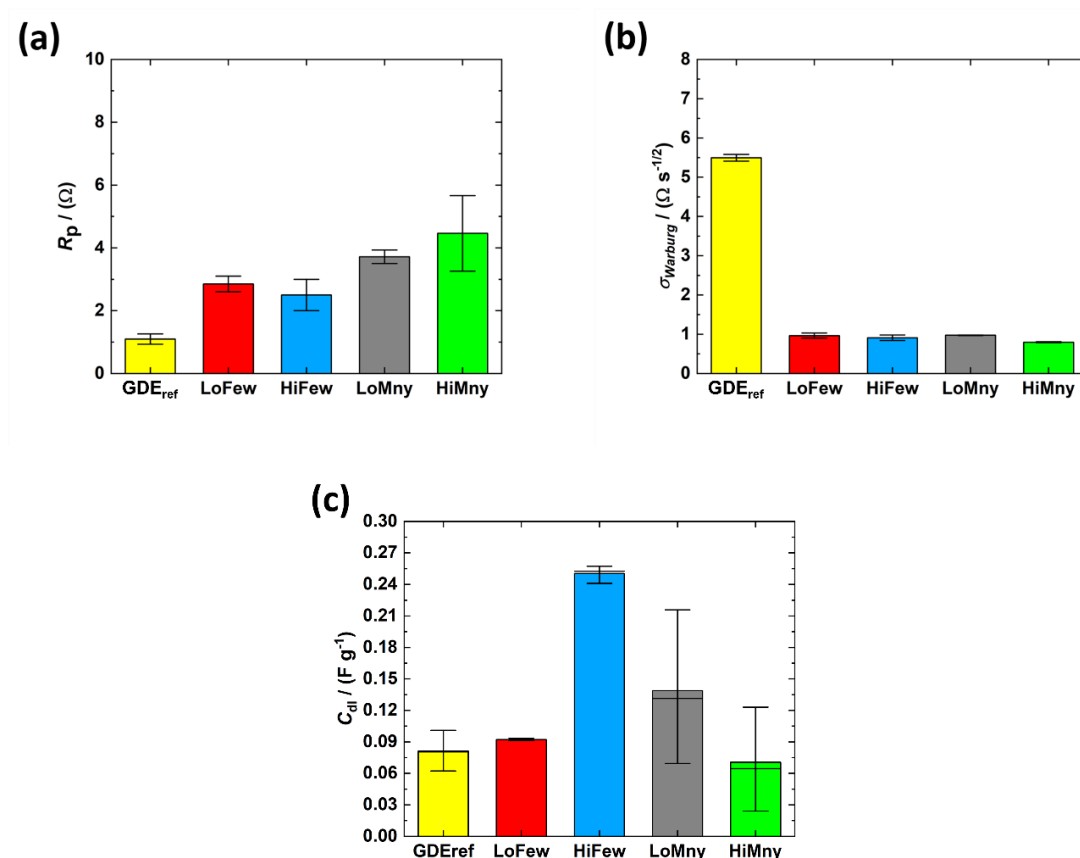
Figure 36. Image of polarization resistance ((a), R_p), Warburg diffusion ((b), $\sigma_{Warburg}$) and specific double layer capacitance ((c) C_{dl}) at 0.37 V vs. Hg/HgO 1 M NaOH. Determined by the equivalent circuit fitting (HiFew: 50 mV s^{-1} & 500 cycles; HiMny: 50 mV s^{-1} & 800 cycles; LoFew: 25 mV s^{-1} & 500 cycles; LoMny: 25 mV s^{-1} & 800 cycles).

Polarization Resistance

It is obvious that GDE$_{ref}$ has the lowest values when comparing the R_p results in Figure 36 (a). All CF-GDEs are approximately in the same R_p value range of 3 – 4 Ω based on their deviation. However, the CF-GDEs with lower cycle number (LoFew and HiFew) tend to be 3 Ω and the others with higher cycle number (LoMny and HiMny) tend to be 4 Ω. This difference in R_p´s or half circle sizes, respectively, indicates an influence of the applied cycle number on the MnO$_x$ pore structure. As the MnO$_x$ deposition time increases with increasing cycle number (Figure 24), pores of different sizes form. Accordingly, the LoFew and HiFew settings formed more pores of favorable size than

LoMny and HiMny for the electrochemical system used. Since no clear difference can be seen in the SEM images (Figure 31).

Cooper et al.[167] investigated different pore shapes and sizes and presented impedance spectroscopy results of narrowing pores that exhibited the largest impedance half circles (see Appendix 6 and Appendix 7). Therefore, LoFew and HiFew are assumed to form less constricting pore structures than LoMny and HiMny, which are formed at higher cycle number. This leads to that LoFew and HiFew have smaller impedance half circles or smaller R_p, respectively, than the other two deposition settings.

Moreover, these results also show the electrocatalytic activity of the carbon-free (CF-)GDEs. Thus, GDE$_{ref}$ exhibits the smallest half circle or the highest electrochemical activity, respectively.

Warburg Diffusion

The *Warburg* diffusion evaluation (Figure 36 (b)) shows that the $\sigma_{Warburg}$ of all CF-GDEs was significantly lower than that of GDE$_{ref}$ (5.50 Ω s$^{-1/2}$). Moreover, all MnO$_x$-coated samples show the same $\sigma_{Warburg}$ of about 1.00 Ω s$^{-1/2}$ without much variation. The GDE$_{ref}$ is a state-of-the-art hydrophobic porous electrode (Figure 2 (b)). It has a GDL covered with catalyst particles which are bound with the hydrophobic PTFE. For this reason, the GDE$_{ref}$ is not flooded. Only the outer surface of the GDE$_{ref}$ is in contact with the electrolyte and forms an electrolyte thin film (Figure 7). *Ergo*, O$_2$ must diffuse through the GDL to the other side where the thin film has formed[23] [95]. The O$_2$ diffusion is more hindered than that of the MnO$_x$-coated nickel foam (pore size: 500 – 600 μm), since the pore size of GDE$_{ref}$ ranges from 0.1 to about 6 μm. In addition, the diffusion distance of GDE$_{ref}$ is also larger than that of CF-GDEs because it does not have a hydrophobic GDL like GDE$_{ref}$. Thus, O$_2$ can immediately diffuse unhindered near the electrolyte film of CF-GDE and dissolves there. It then diffuses further into the vicinity of CL. This is the reason for the much smaller $\sigma_{Warburg}$ of the CF-GDEs. In other words, the diffusion resistance of the GDL has been eliminated, and therefore the $\sigma_{Warburg}$ of the CF-GDEs is lower than that of the GDE$_{ref}$.

In addition, diffusion of OH$^-$ and dissolved O$_2$ (active reactants) affects the $\sigma_{Warburg}$ in impedance measurements. However, the diffusion of O$_2$ into the thin electrolyte film and then onto the electrochemically active site is much more restrictive than the diffusion of ions[72] [94] [95] [23]. As a result, the O$_2$ diffusion resistance dominates the impedance results in the low frequency range. Since the ion diffusion resistance is much smaller than the O$_2$ diffusion resistance. Increasing the electrochemically active surface area and/or decreasing the electrolyte film thickness could decrease the $\sigma_{Warburg}$ value for both reaction directions[94] and thus increase the diffusion flux (m. Eq. 14 and m. Eq. 15).

Specific Double Layer Capacitance

The C_{dl} of all GDEs is shown in Figure 36 (c). It provides a rough estimate of the contributed electrochemical surface area during the impedance measurement. The comparison of C_{dl} shows that CF-GDEs with high cycle number (HiMny and LoMny) have a large deviation and tend to have lower C_{dl} than CF-GDEs with low cycle number. HiFew shows the highest C_{dl} of about 0.25 F g^{-1} and accordingly has the largest electrochemically active surface area. In general, GDE$_{ref}$ and CF-GDE differ in electrolyte wetting, flooded surface area formation, electrolyte thin film meniscus formation, and mass transfer pathways due to their different designs (Figure 2 (b) and Figure 3 (d)).

Based on the CA measurements (Figure 33), it must be considered that the CF-GDEs are hydrophilic. Consequently, all electrodeposited MnO$_x$ is potentially wetted with electrolyte. The thickness of the electrolyte film is smallest on the air side and increases toward the electrolyte bulk side like a meniscus on a flat surface (Figure 5 left, Figure 35). It is assumed that the oxygen flux of ~ 1 Nl min^{-1} reduces the film thickness on the air side of the CF-GDEs to an unknown extent by pushing the electrolyte to the electrolyte bulk side. This is illustrated in Figure 37 below.
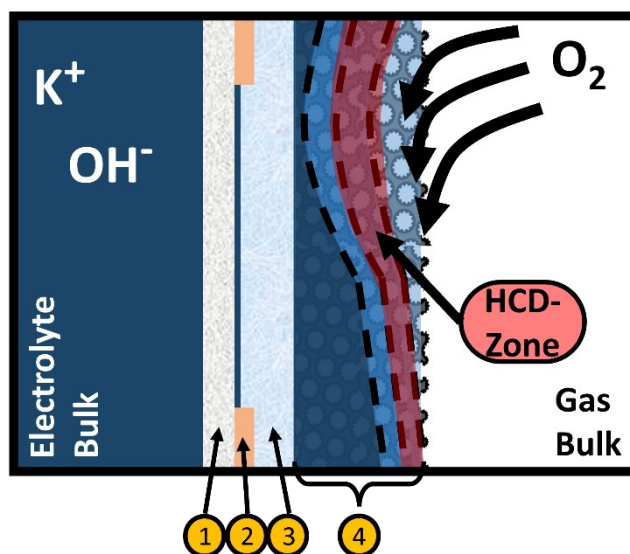
Figure 37. Schematic depiction of ORR high current density (HCD-) zone formation in CF-GDE (1. Zirfon®; 2. O-Ring; 3. glass-fiber-fleece (gff); 4. CF-GDE; HCD-Zone: high current density zone).

It is assumed that the influence of the O$_2$ influx changes the electrolyte film thickness inside the CF-GDE, contributing to the variations in the results. It starts with a higher thickness on the electrolyte bulk side and decreases towards the gas bulk side (Figure 35). The variation in film thickness is indicated by the dashed lines and the different colored areas within the CF-GDE. The red area is the high current density (HCD) ORR zone. This zone theoretically forms within the CF-GDE, if the electrolyte film thickness is not too thick or too thin. The ORR zone has an electrolyte thickness of about several nanometers to one micrometer (about 3[84] – 1000 nm[79]).

The C_{dl} can only be determined when the electrochemically active surface is in contact with the electrolyte. The large variation of the CF-GDEs with high cycle number (HiMny and LoMny) indicates that the contact between electrolyte and active surface was less constant than for the other GDEs. The high cycle number of these CF-GDEs (HiMny and LoMny) suggests that the internal porosity of the MnO_x coating tends to be less in contact with the electrolyte than the CF-GDEs with lower cycle number (HiFew and LoFew). However, this was not investigated further.

Moreover, GDE$_{ref}$ is wetted only on the outer surface where it is in contact with the electrolyte-soaked glass-fiber-fleece (gff). Therefore, only this wetted electroactive surface was determined. In addition, O_2 influx has no effect on the film-thickness of GDE$_{ref}$ due to the thick GDL region.

It is noteworthy that the qualitative comparison of the BET and C_{dl} results (Figure 32 (a) and Figure 36 (c)) shows a slight similarity between the HiFew and LoFew CF-GDE results. However, the BET and C_{dl} results of GDE$_{ref}$ differ from each other. This is because C_{dl} is determined by the chemical interaction between electrode and electrolyte, which is affected by hydrophobic effects and oxygen pressure or volumetric flow rate, respectively. BET, however, is not affected by these properties and circumstances. Consequently, BET measures the total GDE$_{ref}$, including the inactive porous carbon GDL. However, C_{dl} describes the outer surface area of GDE$_{ref}$ that is in contact with the electrolyte. In general, the electrochemically active surface area described by C_{dl} is more significant than the BET results for GDE$_{ref}$.

However, the CF-GDEs are hydrophilic, and their entire surface is electrochemically active. For this reason, the BET and C_{dl} results for CF-GDEs are potentially similar because both potentially describe the entire electrode. Therefore, their electrolyte contact is only affected by oxygen and electrolyte pressure, which can lead to incomplete wetting of CF-GDEs and thus incomplete characterization. This can be seen in the C_{dl} variations (Figure 36 (c)).

Galvanostatic Measurement

The galvanostatic measurement (Figure 38) is performed by applying a constant current density to the half-cell system described above in chapter 3.3.2 (Figure 25). The potential response is further calculated to obtain the overpotential (η_{OER} and η_{ORR}). These overpotentials are compared with each other and with GDE$_{ref}$. From Figure 38, it is possible to distinguish and compare the performance of OER (a) and ORR (b).

Difference Between η_{OER} and η_{ORR}

For all GDEs, the electrical overpotential (η) for OER and ORR increases with current density. In general, all GDEs show much lower η_{OER} than η_{ORR}. Due to the design of GDE$_{ref}$, the GDL and thus the diffusion of oxygen through it causes a higher η_{ORR} than η_{OER}. Since the electrolyte *ergo* the hydroxide ions are already in contact with the catalyst site, they can diffuse directly to it during OER (see chapter 2.1.2, Figure 7).
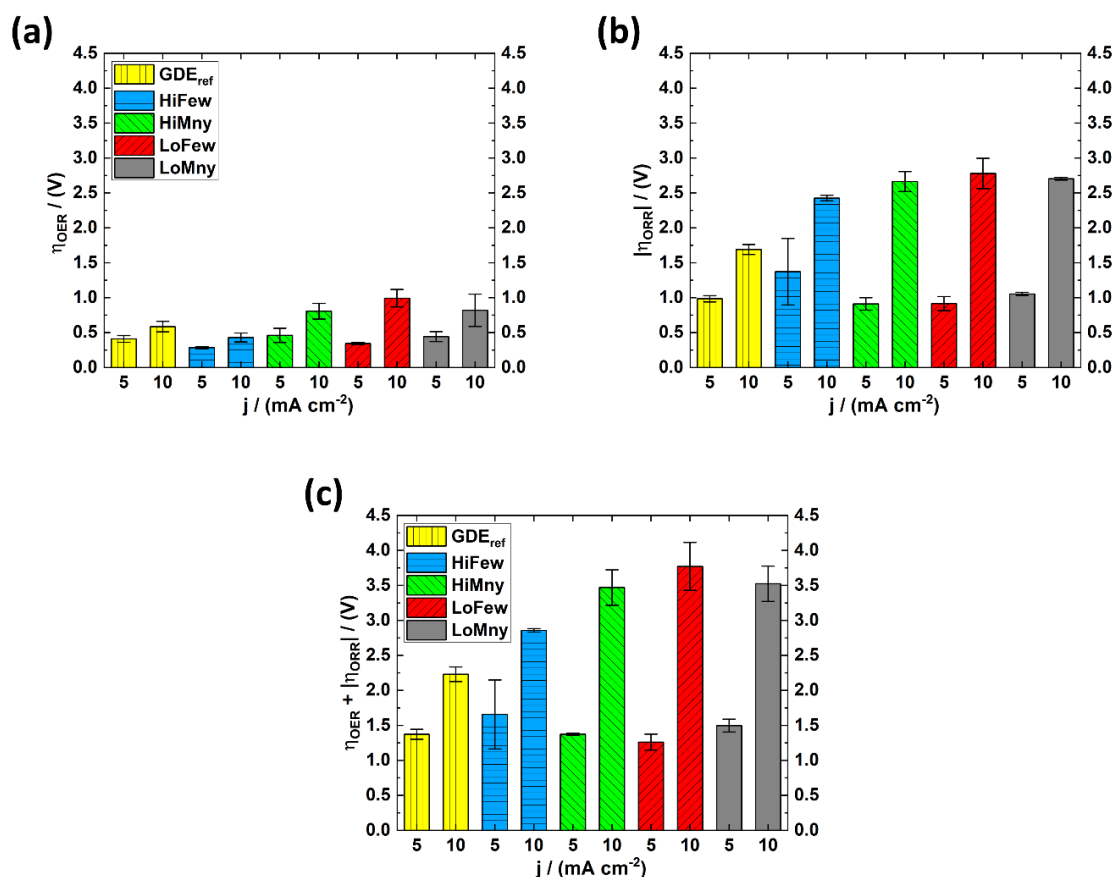
Figure 38. Galvanostatic measurement at different current densities (j / mA cm^{-2}), their overpotential (η / V) response at OER (a) and ORR (b) without ohmic resistance and the corresponding potential-window (c) of carbon-free samples and GDE$_{ref}$ (raw data is shown in Appendix 8, Appendix 10, Appendix 11, Appendix 12, Appendix 13).

On the other hand, the difference between η$_{OER}$ and η$_{ORR}$ of CF-GDEs is based on the different electrochemically active surface area. As shown in Figure 35 and Figure 37, it is assumed that the contact area between the electrolyte and the catalyst of the CF-GDE is much larger than the surface area of the gas-liquid interface (electrolyte thin film meniscus) in the CF-GDE due to its hydrophilic properties (Figure 33). Consequently, the ORR exhibits much larger overpotentials than the OER in CF-GDEs due to its electrochemical dependence on the surface area of the thin electrolyte film[79] [80] [81] [82] [95].

In addition, water activity or hydration of ions, respectively, also contribute to the difference between η$_{ORR}$ and η$_{OER}$. In general, a high current density means a high supply pressure of reactants or products that need to be hydrated. Therefore, the hydrated products contribute to the increase of the overpotentials due to the higher diffusion resistance[87] [91]. While OER OH$^-$ is already hydrated and during ORR, O$_2$ needs to be hydrated to dissolve. O$_2$ requires many more water molecules to dissolve than OH$^-$ formed during ORR[90]. This slower diffusivity of oxygen contributes to the

overpotential difference even at low current densities. However, the K^+ concentration increases at higher current densities near the liquid-gas interface during ORR. Accordingly, the increase in K^+ concentration reduces the water activity near the liquid-gas interface and narrows the ORR zone due to the higher water activity[75] [79] [92] [93]. As a result, the transport pathways for dissolved O_2 are increased. This is the reason why the η_{ORR} of all GDEs is higher than η_{OER} at high current densities. Figure 39 shows the narrowing of the ORR zone by increasing the current density at CF-GDEs.
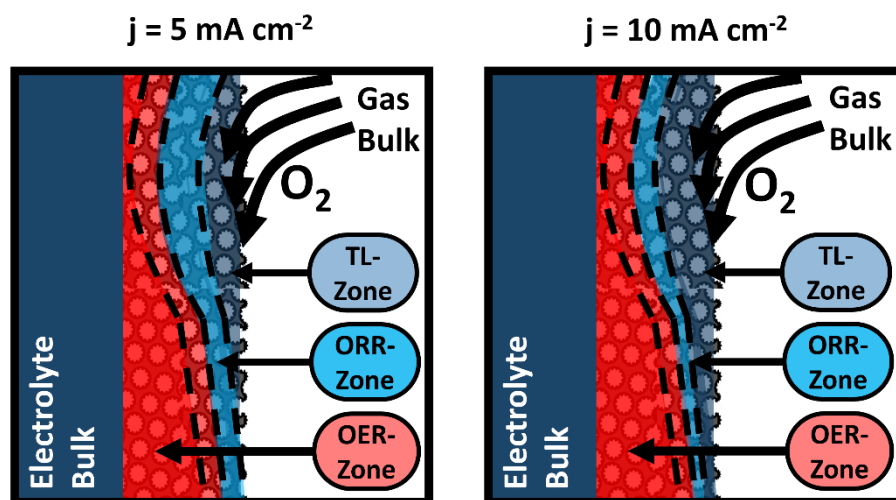
Figure 39. Schematic depiction of ORR Zone narrowing by higher current density in CF-GDEs (TL-Zone: transport limited zone).

Influence of the ORR Zone in CF-GDEs

Results from GDE_{ref} show the lowest ORR overpotential of 1.69 V at 10 mA cm^{-2} compared with CF-GDEs. These results highlight the differences in the design of the GDEs and their influence on the narrowing of the ORR zone by water activity. However, at a current density of 5 mA cm^{-2}, the results of CF-GDEs are similar to those of GDE_{ref} at ORR (about 1 V).

The electrochemically active surface area of the ORR zone of CF-GDEs is assumed to be lower at 10 mA cm^{-2} than at 5 mA cm^{-2} compared with GDE_{ref}, due to the higher overpotential at higher current densities. In general, the PTFE in the GDE_{ref} ensures that the contact of the electrolyte with the catalyst on the outside of the GDE_{ref} is stable. Therefore, the GDE_{ref} surface area of the ORR zone at 10 mA cm^{-2} is assumed to be almost the same as that at 5 mA cm^{-2}. However, the surface area of the ORR zone of CF-GDEs is more affected by the O_2 influx than GDE_{ref}. *Ergo*, the shape of the ORR zone in CF-GDE is potentially more diagonal. In GDE_{ref}, it is more vertical due to hydrophobicity (CF-GDE: Figure 37; GDE_{ref}: Figure 7). As indicated earlier, the ORR zone narrows toward the electrolyte bulk at higher current densities due to water activity. This narrowing is thought to reduce the electrochemically active surface area of the ORR zone in the CF-GDE (Figure 39) more than in the GDE_{ref}. Since CF-GDEs lack hydrophobicity and the property to stabilize the electrolyte film.

In addition, both designs are affected by the contribution of larger transport pathways for dissolved O_2 and the lower O_2 dissolution property due to the lower water activity near the gas-liquid interface. The assumed diagonal shape of the ORR zone of CF-GDEs indicates a higher contribution of the larger transport pathways and lower dissolution properties of oxygen in the upper region of the electrodes at 10 than at 5 mA cm^{-2}. This is illustrated in Figure 39.

As mentioned earlier, the results of CF-GDEs at 5 mA cm^{-2} are similar to GDE$_{ref}$ at ORR (about 1 V). This also indicates that the lower catalytic activity of CF-GDEs (R_p results in Figure 36 (a)) at ORR is compensated by the supply of electrochemically active reactants (Figure 36 (b)) even without a hydrophobic agent. However, this compensation is no longer present at 10 mA cm^{-2}, as mentioned above.

OER Zone in CF-GDEs

It is noteworthy that CF-GDEs (HiFew (0.28 V) and LoFew (0.34 V)) exhibit a lower η_{OER} than GDE$_{ref}$ (0.41 V) at 5 mA cm^{-2}. On the contrary, this is due to the potentially larger OER electrochemically active surface area of CF-GDEs. The water activity during OER is less significant than during ORR because the hydroxide ions in the electrolyte are already hydrated. Therefore, the larger electrochemically active surface area of OER compensates for the lower catalyst activity of CF-GDEs. This is evident from the C_{dl} results (Figure 36 (c)), especially for the CF-GDE HiFew.

Comparison of CF-GDEs

Comparison between the CF-GDEs shows the different electrochemical activities for OER and ORR. HiFew shows the lowest η_{OER} (0.43 V) and η_{ORR} (2.43 V) at 10 mA cm^{-2} among all CF-GDEs. This confirms that the electrodeposition setup HiFew (r_{scan}: 50 mV s^{-1}; cycle number: 500) is the preferred setting for nickel foam as the electrode body.

However, HiFew has a large deviation at 5 mA cm^{-2} during ORR. This illustrates the general dynamics of electrolyte thin film formation in hydrophilic CF-GDEs. The dynamics of electrolyte thin film formation is caused by electrowetting, and the narrowing of the ORR zone (chapter 2.1.5). Both effects occur mainly in the ORR. In general, CF-GDEs tend to form an electrolyte thin film dynamically due to the absence of a hydrophobic agent. This is because hydrophobic additives would stabilize the electrolyte film or the surface area of the gas-liquid interface within the CF-GDEs. This interface is highly dependent on O_2 influx, electrolyte level or pressure, respectively, electrolyte attraction of the hydrophilic MnO$_x$ coating, open pore structure of the nickel foam (capillary pressure of the substrate), and gravity or position of the half-cell, respectively. All in all, these factors favor such outliers, which may occur randomly when a parameter such as the electrolyte level, the O_2 influx or the position of the half-cell changes slightly.

Figure 38 (c) shows the corresponding cumulative overpotential of all samples. In general, HiFew exhibits the lowest value (2.86 V) of all CF-GDEs at 10 mA cm^{-2}. This comparison shows

that the electrodeposited MnO$_x$ coating of HiFew has higher electrochemical activity than the other settings, despite electrowetting and narrowing of the ORR zone. For this reason, HiFew is the preferred deposition setup on a nickel foam for a bifunctional CF-GDE.

Long-term Stability Measurement

The most promising electrodeposition setting (HiFew) was selected for long-term stability measurement to compare its results with GDE$_{ref}$. The GDEs were cycled between 1.5 V (OER) and - 0.75 V (ORR) vs. Hg/HgO 1 M NaOH for 2100 cycles. A cycle is a completed sequence of OER for 20 seconds and ORR for 20 seconds. Figure 40 and Appendix 31 show the normalized results of every 5th cycle. As mentioned earlier, the HiFew sample is not hydrophobic (Figure 33), which resulted in slight leakage throughout the measurement time despite the use of a glass-fiber-fleece. Therefore, electrolyte was added regularly to ensure a uniform and sufficient electrolyte pressure on the Zirfon® membrane during the long-term measurement. The pH of the electrolyte was measured before and after the stability measurements and no significant difference in pH was observed and accordingly there was no increase in KOH concentration.
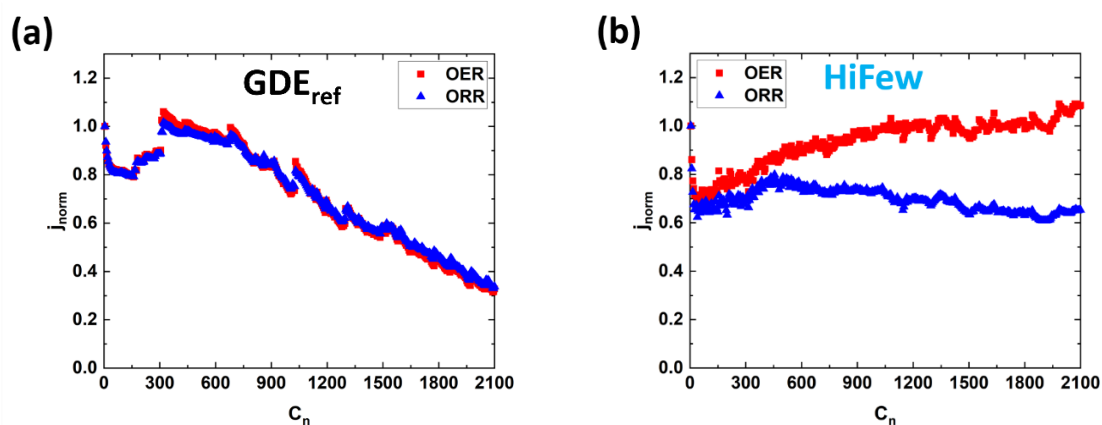
Figure 40. Electrochemical long-term stability measurement of GDE$_{ref}$ and HiFew CF-GDE at 1.5 V and - 0.75 V vs. Hg/HgO 1M NaOH for 2100 cycles and each working mode (OER and ORR) lasted 20 seconds. The second measurement of each sample shown in Appendix 31.

GDE$_{ref}$ (Figure 40 (a)) shows a 20 % drop in current density by the 200th cycle, which rises back above 100 % and drops slightly to 100 % by the 750th cycle. Thereafter, carbon corrosion is indicated, resulting in an overall loss of current density of about 60 %. The corrosion increases steadily until the last 2100th cycle. The first drop is interpreted as initial carbon corrosion, since carbon is less stable in alkaline media and at high electrical loads, as mentioned in chapter 2.2.2. *Ergo*, the carbon contact area of GDE$_{ref}$ wetted by the electrolyte corrodes, which reduces the current density until it increases.

It is assumed that the surface area of the electrolyte film or the electrochemically active surface area, respectively, inside the GDE_{ref}, increases due to the hydrophilization of carbon, which increases the current density. The hydrophilization of carbon is caused by the attack of highly reactive species, which was shown by *Yi et al.*[154] and mentioned in chapter 2.2.2. However, the corrosion of carbon continues to progress inside the carbon-based GDE_{ref}, leading to a steady decrease in current density until the last cycle.

HiFew (Figure 40 (b)) shows much more stable behavior. The first few cycles of HiFew show a drop in current density of about 20 – 30 %, but then begin to increase steadily. The OER- and ORR-stability reaches 75 – 85 % at about the 500th cycle. Thereafter, the ORR current density decreases slightly, but the OER current density increases. These two behaviors remain unchanged until the last 2100th cycle. ORR current density decreases slightly until about 65 % and OER increases until about 110 %. Similar electrochemical stability of pyrolusite MnO_2 was also documented by *Benhangi et al.*[166].

The initial drop in current density of HiFew is thought to indicate dissolution of unstable MnO_x and redeposition of MnO_x, which is known as *Ostwald* ripening[19] [139] [140] [141]. However, thereafter, the OER and ORR current densities increase until the 500th cycle, and then the ORR current density decreases slightly until the last cycle. The trend in the first 500 cycles indicates conditioning of the electrochemically active surface for OER and ORR by the long-term measurement regime.

Lyons et al. [173] have demonstrated this by growing oxy-hydroxide layers on iron foil at - 1.30 V and 0.75 V vs. Hg/HgO 1 M NaOH for 600 cycles at a scan rate of 0.40 V s^{-1}. Therefore, it is possible that oxy-hydroxide layers grew on MnO_x and/or nickel foam due to the long-term measurement. Moreover, oxy-hydroxide layers on nickel have OER and ORR bifunctional activity, which was shown by *Lim et al.* [174]. In addition, it is also possible that *Ostwald* ripening has deposited more stable and active MnO_x or a combination of both. This is also supported by the pink and/or purple discoloration of the electrolyte observed when the HiFew was rinsed with distilled water after measurement. The discoloration indicates the dissolution of unstable MnO_x.

After the 500th cycle ORR decreased slightly until the last cycle. It is assumed that this decrease was caused by the gradual narrowing of the ORR zone or the increase of the flooded electrode surface, respectively. This assumption is supported by the fact that HiFew does not contain hydrophobic agent and is hydrophilic (Figure 33). In addition, the leakage of electrolyte from the CF-GDE supports the assumption that the electrode surface was gradually flooded with electrolyte. In general, flooding is known in the literature as a major problem that reduces ORR performance due to the increase in the transport distance of dissolved oxygen to the catalyst[51] [79]. Accordingly, flooding reduces the ORR zone of GDE when the transport distances are too large[79]. This is mainly due to the reduction of the hydrophobicity of the GDE (see chapter 2.1.5).

Moreover, it is promising that the OER current density increases steadily until the last cycle. This is possibly due to the aforementioned electrochemical formation of oxy-hydroxide layers on

MnO_x and/or on nickel foam and the redeposition of MnO_x due to the long-term measurement regime. It is hypothesized that ORR activity may also have been increased by the redeposition of more active MnO_x, but this was not visible due to dynamic electrolyte film formation or flooding, respectively.

4.1.3   Interim Conclusion I

In this first step towards a sustainable bifunctional CF-GDE, it was shown that the electrodeposition setting HiFew (r_{scan} = 50 mV s^{-1}; cycle number = 500) deposited a MnO_x coating on a nickel foam that exhibited the lowest overpotentials compared to the other settings investigated (Figure 38). The electrochemical stability of MnO_x (HiFew) was demonstrated for 2100 cycles (1.5 V (OER) and - 0.75 V (ORR) vs. Hg/HgO 1 M NaOH, Figure 40).

The results of electrochemical impedance spectroscopy combined with the results of galvanostatic measurement allowed a deeper understanding of the differences between CF-GDE and GDE$_{ref}$. In general, CF-GDE does not have a hydrophobic GDL like GDE$_{ref}$, resulting in a lower transport distance of oxygen, and has nickel foam macropores with a high number of accessible catalytically active sites. For this reason, it has a much lower $\sigma_{Warburg}$ or diffusion resistance, respectively, than GDE$_{ref}$ (Figure 36 (b)). Therefore, the η_{ORR} of CF-GDEs at 5 mA cm^{-2} are similar to those of GDE$_{ref}$ because the lower transport distance of CF-GDEs compensates for the lower electrochemical activity of electrodeposited MnO_x compared to the catalyst in GDE$_{ref}$. The electrochemical activity of the catalyst was indicated by R_p measured by electrochemical impedance spectroscopy (Figure 36 (a)).

However, the electrochemically active surface area (C_{dl} Figure 36 (c)) of CF-GDEs shows variations due to the lack of hydrophobicity (Figure 33). For this reason, the ORR zone varies within the CF-GDE (Figure 37). Furthermore, the measurement at different current densities shows a narrowing of the ORR zone of all GDEs. This narrowing of the ORR zone is caused by the hydration of the formed ions (Figure 39), which is indicated by larger overpotentials at higher current densities. Due to the narrowing of the ORR zone and the lack of hydrophobicity of CF-GDEs, the area of the ORR zone or the electrolyte surface area of the thin film, respectively, was assumed to be much more reduced in CF-GDEs than in GDE$_{ref}$. As a result, the reduction in the electrolyte thin film surface area resulted in a lower amount of dissolved oxygen. In addition, the lack of hydrophobicity indicates that the contact area between electrolyte and CF-GDEs is not beneficially distributed in CF-GDEs.

The hydrophobicity inside the GDEs leads to the largest possible surface area of the electrolyte thin film, resulting in a low η_{ORR}. Therefore, one of the next steps is to introduce hydrophobicity in CF-GDEs.

4.2 Different Metal Substrates and their Coatings

Two different electrode bodies, stainless-steel fleece (Fle) and pressed nickel foam (Fop), were additionally studied in the same manner as shown previously to compare their results. In general, the electrodeposition settings with a dynamic scan rate (r_{scan}) of 25 mV s^{-1} (LoFew and LoMny) displayed lower activities toward OER and ORR (Figure 36 and Figure 38) than with r_{scan} = 50 mV s^{-1}. Therefore, the settings with 25 mV s^{-1} were excluded.

4.2.1 Surface Differences

Figure 41 shows the x-ray tomography computed magnifications of three different electrode bodies as examples. The macroporosity of nickel foam as used before, pressed nickel foam and stainless-steel fleece (20 µm pore size) was investigated.
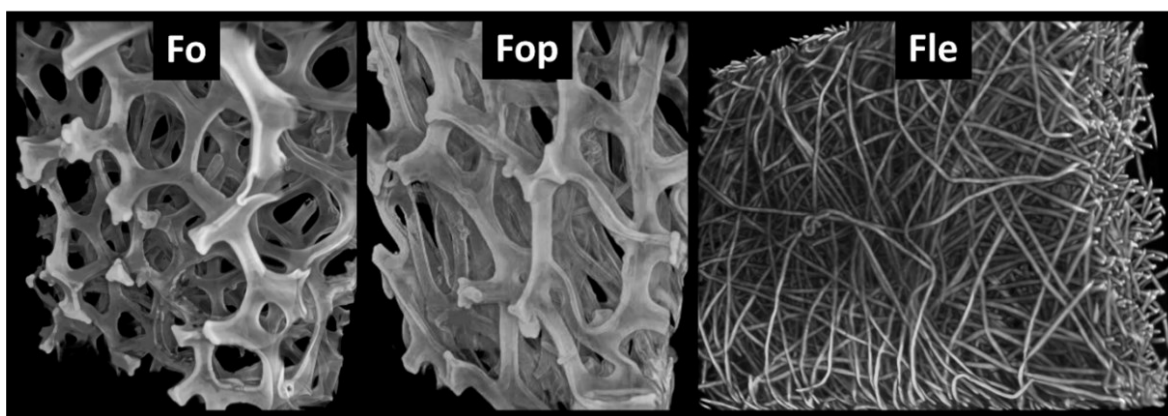
Figure 41. Depiction of computed magnifications of nickel foam (Fo), pressed nickel foam (Fop) and stainless-steel fleece (Fle).

The unpressed nickel foam (Fo) has large pores that create a lot of empty space. The pressed nickel foam (Fop) has deformed pores compared to Fo. Pressing reduced the empty space in the Fop metal substrate, making the pores smaller compared to Fo pores. The stainless-steel fleece (Fle) has a structure of many overlapping thin wires forming small pores (20 µm). Fle has the smallest pores of these three electrode bodies.

Scanning Electron Microscopy

SEM measurements (Figure 42) in 100 µm and 200 nm show the structure of electrode bodies coated with MnO$_x$ by electrodeposition. The settings used are listed in Table 2. Both nickel foams (unpressed and pressed) were coated with the HiFew setting and the stainless steel was coated with the HiMny setting. Therefore, these designations, HiFew and HiMny, describe the electroplating settings, and in chapter 4.1 they are also the names of the samples.
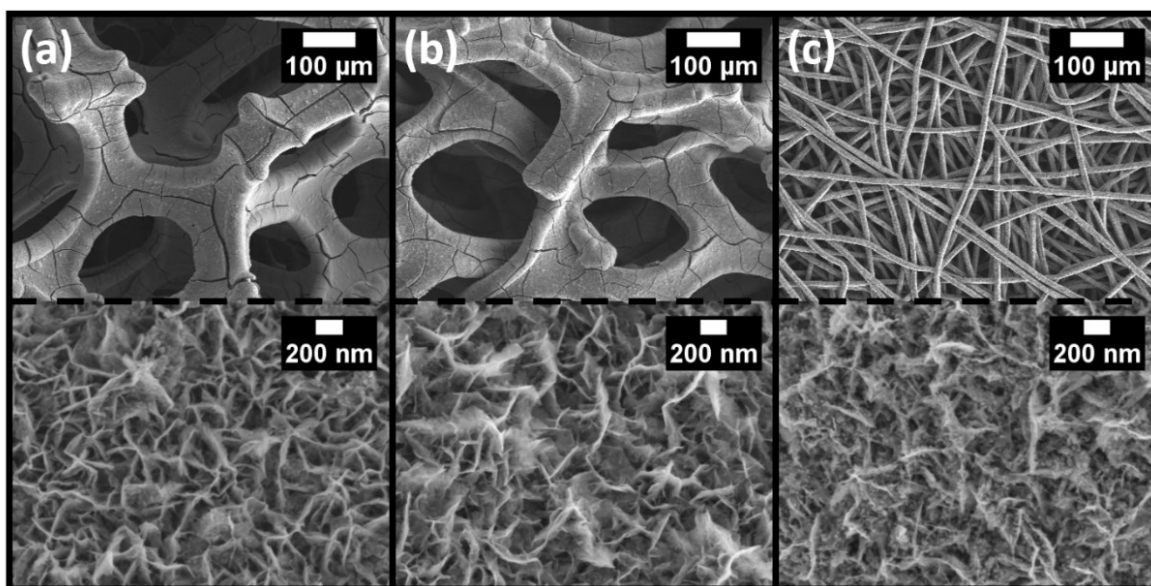
Figure 42. SEM images of nickel foam, Fo, (a), pressed nickel foam, Fop, (b) and stainless-steel fleece, Fle, (c) in 100 μm and 200 nm.

Fo (Figure 42 (a)) shows the coated surface with crack lines on the front of the 100 μm image. Behind it, the coated nickel rod segment and its large pores can be seen. Fop (Figure 42 b), on the other hand, shows the coated nickel rod segments close together in the 100 μm image. It can be concluded that the pores in Fop are smaller than in Fo. Pressing the nickel foam reduces its thickness from 1.95 mm to 0.74 mm. As mentioned earlier, the pore structure of Fle is formed by the overlapping thin wires that form a large surface area, which can be seen in the 100 μm image (Figure 42 c). In addition, the Fle substrate has a thickness of 0.13 mm. All three 200 nm images show approximately the same star fruit like shape as that of *Chou et al.*[133]. However, Fle shows less similarity compared to the other two samples.

In general, the comparison of the surface structure of all three samples indicates that Fle sample has small pores, Fop has medium pores, and Fo has large pores.

X-Ray Tomography

An X-ray tomography measurement of electrodeposited Fo (HiFew: 50 mV s^{-1} and 500 cycles) is shown in Figure 43. The white glowing objects are the hollow nickel foam frameworks used to compute a magnification of the nickel foam for visualization on the right.
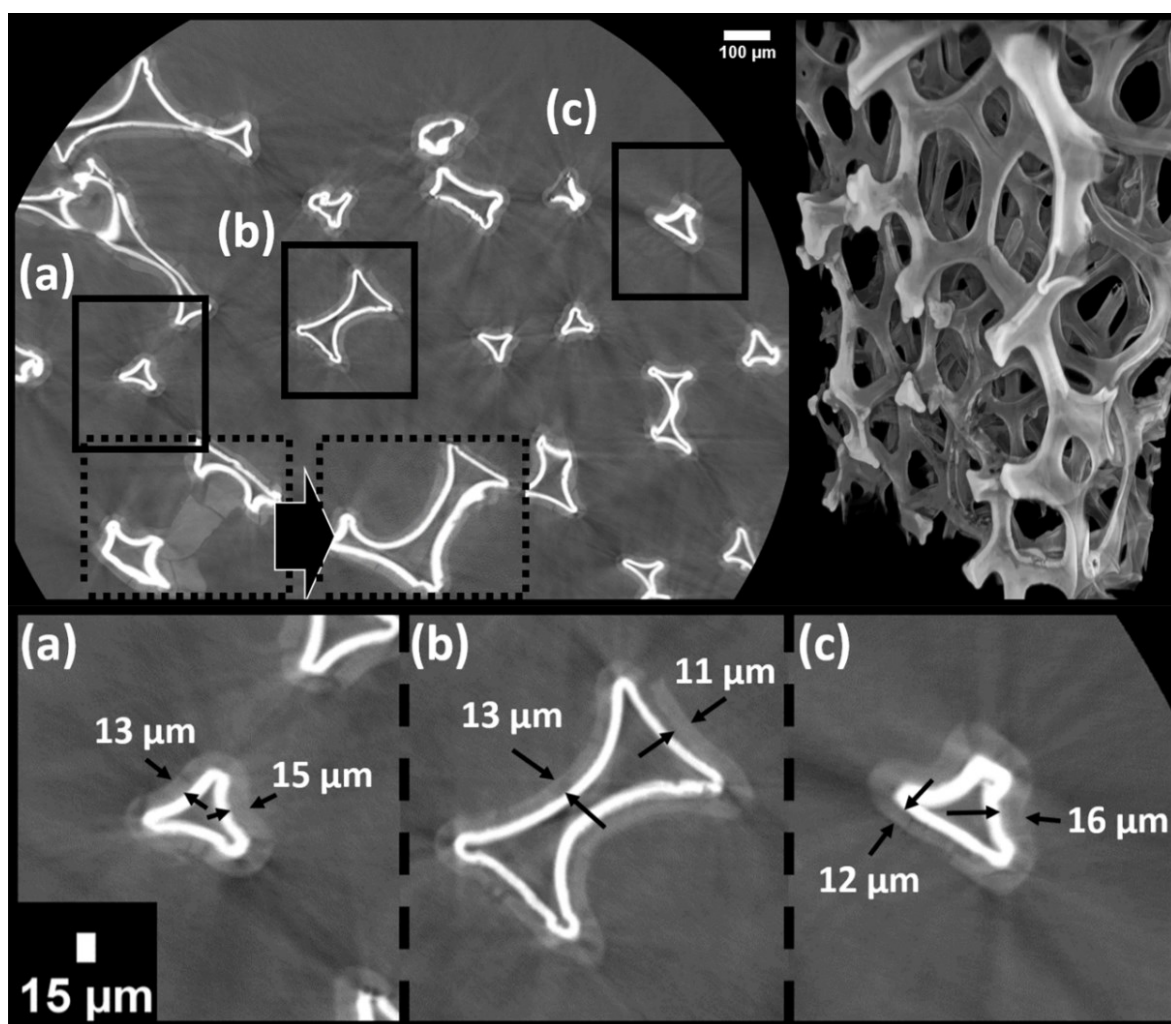
Figure 43. X-ray tomography images of coated nickel foam, Fo, (HiFew: 50 mV s⁻¹ & 500 cycles) in 100 μm and 15 μm.

The pore-like framework can be recognized by the triangular and trapezoidal luminous objects. Fo has a changing frame shape with no constant spacing between the nickel rod segments, shown in the computed magnification of Fo as an example. Some of these changing rod segment spacings are smaller than 100 μm, but most are several 100 μm in size. The Fo samples have a pore size of about 500 – 600 μm.

The rectangular boxes mentioned (a, b and c) have been enlarged and shown below. The black arrows indicate the thickness of the electrodeposited MnO_x layer on the rod segments. The MnO_x layer is light gray and has a thickness of 12 – 16 μm. The thickness of the layers was determined using ImageJ software. However, thicker MnO_x layers can also be observed and are shown in the dotted rectangular box on the left. Beneath this MnO_x layer is a nickel rod inserted into the dotted rectangular box on the right. This right dotted rectangular box shows the same nickel rod that is in the left rectangular box, but just a few scans further. Accordingly, the thick MnO_x layer in the left dotted box is scanned in the cross-section of the flat layer. There are also areas with cracked or delaminated coating and exposed nickel surface.

An X-ray tomography measurement of electrodeposited (HiFew) Fop is shown in Figure 44. As mentioned earlier, the white glowing objects are the hollow nickel foam framework used to compute a magnification of Fop (Figure 41). Fop has a changing frame shape with no constant spacing between nickel rod segments as in Fo (Figure 43), but the pore size is smaller than in Fo.
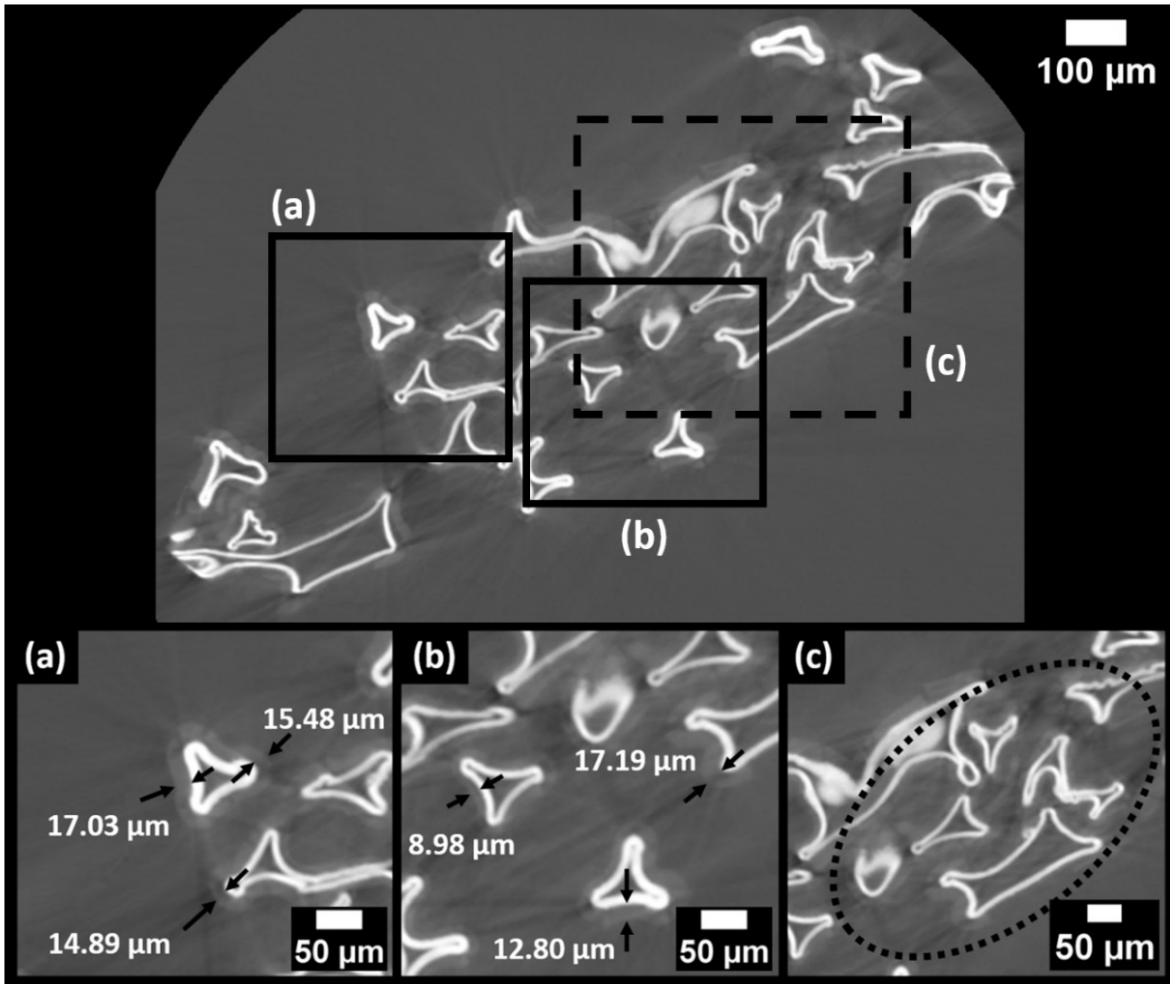
Figure 44. X-ray tomography images of coated pressed nickel foam, Fop, (HiFew: 50 mV s^{-1} & 500 cycles) in 100 μm and 50 μm.

The rectangular boxes (a, b, and c) have been enlarged and shown below. The black arrows indicate the thickness of the electrodeposited MnO$_x$ layer on the rod segments. The MnO$_x$ layer is light gray and has a thickness of about 12 – 17 μm (Figure 44 (a) and (b)). In Figure 44 (c), the dotted ellipse shows an area with closely spaced rod segments. These rod segments all have a MnO$_x$ coating that forms a thin structure of pore channels between the coated rod segments. As mentioned earlier, the thickness of Fop is 0.74 mm and the spacing between rod segments is mostly $20 < x \leq 200$ μm. However, there are a few spots with spacing larger than 100 μm. Nevertheless, Fop has significantly smaller pores ($20 < x \leq 200$ μm) than Fo.

In general, the cracks or delaminated areas of the MnO_x indicate that the nickel surface of Fo and Fop may be in contact with the electrolyte as well as the MnO_x and thus electrochemically active. The comparison of Fo and Fop shows similar MnO_x layer thicknesses. However, the spacing of the rod segments is very different. It is also assumed that the Fo and Fop samples coated with HiMny setting have the same layer thickness range as those coated with HiFew. This is because their electrodeposited MnO_x masses are approx. in the same range (Figure 32 (b) and Figure 46 (b)). It is also assumed that the MnO_x pore channels of Fop between the rod segments (Figure 43 (c)) are distributed over the entire electrode body.

An X-ray tomography measurement of electrodeposited Fle (HiMny: 50 mV s^{-1} and 800 cycles) is shown in Figure 45. The white luminous dots and lines are the stainless-steel fleece framework which were used to compute an enlargement of the fleece (Figure 41).
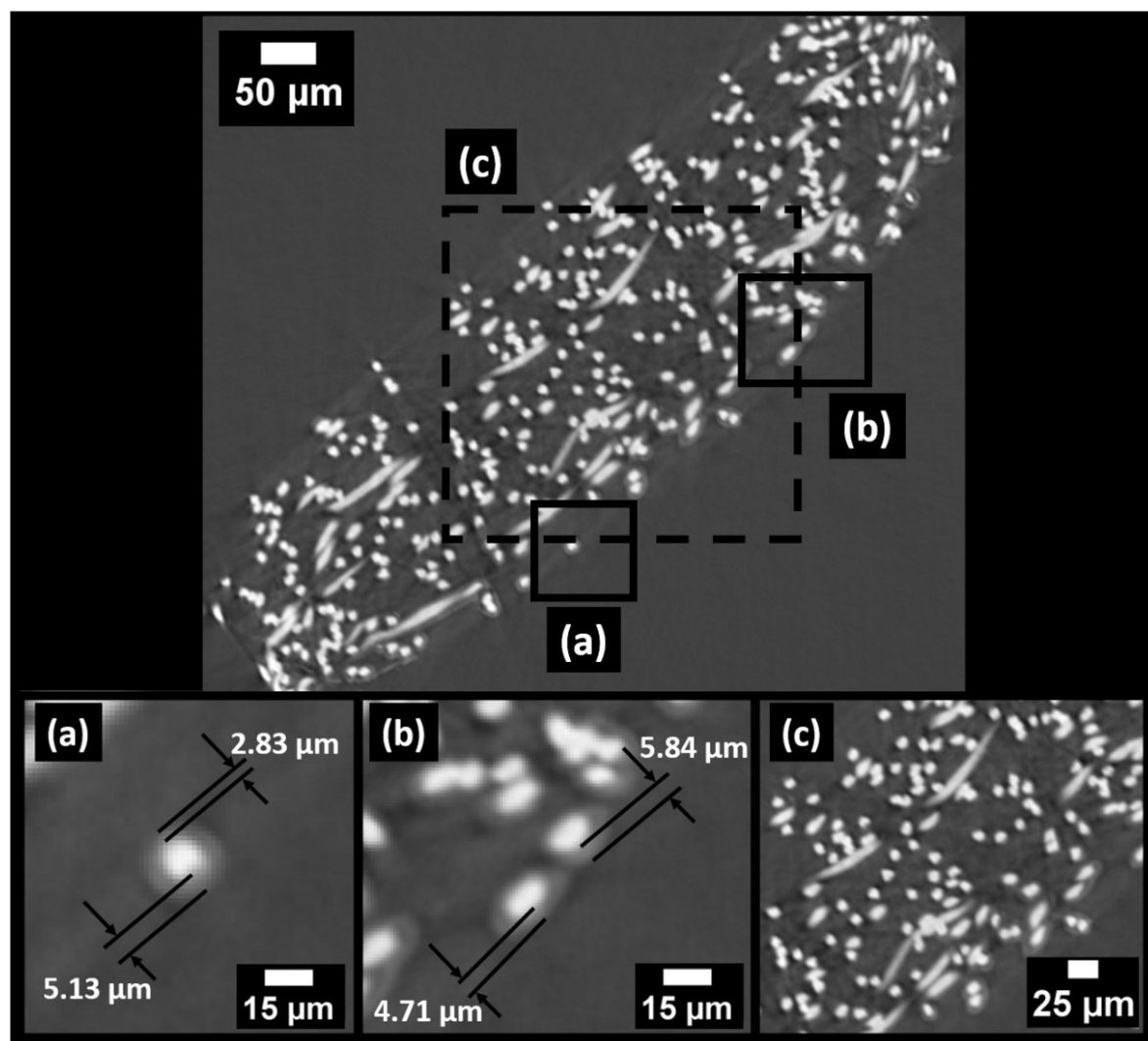
Figure 45. X-ray tomography images of coated stainless-steel fleece, Fle, (HiMny: 50 mV s^{-1} & 800 cycles) in 50 μm, 25 μm (c) and 15 μm ((a) and (b)).

This sample also has an alternating frame shape with no constant spacing between the stainless-steel wires like the other two samples above (Figure 43 and Figure 44). It has the smallest pore size compared to the other electrode bodies above. The rectangular boxes (a, b, and c) were enlarged and are shown below. The black lines with arrows indicate the thickness of the electrodeposited MnO_x layer on the wires. The MnO_x layer is light gray and has a thickness of about 3 – 6 µm (Figure 45 (a) and (b)). In Figure 45 (c), magnification of the wire body does not show a uniform distribution of the MnO_x layer thickness. A layer thickness of less than about 2 µm is difficult to visualize with this method. It is obvious, that the outer lower right side has many more coated individual wires with thicker MnO_x layer than the upper left and inner sides. Consequently, the total thickness of the MnO_x layer is less than 2 µm.

The uneven distribution of MnO_x layer thickness in the Fle sample (Figure 45) is due to the large total surface area of Fle, so that short transport distances are important. The larger total surface area resulted in a strong depletion of manganese ions due to electrodeposition in the area the distance to the electrical contact is the smallest and where the substrate (Fle) faces the counter- and reference-electrode. Since coatable areas on the substrate with shorter transport distances are preferred due to the coatable large total surface area of Fle. The area with short transport distances also has the highest MnO_x layer thickness compared to the opposite and inner sides, confirming the assumption of non-unifrmly distributed layer thickness.

In general, the thickness of the electrode body of Fle is about 130 µm. Moreover, the comparison of the MnO_x layer thickness of all three electrode bodies shows that Fle generally has the smallest layer thickness of less than 2 µm. But the nickel samples (Fo and Fop) have about 12 – 16 µm.

Nitrogen Sorption & Specific MnO_x Mass

The study of the specific surface area (S_{BET}) of the Fle and Fop samples and their electrodeposited specific MnO_x mass at different electrodeposition settings (HiFew: 50 mV s^{-1}; 500 cycles; HiMny: 50 mV s^{-1}; 800 cycles) is shown in Figure 46. It can be seen (Figure 46 (a)) that Fle_{Few} (150 m^2 g^{-1}) and Fle_{Mny} (143 m^2 g^{-1}) have lower S_{BET} than Fop_{Few} (168 m^2 g^{-1}), Fop_{Mny} (172 m^2 g^{-1}), and Fo_{Few} (203 m^2 g^{-1}).

Measurements of the electrodeposited MnO_x mass (Figure 46 (b)) on the three different electrode bodies show that Fo and Fop generally have the same specific mass of about 8.5 mg cm^{-2} at different electrodeposition settings (HiFew and HiMny). The fleece samples contain about 5.5 mg cm^{-2} MnO_x.

The step-like S_{BET} results (Figure 46 (a)) indicate that the pore size of the substrates has a potential influence on them. This is supported by the specific mass results shown for Fle (Figure 46 (b)), which has a much smaller pore size (20 µm) than Fo (500 – 600 µm) and Fop (20 < x ≤ 200 µm).
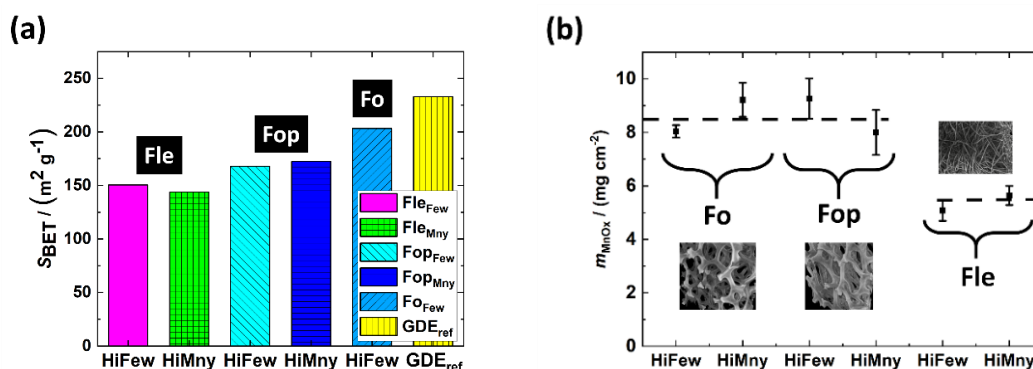
Figure 46. (a) Specific surface area of stainless-steel fleece (Fle) and nickel foam samples (Fo and Fop) measured with the Brunauer-Emmett-Teller (BET) method. (b) Electrodeposited MnO_x specific mass of all electrode bodies at different electrodeposition settings (HiFew: 50 mV s^{-1} & 500 cycles; HiMny: 50 mV s^{-1} & 800 cycles).

In general, the results of BET and the mass measurement (Figure 46) show no significant effect of the number of cycles of the plating settings (__Few: 500 cycles; __Mny: 800 cycles). The variation in specific mass may be due to the difference in electrical contact between the working electrode (Fle, Fo, or Fop) and the clamped nickel wire (chapter 3.2). The connections were made by hand, which caused the electrical conductivity to vary and affect the electrodeposited MnO_x mass. Appendix 2 and Appendix 3 show the potentiostatic deposition (the first 900 seconds) and its electrical contact efficiency can be estimated from the current profile over time.

4.2.2 Hydrophobic Treatment

MnO_x-coated stainless-steel fleece (Fle) and pressed nickel foam (Fop) were hydrophobized with PTFE, resulting in the samples labeled Fle* and Fop*. The exact method is explained in chapter 3.2. The samples were dip coated and their PTFE mass loading is listed in Table 4.

Table 4. PTFE mass of dip coated electrode bodies.

Electrode body	PTFE / mg	Mass fraction PTFE / %	Deviation / mg
Fop	27.5	8.1	2.9
Fle	45.9	22.2	4.0

The Fop samples had 8.1 % and the Fle samples 22.2 % PTFE, based on the total mass of the samples. The deposited PTFE mass deviated slightly more for Fop (~ 10 % based on the total mass of PTFE) than for Fle (~ 9 %). The dip coating was performed manually, which may have caused this PTFE mass deviation.

Contact Angle

The contact angle or hydrophobicity, respectively, of these samples was measured and compared. The results are shown in Figure 47. The contact angle of Fop* is about 130 ° and for Fle* and GDE_{ref} it is 140 °. For this reason, these samples are superhydrophobic (Figure 9). The intrinsic contact angle of electrodeposited MnO_x is 0 °, which makes it extremely hydrophilic (Figure 33 and Figure 47). The MnO_x-coated Fop (Fop*) and Fle (Fle*) change their property from hydrophilic to superhydrophobic due to the PTFE coating.
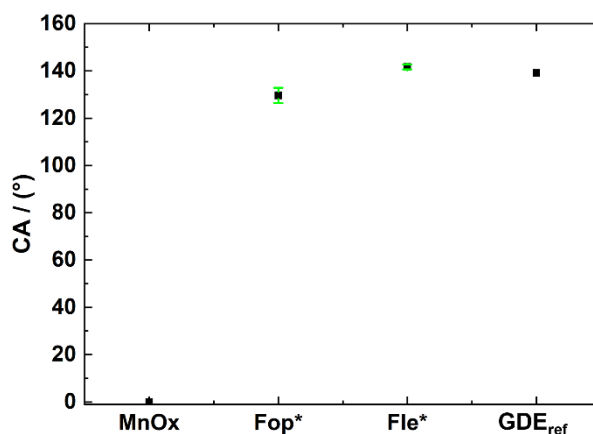
Figure 47. Contact angle measurements of pressed nickel foam (Fop), stainless-steel fleece (Fle) samples and GDE_{ref} (MnO_x: coated nickel sheet; Fop & Fle*: electrode bodies coated with MnO_x and PTFE).*

Scanning Electron Microscopy

The PTFE-coated CF-GDEs had to be coated with carbon for the SEM measurements. This is because a SEM measurement requires an electrically conductive surface, otherwise the recognizability of the transition between coated and uncoated PTFE surface would be weak.

The SEM measurement of Fop* electrodeposited with MnO_x (HiFew) and dip coated with PTFE is shown in Figure 48. The 100 μm image shows the PTFE-coated area as dark spots distributed throughout the Fop*. But the MnO_x coating on Fop* is mostly uncovered. Therefore, Fop* is still hydrophilic to some degree and *ergo* electrochemically active. PTFE is also found in cracks, as shown by the white arrow on the 10 μm image. The PTFE in the crack indicates that it is present to some degree in all cracks in the MnO_x layer.
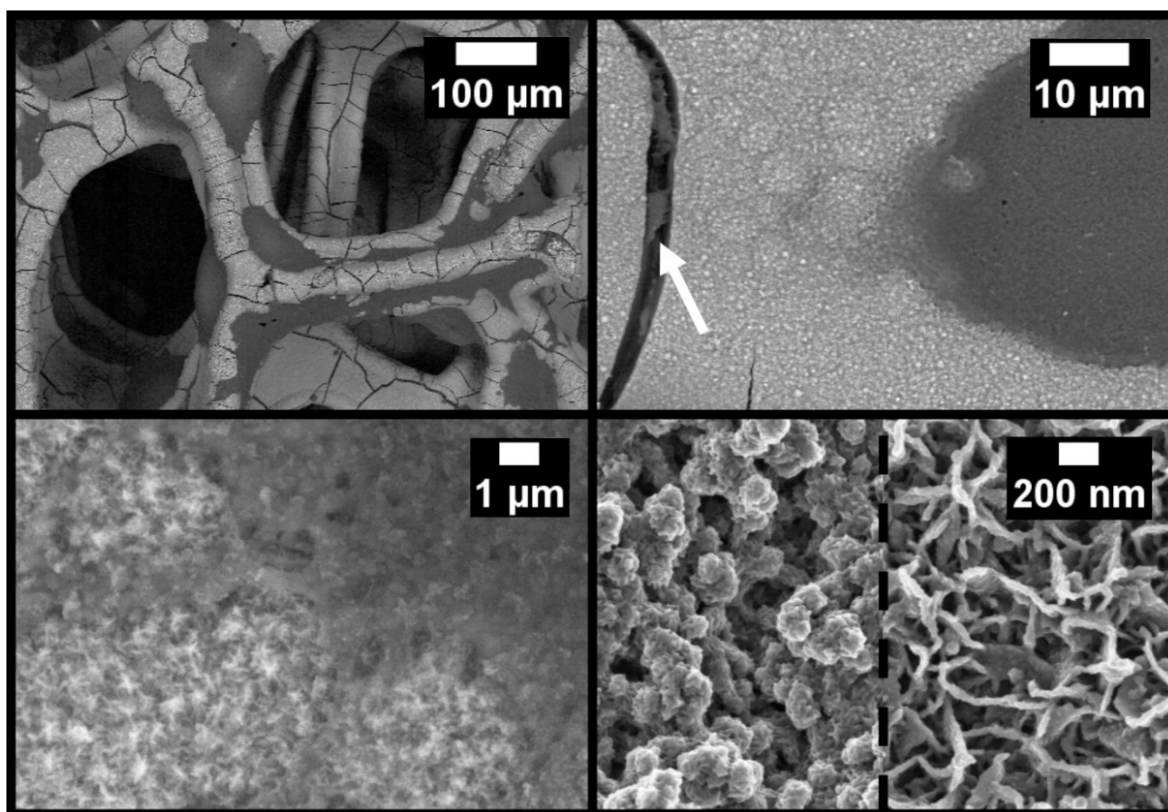
Figure 48. SEM images of pressed nickel foam (Fop*) electrodeposited with MnO_x (HiFew setting) and dip coated with PTFE in 100 μm, 10 μm, 1 μm and in 200 nm. The sample was measured with angle selective Backscatter (AsB) to visualize PTFE.

The transition from the PTFE-coated to PTFE-uncoated MnO_x surface can be seen in the 1 μm image. This can be recognized by the darker surface of PTFE and lighter surface of MnO_x. The 200 nm image shows a carbon coated surface of PTFE and MnO_x, which can be easily distinguished based on their specific shape. PTFE has a much more spherical shape and the MnO_x has the same

shape as previously shown in Figure 31 and Figure 42. However, the MnO_x structure is slightly thicker than in Figure 31 and Figure 42 due to the carbon coating.

In general, the MnO_x-coated (HiFew) hydrophobized Fop has a hydrophilic MnO_x surface with hydrophobic sites. This combination of hydrophilic and hydrophobic surface is similar to the *Salvinia* plant[108]. The *Salvinia* plant and its specificity was explained in chapter 2.1.3. It has a hydrophobic surface with small hydrophilic tips on its plant hairs. Fop*, on the other hand, has a hydrophilic surface with hydrophobic sites, which is the opposite combination of the *Salvinia* plant. It is assumed that the surface property of Fop* has the opposite property of the *Salvinia* plant in aqueous media. This is because the *Salvinia* plant forms a stable air film when immersed in water. Consequently, it is possible that the hydrophobized Fop forms a stable electrolyte film, but the thickness of the electrolyte film is reduced by the PTFE sites inside the Fop.

The SEM measurement of Fle* (stainless-steel fleece) electrodeposited with MnO_x (HiMny) and dip coated with PTFE is shown in Figure 49. The 100 µm image shows the PTFE-coated area as a dark surface that occupies most of the total surface area. In addition, the PTFE increasingly collects in the areas where the wires cross. This can be seen in the 10 µm image. The transition from the PTFE-coated to the uncoated MnO_x surface can be seen in the 1 µm image. This can be recognized by the darker surface of PTFE and the lighter surface of MnO_x.

The 200 nm image shows a carbon coated surface of PTFE and MnO_x, which can be easily distinguished. The displayed MnO_x surface structure (200 nm) is similar to the other displayed MnO_x structures in Figure 31, Figure 42, and Figure 48.

In general, the MnO_x (HiMny setting) and PTFE coated Fle* sample has a hydrophobic surface with hydrophilic sites. This is the same combination of surface properties as in the *Salvinia* plant[108]. Therefore, Fle* is considered to have the same or to some degree similar properties as the plant. *Salvinia* forms a stable air film when immersed in water.
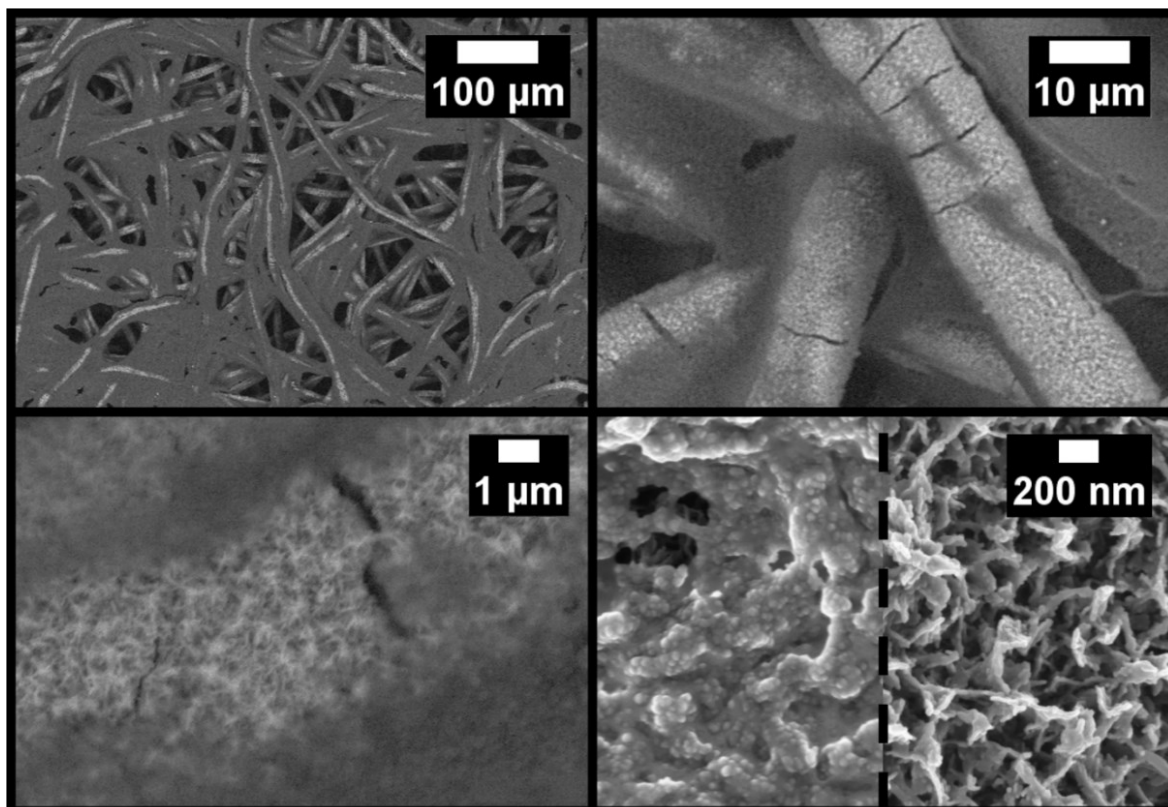
Figure 49. SEM images of stainless-steel fleece (Fle*) electrodeposited with MnO$_x$ (HiMny setting) and dip coated with PTFE in 100 μm, 10 μm, 1 μm and in 200 nm. The sample was measured with angle selective Backscatter (AsB) to visualize PTFE.

It is also assumed that there are also sites of PTFE and PTFE-filled cracks inside Fop* due to the Teflon^{TM} PTFE DISP 30 water emulsion used and the hydrophilic property of MnO$_x$. This is probably also the case with Fle*. As can be seen in Figure 49, PTFE increasingly accumulates in the areas where the wires cross. Therefore, it is assumed that the interior of Fle* is mostly hydrophobic and still has PTFE-free channel-like passages.

4.2.3 Electrochemical Characterization

The three electrode bodies were electrodeposited with two different settings, HiFew (50 mV s^{-1} and 500 cycles) and HiMny (50 mV s^{-1} and 800 cycles). A selection of them was hydrophobized with PTFE. They were then electrochemically characterized to select a setting for each electrode body separately based on the results. In general, the electrodeposition settings with a dynamic scan rate (r_{scan}) of 25 mV s^{-1} (LoFew and LoMny) displayed lower activities toward OER and ORR (Figure 36 and Figure 38) than with r_{scan} = 50 mV s^{-1}. Therefore, the settings with 25 mV s^{-1} were excluded.

Electrochemical Impedance Spectroscopy

The results of electrochemical impedance spectroscopy of all electrode bodies coated with MnO_x only (Figure 50 (a)) and the samples additionally coated with PTFE (Figure 50 (b)) are shown in Figure 50 with their *Nyquist* plots. The measurement was performed at the O_2/OH^- standard potential (0.37 V vs. Hg/HgO in 1 M NaOH) to determine the polarization resistance (R_P), *Warburg* coefficient ($\sigma_{Warburg}$), and the specific double layer capacitance (C_{dl}) at small charge passage overpotentials. The Z' measurement results were shifted for visualization purposes using m. Eq. 8 (chapter 3.3.2).
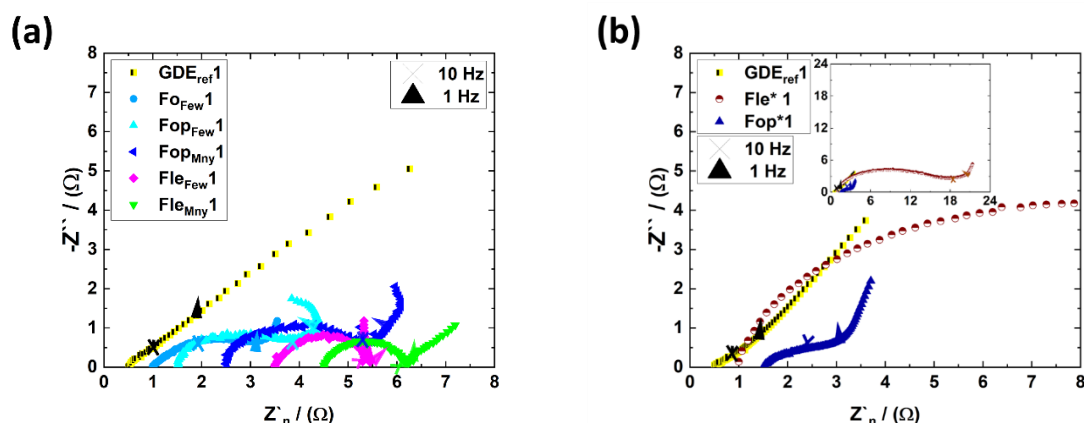
Figure 50. Nyquist plots of all electrode bodies coated with MnO_x at two different settings (HiFew and HiMny) (a) and Fle* (HiMny) and Fop* (HiFew) samples additionally coated with PTFE (b) at a frequency range of approx. 3 kHz – 0.1 Hz (last point) at $\varphi_0 = 0.37$ V vs. Hg/HgO 1 M NaOH. The remaining measurements are shown Appendix 14.

PTFE-coated samples (Figure 50 (b)) were measured without the glass-fiber-fleece (gff) due to the electrolyte retention of the PTFE. The PTFE-uncoated samples require the gff, otherwise the electrolyte would leak heavily. For comparison purposes, GDE_{ref} was measured in both variants. The samples can be clearly identified by their characteristic half circle shape and their straight line upward, which can be interpreted as polarization or electron transfer, respectively, and diffusion (Figure 50 (a) and (b)).

The GDE_{ref} measured with gff has a small half circle and a long straight line with a slope of less than 45 °, and the GDE_{ref} measured without gff has a slope of slightly more than 45 °. This indicates the influence of electrolyte pressure on GDEs in general. The hydrophobic repulsion of PTFE is compensated by the higher electrolyte pressure (without gff). Consequently, the thin electrolyte film penetrates further into the interior of the GDE_{ref}. This subsequently leads to a change in the electrochemically active surface area. This is confirmed (Figure 51) by the results of the regression analysis.

In the high frequency range, only Fop$_{Few}$ and Fop$_{Mny}$ show a line higher than 45 ° in Figure 50 (a), but the second samples of them show a 45 ° line in Appendix 14, indicating a porosity difference between the Fop CF-GDEs. The tomography images of Fop (Figure 44) show smaller pore sizes ($20 < x \leq 200$ μm) than those of Fo ($500 - 600$ μm, Figure 43). Consequently, the 45 ° line in the high frequency range agrees with the tomography images of the porous CF-GDEs.

In the mid-frequency range, the size of the half circle qualitatively indicates the diffusion of dissolved O$_2$ or how much the diffusion of O$_2$ is hindered[158] [167]. For this reason, Fo and Fop CF-GDEs show similar half circle sizes or O$_2$ diffusion, respectively, and Fle CFGDEs present slightly smaller half circles.

At low frequencies, the line of CF-GDEs has a slope higher than 45 °, which looks like a capacitor element, but is interpreted as finite space *Warburg* diffusion[167] [168]. Moreover, the imaginary component of the impedance also approaches 90 ° when the pore end is blocked[167] (compare chapter 4.1.2). In general, the finite space Warburg diffusion implies that an electrochemically active reactant was depleted (transport limited) or the transport of this active reactant was too slow[169] [170] [171] [172]. In the case of CF-GDEs, the $3 - 1000$ nm thin electrolyte film is assumed to represent the finite space and the pores of MnO$_x$ are blocking pores (Figure 35).

Fop CF-GDEs show an asymptotic line approaching 90 ° at low frequencies. However, the slope of the line becomes negative, indicating low penetrability of an electrolyte-wetted MnO$_x$ pore by the a. c. signal, because the frequency was still too high [175]. Low penetrability of pores by the a. c. signal at set frequency was described by *Hyun-Kon Song et al.* [175].

The Fle$_{Mny}$1 (electroplated stainless-steel fleece with HiMny setting) shows a straight line at low frequencies with a slope of about 45 ° or *Warburg* diffusion, respectively. Fle$_{Few}$1 (electrodeposited with HiFew setting), on the other hand, shows a straight line with a slope of about 90 °. However, Fle$_{Few}$2 and Fle$_{Mny}$2 exhibited a negative slope (Appendix 14), indicating low penetrability of the electrolyte-wetted MnO$_x$ pores by the a. c. signal. Since the slopes had negative degrees, it was not possible to quantify $\sigma_{Warburg}$ for Fle$_{Mny}$2, Fle$_{Few}$1, and 2.

The PTFE-coated CF-GDEs measured without gff are shown in Figure 50 (b). In the high-frequency range, only Fop* shows a 45 ° line, but based on the tomography and SEM images (Figure 45 and Figure 49), it is known that Fle* is also a porous electrode. The large half circle size or R_p, respectively, of Fle* in the mid-frequency range indicates a large hindrance of the O$_2$ diffusion[158] [167]. This is due to the PTFE coating, which reduces the electrolyte-electrode contact. It is noteworthy that Fle* has the largest half circle size of all CF-GDEs (Figure 50).

Fop* has a similar half circle size or R_p, respectively, as Fle CF-GDEs, suggesting that O$_2$ diffusion is less hindered than in PTFE-uncoated Fop CF-GDEs. Therefore, fewer PTFE masses of Fop* are beneficial for forming an electrolyte thin film that allows sufficient O$_2$ diffusion. However, the second Fop* half circle size (Appendix 14) is larger than that of Fop$_{Mny}$, indicating some variation in PTFE coating.

In the low frequency range, both PTFE-coated CF-GDEs (Fop* and Fle*) have an asymptotic line shape in the 90 ° direction. This indicates the aforementioned finite space *Warburg* diffusion and blocking pores (MnO_x)[167] [168].

Regression Analysis

For quantitative analysis of the displayed *Nyquist* plots (Figure 50), regression analysis was performed for all samples using the equivalent circuit from Figure 28. These results are shown in Figure 51. The α_{CPE} of the constant phase element is shown in Appendix 15.

GDE$_{ref}$

The results of GDE$_{ref}$ (Figure 51 (a) and (b)) with (0.08 F g^{-1}) and without gff (0.18 F g^{-1}) show that the additional electrolyte pressure had a positive effect on the electrochemically active surface area, as indicated by the specific double layer capacitance (C_{dl}). It resulted in a higher electrochemically active surface area due to deeper penetration of the electrolyte into the interior of the GDE$_{ref}$. In addition, it also resulted in a lower R_p (1.00 Ω → 0.30 Ω) and a lower $\sigma_{Warburg}$ (5.50 Ω s$^{-1/2}$ → 2.05 Ω s$^{-1/2}$) than measured with gff.

It is hypothesized that the higher slope of GDE$_{ref}$ at higher electrolyte pressure (without gff Figure 50 (b)) indicates diffusion of a larger amount of limited electrochemically active reactants (especially dissolved O_2) near the catalyst site. This is confirmed by the C_{dl} results. Consequently, the surface area of the electrolyte-electrode contact (liquid-solid interface) increased, which lowered the R_p value and increased the surface area of the thin electrolyte film within the GDE$_{ref}$ to a lesser extent. The increase in the surface area of the thin electrolyte film lowered $\sigma_{Warburg}$. Accordingly, the demand for reactants increased, but the supply of dissolved O_2 changed little because the slope of the GDE$_{ref}$ without gff was higher than with. Since the supply is limited by the surface area of the gas-liquid interface and the dissolution of gaseous O_2. In contrast, OH$^-$ is abundant, so the supply during OER is more than adequate.

Hydrophilic CF-GDEs

The results in Figure 51 (a) show that Fo$_{Few}$ (unpressed nickel foam coated with HiFew) has the highest specific double layer capacitance (C_{dl}) of 0.25 F g^{-1}, as shown earlier in chapter 4.1.2.

(a)

(b)

(c)

(d)

(e)

(f)
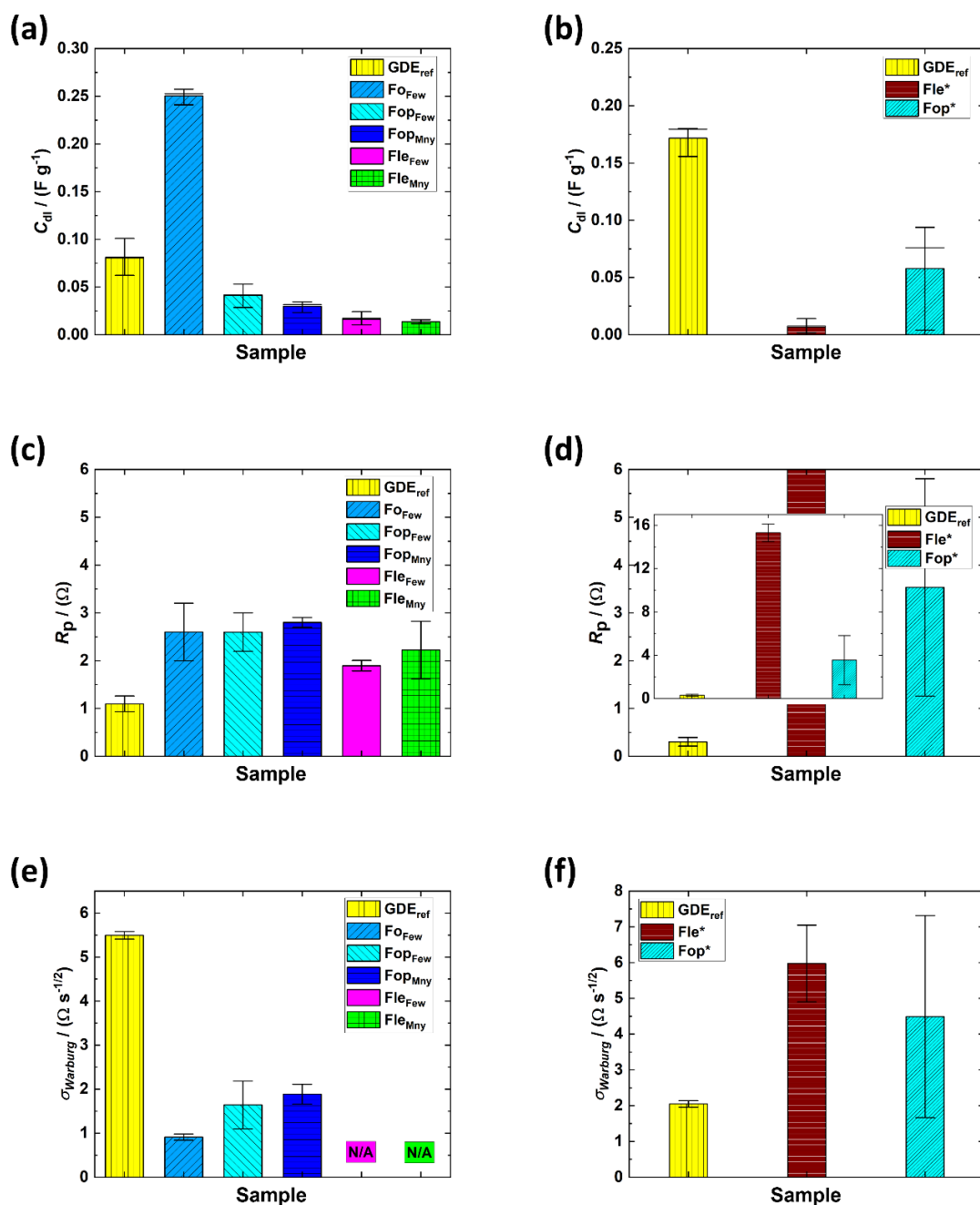
*Figure 51. Image of specific double layer capacitance ((a) and (b), C_{dl}), polarization resistance ((c) and (d), R_p) and Warburg diffusion ((e) and (f), $\sigma_{Warburg}$) at 0.37 V vs. Hg/HgO 1 M NaOH. Determined by the equivalent circuit fitting. MnO$_x$ is electrodeposited with Hi**Few** or Hi**Mny** settings on all electrode bodies (HiFew: 50 mV s^{-1} & 500 cycles; HiMny: 50 mV s^{-1} & 800 cycles), Fle* (stainless-steel fleece, HiMny setting) and Fop* (pressed nickel foam, HiFew setting) are additionally coated with PTFE.*

Fop$_{Few}$ and Fop$_{Mny}$ have approx. the same C_{dl}. However, Fop$_{Few}$ tends to have a higher C_{dl} (0.04 F g^{-1}) than Fop$_{Mny}$ (0.03 F g^{-1}). The lowest C_{dl} (0.02 F g^{-1}) was exhibited by Fle$_{Few}$ and Fle$_{Mny}$, which had nearly the same C_{dl} regardless of the electrodeposition settings. In general, these results indicate that reducing the macropore size from large to medium to small pores (Fo: 500 – 600 μm, Fop: 20 < x ≤ 200 μm and Fle: 20 μm (Figure 43, Figure 44, Figure 45)) and reducing the substrate

thickness (Fo: 1.95 mm, Fop: 0.74 mm, and Fle: 0.13 mm) reduces the electrochemically active surface area. The influence of substrate pore size is confirmed by the results of BET (Figure 46 (a)), specific mass (Figure 46 (b)) and tomography (Figure 45) by comparing Fo and Fop with Fle. Since the results of Fo and Fop CF-GDEs are similar, except for the C_{dl} results. This was not investigated further.

The polarization resistances of the CF-GDEs without PTFE (Figure 51 (c)) generally show higher values than GDE$_{ref}$. The similar R_p results (Fo$_{Few}$: 2.60 Ω, Fop$_{Few}$: 2.59 Ω, Fop$_{Mny}$: 2.80 Ω, Fle$_{Few}$: 1.90 Ω, and Fle$_{Mny}$: 2.22 Ω) indicate that the pore size of the substrate, and its thickness had little effect on the electrochemical activity. Since only Fle CF-GDEs tend to have a slightly lower R_p than Fo and Fop CFGDEs at the O$_2$/OH$^-$ standard potential (0.37 V vs. Hg/HgO 1 M NaOH).

It is hypothesized that the effect of substrate thickness (0.13 mm) combined with the order of magnitude smaller substrate pore size (20 μm) of Fle compared to Fo and Fop led to the lower R_p results. Since Fle CFGDEs have the smallest transport distance to the electroactive sites due to their substrate thickness, O$_2$ diffusion is less hindered.

The *Warburg* diffusion coefficient ($\sigma_{Warburg}$) of CF-GDEs measured with gff shows lower values than GDE$_{ref}$ (Figure 51 (e)). However, the $\sigma_{Warburg}$ of Fle CF-GDEs could not be determined because there was a 90 ° and/or negative degree slope at low frequencies (Figure 50 (a) and Appendix 14).
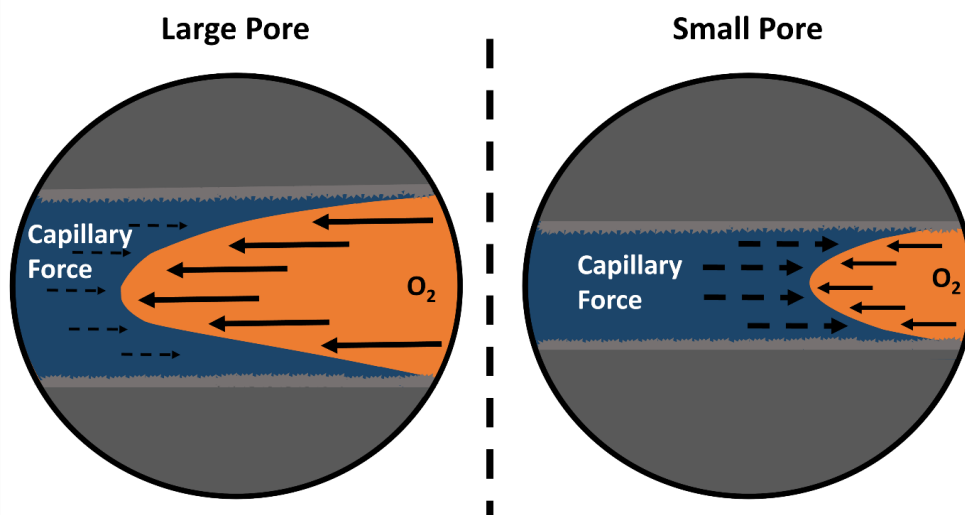
Figure 52. Schematic depiction of a large and small substrate pore with an electrolyte meniscus influenced by capillary pressure of the electrolyte and oxygen influx.

Fo$_{Few}$ has the lowest $\sigma_{Warburg}$ of 0.91 Ω s$^{-1/2}$ and the second lowest are Fop$_{Few}$ and Fop$_{Mny}$, which have approx. the same values (1.64 – 1.89 Ω s$^{-1/2}$). This indicates that the smaller substrate pores of Fop CF-GDEs increase the diffusion resistance or $\sigma_{Warburg}$, respectively.

The smaller substrate pores are assumed to be more completely filled with electrolyte than the larger pores due to the hydrophilic surface. This possibly resulted in a larger surface area of larger electrolyte film thickness of the meniscus than $10 - 1000\,nm$, which increases the diffusion resistance. In addition, the electrolyte in the smaller substrate pores is less pressed out or the size of the electrolyte film is less reduced, respectively, by the oxygen influx than in larger pores (Fo_{Few}) due to capillary pressure of the electrolyte. Consequently, the surface area of the electrolyte thin film meniscus within the CF-GDEs is assumed to be larger in larger pores than in smaller pores. This is shown in Figure 52.

Hydrophobic CF-GDEs

It should be noted that Fop* and Fle* were measured without gff. Therefore, the electrolyte pressure on the hydrophobic CF-GDEs was higher. In Figure 51 (b), the mean C_{dl} ($0.06\,F\,g^{-1}$) of Fop* is higher than that of Fop_{Few}, but has a large deviation. This suggests that the higher electrolyte pressure on Fop* and its hydrophobic to hydrophilic ratio results in a potentially larger electrochemically active surface area than Fop_{Few}. This, along with the SEM images of PTFE-coated Fop* (Figure 48), supports the assumption that Fop* may have the reverse *Salvinia* property that keeps the electrolyte thin film inside. However, the large variation suggests that the correct amount of PTFE coating is critical for the electrochemically active surface area.

The importance of the PTFE amount is particularly evident in Fle*. This is because it had a lower C_{dl} ($0.01\,F\,g^{-1}$) than Fle_{Mny} ($0.02\,F\,g^{-1}$) and a large deviation. These results and the SEM images of Fle* (Figure 49) support the assumption that the electrolyte was more on the outside of the hydrophobic Fle* due to the high amount of PTFE. Therefore, it has the same hydrophobic property as the *Salvinia* plant (Figure 12). Consequently, the surface area of the electrolyte film was much smaller than without PTFE (Fle_{Mny}).

Therefore, the PTFE-coated CF-GDEs (Figure 51 (d)) show a larger R_p than without PTFE. Since the PTFE coating reduces the electrochemically active sites. Consequently, Fle* exhibited the highest R_p ($15.10\,\Omega$) and the mean value of Fop* is slightly higher ($3.53\,\Omega$) than that of hydrophilic Fo and Fop CF-GDEs, but has a large deviation. However, the large deviation of Fop* shows that the lowest R_p was about $1.25\,\Omega$. Therefore, it is assumed that the PTFE coating on Fop* supported the formation of a large electrochemically active surface area. Therefore, the PTFE coating may have a positive effect on the formation of an electrolyte thin film or electrochemically active surface area, respectively. The capillary pressure of the electrolyte can be influenced by introducing the right amount of PTFE into the CF-GDEs. As a result, the surface area of the electrolyte thin film can potentially be increased.

However, the PTFE-coated CF-GDEs have a higher $\sigma_{Warburg}$ than the PTFE-uncoated ones (Figure 51 (f)). Therefore, the right amount of PTFE coating is crucial to achieve a repulsive force that is neither too high nor too low. Nevertheless, the $\sigma_{Warburg}$ results of Fop* ($4.49\,\Omega\,s^{-1/2}$) and

Fle* (5.97 Ω s$^{-1/2}$) are similar to the GDE$_{ref}$ measured with gff (5.50 Ω s$^{-1/2}$). This indicates that the repulsive force of PTFE results in a smaller surface area of the electrolyte thin film than without PTFE coating. It is assumed that at higher electrolyte pressure, the electrolyte thin film area could be increased due to the deeper penetration of electrolyte into the interior of CF-GDE, as shown by the GDE$_{ref}$ measured without gff.

In general, hydrophilic CF-GDE results have shown that a smaller pore size and/or thickness of the substrate has a positive effect on R_p, as the transport distances to the active sites are shorter and thus the diffusion of O$_2$ is less hindered. However, a smaller pore size increases the $\sigma_{Warburg}$ due to a smaller electrolyte thin film meniscus (higher capillary pressure of the electrolyte) than with a larger pore size.

The PTFE coating on CF-GDEs only partially showed its positive effect on R_p, active surface area and $\sigma_{Warburg}$ due to the coverage of the electroactive surface sites and the measurement at the O$_2$/OH$^-$ standard potential (0.37 V vs. Hg/HgO 1 M NaOH). Since no flooding effects occur at this potential. Therefore, these GDEs were also measured at 5 and 10 mA cm^{-2} in the following to investigate their behavior at more realistic electrical loads (Figure 53).

Galvanostatic Measurement

   η_{OER} of Hydrophilic CF-GDEs

The results of galvanostatic measurements of CF-GDEs with and without PTFE and GDE$_{ref}$ are shown in Figure 53. Figure 53 (a) shows the oxygen evolution reaction (OER) results of the CF-GDEs and GDE$_{ref}$. It can be seen that the unpressed nickel foam deposited with the HiFew setting (Fo$_{Few}$) has the lowest overpotentials (η_{OER}: 0.28 V; 0.43 V) at 5 and 10 mA cm^{-2} during OER. The Fop CF-GDEs exhibit higher η_{OER} than Fo$_{Few}$ at 5 (Fop$_{Few}$: 0.63 V; Fop$_{Mny}$: 0.65 V) and 10 mA cm^{-2} (Fop$_{Few}$: 1.12 V; Fop$_{Mny}$: 1.04 V). These results suggest that the smaller pore size of Fop CF-GDEs is responsible for higher overpotentials at high current densities. This can be explained by the OER (E 13, E 14, and E 15) and the transport of new reactants to the active sites deep inside the small pores of Fop CF-GDEs.

The produced H$_2$O during OER (E 14) reduces the concentration of OH$^-$ deep inside the small pores. The transport of new OH$^-$ is insufficient because only the active sites located near the electrolyte bulk are supplied. Consequently, a transport limited zone (TL-zone) of inactive H$_2$O forms (Figure 54). This is referred to as transport limitation. The long transport paths of new reactants (OH$^-$) within the pores lead to a narrowing of the OER high current density zone at the CF-GDE toward the electrolyte bulk side. Unless there is rapid transport of reactants, or the transport paths are short enough to compensate for the production of H$_2$O.

Furthermore, OER leads to bubble-covered catalyst active sites during their formation until they are released into the gas bulk. Therefore, this reduces the electrochemical active surface area

during OER. Nevertheless, the nucleation and expanding of bubbles are moved by capillary pressure of the electrolyte in the hydrophilic pores in the direction of the gas bulk. Therefore, less catalyst active sites are covered with bubbles, resulting in higher electrochemical active surface area. This effect was described by *Tiwari et al.*[176] and summarized by *Swiegers et al.* [21].

Based on reactant transport, Fo_{Few} has an electrolyte bulk-like environment at the active sites, which tend to be inside due to the large pores or low transport limitation, respectively. It is assumed that these large pores provide sufficient reactant transport and lower transport limitation in stationary electrolyte systems. For this reason, more active sites are supplied with reactants in the interior of Fo_{Few} and therefore it has the largest OER electrochemically active surface area or the lowest η_{OER}, respectively. This is shown schematically in Figure 54.
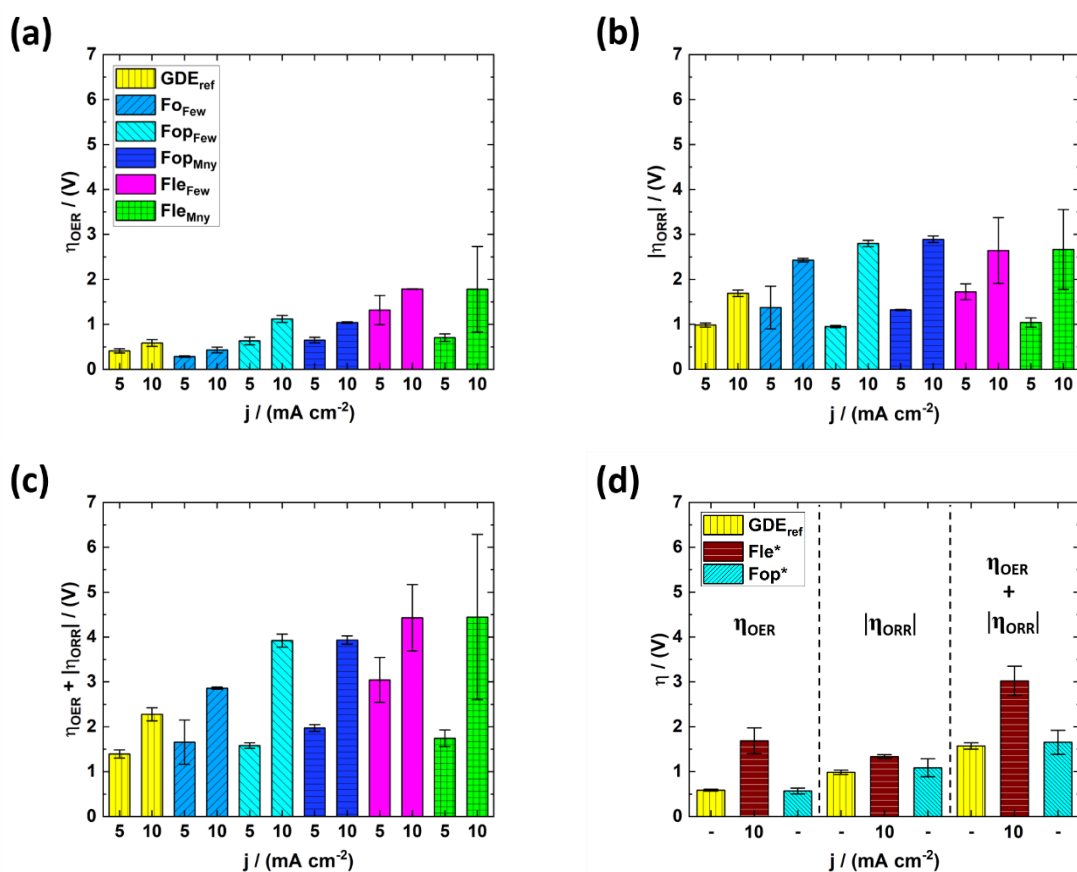
Figure 53. Galvanostatic measurement at different current densities (j / mA cm⁻²), their potential (η / V) response at OER (a) and ORR (b) without ohmic resistance and the corresponding potential-window (c) of MnOₓ coated electrode bodies and GDE_ref. (d) Potential response at OER, ORR and their corresponding potential-window of PTFE-coated samples and GDE_ref (raw data is shown in the Appendix 10; Appendix 16; Appendix 17; Appendix 12; Appendix 13; Appendix 20 and Appendix 21).

Moreover, Fle CF-GDEs show the same behavior as mentioned, they have smaller pores than Fop, and therefore the η_{OER} of Fle are higher than those of Fop CF-GDEs. Fle_{Mny} (0.70 V) exhibited lower η_{OER} than Fle_{Few} (1.31 V) at 5 mA cm⁻² and the same η_{OER} (1.78 V) at 10 mA cm⁻², but with a

large variation. This indicates that Fle_{Mny} has a larger electrochemically active surface area than Fle_{Few} at 5 mA cm^{-2}. It is hypothesized that more uncovered Fle surface area was deposited at the HiMny setting than at HiFew due to the longer deposition time or higher number of cycles, respectively. This is slightly indicated by the specific mass loading of Fle (Figure 46).

GDE$_{ref}$ shows the second lowest η_{OER} of 0.41 V at 5 mA cm^{-2} and 0.59 V at 10 mA cm^{-2}. Its pore size is reported to be between 6 μm and 0.1 μm. Therefore, the reaction zone of GDE$_{ref}$ is on the surface that is in direct contact with the electrolyte, and due to hydrophobicity, the electrolyte contact is more uniformly distributed on GDE$_{ref}$. Based on the pore size and hydrophobicity, the η_{OER} results of GDE$_{ref}$ indicate a higher electrochemically active surface area than Fop and Fle CF-GDEs. However, Fo$_{Few}$ CF-GDE exhibits a lower η_{OER} than GDE$_{ref}$ due to the large pore size of the substrate, which enables a larger OER high current density (HCD-) zone within CF-GDE. Based on the results of Fo$_{Few}$, Fop$_{Few}$, Fle$_{Mny}$, Fop*, and Fle*, the influence of substrate pore and hydrophobicity on the HCD- and transport limited (TL-)zone within the CF-GDEs is schematically shown in Figure 54 and Figure 55.
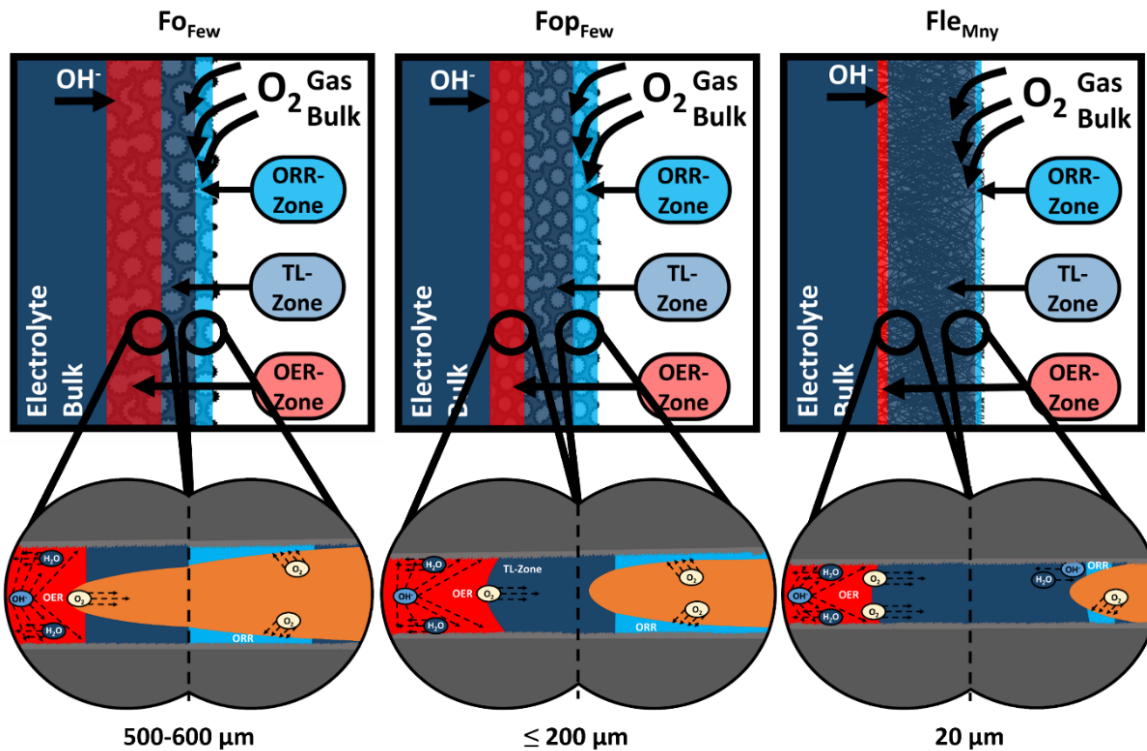
Figure 54. Schematic depiction of the three CF-GDEs (Fo$_{Few}$, Fop$_{Few}$, Fle$_{Mny}$) and their specific ORR- (light blue), OER- (red), and transport limited (TL-) Zone (dark blue) in their whole electrode body and their pores.

η_{ORR} of Hydrophilic CF-GDEs

Moreover, the overpotentials of the oxygen reduction reaction (η_{ORR}) (Figure 53 (b)) are higher than the η_{OER} results (Figure 53 (a)). In general, this is explained by the difference in the

electrochemically active surface area of OER and ORR. As mentioned earlier, ORR only occurs at the thin film meniscus of the electrolyte (10 – 1000 nm), while OER also occurs in the electrolyte flooded region or at higher film thicknesses, respectively. Water activity plays a significant role in ORR at high current densities. High electrical loads can lead to a narrowing of the ORR zone (Figure 39) toward the electrolyte bulk, and thus to a narrowing of the active surface area [15] [144] [145]. In addition, electrowetting is also crucial for ORR, as it is controlled by the applied negative potential, which reduces the surface tension of the liquid-solid phase [112] [143] [144]. Water activity and electrowetting are the reasons (chapter 2.1.5) why the η_{ORR} is much higher at 10 mA cm^{-2} than at 5 mA cm^{-2}.

The η_{ORR} comparison of Fo_{Few} and Fop_{Few} shows the influence of pore size on the electrolyte thin film at different electrical loads. It is assumed that the surface area of the electrolyte thin film of Fop_{Few} is larger than that of Fo_{Few} at 5 mA cm^{-2} because Fop_{Few} (η_{ORR}: 0.95 V) has a lower η_{ORR} than Fo_{Few} (η_{ORR}: about 1.30 V). This can be seen in Figure 54. But the electrolyte thin film surface area decreases more for Fop_{Few} (η_{ORR}: 2.80 V) than Fo_{Few} (η_{ORR}: 2.43 V) at 10 mA cm^{-2}, as indicated by the higher η_{ORR} of Fop_{Few}. This is because higher electrical load causes electrowetting and water movement due to hydration of the produced OH$^-$ [15] [112] [143] [144] [145]. These two mechanisms decrease the electrochemically active surface area for ORR due to the increase in electrolyte film thickness. Consequently, smaller substrate pores ($20 < x \leq 200$ μm) are more filled by these flooding effects than large substrate pores (500 – 600 μm) due to its capillary pressure (Figure 52). For these reasons, Fop_{Few} has a smaller electrolyte thin film meniscus surface area than Fo_{Few} and exhibits a higher η_{ORR} at 10 mA cm^{-2}.

This influence of pore size is also evident in the Fle CF-GDEs, which exhibit a larger η_{ORR} (about 2.65 V) than Fo_{Few} at 10 mA cm^{-2}. Despite the smaller substrate pores of Fle, the comparison between Fop and Fle CF-GDEs shows that Fle has a slightly lower mean η_{ORR} than Fop at 10 mA cm^{-2}, but much larger variations. It is hypothesized that the Fle CF-GDEs are more sensitive to flooding than the Fop CF-GDEs due to their smaller substrate pore size and thus higher capillary pressure. The higher sensitivity of the Fle samples results in less stable electrolyte film formation during the measurement. For this reason, the sensitivity is characterized by high variations. In general, small substrate pores are advantageous for ORR if they are protected from flooding by hydrophobic additives, as shown for GDE_{ref}.

η_{OER} and η_{ORR} of Hydrophobic CF-GDEs

Fop_{Few} and Fle_{Mny} were hydrophobized because they had the lowest overpotentials compared to their counterpart (Fop_{Mny} and Fle_{Few}). Therefore, they are called Fop* and Fle*. They were measured without gff to apply a higher electrolyte pressure to them. GDE_{ref} was also measured without gff for comparison purposes. Their results at 10 mA cm^{-2} are shown in Figure 53 (d).

Results from OER show that Fop* (0.57 V) and Fle* (1.69 V) have lower η_{OER} than their counterparts (Fop_{Few}: 1.12 V; Fle_{Mny}: 1.78 V), and Fle* has a much lower deviation than Fle_{Mny} at 10 mA cm^{-2}. The lower deviation of Fle* supports the assumption that the sensitivity of Fle CF-GDEs is reduced by hydrophobic additives. In addition, GDE_{ref} measured without gff shows no difference in η_{OER} (0.59 V) compared to with gff (0.59 V). This is due to the strong hydrophobicity of the GDL of GDE_{ref}.

In general, hydrophobization of Fop and Fle decreased the total electrochemical surface area. However, this resulted in an increase in the active electrochemical surface area during OER. Since the capillary pressure of the electrolyte in the pores is supported by the hydrophobic sites to attract the O_2 bubble formation more to the gas bulk side. This results in less bubble covering of active sites and thus larger active surface area[21]. However, Fo_{Few} has the lowest transport limitation deep inside due to the large pores of the substrate and the capillary pressure effect of hydrophilic pores, resulting in a larger supply of reactants to the active sites (η_{OER}: 0.43 V) than for smaller substrate pore sizes. The schematic depiction of Fop* and Fle* and their OER and ORR zone formation is shown in Figure 55.

The ORR results of Fop* (η_{ORR}: 1.09 V) and Fle* (η_{ORR}: 1.33 V) clearly show the positive effect of hydrophobization, which resulted in a higher electrolyte thin film meniscus surface area. For this reason, more O_2 dissolved and more catalytic sites were active to reduce it, leading to a lower η_{ORR} than hydrophilic Fop_{Few} (η_{ORR}: 2.80 V) and Fle_{Mny} (η_{ORR}: about 2.65 V) at 10 mA cm^{-2}.
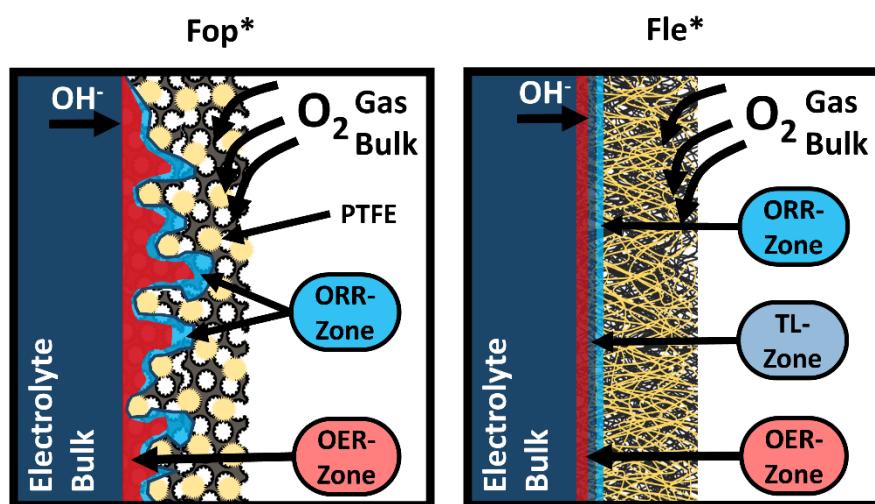
Figure 55. Schematic depiction of hydrophobized CF-GDEs (Fop* and Fle*) and their specific ORR- (light blue), OER- (red), and transport limited (TL-) Zone (dark blue) in their electrode body.

In addition, the more extensive PTFE coating on Fle* (Figure 49) probably resulted in a slightly higher η_{ORR} than Fop*. This is because, Fle* has less uncovered electrochemically active surface area (MnO_x) than Fop*, as shown by the SEM and C_{dl} results (Figure 48, Figure 49 and Figure 51 (a)). The η_{ORR} deviation from Fop* is assumed to have different electrolyte thin film

surfaces, which are affected by the distribution of PTFE coating (Figure 48). This is also supported by the C_{dl} results (Figure 51 (a)).

Remarkably, the ORR results of GDE$_{ref}$ measured at 10 mA cm^{-2} with (η_{ORR}: 1.69 V) and without gff (η_{ORR}: 0.98 V) show how the additional electrolyte pressure increased the electrolyte thin film surface area or the electrochemically active surface area, respectively. *Ergo*, some electrolyte pressure combined with PTFE repulsive force is beneficial.

OER and ORR Active Zone Formation in Dependence of Pore Size and Hydrophobicity

Comparison of the OER and ORR active zones in dependence of pore size and hydrophobicity of the GDEs shows their different preference of electrochemically active environment. This was indicated by the galvanostatic measurement (Figure 53, Figure 54, and Figure 55). Figure 56 shows the OER- and ORR-zone of Fop$_{Few}$ and Fop* as examples.

In general, the OER-zone is near the electrolyte bulk and the ORR-zone is near the gas bulk. However, the hydrophilic Fop$_{Few}$ has a TL-zone in the middle of the OER- and ORR-zone due to transport limitation. The TL-zone is estimated to be larger than the other two zones. It is assumed that this TL-zone no longer exists to the same extent in hydrophobized Fop* CF-GDE. The hydrophobization of Fop$_{Few}$ prevented the deep penetration of the electrolyte into the electrode, which allowed the enlargement of the OER- and ORR-zone. OER-zone is enlarged by decreasing the transport limitation. In this case, the transport limitation is reduced by partially flooded substrate pores. This is because the hydrophobicity of Fop* causes the electrolyte to back up or accumulate, respectively, in the substrate pores near the electrolyte side. Therefore, the removal of the glass-fiber-fleece (gff) results in the increase of the capillary pressure of the electrolyte in the pores. Thus, less bubbles are covering active sites during OER, leading to higher electrochemical active surface area. In addition, the filled pores of Fop* ensure a faster supply of reactants than the less filled pores of Fop$_{Few}$ (measured with gff), since there are more transport paths to the active sites. Consequently, a larger portion of the active surface can be used electrochemically. This is illustrated in Figure 56. However, if the hydrophobicity or PTFE mass, respectively, is too high, as in Fle* (Figure 49), the active surface area for both reactions are reduced, as shown by the OER and ORR results of Fle*.
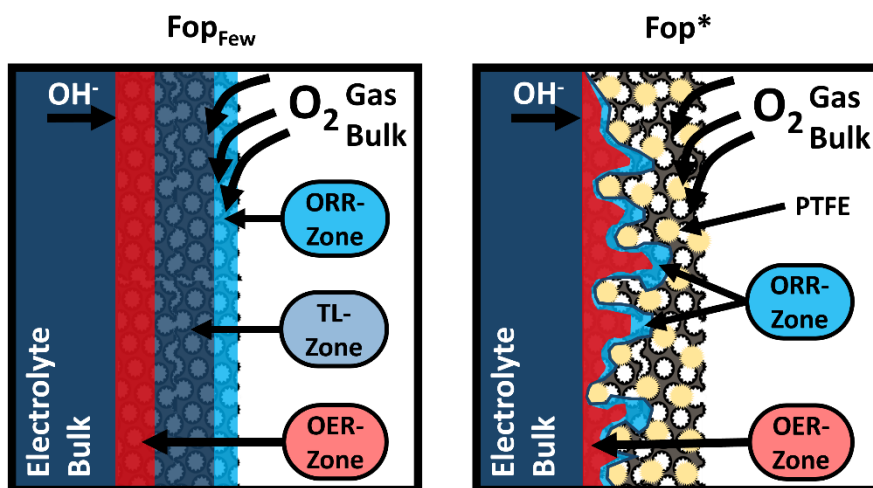
Figure 56. Schematic depiction of OER- and ORR-zone in Fop_{Few} and Fop* CF-GDEs.

In addition, the OER- and ORR-zone depends on the electrolyte film thickness. The film thickness should be large enough to rapidly deliver new reactants and remove the H_2O during OER. This is indicated by the red area in Figure 56. On the other hand, the film thickness should be thin enough (10 – 1000 nm) to provide sufficient dissolved O_2 for ORR, as indicated by the light blue area. However, a too thin film thickness and/or a high current density will result in an inactive region, since the dissolved O_2 is less hydrated during ORR (see above). This is illustrated by the dark blue line in front of the light blue area in Figure 56.

In general, comparison of hydrophobic Fle* and Fop* indicates that the OER-zone of Fle* is much smaller than that of Fop*, but the ORR-zones are similar (Figure 55). This suggests that the electrolyte thin film surface area of Fle* is large enough to provide a similar dissolution area for O_2. Remarkably, comparison of the galvanostatic results of GDE_{ref} and Fop* (Figure 53 (d)) shows that the OER- and ORR-zone have similar sizes. This means that the design of Fop* is comparable to the state-of-the-art GDE_{ref}.

Cumulative Overpotential

The cumulative overpotential generally indicates the overall performance of the measured GDEs (Figure 53 (c) and (d)). Fo_{Few} shows the lowest cumulative overpotential (2.86 V) at 10 mA cm^{-2} compared to the other hydrophilic CF-GDEs. Next, Fop_{Few} and Fop_{Mny} show similar overpotentials (3.92 V) at 10 mA cm^{-2}, but Fop_{Few} has a lower cumulative overpotential (1.58 V) than Fop_{Mny} (1.97 V) at 5 mA cm^{-2}. Fle CF-GDEs also show similar values (4.44 V) at 10 mA cm^{-2}, but Fle_{Mny} has a nearly 50 % lower overpotential (1.74 V) than Fle_{Few} (3.04 V) at 5 mA cm^{-2}. However, the deviation of Fle_{Mny} at 10 mA cm^{-2} is large.

Based on these results, Fop_{Few} and Fle_{Mny} were selected for hydrophobic treatment. The cumulative overpotential of these hydrophilic CF-GDEs was reduced. This is evident from the results

of Fop* and Fle* (Figure 53 (d)). Fle* presented about 32 % lower cumulative overpotential (3.02 V) than Fle_{Mny} (4.44 V) and Fop* showed about 58 % lower cumulative overpotential (1.65 V) than Fop_{Few}.

4.2.4 Interim Conclusion II

Electrochemical impedance spectroscopy and galvanostatic results indicate that reactant transport plays a key role in understanding the improvement potential of CF-GDEs. The advantages of CF-GDEs are the larger pore size of the substrate coated with MnO_x, the absence of an additional gas diffusion layer (GDL), and its carbon-free configuration compared to GDE_{ref}, leading to the following circumstances.

The influence of pore size was investigated using unpressed nickel foam (Fo), pressed nickel foam (Fop), and stainless-steel fleece (Fle) as CF-GDE substrates. It was found that a large pore size ensured reactant supply (Fo_{Few}) for the nanometer-sized patterned MnO_x coating deep inside the CF-GDE with low transport limitation during OER. Thus, reactant supply deep inside the CF-GDE with low transport limitation resulted in a much larger electrochemically active surface area, as indicated by the η_{OER} results especially for Fo_{Few} (Figure 53 (a)). On the other hand, a smaller pore size resulted in a higher η_{OER} value. This is because a larger pore size (500 – 600 μm) provides more reactant transport pathways to the active sites than smaller pore sizes (20 μm).

The design of CF-GDEs does not have a GDL like GDE_{ref}, and therefore the diffusion path to the electrolyte thin film in CF-GDEs is much smaller than in GDE_{ref} during ORR. This is indicated by the lower $\sigma_{Warburg}$ of CF-GDEs, since the diffusion is much more controlled by the slowest or weakest process, namely the diffusion of O_2. However, the η_{ORR} results at different current densities do not show a positive effect of the absence of GDL in CF-GDEs. GDE_{ref} exhibited much lower η_{ORR} than the hydrophilic CF-GDEs. Since the hydrophobicity of GDE_{ref} is much more able to control the flooding of the electrolyte caused by electrowetting and hydration of the reactants at higher electrical loads. This flooding generally leads to an increase in electrolyte film thickness and consequently to a narrowing of the ORR reaction zone, as evidenced by a high η_{ORR}.

For this reason, Fop_{Few} and Fle_{Mny} were hydrophobized to control flooding and the formation of a thin electrolyte film. Fop* and Fle* exhibited significantly lower η_{OER} and η_{ORR} (Figure 50) than their hydrophilic counterparts (Fop_{Few} and Fle_{Mny}). It was concluded that the formation of the thin electrolyte film and the flooding of the pores on the electrolyte side were controlled by hydrophobicity to form a larger electrochemically active surface area within the CF-GDEs than for the hydrophilic surfaces (Figure 54, Figure 55, and Figure 56). In general, OER and ORR results of Fop* are similar to GDE_{ref}. However, Fo_{Few} (unpressed nickel foam) still has the lowest η_{OER} due to the large pores leading to low transport limitation.

All in all, the obtained results show that Fo_{Few}, Fop_{Few} and Fle_{Mny} have the lowest η_{OER} and η_{ORR} compared to their electrode body specific counterparts (Fo_{Mny}, Fop_{Mny} and Fle_{Few}). The PTFE

coating of Fop_{Few} (Fop*) and Fle_{Mny} (Fle*) resulted in lower η_{OER} and η_{ORR} than their hydrophilic counterparts (Figure 53 (d)). Thus, the next step is to design a gradient pore system with the selected CF-GDEs to combine their advantages. This gradient pore system is formed by combining CF-GDE substrates with different pore sizes (L: large, M: medium, and S: small pores).

4.3 Design of Different Porosity Gradients in CF-GDEs

The gradient pore system is constructed by combining different catalyst-coated substrates presented in the previous chapters. Figure 57 shows the combinations studied based on the X-ray tomography computed magnifications of the characterized electrode bodies. Based on the previous electrochemical results, MnO_x was electrodeposited on the porous substrates with the settings that exhibited the lowest overpotentials for OER (oxygen evolution reaction) and ORR (oxygen reduction reaction). Therefore, Fo was coated with the HiFew setting, Fop was also coated with the HiFew setting and Fle was coated with the HiMny setting (Table 2) for the design of the layered carbon-free bifunctional GDE. The different designs of the porosity gradient are shown in Table 3. The order of the layers starts with the left side, the electrolyte side, and ends with the third layer, the gas side.
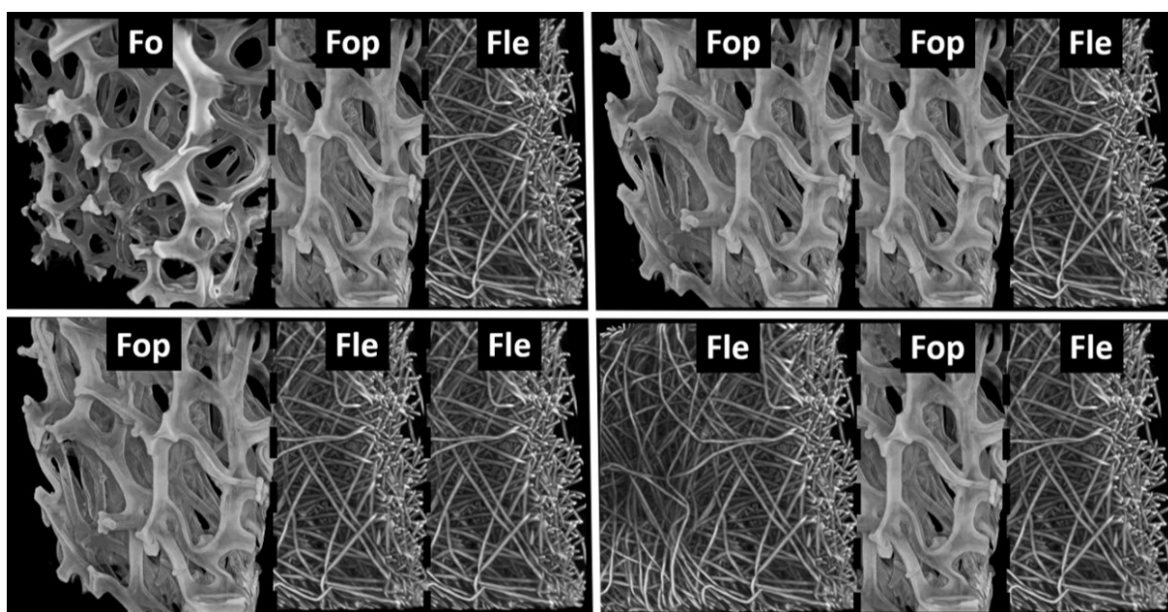
Figure 57. Depiction of X-ray tomography computed magnifications of the combined electrode bodies (Fo: nickel foam; Fop: pressed nickel foam; Fle: stainless-steel fleece).

The gas diffusion layer (Fle*) is the same for all combinations due to its high PTFE loading, as shown in chapter 4.2.2. The electrochemical activity of Fle* was shown in chapter 4.2.3. Thus, the main differences are in the first and second layers of the layered CF-GDEs. They are referenced by their relative pore size as determined by X-ray tomography. Large (Fo_{Few} = L), medium (Fop_{Few} = M) and small (Fle_{Mny} = S) pores. Their hydrophobic or hydrophilic property is indicated by a full or empty square (■ = hydrophobic; □ = hydrophilic). There are five combinations (Table 3) and one of them is illustrated by M□|M■|S■. The first layer is hydrophilic and the other two layers are hydrophobic. In the following, the electrochemical impedance spectroscopy, its regression analysis (Figure 58 and Figure 59) and the galvanostatic measurement results (Figure 60 and Figure 63) of all combinations are shown. Based on the previous electrochemical measurements, the combined layers

are interpreted electrochemically. In addition, a long-term stability measurement of the best performing bifunctional layered CF-GDE and GDE$_{ref}$ was performed (Figure 64).

4.3.1   Electrochemical Results of Layered CF-GDEs

Electrochemical Impedance Spectroscopy

The results of electrochemical impedance spectroscopy of different electrode body combinations are shown in the following *Nyquist* plots (Figure 58). They were measured with (Figure 58 (a)) and without (Figure 58 (b)) glass-fiber-fleece (gff). The measurement was performed at the O$_2$/OH$^-$ standard potential (0.37 V vs. Hg/HgO 1 M NaOH) to determine the polarization resistance (R_p), *Warburg* coefficient ($\sigma_{Warburg}$), and the specific double layer capacitance (C_{dl}) at small charge passage overpotential. The Z' measurement results were shifted for visualization purposes using m. Eq. 8. The first graph was set to x$_{intersection}$ = 0.5 Ω and the next three graphs are set in 0.5 Ω steps. The fifth and final graph in Figure 58 (a) was set at x$_{intersection}$ = 3.5 Ω. The graphs in Figure 58 (b) were set in a similar way, except that the last graph was set to x$_{intersection}$ = 2.5 Ω.
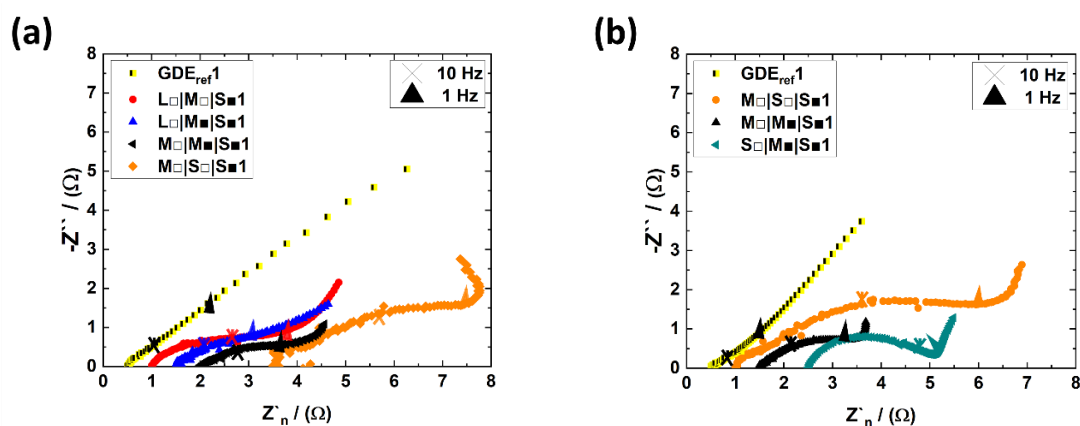
Figure 58. Nyquist plots of all combined electrode bodies that were measured with gff (glass-fiber-fleece) (a) and measured without gff (b) at a frequency range of approx. 3 kHz – 0.1 Hz (last point) at φ$_0$ = 0.37 V vs. Hg/HgO 1 M NaOH. The remaining measurements are at the Appendix 22. This sign "■" indicates the electrode body parts which were coated with PTFE and this "□" which is not coated with PTFE.

Layered CF-GDEs measured with glass-fiber-fleece

In the high frequency range, all layered CF-GDEs measured with gff had a slope around 45 °, except M□|S□|S■ (Figure 58 (a)). In general, this 45 ° line (high frequency) indicates porous electrodes. This is confirmed by SEM (Figure 48 and Figure 49) and tomography images (Figure 43, Figure 44, and Figure 45).

In the middle frequency range, the smallest half circle size of the layered CF-GDE had M□|M■|S■ and the largest had M□|S□|S■. L□|M□|S■ and L□|M■|S■ are in between, but L□|M■|S■ shows a slightly smaller half circle size than L□|M□|S■. It is well known that the hindrance of O$_2$

diffusion is indicated by the size of the half circle [158]. Therefore, the single CF-GDE layers of M□|M■|S■ in combination with each other lead to the lowest O_2 diffusion hindrance compared to the other designs.

Moreover, at low frequencies, the asymptotic line progression in the 90 ° direction is interpreted as finite space *Warburg* diffusion [167] [168]. Since the transport of dissolved O_2 is too slow or slower than OH$^-$ [169] [170] [171] [172]. In addition, the blocking MnO_x pore ends also contribute to the 90 ° approach [167]. In the low frequency range, all layered CF-GDEs showed asymptotic progression toward a 90 ° line except for L□|M■|S■, which exhibited less than 45 °, and M□|S□|S■, which exhibited negative degrees.

The line shape with negative degrees indicates low penetrability of the MnO_x pores by the a. c. signal, because the frequency range was still too high[175]. It is assumed that the electrolyte thin film meniscus (Figure 61 and Figure 62) has a very small thickness on the MnO_x, pores which contributes to such slopes with negative degrees at low frequencies. Thus, if the impedance line does not have an asymptotic slope and is less than 45 ° at low frequencies, then there is no blocking pore end and the pores are large or the space for the a. c. signal to penetrate is large, respectively.

Layered CF-GDEs measured without glass-fiber-fleece

The layered CF-GDEs (M□|M■|S■, M□|S□|S■, and S□|M■|S■) measured without gff had higher electrolyte pressure, so the electrolyte penetrated further into them (Figure 58 (b)). All show a 45 ° line in the high frequency range, indicating porous electrodes. M□|M■|S■ has the smallest half circle size compared with the layered CF-GDEs, and S□|M■|S■ has the largest, as measured previously with gff in the mid-frequency range. Consequently, the O_2 diffusion hindrance can be estimated by the half circle size, as mentioned earlier. All layered CF-GDEs exhibited an asymptotic trend toward 90 ° at low frequencies.

GDE$_{ref}$ was already described in the previous chapters 4.2.3.

Regression Analysis

The results of the regression analysis from electrochemical impedance spectroscopy at 0.37 V vs. Hg/HgO 1 M NaOH are shown in Figure 59. The α_{CPE} of the constant phase element are shown in Appendix 23.
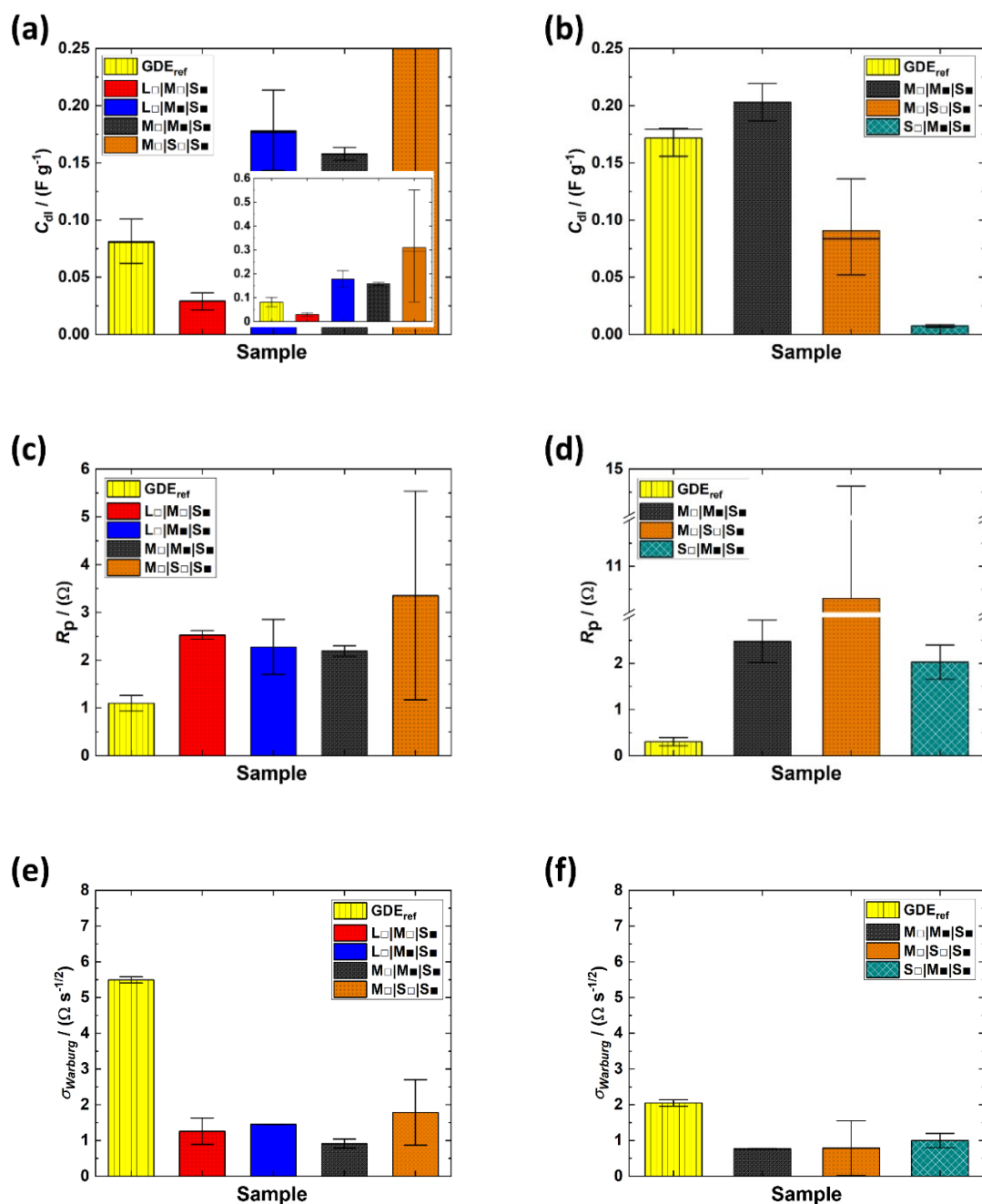
Figure 59. Image of specific double layer capacitance ((a) and (b), C_{dl}), polarization resistance ((c) and (d), R_p) and Warburg diffusion ((e) and (f), $\sigma_{Warburg}$) at 0.37 V vs. Hg/HgO 1 M NaOH. Determined by the equivalent circuit fitting. The remaining results are at the Appendix 23. This sign "■" indicates the electrode body parts which were coated with PTFE.

L□|M□|S■ (red) and L□|M■|S■ (blue)

Based on the earlier results of Fo$_{Few}$ (0.25 F g^{-1}) and Fop$_{Few}$ (0.04 F g^{-1}) in chapter 4.2.3 (Figure 51), it was generally expected that L□|M□|S■ (0.03 F g^{-1}) would have the same or even a higher C_{dl} (Figure 59 (a)) than L□|M■|S■ (0.18 F g^{-1}), but this was not the case. Their comparison shows that the combination of hydrophilic Fo$_{Few}$ and Fop$_{Few}$ results in a similar C_{dl} as a single Fop$_{Few}$. However, when Fop$_{Few}$ in the combination is hydrophobic (M■), the C_{dl} tends toward a single Fo$_{Few}$ value.

114

These observations suggest that the dominant part of L□|M□|S■ is the hydrophilic Fop$_\text{Few}$ (M□). On the other hand, when Fop$_\text{Few}$ is hydrophobic (L□|M■|S■), the dominant part shifts to the hydrophilic Fo$_\text{Few}$ (L□) for the C_dl. However, this difference does not affect R_p and σ_Warburg, because L□|M□|S■ (2.52 Ω; 1.26 Ω s$^{-1/2}$) and L□|M■|S■ (2.28 Ω; 1.45 Ω s$^{-1/2}$) have similar values (Figure 59 (c) and (e)).

M□|M■|S■

It is noteworthy that when Fo$_\text{Few}$ (L□) in L□|M■|S■ is replaced by Fop$_\text{Few}$ (M□|M■|S■), C_dl (0.16 F g^{-1}) and R_p (2.19 Ω) remain the same, but their deviations and σ_Warburg are reduced (Figure 59 (a) and (c)). This indicates that the surface area of the electrolyte thin film inside M□|M■|S■ is larger than that of L□|M□|S■ and L□|M■|S■, as suggested by the reduction of σ_Warburg. Therefore, M□|M■|S■ potentially has a larger electrochemically active surface area during ORR. In addition, an increase in electrolyte pressure on M□|M■|S■ resulted in a decrease in σ_Warburg (0.90 → 0.77 Ω s$^{-1/2}$) or an increase in diffusion flux, respectively, indicating an increase in ORR active surface area. This is also supported by the increased C_dl (0.16 → 0.20 F g^{-1}). However, the increase in C_dl mainly indicates the sum of OER and ORR active surface area, with the OER active surface area (flooded catalyst sites) generally larger than the ORR surface area (electrolyte thin film, Figure 56). These results indicate that more ORR and OER active surface area is available at higher electrolyte pressure. The R_p (2.19 Ω → 2.47 Ω) changed slightly, but shows a slightly larger variation at higher than at lower electrolyte pressure.

M□|S□|S■

Furthermore, if the hydrophobic Fop$_\text{Few}$ (M■) of M□|M■|S■ is replaced by hydrophilic Fle$_\text{Mny}$ (S□) then M□|S□|S■ is designed. This change resulted in a large variation of C_dl (0.29 F g^{-1}), R_p (3.35 Ω), and σ$_\text{Warburg}$ (1.78 Ω s$^{-1/2}$) and increased their values. This indicates that the electrolyte thin film and the total electrochemically active surface area inside M□|S□|S■ are strongly affected by the introduced hydrophilic Fle$_\text{Mny}$. This leads to the assumption that the electrolyte is mainly held between the first two layers of M□|S□|S■ (M□|S□). For this reason, the electrochemical processes (OER | ORR) mainly take place there due to the high capillary pressure of S□. The C_dl results of M□|S□|S■ show that the electrolyte-electrode contact has a large variation.

However, the increase in electrolyte pressure (measurement without gff) resulted in a decrease in C_dl (0.29 → 0.08 F g^{-1}) and its deviation. The change in σ_Warburg showed a decrease (1.78 → 0.79 Ω s$^{-1/2}$). The R_p and its deviation increased extremely (3.35 → 10.30 Ω) when a higher electrolyte pressure was applied. Consequently, the values of M□|S□|S■ with and without gff can be interpreted as similar due to the large deviation ranges. Nevertheless, the electrolyte continues to penetrate into the interior of the M□|S□|S■. Thus, the penetration of the electrolyte ensures that it

mainly floods the first two layers and is most likely stopped by the last layer (hydrophobic Fle$_{Mny}$). This indicates that the electrolyte thin film is located between S□ (hydrophilic) and S■ (hydrophobic) of M□|S□|S■. It is assumed that the second layer S□ of M□|S□|S■ dominates the electrochemical processes during the measurements with and without gff because of the large deviations of C_{dl}, R_p, and $\sigma_{Warburg}$.

S□|M■|S■

S□|M■|S■ was designed by replacing the first layer of M□|M■|S■, Fop$_{Few,}$ with Fle$_{Mny}$. S□|M■|S■ is measured without gff and *ergo* with higher electrolyte pressure. The results of the regression analysis show that it has a similar C_{dl} (0.01 F g^{-1}) to Fle$_{Few}$, Fle$_{Mny}$, and Fle*, as shown in Figure 51 (a) and (b). Accordingly, the electrolyte thin film is assumed to be located between the first two layers of S□|M■|S■. Thus, Fle$_{Mny}$ is assumed to be flooded. However, R_p (2.03 Ω) and $\sigma_{Warburg}$ (1.00 Ω s$^{-1/2}$) are similar to M□|M■|S■, indicating that the surface area of the electrolyte thin film must be the same.

The quantitative results of the regression analysis presented which combination of substrate pore sizes had the highest electrochemically active surface area, activity, and diffusion flux or $\sigma_{Warburg}$, respectively, at 0.37 V vs. Hg/HgO 1 M NaOH. The M□|M■|S■ CF-GDE design meets all the above criteria. However, a more realistic scenario needs to be considered and thus measurements at higher electrical loads are required. Therefore, galvanostatic measurements are performed to investigate the control of flooding as a function of different porosity gradients and hydrophilic/hydrophobic transitions by evaluating the OER and ORR overpotentials.

Galvanostatic Measurement

The galvanostatic OER (a) and ORR (b) measurements of carbon-free bifunctional layered GDEs and GDE$_{ref}$ are shown in Figure 60. They were measured at 5 and 10 mA cm^{-2} vs. Hg/HgO in 1 M NaOH with low electrolyte pressure (with gff). The cumulative overpotentials are shown in Figure 60 (c). A particular selection (Figure 60 (d)) was measured only at 10 mA cm^{-2} with high electrolyte pressure (without gff). In general, the results show which combination has the lowest overpotentials for OER and ORR. Low overpotentials indicate high electrochemical activity at high current densities.

It should be added that galvanostatic measurement of the second M□|S□|S■ sample was not possible at high pressure (Appendix 29). This is because the second M□|S□|S■ sample exceeded the measurement limits of the potentiostat SP-240, which caused the measurement to be aborted.

L□|M□|S■ VS. L□|M■|S■

The second electrode body part was first investigated by comparing L□|M□|S■ and L□|M■|S■. The hydrophobicity of their middle part M was changed. Based on their variations, they exhibited the same η_{OER} (L□|M□|S■: 0.52 V; L□|M■|S■: 0.62 V) and η_{ORR} (L□|M□|S■: 0.73 V; L□|M■|S■: 0.79 V) at low electrolyte pressure (with gff) and at 5 mA cm^{-2}. Moreover, at 5 mA cm^{-2}, they exhibit a η_{ORR} that is about 23 % lower than that of GDE$_{ref}$ (0.98 V), but similar values (1.69 V) to that of GDE$_{ref}$ at 10 mA cm^{-2}.
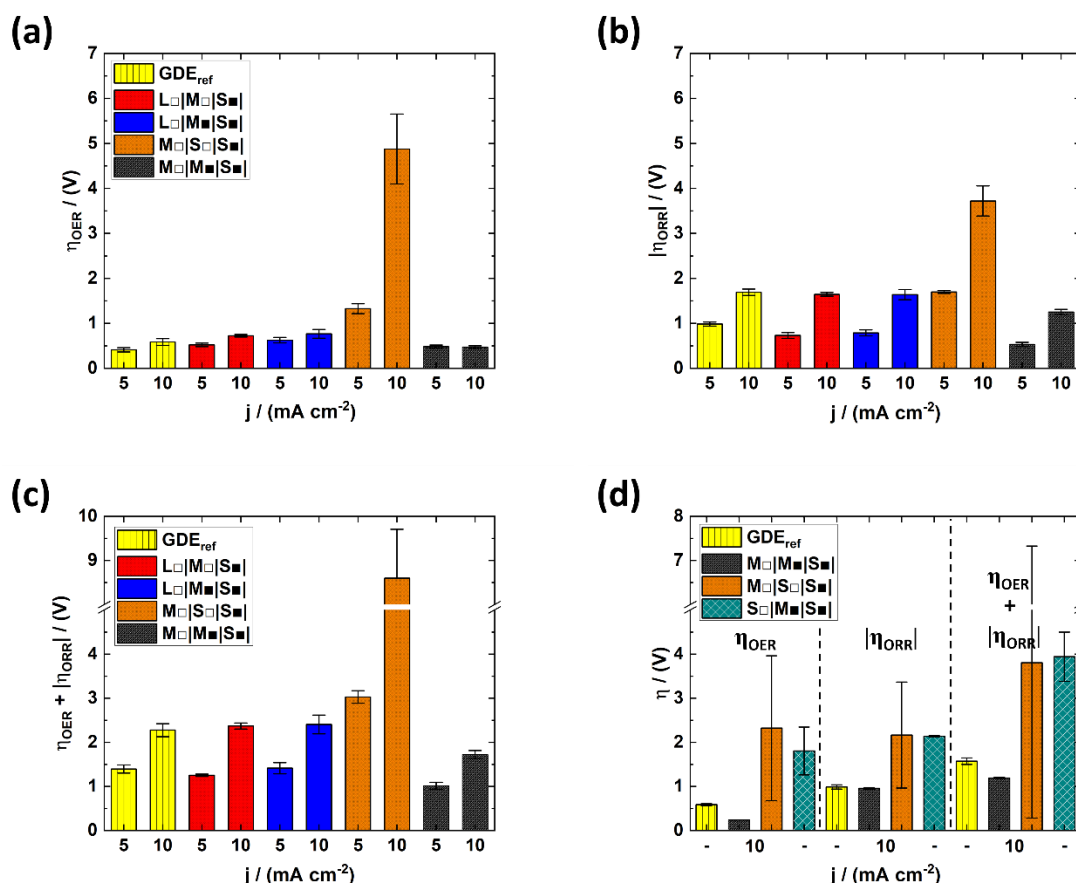
Figure 60. Galvanostatic measurement at different current densities (j / mA cm^{-2}), their potential (η / V) response at OER (a) and ORR (b) without ohmic resistance and the corresponding potential-window (c) of carbon-free bifunctional layered GDEs and GDE$_{ref}$. (d) Potential response at OER, ORR and their corresponding potential-window of a certain selection of samples measured with high electrolyte pressure (raw data is shown in Appendix 24; Appendix 25; Appendix 26; Appendix 27; Appendix 28; Appendix 29; Appendix 30).

The same results suggest that there is no significant effect of hydrophilic or hydrophobic property on the electrochemical OER and ORR for these designs. However, L□|M■|S■ showed a higher C_{dl} (0.17 F g^{-1}) than L□|M□|S■ (0.03 F g^{-1}) in the regression analysis (Figure 59 (a)). For this reason, it is assumed that there is a shift in the electrochemically active zone due to the introduction of M■ into L□|M■|S■. The C_{dl} difference indicates that the electrolyte retention of PTFE-coated

Fop* (M■) causes a higher holdup or accumulation of the electrolyte in L□ of L□|M■|S■ than in L□|M□|S■.

However, no similar influence was observed at higher current densities (10 mA cm^{-2}), as the η_{OER} (L□|M□|S■: 0.72 V; L□|M■|S■: 0.77 V) and η_{ORR} (L□|M□|S■: 1.64 V; L□|M■|S■: 1.64 V) remained the same. There was also no influence of the different flooding effects in the GDE during the ORR (see chapter 2.1.5). Consequently, both layered CF-GDEs have similar electrochemically active surface area for OER (flooded active sites) and ORR (electrolyte thin film meniscus area).

M□|M■|S■ VS. L□|M□|S■ & L□|M■|S■

On this basis, L□, the first layer of L□|M■|S■, was changed to M□, and *ergo* M□|M■|S■ was designed. The comparison of the overpotentials shows that this change of the first layer is clearly beneficial for the electrochemical activity of OER and ORR. In general, the electrolyte is mainly in the first layer and is repelled by the second hydrophobic layer of both designs. Consequently, the electrolyte accumulates in the first layer, resulting in pore filling. Due to the smaller substrate pore size of M□ (20 < x ≤ 200 μm), more M□ pores are filled than L□ pores (500 – 600 μm), resulting in higher capillary pressure of electrolyte in the smaller pores. In addition, the substrate pores of M■ are also partially filled because the thickness of Fop (0.74 mm) is less than that of Fo (1.95 mm). Therefore, more active sites of M□|M■ are in contact with a thick enough electrolyte film to allow sufficient reactant transport during OER. For this reason, less bubble covered active sites are present and fewer transport limitations occur, resulting in a lower η_{OER} (0.48 V; 0.47 V) for M□|M■|S■ than for (0.62 V; 0.67 V) L□|M■|S■ at both current densities. This is shown schematically in Figure 61.

It is noteworthy that the η_{ORR} (0.53 V; 1.25 V) of M□|M■|S■ at 5 and 10 mA cm^{-2} is also lower than that of L□|M■|S■, so the electrolyte thin film surface area of M□|M■|S■ must be larger. The formation of the electrolyte film thickness within the layered CF-GDEs plays a significant role in OER and ORR active zone. The differences in film formation between L□|M■|S■ and M□|M■|S■ and their active zones are shown schematically in Figure 61. The film thickness in L□, the first layer of L□|M■|S■, is assumed to decrease steadily faster than in M□, the first layer of M□|M■|S■, because the pore size and substrate thickness of L□ are larger than those of M□. This is illustrated by the schematic enlargement of the pores in Figure 61.
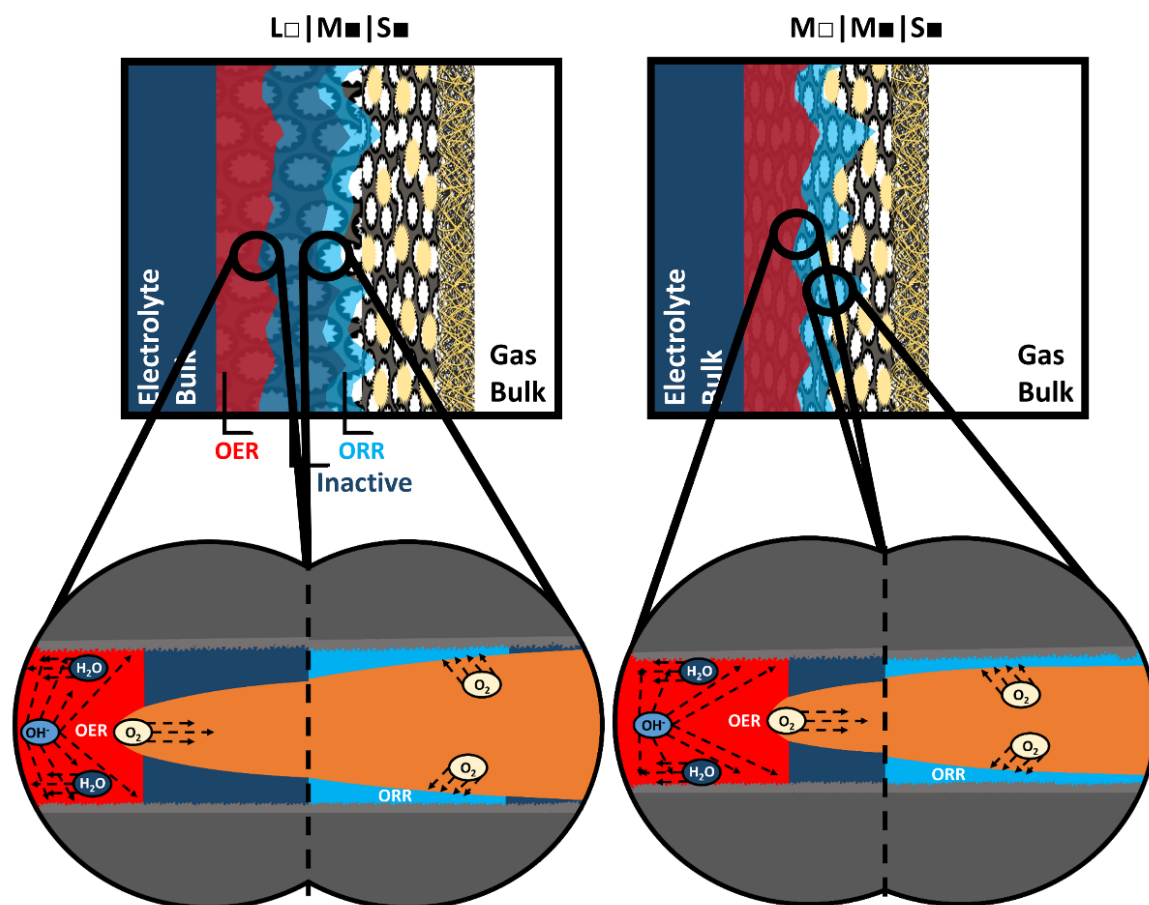
Figure 61. Schematic depiction of OER (red), inactive (dark blue) and ORR zone (light blue) of L□|M■|S■ and M□|M■|S■ and their difference in electrolyte film formation.

However, comparison of the single-layer η_{OER} results at 5 and 10 mA cm^{-2} of Fop$_{Few}$ (M□: 0.63 V; 1.12 V) and Fo$_{Few}$ (L□: 0.28 V; 0.43 V) shows the opposite behavior (chapter 4.2.3). This can be explained by the absence of the repulsive force. Without the M■ repulsive force, fewer Fop$_{Few}$ substrate pores are filled and a larger electrolyte thin film surface is formed in them, which is too thin for sufficient OER reactant transport. In addition, the capillary pressure of electrolyte in pores pushes the bubble formation towards gas bulk side, which is supported by the hydrophobic layer M■[21]. This results in less bubble-covered active sites during OER and thus higher electrochemical active surface area. This is also confirmed by the results of Fop*, because Fop* is a hydrophobized Fop$_{Few}$ and was measured without gff and thus with higher electrolyte pressure. As a result, the electrolyte was dammed-up in Fop*, which resulted in sufficient OER reactant transport and additionally less bubble-covered active sites and thus gave almost the same OER activity as Fo$_{Few}$.

In general, the combination of L□ with M□ or M■ resulted in lower OER activity than compared with a single L□, probably due to the formation of an electrolyte film too thin for OER reactant transport (dark blue /light blue area in Figure 61). This is caused by the second layer increasing the space of the wettable hydrophilic catalyst surface by 0.74 mm (M□ or M■). The

increase in wettable hydrophilic area decreased the thickness of the electrolyte film within the CF-GDE, which decreased the electrochemical OER activity but increased the ORR activity.

The η_{ORR} of L□|M■|S■ (1.64 V at 10 mA cm^{-2}) is much lower than that of a single L□ (chapter 4.2.3; L□ = Fo$_{Few}$; 2.43 V at 10 mA cm^{-2}). This is because a larger ORR active electrolyte thin film surface area was formed, but the OER active surface area was reduced. It was expected that L□|M■|S■ would have a lower η_{OER} than L□|M□|S■ due to its hydrophobic repulsive force. However, the large substrate pores and thickness of L□ were too large for the electrolyte to accumulate sufficiently in the substrate pores to achieve a similar OER activity as Fo$_{Few}$. But their ORR activity is the same.

M□|S□|S■

The next design was created by replacing the second layer of M□|M■|S■ (M■) with S□, and thus, M□|S□|S■ was designed. The OER and ORR activity results of M□|S□|S■ show that this design is not advantageous. This is particularly evident when comparing the results at 5 (η_{OER}: 1.33 V; η_{ORR}: 1.70 V) and 10 mA cm^{-2} (η_{OER}: 4.89 V; η_{ORR}: 3.72 V), which indicate insufficient reactant transport at higher electric loads (Figure 60 (a)).

In general, the electrolyte in M□|S□|S■ goes from $20 < x \leq 200$ µm hydrophilic substrate pores to 20 µm hydrophilic substrate pores and is stopped at 20 µm hydrophobic substrate pores. For this reason, the 20 µm hydrophilic pores are assumed to be more filled than the first $20 < x \leq 200$ µm hydrophilic pores. This is because the ten times smaller pores of S□ have stronger hydrophilic attraction (capillary forces), which partially reduce the electrolyte film of M□ and partially create electrolyte thin films in $20 < x \leq 200$ µm pores. For OER, reactant transport through M□ to S□ is assumed to be limited by the electrolyte film thickness inside M□ and by the substrate thickness of M□ during OER. Therefore, only a portion of M□ is supplied with reactants that is close to the electrolyte bulk, which results in small active surface area. This is shown schematically in Figure 62. In addition, the bubble formation is not pushed sufficiently as at M□|M■|S■ more to the gas bulk side and thus results in bubble-covered active sites. The large difference in η_{OER} results at 5 and 10 mA cm^{-2} (1.33 V; 4.89 V) indicates that more electrochemical active sites were covered by bubbles and that its release to the gas bulk was insufficient. Furthermore, this possibly resulted in the entrapment of air during OER inside M□, which may also reduce additionally the OER active site due to the created O$_2$, which has to accumulate until its pressure is high enough to escape through S□|S■ of M□|S□|S■. This could be a possible reason for the high deviation and the reason for the infeasible measurement at higher electrolyte pressure (Appendix 29).

Moreover, the surface area of the electrolyte thin film meniscus at which ORR occurs is probably between S□ and S■. Comparison of the individual S■ (Fle*) results (Figure 53) shows that S□|S■ has a much lower and inconsistent electrochemically active surface area during OER and ORR. It is assumed that the lower electrolyte pressure on S■ of M□|S□|S■ is caused by M□|S□. The

lower pressure resulted in the formation of a smaller electrolyte thin film meniscus surface area, so the ORR activity of M□|S□|S■ is lower than that of single S■. Moreover, the transport distance of H_2O (hydration) to the ORR active zone of M□|S□|S■ is greater than that of single S■ in direct contact with the electrolyte bulk. This is because fresh H_2O must cross M□|S□ to reach the active zone. This is made clear by the schematic illustration of M□|S□|S■ in Figure 62.
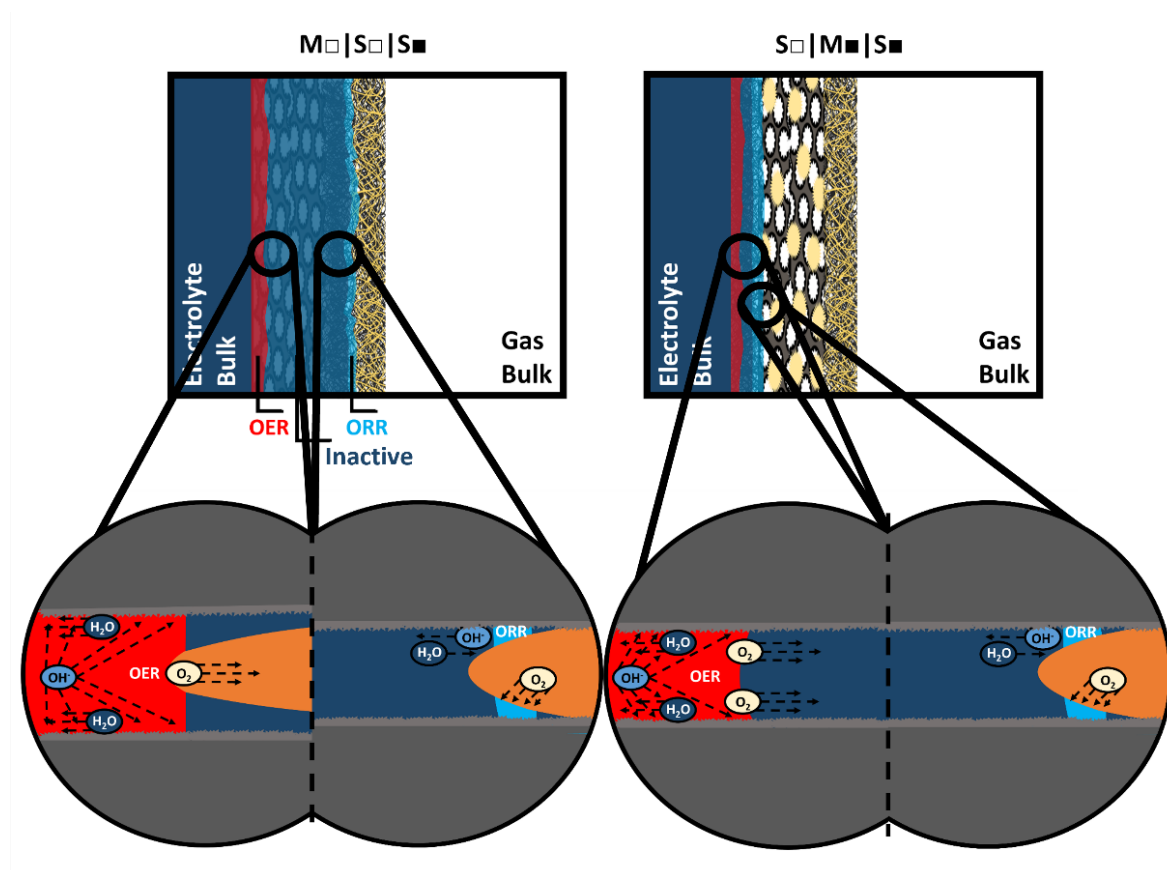
Figure 62. Schematic depiction of OER (red), inactive (dark blue) and ORR zone (light blue) of M□|S□|S■ and S□|M■|S■ and their difference in electrolyte film formation.

S□|M■|S■

The final design was created by replacing the first and second layers of M□|S□|S■ with S□ and M■, resulting in S□|M■|S■. The electrolyte in S□|M■|S■ goes from 20 µm hydrophilic substrate pores to 20 < x ≤ 200 µm hydrophobic substrate pores, where it partially wets M■ but the electrolyte does not penetrate further. Thus, the electrolyte is mainly retained in S□ and not extended as in M□|S□|S■. This resulted in a higher OER activity for S□|M■|S■ compared with M□|S□|S■. Consequently, η_{OER} (1.80 V) and its deviation is lower than that of M□|S□|S■. *Ergo*, the OER activity could be increased by presumably more filled pores (higher capillary pressure) than compared with M□|S□|S■, which reduced the transport limitation. The OER active zone is located near the electrolyte bulk of the first layer of S□|M■|S■ (S□), as schematically shown in Figure 62. The OER

active surface area must have the same size as a single S■ (Fle*) because it has the same η_{OER} (Figure 53).

However, the η_{ORR} (2.14 V) of S□|M■|S■ is the same as that of M□|S□|S■, but with much less variation. This suggests that the ORR active surface area of S□|M■|S■ has a comparable size to M□|S□|S■ but is more stable than M□|S□|S■. Its electrolyte thin film meniscus surface lies between S□|M■ and S□|S■ (Figure 62). Comparison with a single S■ (Figure 53) shows that it has a lower η_{ORR} (1.33 V) than S□|M■|S■, which is due to the larger electrolyte thin film surface area and shorter reactant transport distance, as mentioned earlier. It is assumed that as the electrolyte penetrates further into the hydrophobic part (higher pressure), the surface area of the electrolyte thin film meniscus increases, and so does the ORR activity. However, the transport distance of the reactants cannot be shortened.

Cumulative Overpotential

The cumulative overpotential results show that M□|S□|S■ obviously has the highest overpotentials at both current densities in Figure 60 (c). L□|M□|S■ and L□|M■|S■ show similar results to GDE$_{ref}$, except for L□|M□|S■ at 5 mA cm^{-2}, which has slightly lower overpotentials. As indicated, M□|M■|S■ has the lowest cumulative overpotential values of 1.01 V at 5 mA cm^{-2} and 1.72 V at 10 mA cm^{-2}.

The corresponding cumulative overpotential results of GDEs measured at higher electrolyte pressure (Figure 60 (d)) show that M□|M■|S■ has the lowest value, GDE$_{ref}$ has the second lowest value, and M□|S□|S■ and S□|M■|S■ have the highest overpotentials. M□|S□|S■ has the largest deviation of all the measured GDEs in this chapter. The comparison between M□|M■|S■ results at different electrolyte pressures (Figure 60) shows that η_{OER} and η_{ORR} are reduced by the additional pressure. The same behavior is also seen for M□|S□|S■ and GDE$_{ref}$.

M□|M■|S■ Summarized

Moreover, the η_{OER} of S□|M■|S■ is much higher than that of M□|M■|S■. Consequently, the substrate pore size of M□ (20 < x ≤ 200 µm) in this design is much more favorable for OER activity than the pore size of S□ (20 µm). It is assumed that the reactant transport within a large substrate pore size provides more active sites than within a small substrate pore size. The ORR results of M□|M■|S■ are also much lower than those of S□|M■|S■, indicating a much larger electrolyte thin film surface area between M□|M■ than between S□|M■. This difference in the surface area of the electrolyte thin film indicates that the electrolyte penetrates further into the interior if the pore size of the substrate in the first part of the design is not too small (S□|M■) or too large (L□|M■). Consequently, the pore size of M□|M■ obviously has the most favorable size for high ORR activity.

Comparison of M□|M■|S■ results at different electrolyte pressures (with or without gff) shows that both OER and ORR activity were increased by higher electrolyte pressure (without gff). This

increase in activity indicates that more substrate pores were sufficiently filled with electrolyte, which reduced the transport limitations within M□|M■|S■. The reduction in transport limitations significantly increased the supply of active sites during OER. In addition, the higher capillary pressure of the electrolyte pushed more sufficiently the bubble formation to the gas bulk side and results in less gas-bubble-covered active sites. Moreover, a larger electrolyte thin film surface area formed inside M□|M■|S■ due to the higher electrolyte pressure, which led to the formation of a larger electrochemically active surface area during ORR.

All in all, M□|M■|S■ is more electrochemically active than the state-of-the-art GDE$_{ref}$, exhibiting the lowest OER (0.24 V) and ORR (0.96 V) overpotentials at 10 mA cm^{-2} and high electrolyte pressure (Figure 60 (d)).

Overpotential Ratio Comparison

The overpotential results of bifunctional layered CF-GDE M□|M■|S■, L□|M□|S■, and L□|M■|S■ were compared with GDE$_{ref}$ and their ratio differences are shown in Figure 63. Positive ratios (*q*) mean that the CF-GDEs have lower overpotentials (η) than GDE$_{ref}$, which were calculated using m. Eq. 19.
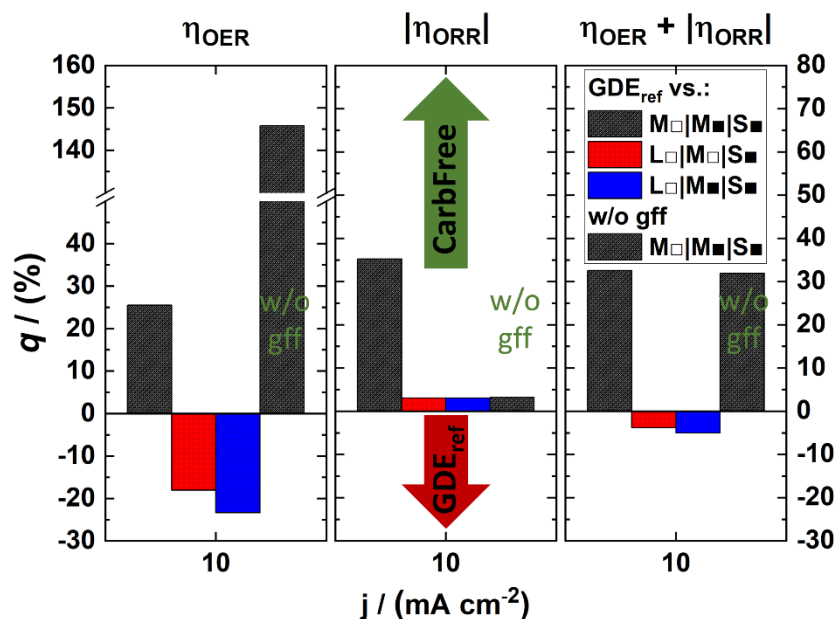
Figure 63. Ratio comparison between the performance difference of certain bifunctional layered CF-GDE configurations and GDE$_{ref}$.

There are two M□|M■|S■. The first black bar shows the measurement with gff, and the last black bar shows the measurement without gff to show the influence of electrolyte pressure. Accordingly, the first black bar shows the comparison of M□|M■|S■ and GDE$_{ref}$ with gff and the

second black bar without gff. L□|M□|S■ and L□|M■|S■ are both measured with gff and were therefore compared with GDE$_{ref}$, which was also measured with gff.

M□|M■|S■ (first black bar) shows 26 % lower η_{OER} and almost 35 % lower η_{ORR} than GDE$_{ref}$. L□|M□|S■ and L□|M■|S■ show about 20 % higher η_{OER} but about 3 % lower η_{ORR} than GDE$_{ref}$.

The M□|M■|S■ without gff (last black bar) shows 146 % lower η_{OER} and about 3 % lower η_{ORR} than GDE$_{ref}$. This indicates an impressive superior OER activity of M□|M■|S■, which is achieved by less gas-bubble-covered active sites and the accessibility of the catalyst surface in the interior porous substrate. The corresponding results for cumulative overpotential show that L□|M□|S■ and L□|M■|S■ have about 5 % higher cumulative overpotential than the commercial GDE. However, M□|M■|S■ with and without gff show a cumulative overpotential more than 30 % lower than GDE$_{ref}$.

These results generally indicate that specifically M□|M■|S■ has higher OER and ORR activity than GDE$_{ref}$. Moreover, the comparison of M□|M■|S■ measurements with and without gff shows the preference shift between OER and ORR, which can be controlled by the applied gff. This is because gff controls the electrolyte pressure and thus the penetration depth of the electrolyte and its capillary pressure.

Long-term Stability Measurement

The long-term stability of M□|M■|S■ was examined and compared with GDE$_{ref}$. This is shown in Figure 64 below. GDEs were cycled between OER and ORR working modes at 1.50 V (OER) and - 0.75 V (ORR) vs. Hg/HgO 1 M NaOH for 2100 cycles with gff. A cycle is a completed sequence of OER and ORR. Figure 64 and Appendix 31 show the normalized results of every 5th cycle.

Measurement of GDE$_{ref}$ (Figure 64 (a)) shows a decrease in OER and ORR current density from the 600th cycle, indicating corrosion. The current density steadily decreases to about 35 % (2100th cycle) of the original value. Consequently, the alkyl site chains of the carbon material are attacked by peroxide radicals during ORR and additionally oxidized directly by the OER as the applied potential is 1.5 V vs. Hg/HgO 1 M NaOH or 1.38 V vs. SHE. This is due to the fact that carbon corrosion starts at 1.2 V vs. SHE[154].

In general, the corrosion of carbon leads to more and more hydrophilic carbon due to the formation of C=O bonds. Until the π–π interaction weakens and eventually dissolves in the electrolyte. The carbon dissolution was confirmed by the brown discoloration of the electrolyte after the long-term stability measurement of GDE$_{ref}$.
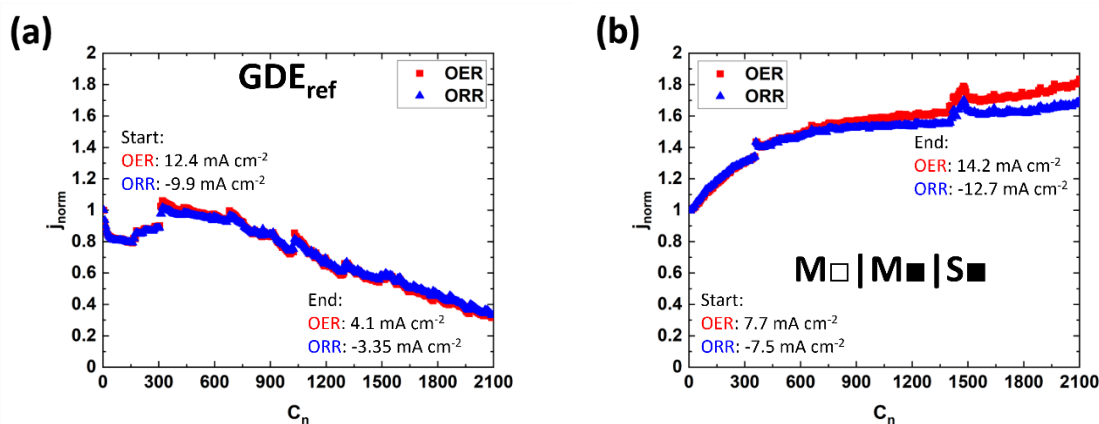
Figure 64. Electrochemical long-term stability measurement of GDE_ref and M□|M■|S■ at 1.5 V and -0.75 V vs. Hg/HgO 1M NaOH for 2100 cycles and each working mode (OER and ORR) lasted 20 seconds. The second measurement of each sample is in the Appendix 31.

On the contrary, M□|M■|S■ shows an asymptotic increase in OER and ORR current density by about 50 % until the 750th cycle. Thereafter, the increase becomes more linear and slows down, but the M□|M■|S■ current density of OER increases more than the ORR until the last 2100th cycle. This increase in current density indicates a steady growth of the electrochemically active ORR surface area due to the enlargement of the electrolyte thin film meniscus within M■. Therefore, the pores of M□ were more filled with electrolyte, which reduced the transport limitation for OER. This increase in active surface area was possibly caused by the combination of two flooding mechanisms described in chapter 2.1.5. One of these mechanisms is electrowetting, which occurs at negative potentials greater than – 0.60 V vs. RHE[112]. The second mechanism is the local OH⁻ concentration increase, which causes water movement from the electrolyte bulk toward the high ion concentration[145].

In addition, it is assumed that a change in the MnO_x catalyst occurred toward an increase in activity caused by the long cycling at high electrical load. The pyrolusite MnO_2 found in the X-ray amorphous MnO_x (Figure 29 (b)) is known to be highly OER/ORR bifunctionally active[166] and electrochemically stable for high cycle numbers[12] [166]. However, the great amount of X-ray amorphousness of MnO_x suggests that there may also be unstable structures that have been altered. This alteration resulted in an increase in the number of electroactive centers, which are more OER and/or ORR active, thus increasing the current density.

XRD measurements to prove this assumption were not possible, since measurements of the coating with the metallic substrate gave only reflexes of the substrate. Since the MnO_x coating is too thin to provide its specific reflexes. Only MnO_x powder was measurable, as shown in chapter 4.1.1. But scratching off the coatings of the nickel foams or the stainless-steel fleece is not feasible due to their specific surface structure.

However, a pink or purple discoloration of the electrolyte was observed when the layered CF-GDEs were rinsed with distilled water. This indicates the dissolution of unstable MnO_x and supports the assumption that MnO_x was conditioned and led to an increase in electrochemical activity. In addition, it is also possible that oxy-hydroxide layers grew on MnO_x and/or the uncoated substrate surface (nickel or stainless-steel) [173] [174]. Therefore, it is highly probable that both process contributed to the increase in electrochemical activity.

The overall increase in OER was about 80 % and for ORR about 70 %. The results of the second M□|M■|S■ CF-GDE show basically a similar pattern of OER and ORR current densities (Appendix 31).

Consequently, it is obvious that the bifunctional layered CF-GDE M□|M■|S■ is superior to the state-of-the-art carbon-based GDE_{ref} due to its corrosion resistance and higher electrochemical activity.

4.3.2 Interim Conclusion III

Various combinations of layered bifunctional CF-GDEs (Table 3) were designed by combining different MnO_x and PTFE coated substrates (Table 2) to create specific hydrophilic/hydrophobic pore gradients. The designs were found to have different electrochemical activities compared to their individual substrate layers (Figure 51, Figure 53, Figure 59 and Figure 60).

As mentioned earlier, the electrolyte thickness at the active site affects the electrochemical activity for OER and ORR. It has been shown that the highest OER activity was obtained with Fo_{Few} or L□, respectively, (Figure 53) which has the largest pore size (500 – 600 μm). Since the low transport limitation resulted in a large OER active surface area in Fo_{Few} which is supported by its capillary pressure of the electrolyte. However, the OER activity decreases in combination with a smaller pore size (M□ or M■). This decrease indicates the influence of the thickness of the electrolyte film within the substrate pores, which directly affect the transport limitation and thus the OER active surface area. This combination resulted in fewer substrate pores with large electrolyte film thickness and thus fewer active sites were supplied with reactants as the transport limitation increased. In general, the thickness of the electrolyte film is affected by the pore size and the surface property to attract (hydrophilic) or repel (hydrophobic) the water-based electrolyte.

Consequently, if the pore size of the first layer is too small (S□|M■|S■ → S□: 20 μm), the thickness of the electrolyte film is not large enough. This leads to a limitation of transport and reduces the OER active surface area (Figure 60). On the contrary (L□|M□|S■ and L□|M■|S■), if the pore size of the first layer is too large (500 – 600 μm), the electrolyte film is not thick enough to form a small transport limitation. As the electrolyte expands further into the interior of the layered CF-GDE, the thickness of the electrolyte decreases, as shown in Figure 60.

Moreover, due to hydrophobicity, the ORR of GDE$_{ref}$ is in the same location as OER. *Ergo*, the diffusion distance of O_2 in GDE$_{ref}$ has to be crossed to reach the electrolyte thin film where O_2 dissolves. This diffusion distance does not occur in the layered CF-GDE because the pore size of the last layer (S■) is 20 μm and the diffusion distance to the electrolyte film is shorter. For this reason, the $\sigma_{Warburg}$ of CF-GDEs were lower than GDE$_{ref}$, which is an advantage over GDE$_{ref}$. However, the electrolyte film must be sufficiently thin and its surface area large to ensure high ORR activity. This requires a hydrophobic layer and sufficient electrolyte pressure or penetration of the electrolyte into the hydrophobic layer, respectively.

The layered CF-GDEs L□|M■|S■ and S□|M■|S■ have shown the influence of low electrolyte penetration within the hydrophobic second layer (M■). This is because the hydrophilic pores of L□ are too large and need to be filled first to penetrate far enough into the second hydrophobic layer. However, even if the second layer of L□|M■|S■ is hydrophilic (L□|M□|S■), the surface area of the electrolyte thin film does not change. This unchanged surface of the electrolyte thin film is indicated by its η$_{ORR}$ (Figure 60). However, the pores of the first hydrophilic layer should not be too small (S□), because then the electrolyte pressure is greatly reduced by its capillary forces. The reduction of electrolyte pressure leads to low penetration of electrolyte into the second hydrophobic layer. This was shown by S□|M■|S■ and its ORR results. The S□|M■|S■ results indicate that the ORR active zone is in the first S□ layer because it has the same η$_{ORR}$ as M□|S□|S■. Since the ORR active zone of M□|S□|S■ is located at S□, it is held by S■.

In general, these results show:
- How the electrolyte is affected by the different layered CF-GDEs.
- Why the porosity gradient and hydrophilic/hydrophobic property of M□|M■|S■ exhibited the largest OER and ORR active zones or the lowest overpotentials, respectively.

It can be concluded that the first hydrophilic layer of M□|M■|S■ (M□) has sufficiently large pores (20 < x ≤ 200 μm) to be filled with electrolyte. This electrolyte can then further penetrate into the second hydrophobic layer (M■), where it is stopped. The electrolyte-filled substrate pores of the first hydrophilic layer are large enough to form a low transport limitation and a large electrochemically active surface area. Then, the electrolyte penetrates deep enough into the second hydrophobic layer to form a large ORR active zone (electrolyte thin film surface area). The pore size of both layers is the same (20 < x ≤ 200 μm). The third layer (S■: 20 μm) serves as a strongly hydrophobic layer to prevent further penetration of the electrolyte, and it serves as a gas diffusion layer. In addition, it is highly probable that the combination of hydrophilic and hydrophobic layers result in a displacement of the bubble formation in the direction of the gas side during OER.

Therefore, M□|M■|S■ has a 146 % lower η_{OER} (0.24 V) and an approx. 3 % lower η_{ORR} (0.96 V) than GDE$_{ref}$ at 10 mA cm^{-2} vs. Hg/HgO 1 M NaOH.

The measurement of the long-term stability of M□|M■|S■ clearly shows its superiority over carbon-based GDE$_{ref}$, which decomposes significantly due to carbon corrosion. The superiority is based on the fact that the OER and ORR current density of M□|M■|S■ increased with each successive cycle. It started at j_{OER}^{start}: 7.70 mA cm^{-2} and j_{ORR}^{start}: 7.50 mA cm^{-2} and ended at j_{OER}^{end}: 14.20 mA cm^{-2} and j_{ORR}^{end}: 12.70 mA cm^{-2}.

Table 5. Summary of the main overpotential results (gff: glass-fiber-fleece).

Gas Diffusion Electrode	Galvanostatic Measurement Results		
at 10 mA cm^{-2}	η_{OER} / V	η_{ORR} / V	$\eta_{OER} + |\eta_{ORR}|$ / V
GDE$_{ref}$ (with|without gff)	0.59 | 0.59	1.69 | 0.98	2.28 | 1.57
Fo (with gff | xxx)	0.43 | x.xx	2.43 | x.xx	2.86 | x.xx
Fop* (xxx | without gff)	x.xx | 0.57	x.xx | 1.09	x.xx | 1.65
Fle* (xxx | without gff)	x.xx | 1.69	x.xx | 1.33	x.xx | 3.02
M□|M■|S■ (with|without gff)	0.47 | 0.24	1.25 | 0.96	1.72 | 1.19

4.3.3 Benchmarking of state-of-the-art GDEs

Since this bifunctional layered CF-GDE (M□|M■|S■) is capable of OER and ORR, it must be benchmarked against bifunctional GDEs used in alkaline energy converters such as metal-air batteries (MAB) or unitized regenerative fuel cells (URFC). Therefore, M□|M■|S■ is compared with four different bifunctional GDEs used in half-cells, MABs, and/or URFCs.

The first GDE is a state-of-the-art carbon-based layered electrode design (Figure 2) with a catalyst layer (CL) and a gas diffusion layer (GDL) containing PTFE as a binder and hydrophobic additive. *Marini et al.*[177] used a mixture of MnO_2, Ni/NiO, carbon black and PTFE for the CL and a macroporous carbon layer as GDL. This carbon-based GDE was studied in a half-cell setup with 6 M KOH at 10 mA cm^{-2}. It exhibited a η_{OER} of 0.41 V and a η_{ORR} of also 0.41 V. Long-term stability was also measured with an interval of OER and ORR of 2 h with a 5 minute interruption of an open circuit potential period between load changes (OER ⇆ ORR) for 100 cycles. The carbon-based GDE shows stable electrochemical performance for 80 or 90 cycles and then an increase in OER and ORR overpotentials.

The OER and ORR overpotentials of M□|M■|S■ are expected to be lower at 6 M than at 0.1 M KOH because of the increase in ionic conductivity. Since M□|M■|S■ was measured with 0.1 M KOH. Nevertheless, the η_{OER} of M□|M■|S■ is 0.24 V, which is about 42 % lower than that of the

carbon-based GDE of *Marini et al.* but the η_{ORR} of M□|M■|S■ is higher (0.96 V). Moreover, the comparison of the long-term stability measurements shows that the setup with the shorter OER and ORR intervals (20 seconds vs. 2 hours) would lead to faster corrosion of the carbon materials. Therefore, M□|M■|S■ is expected to be much more stable than the carbon-based GDE of *Marini et al.*[177].

Wang et al.[6] deposited $Ni_{1.9}FeS_{1.09}(OH)_{4.6}$ on nickel foam to develop a GDE, which is discussed in more detail above in chapter 2.1.2. This GDE was first used in an alkaline water splitting application as an anode and cathode. It achieved a η_{OER} of 0.27 V and η_{HER} of $-$ 0.18 V at 10 mA cm^{-2} in 0.1 M KOH. In addition, it was also used as a GDE in a Zn-air battery containing 6.0 M KOH and 0.2 M $ZnCl_2$. *Wang et al.*[6] compared commercial catalysts (mixture of Pt/carbon for ORR and Ir/carbon for OER) in the same experimental setup, with both setups cycled at 2.0 mA cm^{-2}. The noncommercial GDE achieved a discharge potential (ORR) of 1.14 V and a charge potential (OER) of 1.90 V, resulting in a potential gap of 0.76 V. Thus, it has a round-trip efficiency of 60 % that is higher than the activity of the commercial catalyst mixture, which achieved an efficiency of 53 %.

M□|M■|S■ shows a slightly lower η_{OER} of 0.24 V compared to the water splitting activity of *Wang′s* GDE[6]. Thus, M□|M■|S■ indicates a slightly higher OER activity. However, the ORR was not specified in a similar manner as OER by *Wang et al.*. Nevertheless, it is expected that M□|M■|S■ would achieve a similar round-trip efficiency of 60 % as $Ni_{1.9}FeS_{1.09}(OH)_{4.6}$ on nickel foam due to the slightly higher OER activity and the similarity of the nickel foam substrate in the same Zn-air battery setup.

Ke Xu et al.[7] hydrothermally coated a nickel foam with MnO_2 and added a mixture of carbon-nanotubes (CNTs) and PTFE as GDL on the coated nickel foam (Figure 3). The discharge efficiency (ORR) was measured in a half-cell and a Zn-air battery assembly in 6 M KOH at 10 mA cm^{-2} (half-cell) and 100 mA cm^{-2} (MAB). The half-cell measurements were performed with and without GDL on the MnO_2-coated nickel foam. The ORR potential of Ni/MnO_2 with GDL exhibited about 0.2 V vs. Hg/HgO at 10 mA cm^{-2}, which is about 50 % lower than Ni/MnO_2 without GDL. In the Zn-air battery, the Ni/MnO_2 with GDL showed a stable discharge potential (ORR) of about 0.8 V vs. Zn at 100 mA cm^{-2} for four hours.

It is assumed that M□|M■|S■ would possibly achieve higher discharge potential than the GDE of *Ke Xu et al.*[7]. Since M□|M■|S■ achieved 0.96 V η_{ORR} at 10 mA cm^{-2}. Therefore, M□|M■|S■ would most likely achieve higher discharge potential than Ni/MnO_2 with GDL in a similar Zn-air battery setup. Thus, it is necessary to increase the ORR activity of M□|M■|S■ further. Nevertheless, the GDE of *Ke Xu et al.* is not expected to be long-term stable when the same setup is used for long-term stability measurement as in this work (OER ⇆ ORR, 20 second interval for 2100 cycles). A

possible indication of this is the lack of OER results in the work of *Ke Xu et al.*[7] and the carbon-based GDL used.

The last GDE compared with M□|M■|S■ is a MnO_x-coated stainless-steel mesh of *Ng et al.*[8].

The GDE was used in a unitized regenerative fuel cell with an anion exchange membrane (AEM-URFC). In the electrolyzer mode (HER/OER), it maintained a current density of about 60 mA cm^{-2} at 1.75 V and in the fuel cell mode (HRR/ORR), it exhibited 43 mA cm^{-2} at 0.45 V for 10 cycles. These results were compared with a carbon-based GDE (mixture of MnO_x/carbon and Ni/carbon), which exhibited an activity drop of 97 % after 10 cycles in fuel cell mode at 0.45 V and an activity drop of 79 % in electrolyzer mode at 1.75 V. *Ng et al.*[8] demonstrated the superiority of carbon-free MnO_x-coated stainless-steel mesh used in a AEM-URFC.

The MnO_x-coated stainless-steel mesh has a similar production scheme to the standard coating method mentioned in the experimental part of this dissertation (chapter 3). Therefore, the single layered CF-GDEs (Fo$_{Few}$, Fop$_{Few}$, etc.) are expected to achieve similar results as the MnO_x-coated stainless-steel mesh. It is also expected that M□|M■|S■ would achieve higher current densities in the electrolyzer (OER) and fuel cell (ORR) mode. Since M□|M■|S■ has the highest overall activity compared to the measured samples in this work (Table 5).

All in all, it can be concluded that the developed M□|M■|S■ is a competitive bifunctional GDE for MABs and URFCs and potentially for electrolyzers. Therefore, it is among the most advanced gas diffusion electrodes for alkaline applications.

5 Conclusion and outlook

5.1 Conclusion

In this work, a special design of a layered bifunctional carbon-free (CF-) gas diffusion electrode (GDE) was demonstrated, which exhibits higher oxygen evolution (OER) and oxygen reduction reaction (ORR) activity and long-term stability than the state-of-the-art carbon-based GDE$_{ref}$. The superior electrode design was achieved by combining three different catalyst-coated porous substrates, some of which were hydrophobized with PTFE.

Thus, the goal of proposing a novel, long-term stable, bifunctional CF-GDE design for alkaline energy converters such as metal-air batteries or unitized regenerative fuel cells was successfully achieved.

The first step was to develop a standard method for the electrodeposition of an electrocatalytically active MnO$_x$ coating that can be applied to three different substrates. Nickel foam was electrochemically coated with different electrodeposition settings. The HiFew setting ($r_{scan} = 50$ mV s^{-1}; cycle number = 500) exhibited the lowest overpotentials ($\eta_{OER} = 0.43$ V; $\eta_{ORR} = 2.43$ V at 10 mA cm^{-2} vs. Hg/HgO 1 M NaOH) compared to the other settings studied (Figure 38). The electrochemical stability of the deposited MnO$_x$ was demonstrated for 2100 cycles (1.5 V (OER) and - 0.75 V (ORR) vs. Hg/HgO 1 M NaOH, Figure 40).

In a second step, the influence of pore size and surface properties (hydrophobic and hydrophilic) on the OER and ORR activity of CF-GDEs and the design difference of GDE$_{ref}$ were shown. Three MnO$_x$ coated substrates with different pore sizes were electrochemically investigated: Nickel foam (500 – 600 μm), pressed nickel foam ($20 < x \leq 200$ μm) and stainless-steel fleece (20 μm). They were designated as CF-GDEs and investigated for the influence of the pore size of the substrate. The flooded CF-GDEs with large pores have a very large electrochemically active surface area, as shown by the C_{dl} and η_{OER} results, especially for Fo$_{Few}$ (C_{dl}: 0.25 F g^{-1}, η_{OER}: 0.43 V at 10 mA cm^{-2}). However, with smaller pore size, the η_{OER} increased and it was concluded that flooded small pores lead to reactant transport limitation within the CF-GDE. The limitation of reactant transport indicates a reduced reactant supply to the active surface. Since the electrolyte-filled large pores have more reactant transport pathways to the catalytic site (bulk electrolyte) than smaller substrate pores within the CF-GDE during OER.

Moreover, the design of CF-GDEs does not have a GDL like GDE$_{ref}$. *Ergo*, the diffusion pathway distance to the electrolyte thin film in CF-GDEs during ORR is much smaller than in GDE$_{ref}$. The smaller diffusion distance is indicated by the lower $\sigma_{Warburg}$ of CF-GDEs. However, the η_{ORR} results at different current densities do not show any positive effect of the lack of gas diffusion layer (GDL) in CF-GDEs. GDE$_{ref}$ exhibited a much lower η_{ORR} value than the hydrophilic CF-GDEs. Since

the hydrophobicity of GDE$_{ref}$ is much more able to control the electrolyte flooding and the increase in film thickness caused by the electrowetting and hydration of reactants at higher electrical loads. High electrolyte film thickness narrows the ORR high current density zone, as indicated by a high η_{ORR}.

Therefore, some CF-GDEs have been hydrophobized to control flooding and the formation of electrolyte thin film. They (Fop* and Fle*) exhibited much lower η_{OER} and η_{ORR} (Figure 53) than their hydrophilic counterparts (Fop$_{Few}$ and Fle$_{Mny}$). It was concluded that the formation of the electrolyte thin film was assisted by the hydrophobicity to form a larger ORR active surface area within the CF-GDE than when the surface was hydrophilic only (Figure 54, Figure 55, and Figure 56). Moreover, the bubble formation was displaced by the PTFE coating towards the gas side and thus larger OER active surface was available.

These catalyst-coated substrates of the second part with the lowest η_{OER} and η_{ORR}, were used in the last part of this work to show the combinations of different pore sizes and surface properties and their influence on the electrochemical activity. Specific pore gradients were designed by combining different substrate pore sizes with a specific hydrophilic/hydrophobic transition to control the formation of the electrolyte film within the layered CF-GDE. This is because the formation of the electrolyte film directly affects the OER and ORR activity. The different layer combinations of CF-GDE showed that the transport limitation of reactants reduces the OER activity (Figure 60) when the pore size of the first substrate layer is too small (20 µm → S□|M∎|S∎). When the pore size of the first layer is too large (500 – 600 µm → L□|M□|S∎ and L□|M∎|S∎). Then the pores are not filled or the electrolyte film is not thick enough, respectively, resulting in lower OER activity.

Moreover, the flooding of the first substrate layer affects the formation of the electrolyte film of the second substrate layer, which forms thin electrolyte films. Consequently, ORR takes place there, because the supply of dissolved O_2 to the catalyst sites is affected by the thickness of the electrolyte film and its surface area. If the substrate pores of the first hydrophilic layer are too large (L□), then the electrolyte does not penetrate deeply enough into the second hydrophobic substrate layer (M∎). This is because the pores must first be filled to penetrate far enough into the second layer. But the pore size of the first hydrophilic substrate layer should not be too small (S□). Small hydrophilic pores greatly reduce the electrolyte pressure due to its capillary forces, resulting in low penetration of the electrolyte into the second hydrophobic substrate layer. These combinations resulted in low ORR activity.

From these results, it was concluded that the first hydrophilic layer requires sufficiently large pores (M□: $20 < x \leq 200$ µm) to be filled with electrolyte. This electrolyte can further penetrate into the second hydrophobic layer (M∎), and the electrolyte additionally accumulates in front of it. As a result, the pores of the first layer are large enough to achieve high reactant transport in it (high OER activity). Moreover, the electrolyte film penetrates deep enough into the second layer (M∎:

$20 < x \leq 200$ μm) to form a large electrolyte thin film surface area (high ORR activity). The third layer (S■) serves as highly hydrophobic layer to prevent further penetration of the electrolyte, and it serves as a gas diffusion layer.

These combined substrate layers lead to M□|M■|S■ which exhibits a 146 % lower η_{OER} (0.24 V) and 3 % lower η_{ORR} (0.96 V) than the state-of-the-art GDE$_{ref}$ at 10 mA cm^{-2}. In addition, M□|M■|S■ demonstrates its superior durability at high cycle rates and high electrical loads. Since it started at j_{OER}^{start}: 7.70 mA cm^{-2} and j_{ORR}^{start}: 7.50 mA cm^{-2} and ended at j_{OER}^{end}: 14.20 mA cm^{-2} and j_{ORR}^{end}: 12.70 mA cm^{-2} at a constant potential of (OER) 1.5 V and (ORR) 0.75 V vs. Hg/HgO in 1 M NaOH. Consequently, the current density of M□|M■|S■ increased with each cycle.

As mentioned above, the goal of this work was successfully achieved by understanding the influence of pore size and surface properties on OER and ORR activity of electrodes. In general, both parameters control the formation of the electrolyte thin film meniscus and the flooding of the pores. The electrolyte thin film meniscus is critical for ORR activity and the flooded pores are critical for OER activity. With this knowledge, different pore sizes and surface properties were combined to design different pore gradients with a hydrophilic/hydrophobic transition. It was shown above that the formation of the electrolyte film and its thickness can also be controlled by additional CF-GDE layers. Understanding this led to the M□|M■|S■ design.

The applied research strategy led to this success. Surface measurement methods such as SEM, X-ray tomography, contact angle, electrochemical impedance, galvanostatic and potentiostatic polarization helped to understand how pore size and surface properties affect electrochemical activity. In particular, SEM and X-ray tomography allowed the figurative imagination of the formation of an electrolyte thin film and how it is affected by pore size, hydrophobic/hydrophilic surfaces and their combinations.

The benchmark of the developed M□|M■|S■ revealed that it is a competitive bifunctional GDE for metal-air batteries and unitized regenerative fuel cells and potentially for electrolyzers. Therefore, it is among the most advanced gas diffusion electrodes for alkaline applications.

A comparison of costs shows that the state-of-the-art carbon-based GDE has lower material costs. The GDE$_{ref}$ is mainly composed of activated carbon (≈ 1.85 € kg^{-1})[178], which is much cheaper than nickel (≈ 16.37 € kg^{-1})[179] or the stainless-steel alloy 1.4404 (≈ 3.92 € kg^{-1})[179]. The price data were obtained in peacetime for representative reasons. Since wartime is an exception, wartime prices are not representative.

Nevertheless, the superior electrochemical stability and catalytic activity of nickel and stainless-steel alloy is a key feature and has to be taken into account. The results of long-term measurements clearly show that the lifetime of carbon-based GDE$_{ref}$ ends at about the 900th cycle.

This is because the current density of GDE$_{ref}$ decreases by about 20 % at this number of cycles and continues to decrease (60 % total decrease). However, the life of the layered CF-GDE does not end at the last 2100th cycle. The layered CF-GDE increases its current density by 70 – 80 % until the last measurement point. Therefore, the lifetime of alkaline energy conversion systems can be increased by more than 50 % if layered CF-GDEs are used instead of carbon-based GDEs.

In general, the capital expenditure (capex) of layered CF-GDEs is potentially higher. However, the total electrical energy converted during their lifetime is potentially more than 50 % higher than carbon-based GDEs, making them more economical. Also, fewer alkaline energy conversion systems need to be manufactured to replace the defective ones when layered CF-GDEs are used, making it more resource efficient.

In general, the use of carbon-based GDEs in small, non-rechargeable batteries such as button-cells or similar small batteries is still more attractive to ordinary consumers because of the lower capex. However, the use of layered CF-GDEs in large rechargeable alkaline energy conversion systems is more attractive than carbon-based GDEs. Despite the higher capex, CF-GDE is more economical and resource efficient than carbon-based GDEs.

5.2 Outlook

In the present work, the development of a layered bifunctional CF-GDE was demonstrated. It showed higher electrochemical activity and superior long-term durability compared to the state-of-the-art carbon-corrosion-prone GDE$_{ref}$ in alkaline media. However, further work on different catalysts, a different method of catalyst coating, more precise PTFE coating, and different pore sizes of catalyst-coated substrates can be carried out to reduce the overpotentials and/or design the CF-GDE for specific alkaline energy converters.

Catalysts

The use of other catalysts such as metal oxides or perovskites or others with higher electrochemical activity than the MnO$_x$ shown could further reduce the overpotentials.

Coating Method

The electrodeposited surface structure can be modified toward a higher electrochemically active specific surface area by various supporting additives or main components (cobalt, nickel and/or iron) other than manganese or in combination with manganese. In addition, the electrochemically active specific surface area can be increased by various electrodeposition settings.

In addition, other coating methods such as atmospheric plasma spraying (APS), electroless plating, or chemical vapor deposition (CVD) can be used for a variety of catalysts and parameters that need to be considered.

PTFE Coating

It is possible to adjust the formation of the electrolyte film and its retention by a more precise hydrophobization method. Therefore, a series of measurements is required to determine certain parameters for the dip coating method such as the cleaning time with ethanol or the annealing temperature. However, different electrode bodies with their specific pore size require different parameters for their specific purpose.

Different Pore Gradients

The pore gradient can be adjusted by the specific pore sizes of the electrode bodies or substrate, respectively. This leads to different electrolyte pressure applications. Therefore, metal foams, metal fleeces or other porous metal substrates with different pore sizes are required to be combined for specific electrolyte pressure applications.

In general, the combinations of all four mentioned points and their inherent parameters depend on the specific conditions of a particular alkaline energy converter and its specific operating parameters. Nevertheless, it is necessary to understand the behavior of electrolyte film formation as a function of varying pore size, hydrophobic properties, and electrolyte pressure. The reason is that these factors affect the electrochemical activity by the transport of reactants. Therefore, further studies such as electrochemical impedance spectroscopy at OER and ORR current densities are needed.

6 Summary in German

Das Ziel dieser Arbeit, eine langlebige und kohlenstofffreie Gasdiffusionselektrode (GDE) für alkalische Energiewandler (Metall-Luft Batterie und/oder regenerative Brennstoffzellen) zu entwickeln, wurde erfolgreich abgeschlossen.

Die von mir entwickelte bifunktionale kohlenstofffreie (KF-) GDE erzielte höhere Sauerstoffbildungs- (OER) und -reduzierungsreaktion (ORR) Aktivitäten und wies eine längere Langzeitstabilität als die Stand-der-Technik GDE (GDE$_{ref}$) auf. Diese geschichtete KF-GDE besteht aus drei unterschiedlichen einzelnen porösen Substraten, die elektrochemisch mit Manganoxid (MnO$_x$) beschichtet und einige zusätzlich mit PTFE hydrophobiert worden sind.

Hierfür wurden als erstes die Einstellungen für die Elektroabscheidungsmethode bestimmt, um eine standardisierte MnO$_x$ Schicht auf unterschiedliche poröse Substrate (Nickel-Schaum: Fo; gepresster Nickel-Schaum: Fop; Edelstahl-Vlies: Fle) aufbringen zu können. Diese wurden mit optischen Bildgebungsverfahren und elektrochemischen Methoden charakterisiert. Als Basis wurden Fo Substrate mit jeweils unterschiedlichen Elektroabscheidungseinstellungen untersucht. Die Einstellung HiFew (r_{scan} = 50 mV s^{-1}; Zyklenzahl = 500) hat eine MnO$_x$ Schicht auf Fo abgeschieden, die die geringsten Überpotentiale (η_{OER} = 0.43 V; η_{ORR} = 2.43 V bei 10 mA cm^{-2}) im Vergleich zu den anderen Einstellungen vorweist (Figure 38). Zusätzlich ist die elektrochemische Stabilität dieser MnO$_x$ Schicht für 2100 Zyklen (1,5 V (OER) und – 0,75 V (ORR) vs. Hg/HgO 1 M NaOH, Figure 40) bestätigt worden.

Als zweites wurden die Einflüsse der Porengröße und Oberflächeneigenschaften (hydrophob und hydrophil) auf die OER und ORR Aktivität der KF-GDEs untersucht, sowie die Designunterschiede von GDE$_{ref}$ aufgezeigt. Hierfür sind die Elektrodenkörper (Fo, Fop und Fle) und deren Porengrößeneinfluss elektrochemisch untersucht und miteinander verglichen worden. Elektrolyt geflutete große Poren (500 – 600 μm) haben eine sehr große elektroaktive Oberfläche. Das ist durch C_{dl} und η_{OER} Ergebnisse, speziell bei Fo$_{Few}$, verdeutlicht (C_{dl}: 0.25 F g^{-1}, η_{OER}: 0.43 V at 10 mA cm^{-2}). Es ist geschlussfolgert worden, dass große Poren (500 – 600 μm) mehr Reaktanten-Transportwege zu den Katalysatorstellen besitzen als kleinere Poren (200 – 20 μm). Denn bei Substraten mit kleineren Poren stieg das η_{OER} an, das darauf hindeutet, dass eine Reaktanten-Transportlimitierung im Inneren der KF-GDEs vorhanden war.

KF-GDEs haben keine Gasdiffusionsschicht (GDL) und viel größere Poren als GDE$_{ref}$. Dadurch ist während ORR die Distanz der O$_2$ Diffusionswege zum Elektrolyt-Dünnfilm bei KF-GDEs kleiner als bei GDE$_{ref}$. Das ist an den kleineren $\sigma_{Warburg}$ von KF-GDEs erkennbar. Jedoch hat GDE$_{ref}$ trotz dieser vorhandenen Eigenschaften geringere η_{ORR} als die hydrophilen KF-GDEs. Das ist auf die vorhandene Hydrophobizität der GDE$_{ref}$ und deren Begrenzung der Elektrodenflutung zurückzuführen, die durch Elektrobenetzung und Hydration der Reaktanten bei höheren elektrischen

Potentialen verursacht wird. Im Allgemeinen führt die Flutung bzw. der Anstieg der Elektrolytfilmdicke in den Poren zur Verkleinerung der ORR aktiven Oberfläche, die durch hohe η_{ORR} angedeutet ist.

Deswegen sind einige KF-GDEs hydrophobiert worden, um den Anstieg der Elektrolytfilmdicke während der ORR einzugrenzen. Deren elektrochemischen Ergebnisse (Fop* und Fle*) zeigten viel geringere η_{OER} und η_{ORR} (Figure 50) als deren hydrophile Gegenstücke (Fop$_{Few}$ und Fle$_{Mny}$). Somit ist die Bildung großer Oberflächen von Elektrolyt-Dünnfilms bzw. einer großen ORR aktiven Oberfläche durch die Hydrophobizität im Innern der KF-GDEs unterstützt (Figure 54, Figure 55 und Figure 56). Des Weiteren wurde durch die PTFE-Schicht die Gasblasenbildung in Richtung der Gas-Seite verschoben und führte somit zu einer größeren verfügbaren OER aktiven Oberfläche.

Als letzten Schritt wurden die einzelnen hydrophilen und hydrophoben KF-GDEs in Reihe aufgeschichtet, um den Einfluss der kombinierten Eigenschaften, wie Porengröße und Hydrophobie/Hydrophilie, auf die elektrochemische Aktivität zu untersuchen. Es sind unterschiedliche Porengradienten mit spezifischen hydrophilen/hydrophoben Übergängen entworfen worden. Im Allgemeinen beeinflusst die Elektrolytfilmdicke an der aktiven Katalysatorstelle die OER und ORR Aktivität. Es ist möglich mit großen Poren die OER Aktivität, aufgrund von reduzierter Transportlimitierung, zu erhöhen. Jedoch zeigte sich, wenn die erste Schicht der geschichteten KF-GDEs zu klein ist (S□|M■|S■ → 20 µm), führt das zur Vergrößerung des transportlimitierenden Bereichs im Innern der geschichteten KF-GDE. Bei zu großen Poren der ersten Schicht (500 – 600 µm → L□|M□|S■ and L□|M■|S■) werden nicht ausreichend dicke Elektrolytfilme für die OER erreicht. Da der Elektrolytfilm weiter ins Innere der geschichteten KF-GDE ausgedehnt wird. Diese Abhängigkeit wird durch geringe η_{OER} angedeutet (Figure 60).

Des Weiteren beeinflusst das Fluten der ersten Substratschicht die Elektrolyt-Dünnfilmbildung im Innern der zweiten Substratschicht. Aufgrund dessen findet die ORR dort statt, da die Versorgung der Katalysatorstellen mit gelöstem O_2 von der Elektrolytfilmdicke und deren Oberfläche abhängig ist. Denn wenn die Poren der ersten hydrophilen Substratschicht (L□) zu groß sind, dann dringt der Elektrolytfilm nicht tief genug in die zweite hydrophobe Substratschicht (M■) vor, da die Poren vorher geflutet werden müssen. Jedoch darf die erste hydrophile Schicht auch nicht zu klein sein (S□). Kleine hydrophile Poren reduzieren den Elektrolytdruck stark durch deren Kapillarkräfte. Das führt auch wieder zu einem geringen vordringen des Elektrolytfilms in die zweite hydrophobe Schicht. Diese Kombinationen führten zu geringer ORR Aktivität aufgrund von geringer ORR aktiver Oberfläche.

Somit sollte die erste hydrophile Schicht ausreichend große Poren (M□: $20 < x \leq 200$ µm) haben, dass der Elektrolyt ausreichend aufgestaut wird und dadurch bis in die zweite hydrophobe Schicht (M■) vordringt. Dadurch ist ein hoher Reaktanten-Transport in M□ vorhanden (hohe OER

Aktivität) und die Elektrolytpenetration reicht tief genug ins Innere von M■ und bildet eine hohe Elektrolyt-Dünnfilm-Oberfläche (hohe ORR Aktivität). Die stark hydrophobe dritte Schicht (S■) dient als Elektrolyt-Barriere und als GDL.

Die Aufschichtung dieser drei KF-GDEs zu M□|M■|S■ hat 146 % geringere η_{OER} (0,24 V) und 3 % geringere η_{ORR} (0,96 V) als GDE$_{ref}$ bei 10 mA cm^{-2} erreicht und zeigt eine überlegene Haltbarkeit für hohe Zyklenzahlen bei hohen elektrischen Belastungen. Denn M□|M■|S■ startete bei einer Stromdichte von j_{OER}^{start}: 7,70 mA cm^{-2} und j_{ORR}^{start}: 7,50 mA cm^{-2} und endete bei j_{OER}^{end}: 14,20 mA cm^{-2} und j_{ORR}^{end}: 12,70 mA cm^{-2} bei einer jeweiligen gleichbleibenden Spannung von (OER) 1,5 V und (ORR) 0,75 V gegen Hg/HgO in 1 M NaOH. Somit hat sich die Stromdichte von M□|M■|S■ mit jedem Zyklus erhöht.

Wie oben bereits erwähnt, das Ziel dieser Dissertation wurde erfolgreich erreicht, indem der Einfluss von Porengröße und Oberflächeneigenschaften (Hydrophobie/Hydrophilie) auf OER und ORR Aktivität in Elektroden untersucht und verstanden wurde. Allgemein kontrollieren diese Parameter die Bildung des Elektrolyt-Dünnfilm-Meniskus und das Fluten der Poren. Der Elektrolyt-Dünnfilm-Meniskus ist essentiell für die ORR Aktivität und elektrolytgeflutete Poren sind essentiell für die OER Aktivität. Mit diesem Wissen wurden verschiedene Porengrößen und Oberflächeneigenschaften miteinander kombiniert, um unterschiedliche Porengradiente mit hydrophilien/hydrophoben Übergang zu fertigen. Die Bildung des Elektrolytfilms und dessen Dicke kann auch durch die zusätzlichen KF-GDE Schichten kontrolliert werden, wie oben gezeigt. Das zu verstehen führte zum M□|M■|S■ Aufbau.

Dieser Erfolg wurde durch die verwendete Forschungsstrategie erreicht. Messmethoden wie REM, Röntgentomographie, Kontaktwinkel, elektrochemische Impedanz, galvanostatische und potentiostatische Polarisierung haben geholfen Porengrößen- und Oberflächeneigenschaftseinflüsse auf die elektrochemische Aktivität zu verstehen. Besonders durch REM und Röntgentomographie war die Visualisierung der Elektrolyt-Dünnfilm-Bildung in den Poren möglich und wie dieser Elektrolytfilm von Porengröße, von hydrophober/hydrophiler Oberflächen und deren Kombinationen beeinflusst wird.

Der Benchmark der entwickelten bifunktionalen KF-GDE M□|M■|S■ hat gezeigt, dass es eine kompetitive bifunktionale GDE für Metall-Luft Batterien und regenerativen Brennstoffzellen und voraussichtlich für Elektrolyseure ist. Somit gehört es zu den fortschrittlichsten Gasdiffusionselektroden für alkalische Anwendungen.

Der erste Kostenvergleich zeigt auf, dass die Stand-der-Technik kohlenstoffbasierte GDE geringere Materialkosten hat. Da es hauptsächlich aus Aktivkohle (≈ 1.85 € kg^{-1})[178] besteht, das günstiger ist als Nickel (≈ 16.37 € kg^{-1})[179] oder Edelstahl Legierung 1.4404 (≈ 3.92 € kg^{-1})[179]. Aus

repräsentativen Gründen wurden die Materialpreise in Friedenszeiten ermittelt. Da Kriegszeiten Ausnahmesituationen sind, sind Materialpreise in diesen Zeiten nicht repräsentativ.

Nichtsdestotrotz ist die überlegene elektrochemische Stabilität von Nickel und Edelstahl Komponenten in alkalischen Anwendungen deutlich gezeigt worden und somit ein Schlüsselfaktor beim Kostenvergleich. Denn die Langzeitstabilitätsergebnisse zeigen deutlich, dass die Lebensdauer der kohlenstoffbasierten GDE_{ref} beim 900. Zyklus endet, da dort die Stromdichte ca. um 20 % reduziert ist und weiter kontinuierlich mit jedem Zyklus abnimmt (60 % Gesamtverlust). Im Vergleich dazu zeigt die geschichtete KF-GDE am letzten 2100. Zyklus kein Ende ihrer Lebensdauer, weil die Stromdichte von Anfang bis Ende kontinuierlich um 70 – 80 % angestiegen ist. Womit die Lebensdauer von alkalischen Energiewandler-Systemen durch den Einsatz von geschichteten KF-GDEs potenziell um mehr als 50 % erhöht werden kann.

Auf Basis dessen lässt sich schlussfolgern, dass die Investitionsausgaben (capital expenditure: capex) für die geschichteten KF-GDEs potenziell höher sind. Aber die gesamte gespeicherte elektrische Energie während der Lebensdauer potenziell um mehr als 50 % größer ist als im Vergleich zur kohlenstoffbasierten GDE, womit es eine höhere Wirtschaftlichkeit hat. Daran anschließend müssen weniger alkalische Energiewandler Systeme produziert werden, um die Defekten zu ersetzen und somit ist die Verwendung von geschichteten KF-GDEs ressourcenschonender.

Im Allgemeinen ist die Verwendung von kohlenstoffbasierten GDEs in kleinen nicht aufladbaren Batterien wie z.B. Knopfzellen für den Normal-Verbraucher aufgrund der geringeren Capex weiterhin sehr attraktiv. Jedoch ist die Verwendung von geschichteten KF-GDEs in größeren aufladbaren alkalischen Energiewandler-Systemen attraktiver als die kohlenstoffbasierten GDEs trotz der höheren Capex. Da eine höhere Wirtschaftlichkeit und höhere Ressourcenschonung gewährleistet wird.

7 Literature

[1] D. U. Lee, P. Xu, Z. P. Cano, A. G. Kashkooli, M. G. Park, Z. Chen, *J. Mater. Chem. A* **2016**, *4*, 7107.

[2] Sören Dresp and Peter Strasser, *ChemCatChem* **2018**, 4162.

[3] Hao-Fan Wang, Cheng Tang, and Qiang Zhang, *Advanced Functional Materials* **2018**.

[4] Jing Pan, Yang Yang Xu, Huan Yang, Zehua Dong, Hongfang Liu, and Bao Yu Xia, *Advanced Science* **2018**.

[5] Weng Cheong Tana, Lip Huat Sawa,∗, Hui San Thiama, Jin Xuanb, Zuansi Caic, Ming Chian Yewa, *Renewable and Sustainable Energy Reviews* **2018**, 181.

[6] Bin Wang, Cheng Tang, Hao-Fan Wang, Bo-Quan Li, Xiaoyang Cui, and Qiang Zhang, *Small Methods* **2018**.

[7] Ke Xu, Adeline Loh, Baoguo Wang and Xiaohong Li, *Journal of The Electrochemical Society* **2018**, A809-A818.

[8] J. W. D. Ng, M. Tang, T. F. Jaramillo, *Energy Environ. Sci.* **2014**, *7*, 2017.

[9] Gwenaëlle Toussaint*a, Philippe Stevensa, Laurent Akroura, Robert Rougetb and Fabrice, *The Electrochemical Society*, *2010*, 25.

[10] Panagiotis Trogadas, Thomas F.Fuller, PeterStrasser, *Carbon* **2014**, 5.

[11] P. Gu, M. Zheng, Q. Zhao, X. Xiao, H. Xue, H. Pang, *J. Mater. Chem. A* **2017**, *5*, 7651.

[12] Tsai Yi-Chiun, Yang Wein-Duo, Lee Kuan-Ching, Huang Chao-Ming, *Materials (Basel, Switzerland)* **2016**, *9*.

[13] Yun Wang, Daniela Fernanda Ruiz Diaz, Ken S. Chen, Zhe Wang, Xavier Cordobes Adroher, *Materials Today* **2020**, 178.

[14] T. B. Ferriday, Peter Hugh Middleton, *International Journal of Hydrogen Energy* **2021**, in press.

[15] F. Bidault, D.J.L. Brett, P.H. Middletonc, N.P. Brandon, *Journal of Power Sources*, *2009*, 39.

[16] E. Wagner, H.-J. Kohnke, *Fuel Cells* **2020**, *20*, 718.

[17] Qianfeng Liu, Zhefei Pan, Erdong Wang, Liang An b, Gongquan Sun, *Energy Storage Materials* **2020**, 478.

[18] H. A. Miller, K. Bouzek, J. Hnat, S. Loos, C. I. Bernäcker, T. Weißgärber, L. Röntzsch, J. Meier-Haack, *Sustainable Energy Fuels* **2020**, *4*, 2114.

[19] Maximilian Schalenbach, Aleksandar R. Zeradjanin, Olga Kasian, Serhiy Cherevko, Karl J.J. Mayrhofer, *International Journal of Electrochemical Science* **2018**, 1173.

[20] Sandra Hernandez-Aldave and Enrico Andreoli, *catalysts*, *2020*.

[21] Gerhard F. Swiegers, Richard N. L. Terrett, George Tsekouras, Takuya Tsuzuki, Ronald J. Pace, Robert Stranger, *Sustainable Energy & Fuels* **2021**, 1280.

[22] W. Vielstich (Hrsg.) *Handbook of fuel cells*, *Volume 2*, Wiley, Chichester, **2007**.

[23] Fabian Kubannek, Thomas Turek, and Ulrike Krewer, *Chemie Ingenieur Technik 2019*, *2019*, 1.

[24] Osamu Yamamoto, *Electrochimica Acta* **2000**, 2423.

[25] Nigel Sammes, Roberto Bove, Knut Stahl, *Current Opinion in Solid State and Materials Science* **2004**, 372.

[26] H. S. Alexander Buttler, *Renewable and Sustainable Energy Reviews* **2018**, 2440.

[27] Chao Wei, Reshma R. Rao, Jiayu Peng, Botao Huang, Ifan E. L. Stephens, Marcel Risch, Zhichuan J. Xu, and Yang Shao-Horn, *Adv. Mater.* **2019**, 1.

[28] R.J. Gilliam, J.W. Graydon, D.W. Kirk, S.J. Thorpe, *International Journal of Hydrogen Energy* **2007**, 359.

[29] P. Vermeiren, J. P. Moreels, R. Leysen, *J Porous Mater* **1996**, *3*, 33.

[30] Géraldine Merle, Matthias Wessling, Kitty Nijmeijer, *Journal of Membrane Science* **2011**, 1.

[31] J. R. Varcoe, P. Atanassov, D. R. Dekel, A. M. Herring, M. A. Hickner, P. A. Kohl, A. R. Kucernak, W. E. Mustain, K. Nijmeijer, K. Scott et al., *Energy Environ. Sci.* **2014**, *7*, 3135.

[32] Christopher G. Arges and Le Zhang, *ACS Appl. Energy Mater.* **2018**, 2991.

[33] Shimshon Gottesfeld, Dario R. Dekel, Miles Page, Chulsung Bae, Yushan Yan, Piotr Zelenay, Yu Seung Kim, *Journal of Power Sources* **2018**, 170.

[34] Sangtaik Noh, Jong Yeob Jeon, Santosh Adhikari, Yu Seung Kim, and Chulsung Bae, *Acc. Chem. Res.* **2019**, 2745.

[35] M. G. Marino and K. D. Kreuer, *ChemSusChem* **2015**, 513.

[36] Kristina M. Hugar, Henry A. Kostalik, IV, and Geoffrey W. Coates, *J. Am. Chem. Soc.* **2015**, 8730.

[37] Shuang Gu, Rui Cai, Ting Luo, Zhongwei Chen, Minwei Sun, Yan Liu, Gaohong He, and Yushan Yan, *Angew. Chem. Int. Ed.* **2009**, 6499.

[38] Dirk Henkensmeier, Malikah Najibah, Corinna Harms, Jan Žitka, Jaromír Hnát, Karel Bouzek, *Journal of Electrochemical Energy Conversion and Storage* **2021**, 1.

[39] S.J. Peighambardoust, S. Rowshanzamir, M. Amjadi, *International Journal of Hydrogen Energy* **2010**, 9349.

[40] M. Hunsom, D. Kaewsai, A.M. Kannan, *International Journal of Hydrogen Energy* **2018**, 21478.

[41] P. Millet, R. Ngameni, S.A. Grigoriev, V.N. Fateev, *International Journal of Hydrogen Energy* **2011**, 4156.

[42] Wilson A. Smith, Thomas Burdyny, David A. Vermaas, and Hans Geerlings, *Joule* **2019**, 1822.

[43] Kunna Wu, Erik Birgersson, Byoungsu Kim, Paul J. A. Kenis, and Iftekhar A. Karimi, *Journal of The Electrochemical Society*, *2015*, F23-F32.

[44] Cao-Thang Dinh, Thomas Burdyny, Md Golam Kibria, Ali Seifitokaldani, Christine M. Gabardo, F. Pelayo García de Arquer, Amirreza Kiani, Jonathan P. Edwards, Phil De Luna, Oleksandr S. Bushuyev, Chengqin Zou, Rafael Quintero-Bermudez, Yuanjie Pang, David Sinton, Edward H. Sargent, *Science*, *2018*, 783.

[45] Yuguang C. Li, Dekai Zhou, Zhifei Yan, Ricardo H. Gonçalves, Danielle A. Salvatore, Curtis P. Berlinguette, and Thomas E. Mallouk, *ACS Energy Lett.*, *2016*, 1149.

[46] Angelica Reyes, Ryan P. Jansonius, Benjamin A. W. Mowbray, Yang Cao, Danika G. Wheeler, Jacky Chau, David J. Dvorak, and Curtis P. Berlinguette, *ACS Energy Lett.*, *2020*, 1612.

[47] Tu N. Nguyen and Cao-Thang Dinh, *Chem. Soc. Rev.*, *2020*, 7488.

[48] Thomas Burdyny and Wilson A. Smith, *Energy Environ. Sci* **2019**, 1442.

[49] David M. Weekes, Danielle A. Salvatore, Angelica Reyes, Aoxue Huang, and Curtis P. Berlinguette, *Acc. Chem. Res.* **2018**, 910.

[50] Recep Kas, Kailun Yang, Divya Bohra, Ruud Kortlever, Thomas Burdyny and Wilson A. Smith, *Chem. Sci.* **2020**, 1738.

[51] Uzoma O. Nwabara, Emiliana R. Cofell, Sumit Verma, Emanuela Negro and Paul J. A. Kenis, *ChemSusChem*, *2020*, 855.

[52] Yihong Chen, Christina W. Li, and Matthew W. Kanan, *Journal of the American Chemical Society* **2012**, 19969.

[53] Y. Hori in *Modern Aspects of Electrochemistry*, *Vol. 42* (Hrsg.: C. G. Vayenas, R. E. White, M. E. Gamboa-Aldeco), Springer New York, **2008**, S. 89–189.

[54] Ezra L. Clark, Joaquin Resasco, Alan Landers, John Lin, Linh-Thao Chung, Amber Walton, Christopher Hahn, Thomas F. Jaramillo, and Alexis T. Bell, *ACS Catal.* **2018**, 6560.

[55] M. Kusnezoff, M. Jahn, S. Megel, S. Rothe, S. Hielscher, E. Reichelt, N. Trofimenko, G. Herz, W. Beckert, J. Schilm, A. Rost, J. Schöne, G. Ganzer, D. Wagner, L. Nousch, V. Sauchuk, M. Hartmann and A. Michaelis, *The Electrochemical Society* **2021**, 307.

[56] Henning Weinrich, Yasin Emre Durmus, Hermann Tempel, Hans Kungl, and Rüdiger-A. Eichel, *materials* **2019**, 1.

[57] Chunlian Wang, Yongchao Yu, Jiajia Niu, Yaxuan Liu, Denzel Bridges, Xianqiang Liu, Joshi Pooran, Yuefei Zhang and Anming Hu, *Appl. Sci.* **2019**, 1.

[58] Hao-Fan Wang and Qiang Xu, *Matter* **2019**, 565.

[59] Kyeongse Song, Daniel Adjei Agyeman, Mihui Park, Junghoon Yang, and Yong-Mook Kang, *Adv. Mater.* **2017**, 1.

[60] Vyacheslav S. Bryantsev, Vincent Giordani, Wesley Walker, Mario Blanco, Strahinja Zecevic, Kenji Sasaki, Jasim Uddin, Dan Addison, and Gregory V. Chase, *J. Phys. Chem. A* **2011**, 12399.

[61] Reza Younesi, Gabriel M. Veith, Patrik Johansson, Kristina Edström and Tejs Vegge, *Energy Environ. Sci.* **2015**, 1905.

[62] J. Fu, Z. P. Cano, M. G. Park, A. Yu, M. Fowler, Z. Chen, *Advanced materials (Deerfield Beach, Fla.)* **2017**, *29*.

[63] J. Park, M. Park, G. Nam, J.-S. Lee, J. Cho, *Advanced materials (Deerfield Beach, Fla.)* **2015**, *27*, 1396.

[64] Y. Xu, Y. Zhao, J. Ren, Y. Zhang, H. Peng, *Angewandte Chemie (International ed. in English)* **2016**, *55*, 7979.

[65] L. Fan, S. Wei, S. Li, Q. Li, Y. Lu, *Adv. Energy Mater.* **2018**, 1.

[66] Arumugam Manthiram, Xingwen Yu and Shaofei Wang, *NATURE REVIEWS MATERIALS* **2017**, 1.

[67] Pankaj Arora and Zhengming (John) Zhang, *Chem. Rev.* **2004**, 4419.

[68] C. H. Hamann, W. Vielstich, *Elektrochemie,* 4. Aufl., Wiley-VCH, Weinheim, **2005**.

[69] J. Giner and C. Hunter, *Journal of The Electrochemical Society* **1969**, 1124.

[70] Guangyu Lin and Trung Van Nguyen, *Journal of The Electrochemical Society*, *2005*, A1942-A1948.

[71] Han-Kyu Lee, Jong-Ho Park, Do-Young Kim, Tae-Hee Lee, *Journal of Power Sources*, *2004*, 200.

[72] Maximilian Röhe, Fabian Kubannek, and Ulrike Krewer, *ChemSusChem* **2019**, 2373.

[73] Yu.G. Chirkov, *Russian Journal of Electrochemistry* **1999**, 1281-1290.

[74] Dennis Wittmaier, Simon Aisenbrey, Norbert Wagner, K. Andreas Friedrich, *Electrochimica Acta* **2014**, 355.

[75] Maximilian Röhe, Alexander Botz, David Franzen, Fabian Kubannek, Barbara Ellendorff, Denis Öhl, Wolfgang Schuhmann, Thomas Turek and Ulrike Krewer, *ChemElectroChem* **2019**, 5671.

[76] Marcus Gebhard, Tim Tichter, David Franzen, Melanie C. Paulisch, Konstantin Schutjajew, Thomas Turek, Ingo Manke, and Christina Roth, *ChemElectroChem* **2020**, 830.

[77] Kai Li, Qun Fan, Hongyuan Chuai, Hai Liu, Sheng Zhang, Xinbin Ma, *Transactions of Tianjin University* **2021**, 202.

[78] Vinoba Vijayaratnam, *Dissertation*, Universität des Saarlands, Saarbrücken, **2017**.

[79] Nathan T. Nesbitt, Thomas Burdyny, Hunter Simonson, Danielle Salvatore, Divya Bohra, Recep Kas, and Wilson A. Smith, *ACS Catal.* **2020**, 14093.

[80] Othonas A. Moultos, Ioannis N. Tsimpanogiannis, Athanassios Z. Panagiotopoulos, and Ioannis G. Economou, *J. Phys. Chem. B* **2014**, 5532.

[81] Karl J. Sladek, Edwin R. Gilliland, and Raymond F. Baddour, *Ind. Eng. Chem. Fundamen.* **1974**, 100.

[82] David McLaughlin, Markus Bierling, Riko Moroni, Christoph Vogl, Günter Schmid, and Simon Thiele, *Adv. Energy Mater.* **2020**, 1.

[83] Artur Bekisch, Karl Skadell, David Poppitz, Matthias Schulz, Roland Weidl, Michael Stelter, *Journal of The Electrochemical Society* **2020**, *2020*.

[84] J. O'M. BOCKRIS AND B. D. CAHAN, *The Journal of Chemical Physics* **1969**, 1307.

[85] T. Somasundaram, M. in het Panhuis, R. M. Lynden-Bell, and C. H. Patterson, *J. Chem. Phys.* **1999**, 2190.

[86] Robert Vaˊcha, Petr Slavıˊcˇek, Martin Mucha, Barbara J. Finlayson-Pitts, and Pavel Jungwirth, *J. Phys. Chem. A* **2004**, 11573.

[87] Wei Xing, Min Yin, Qing Lv, Yang Hu, Changpeng Liu and Jiujun Zhang in *Rotating Electrode Methods and Oxygen Reduction Electrocatalysts*, S. 1–31.

[88] A. Botti, F. Bruni, S. Imberti, M. A. Ricci, A. K. Soper, *Journal of Chemical Physics* **2003**, 5001.

[89] J. BALEJ, *Int. J. Hydrogen Energy* **1985**, 233.

[90] L. A. Curtiss and C. A. Melendres, *J. Phys. Chem.* **1984**, 1325.

[91] Cunzhong Zhang, Fu-Ren F. Fan and Allen J. Bard, *J. Am. Chem. Soc.* **2009**, *131*, 177.

[92] Lien-Chun Weng, Alexis T. Bell and Adam Z. Weber, *Phys.Chem.Chem.Phys.* **2018**, 16973.

[93] E. Gileadi (Hrsg.) *Electrode Kinetics for Chemists, Chemical Engineers and Material Scientists*, Wiley-VCH, Weinheim, New York, Basel, Cambridge, Tokyo, **1993**.

[94] Fritz G. Will* and David J. BenDaniel, *The Electrochemical Society* **1969**.

[95] Pehr Björnbom, *Electrochimica Acta*, *1987*, 115.

[96] M. Bockelmann, U. Kunz, T. Turek, *Electrochemistry Communications* **2016**, *69*, 24.

[97] Stefan Pinnow, Naresh Chavan, Thomas Turek, *Journal of Applied Electrochemistry*, *2011*, 1053.

[98] M. B. Cutlip, *Electrochimica Acta*, *1974*, 767.

[99] Mike L. Perry, John Newman and Elton J. Cairns, *The Electrochemical Society*, *1998*.

[100] Antoni Forner-Cuenca , Johannes Biesdorf , Lorenz Gubler , Per Magnus Kristiansen , Thomas Justus Schmidt , and Pierre Boillat, *Adv. Mater.* **2015**, 6317.

[101] Y. Yuan, T. R. Lee, *Surface Science Techniques*, *2013*, 3.

[102] G. Barati Darband, M. Aliofkhazraei, S. Khorsand, S. Sokhanvar, A. Kaboli, *Arabian Journal of Chemistry* **2018**.

[103] Robert N. Wenzel, *Industrial and Engineering Chemistry* **1936**, 988.

[104] Ralf Blossey, *Nature materials* **2003**, 301.

[105] A. B. D. Cassie and S. Baxter, *Trans. Faraday Soc.* **1944**, 546.

[106] Edward Bormashenko & Victor Starov, *Colloid Polym Sci* **2013**, 343.

[107] Gyoko Nagayama and Dejian Zhang, *Soft matter* **2020**, 3514.

[108] W. Barthlott, T. Schimmel, S. Wiersch, K. Koch, M. Brede, M. Barczewski, S. Walheim, A. Weis, A. Kaltenmaier, A. Leder et al., *Adv. Mater.* **2010**, *22*, 2325.

[109] Gastón O. Larrazábal, Patrick Strøm-Hansen, Jens P. Heli, Kevin Zeiter, Kasper T. Therkildsen, Ib Chorkendorff, Brian Seger, *ACS Appl. Mater. Interfaces* **2019**, 41281.

[110] Jie Zhang, Wen Luo and Andreas Züttel, *J. Mater. Chem. A* **2019**, 26285.

[111] Wen Luo, Jie Zhang, Mo Li, Andreas Züttel, *ACS Catal.* **2019**, 3783.

[112] Kailun Yang, Recep Kas, Wilson A. Smith, Thomas Burdyny, *ACS Energy Lett.* **2021**, 33.

[113] Chan Lim, C. Y. Wang, *Electrochimica Acta*, *2004*, 4149.

[114] Z. L. Jinjin Xuan, *Int. J. Electrochem. Sci.* **2017**, 10471.

[115] Prasad Prakash Patel, Moni Kanchan Datta, Oleg I. Velikokhatnyi, Ramalinga Kuruba, Krishnan Damodaran, Prashanth Jampani, Bharat Gattu, Pavithra Murugavel Shanthi, Sameer S. Damle, Prashant N. Kumta, *Scientific reports* **2016**, 1.

[116] H. A. Gasteiger, S. S. Kocha, B. Sompalli, F. T. Wagner, *Applied Catalysis B: Environmental* **2005**, *56*, 9.

[117] S. Trasatti, *Electrochim. Acta* **1984**, *29*, 1503.

[118] V. Baglio, C.D'Urso, A. Di Blasi, R. Ornelas, L. G. Arriaga, V. Antonucci, A. S. Aric `o, *International Journal of Electrochemistry* **2011**, 1.

[119] E. Rasten, G. Hagen, R. Tunold, *Electrochim. Acta* **2003**, *48*, 3945.

[120] Woong Hee Lee and Hansung Kim, *Journal of The Electrochemical Society*, *2014*, F729-F733.

[121] L. M. Roen, C. H. Paik, and T. D. Jarvi, *Electrochemical and Solid-State Letters*, *2004*, A19-A22.

[122] Zhiming Cui, Yutao Li, Gengtao Fu, Xiang Li, and John B. Goodenough, *Adv. Mater.* **2017**, 1.

[123] Zhaoqing Ding, Zhenghua Tang, Ligui Li, Kai Wang, Wen Wu, Xiaoning Chen, Xiao Wua, Shaowei Chen, *Inorg. Chem. Front.* **2018**, 2425.

[124] Jie Hu, Qiunan Liu, Lina Shi, Ziwei Shi, Hao Huang, *Applied Surface Science* **2017**, 61.

[125] Ziyang Guo, Chao Li, Wangyu Li, Hua Guo, Xiuli Su, Ping He, Yonggang Wang, Yongyao Xia, *J. Mater. Chem. A* **2016**, 6282.

[126] M. Tahir, L. Pan, F. Idrees, X. Zhang, L. Wang, J.-J. Zou, Z. L. Wang, *Nano Energy* **2017**, *37*, 136.

[127] K. Zhang, X. Han, Z. Hu, X. Zhang, Z. Tao, J. Chen, *Chemical Society reviews* **2015**, *44*, 699.

[128] Xing Wu, Chongjian Tang, Yi Cheng, Xiaobo Min, San Ping Jiang, Shuangyin Wang, *Chem. Eur. J.*, *2020*, 3906.

[129] Dennis Wittmaier, Timo Danner, Norbert Wagner, K. Andreas Friedrich, *J Appl Electrochem* **2014**, 73.

[130] Daniel Chade, Leonard Berlouis, David Infield, Andrew Cruden, Peter Tommy Nielsen, Troels Mathiesen, *International Journal of Hydrogen Energy* **2013**, 14380.

[131] X. Zhang, B. Li, C. Liu, Q. Chu, F. Liu, X. Wang, H. Chen, X. Liu, *Mater. Res. Bull.* **2013**, *48*, 2696.

[132] J. Chu, D. Lu, J. Ma, M. Wang, X. Wang, S. Xiong, *Materials Letters* **2017**, *193*, 263.

[133] S. Chou, F. Cheng, J. Chen, *Journal of Power Sources* **2006**, *162*, 727.

[134] Xueying Cao, Dedong Jia, Da Li, Liang Cui, Jingquan Liu, *Chemical Engineering Journal* **2018**, 310.

[135] M. Pourbaix, *Atlas of electrochemical equilibria in aqueous solutions*, Nat'L Assoc. Of Corrosion, Houston, Tex.: National Association of Corrosion Engineers, **1974**.

[136] Hyo Sang Jeon, Sebastian Kunze, Fabian Scholten, Beatriz Roldan Cuenya, *ACS Catal.* **2018**, 531.

[137] Norihito Ikemiya, Keisuke Natsui, Kazuya Nakata, Yasuaki Einaga, *ACS Sustainable Chem. Eng.* **2018**, 8108.

[138] Jingjie Wu, Shi-GangSun, Xiao-DongZhou, *Nano Energy* **2016**, 225.

[139] Preethy Parthasarathy, Anil V. Virkar, *Journal of Power Sources* **2013**, 82.

[140] Josef C. Meier, Carolina Galeano, Ioannis Katsounaros, Angel A. Topalov, Aleksander Kostka, Ferdi Schüth, Karl J. J. Mayrhofer, *ACS Catal.* **2012**, 832.

[141] Josef C. Meier, Ioannis Katsounaros, Carolina Galeano, Hans J. Bongard, Angel A. Topalov, Aleksander Kostka Arndt Karschin, Ferdi Schüth, Karl J. J. Mayrhofer, *Energy Environ. Sci.* **2012**, 9319.

[142] E. Guilminot, A. Corcella, M. Chatenet, F. Maillard, F. Charlot, G. Berthomé, C. Iojoiu, J.-Y. Sanchez, E. Rossinot, E. Clauded, *Journal of The Electrochemical Society* **2007**, B1106-B1114.

[143] Philippe Jeanty, Christian Scherer, Erhard Magori, Kerstin Wiesner-Fleischer, Olaf Hinrichsen, Maximilian Fleischer, *Journal of CO2 Utilization* **2018**, 454.

[144] Trygve Burchardt, *Journal of Power Sources* **2004**, 192.

[145] Michael N. Hull, Herbert I. James, *Journal of The Electrochemical Society* **1977**, 332.

[146] D. Pletcher, N. A. Hampson and A. J. S. McNeil in *Electrochemistry: Volume 9*, S. 1–65.

[147] Bert De Mot, Jonas Hereijgers, Miguel Duarte, Tom Breugelmans, *Chemical Engineering Journal* **2019**, 1.

[148] G. S. Shapoval, A. P. Tomilov, A. A. Pud, V. A. Vonsyatskii, *Theoretical and Experimental Chemistry* **1984**, 234.

[149] M. Schulze, K. Bolwin, E. Giilzow, W. Schnurnberger, *Fresenius' Journal of Analytical Chemistry volume* **1995**, 778.

[150] J. O. Bockris, *J. Chem. Phys.* **1956**, *24*, 817.

[151] Y. Matsumoto, E. Sato, *Materials Chemistry and Physics* **1986**, *14*, 397.

[152] L. Giordano, B. Han, M. Risch, W. T. Hong, R. R. Rao, K. A. Stoerzinger, Y. Shao-Horn, *Catalysis Today* **2016**, *262*, 2.

[153] J.L. Diaz de Tuesta, A. Quintanilla∗, J.A. Casas, J.J. Rodriguez, *Catalysis Communications* **2017**, 131.

[154] Youngmi Yi, Gisela Weinberg, Marina Prenzel, Mark Greiner, Saskia Heumann, Sylvia Becker, Robert Schlögl, *Catalysis Today* **2017**, 32.

[155] S. Maass, F. Finsterwalder, G. Frank, R. Hartmann, C. Merten, *Journal of Power Sources* **2008**, 444.

[156] Jun Huang, *Electrochimica Acta* **2018**, 170.

[157] Seung-Beom Yoon, Jong-Pil Jegal Kwang Chul Roh and Kwang-Bum Kim, *The Electrochemical Society* **2014**, H207-H2013.

[158] Jun Huang, Yu Gao, Jin Luo, Shangshang Wang, Chenkun Li, shengli Chen, Jianbo Zhang, *Journal of The Electrochemical Society* **2020**.

[159] W. S. C.A. Schiller, *Electrochimica Acta* **2001**, 3619.

[160] W.H. Molder and J.H. Sluyters, *J. Electroanal. Chem.* **1990**, 103.

[161] Chang-Hee Kim, Su-Il Pyun, Jong-Huy Kim, *Electrochimica Acta* **2003**, 3455.

[162] A. J. Bard, L. R. Faulkner, *Electrochemical methods: Fundamentals and applications,* 2. Aufl., John Wiley & Sons Inc, New York, **2001**.

[163] Pete Peterson, "Capacitance Value from CPE, RParallel: A Calculator", zu finden unter http://www.consultrsr.net/resources/eis/cpecalc.htm, **2014**.

[164] M. Pudukudy, Z. Yaakob, *Journal of Nanoparticles* **2016**, *2016*, 1.

[165] P. W. Menezes, A. Indra, P. Littlewood, M. Schwarze, C. Göbel, R. Schomäcker, M. Driess, *ChemSusChem* **2014**, *7*, 2202.

[166] Benhangi, P. Hosseini, A. Alfantazi, E. Gyenge, *Electrochimica Acta*, *2014*, 42.

[167] S. J. Cooper, A. Bertei, D. P. Finegan, N. P. Brandon, *Electrochimica Acta* **2017**, 681.

[168] Fritz Scholz, *Electroanalytical Methods. Guide to Experiments and Applications*. Second, Revised and Extended Edition, Springer, **2010**.

[169] J. Bisquert, G. Garcia-Belmonte, F. Fabregat-Santiago, P. R. Bueno, *Journal of Electroanalytical Chemistry* **1999**, *475*, 152.

[170] Richard P. Buck, *J. Electroanal. Chem.*, *1986*, 1.

[171] Richard P. Buck and Marcel B. Mâdâras, Reiner Mäckel, *Journal of Electroanalytical Chemistry*, *1993*, 33.

[172] T. E. Springer and I. D. Raistrick, *The Electrochemical Society* **1989**, 1594.

[173] Michael E. G. Lyons, Richard L. Doyle and Michael P. Brandon, *Phys. Chem. Chem. Phys.* **2011**, 21530.

[174] Chee Shan Lim, Chun Kiang Chua, Zdenˇek Sofer, Kateˇrina Kl´ımová, Christopher Boothroyd, and Martin Pumera, *Journal of Materials Chemistry A*, *2015*, 11920.

[175] Hyun-Kon Song, Hee-Young Hwang, Kun-Hong Lee, Le H. Dao, *Electrochimica Acta* **2000**, 2241.

[176] Prerna Tiwari, George Tsekouras, Klaudia Wagner, Gerhard F. Swiegers, Gordon G. Wallace, *International Journal of Hydrogen Energy* **2019**, 23568.

[177] Emanuele Marini, Ludwig Jörissen, Sylvain Brimaud, *Journal of Power Sources* **2021**, 228900.

[178] Marcelo Leon, Javier Silva, Samuel Carrasco, Nelson Barrientos, *processes MDPI* **2020**.

[179] Kindlimann AG, *Preisentwicklung Edelstahl*, **2021**.

[180] H. Keiser, K. D. Beccu und M. A. Gutjahr, *Electrochimica Acta* **1976**, 539.

8   Table Directory

9   List of Figures

10 Appendix

Appendix 1. Python code

```
data = 'name_of_data.txt'
file=open('name_of_data.txt', 'r')
lines=file.readlines()
separate_data=[data.split('\n') and data.split('\t') for data in lines]

dict_data=dict(separate_data)
value=list(dict_data.values())
key=list(dict_data.keys())

for a in range(len(key)):
        key[a] = float(key[a])


for b in range(len(value)):
        value[b] = float(value[b])


float_dict = dict(zip(key, value))
end = len(key)-1

list_end=len(value)-1

new_value=[]
keyList=[]

for k in range(len(key)-1):
        m=k+1
        if key[m] - key[k] > 20:
                keyList.append(key[k])

for a in keyList:
        b=a-1
        new_value.append(float_dict[a])

        keyList_end = len(keyList)-1
        if a == keyList[keyList_end]:
                break

import pandas as pd

new_value

df= pd.DataFrame()
df['I [mA]'] = new_value[0::1]

df.to_excel('name_of_data_splitted.xlsx', index=False)
```
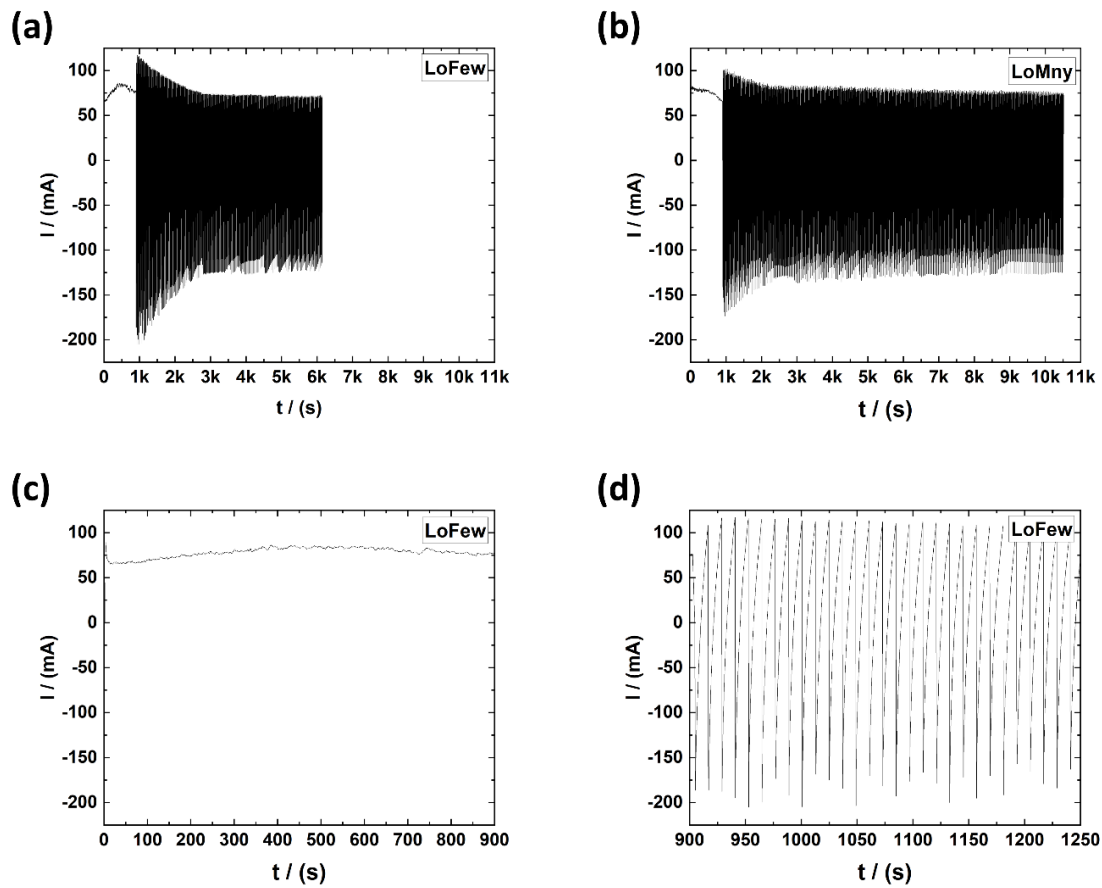
Appendix 2. Image of current-time course during potentiostatic and potentiodynamic electrochemical deposition for (a) ((c) and (d)) LoFew and (b) LoMny settings.
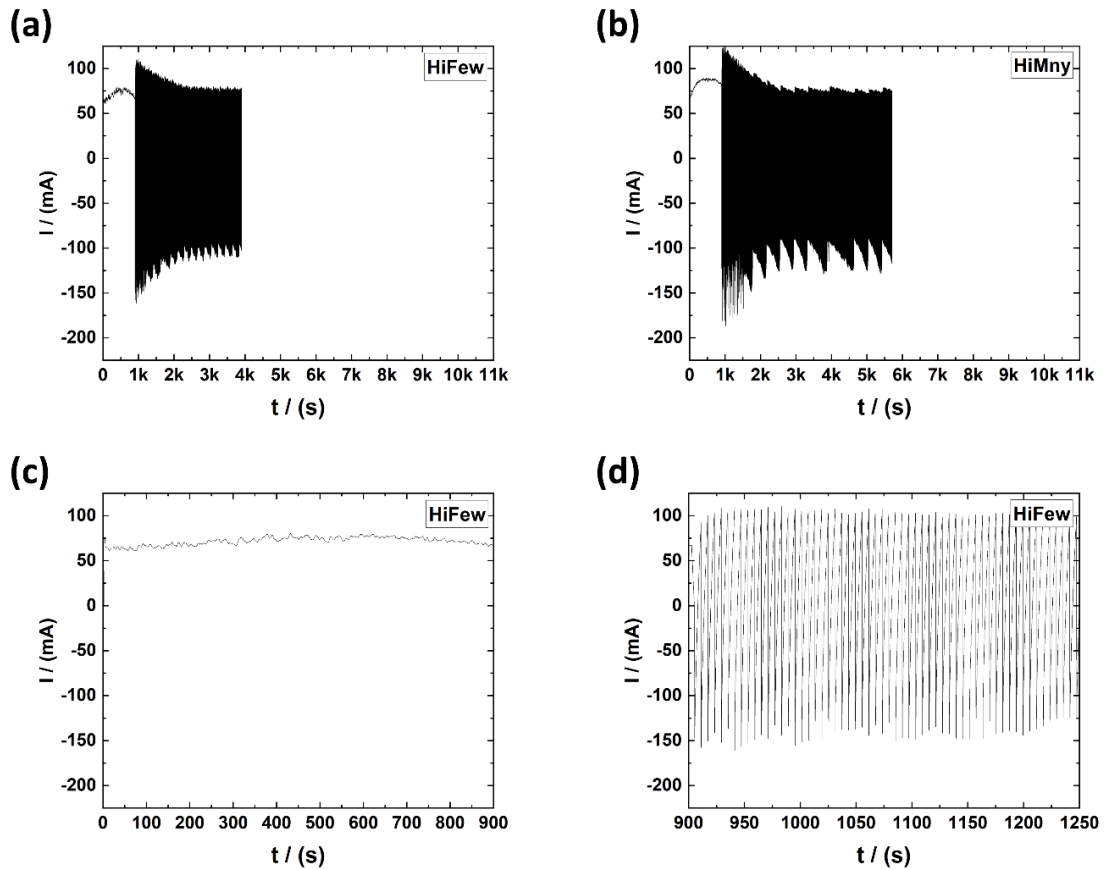
Appendix 3. Image of current-time course during potentiostatic and potentiodynamic electrochemical deposition for (a) ((c) and (d)) HiFew and (b) HiMny settings.
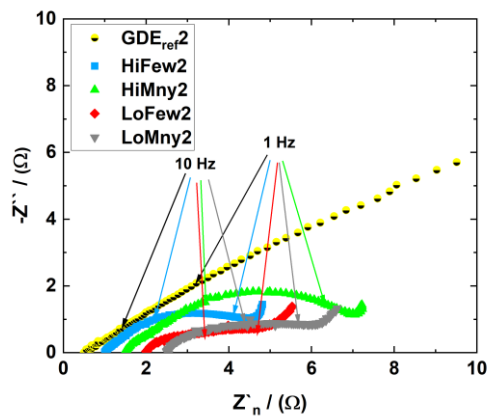
Appendix 4. Impedance spectroscopy measurement Nyquist plots of the second nickel foam samples and GDE$_{ref}$ at a frequency range of approx. 3 kHz – 0.1 Hz (last point) at $\varphi_0 = 0.37$ V vs. Hg/HgO 1 M NaOH.
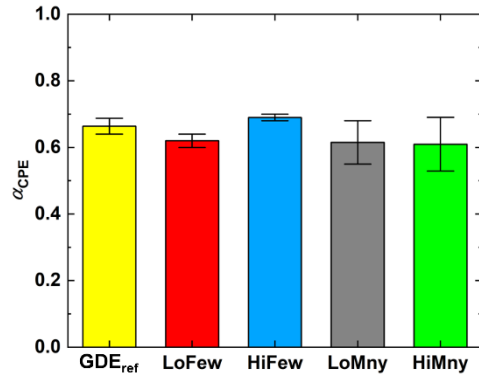
Appendix 5. Image of α_{CPE} at 0.37 V vs. Hg/HgO 1 M NaOH. Determined by the equivalent circuit fitting (HiFew: 50 mV s^{-1} & 500 cycles; HiMny: 50 mV s^{-1} & 800 cycles; LoFew: 25 mV s^{-1} & 500 cycles; LoMny: 25 mV s^{-1} & 800 cycles)
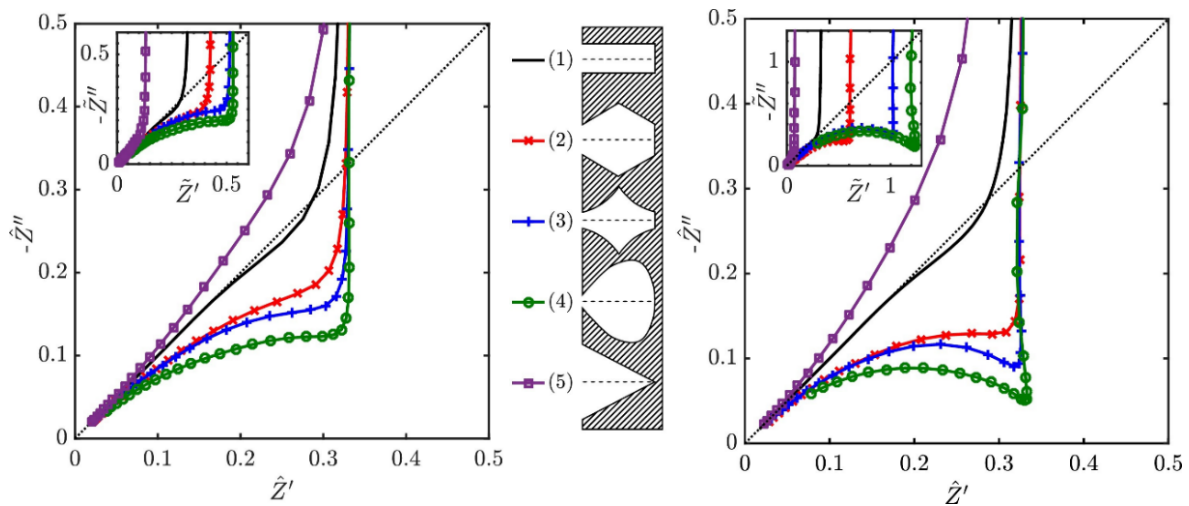
Appendix 6. Simulated impedance spectra for 2D (l) and 3D (r) recreations of the 5 simple closed-pore geometries investigated by Keiser et al.[180]. Reprinted with permission from Cooper et al.[167] under the terms of the Creative Commons CC-BY license.
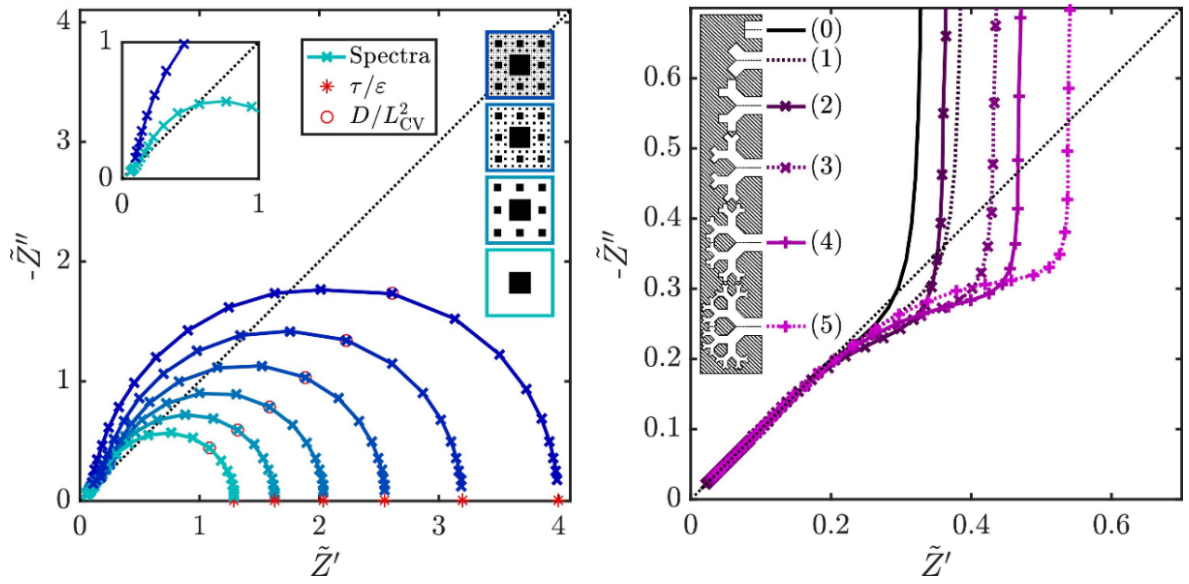
Appendix 7. Simulated impedance spectra of two 2D fractals, as the fractal order increases for (a) Sierpinski Carpet fractal with open boundaries and (b) Pythagoras Tree fractal with closed ends. Reprinted with permission from Cooper et al.[167] under the terms of the Creative Commons CC-BY license.
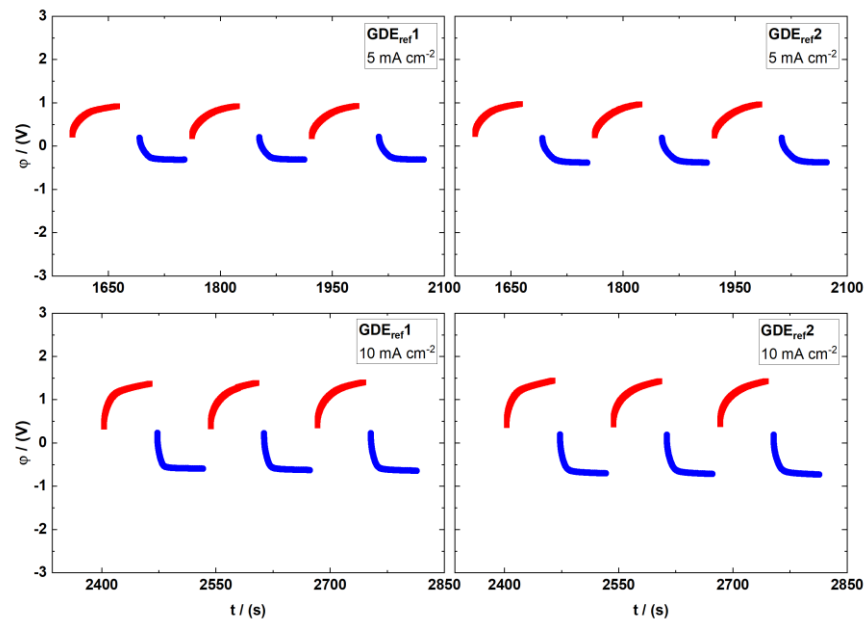
Appendix 8. Image of galvanostatic measurement raw data of GDE$_{ref}$ samples.
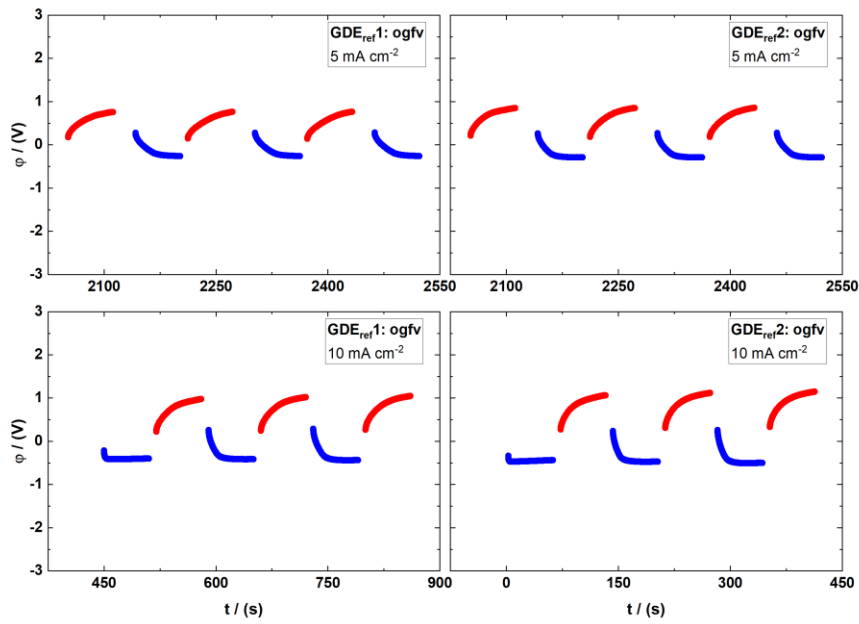
Appendix 9. Image of galvanostatic measurement raw data of GDE_{ref} samples measured without glass fiber fleece.
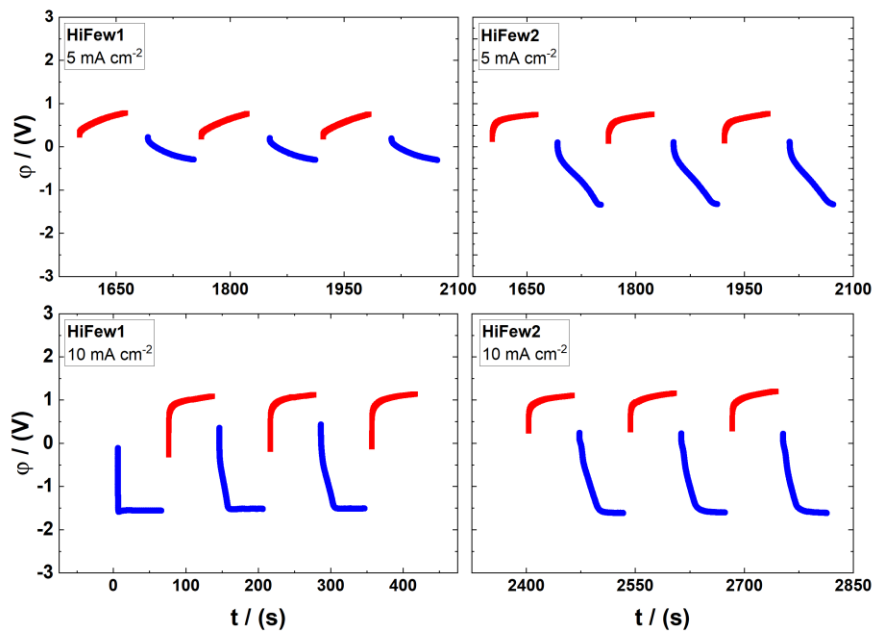
Appendix 10. Image of galvanostatic measurement raw data of HiFew samples.
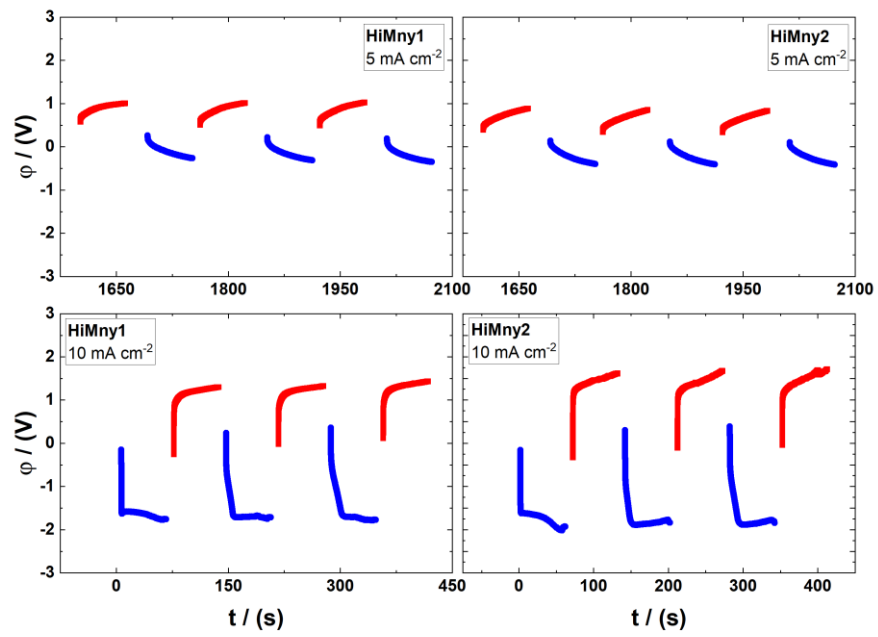
Appendix 11. Image of galvanostatic measurement raw data of HiMny samples.
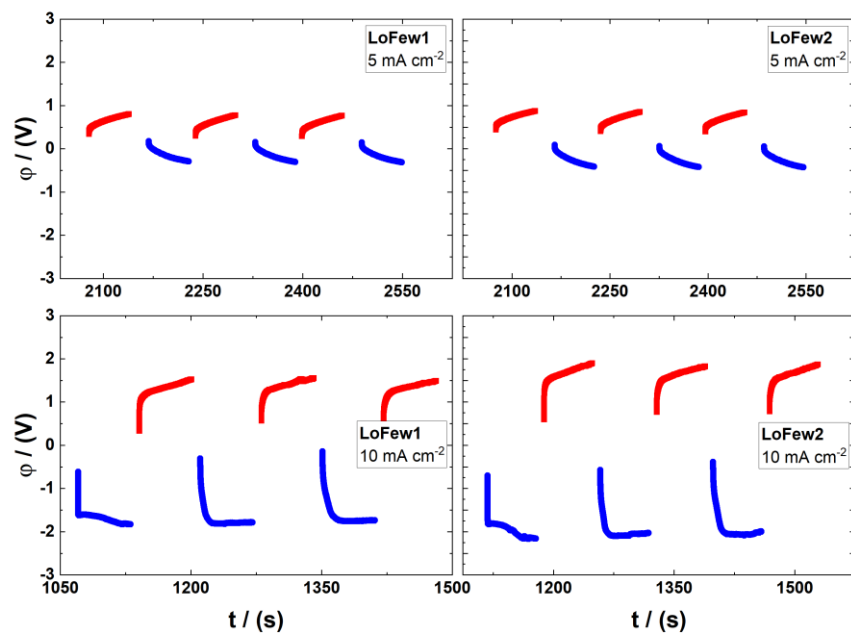
Appendix 12. Image of galvanostatic measurement raw data of LoFew samples.
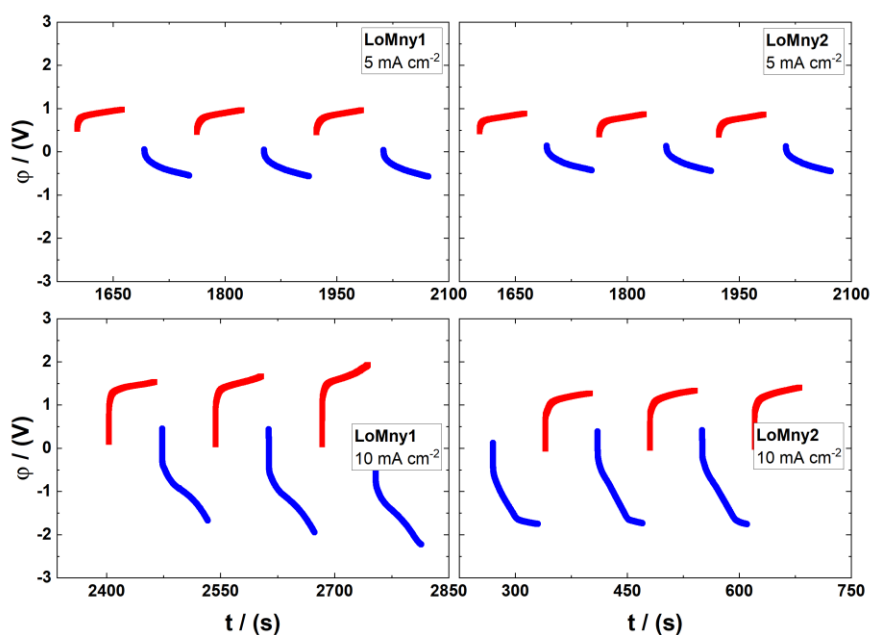
Appendix 13. Image of galvanostatic measurement raw data of LoMny samples.
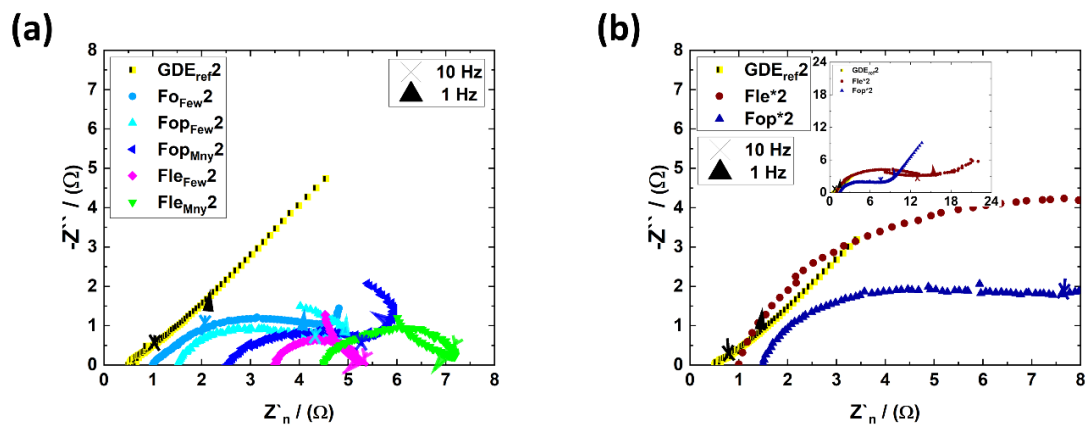
Appendix 14. Impedance spectroscopy measurement Nyquist plots of the second samples ((HiFew and HiMny) (a) and Fle* (HiMny) and Fop* (HiFew) samples additionally coated with PTFE (b) at a frequency range of approx. 3 kHz – 0.1 Hz (last point) at φ_0 = 0.37 V vs. Hg/HgO 1 M NaOH).
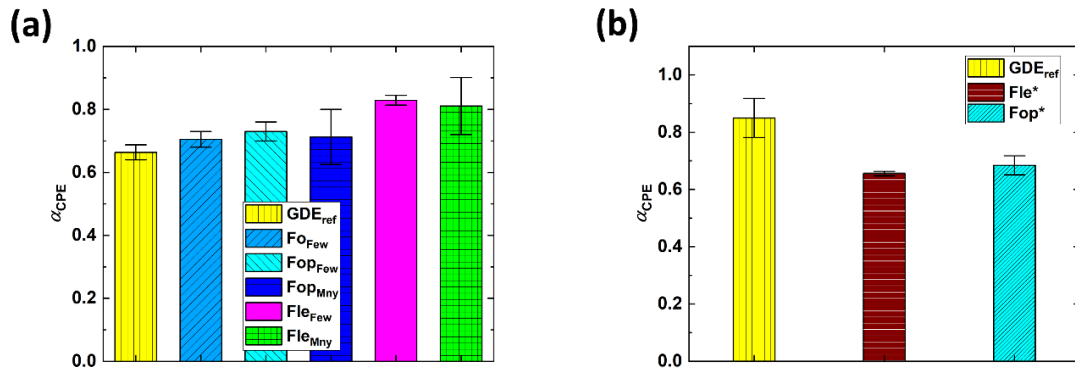
*Appendix 15. Image of αCPE at 0.37 V vs. Hg/HgO 1 M NaOH. Determined by the equivalent circuit fitting. MnOx is electrodeposited with Hi**Few** or Hi**Mny** settings on all electrode bodies (HiFew: 50 mV s⁻¹ & 500 cycles; HiMny: 50 mV s⁻¹ & 800 cycles), Fle* (stainless-steel fleece, HiMny setting) and Fop* (pressed nickel foam, HiFew setting) are additionally coated with PTFE.*
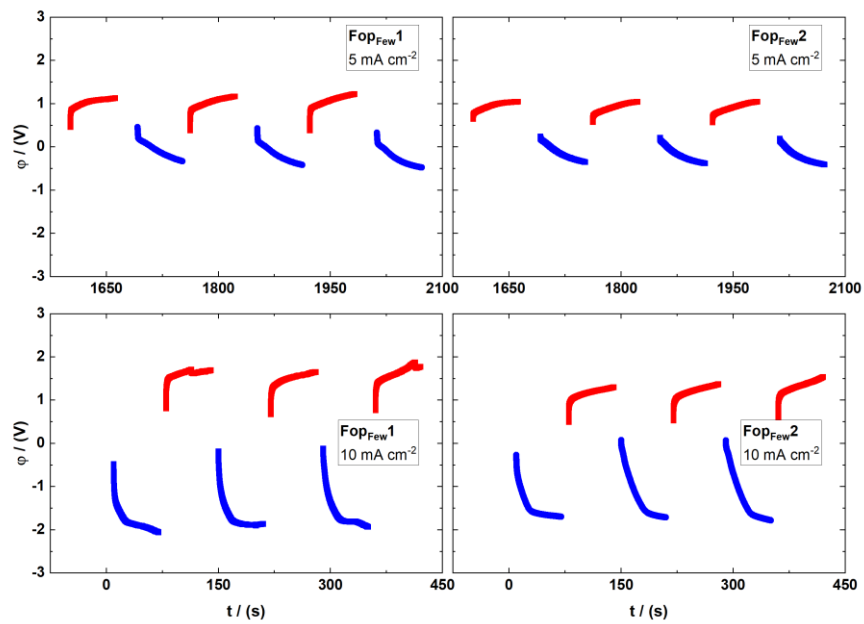
Appendix 16. Image of galvanostatic measurement raw data of Fop_Few samples.
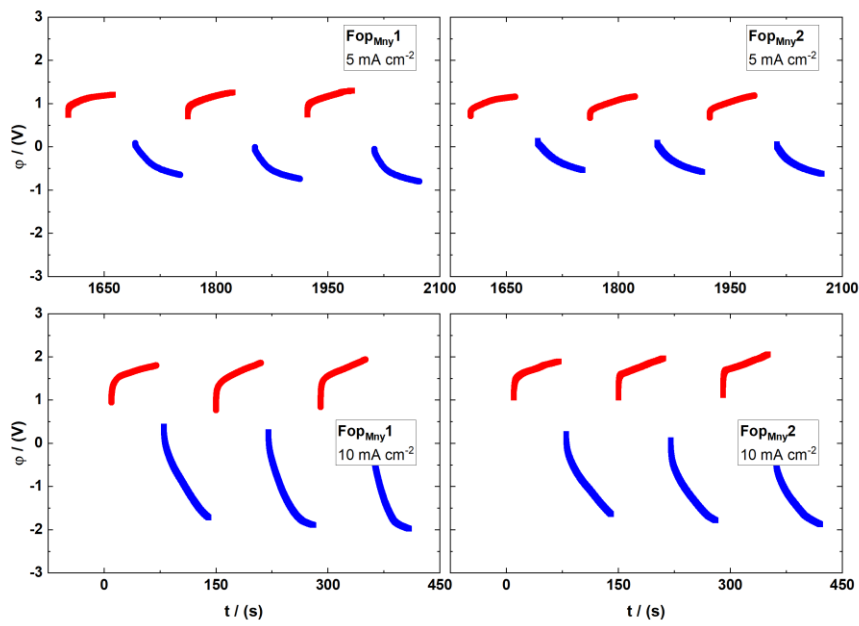
Appendix 17. Image of galvanostatic measurement raw data of Fop$_{Mny}$ samples.
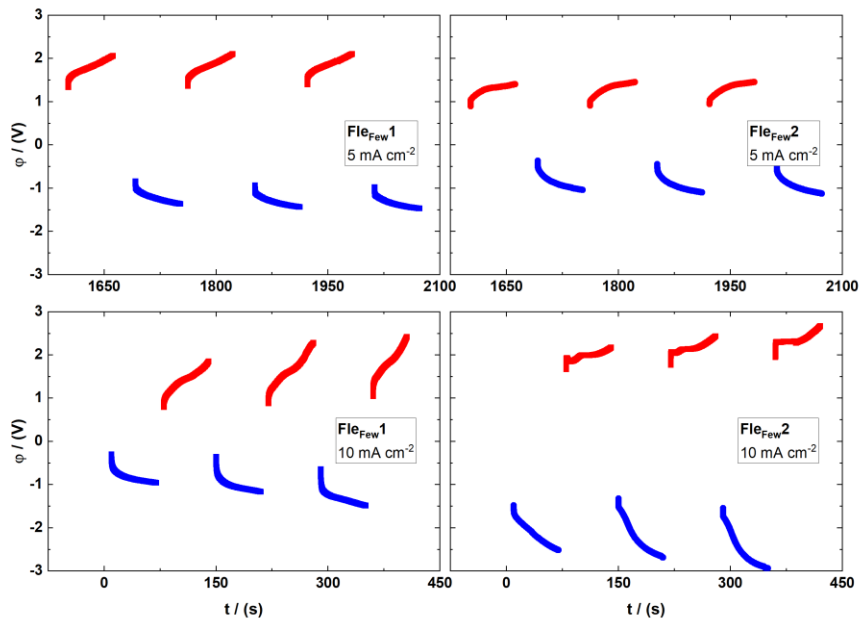
Appendix 18. Image of galvanostatic measurement raw data of Fle$_{Few}$ samples.
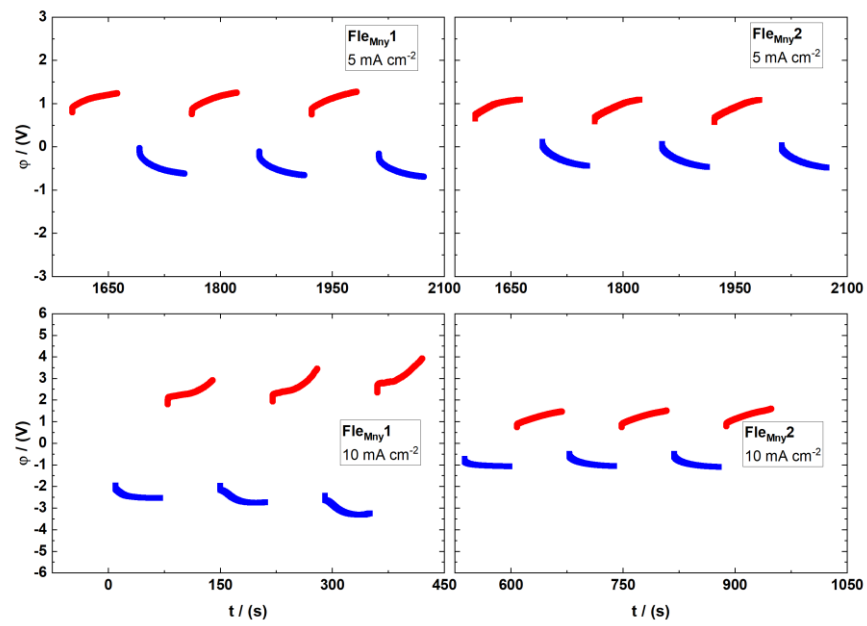
Appendix 19. Image of galvanostatic measurement raw data of Fle$_{Mny}$ samples.
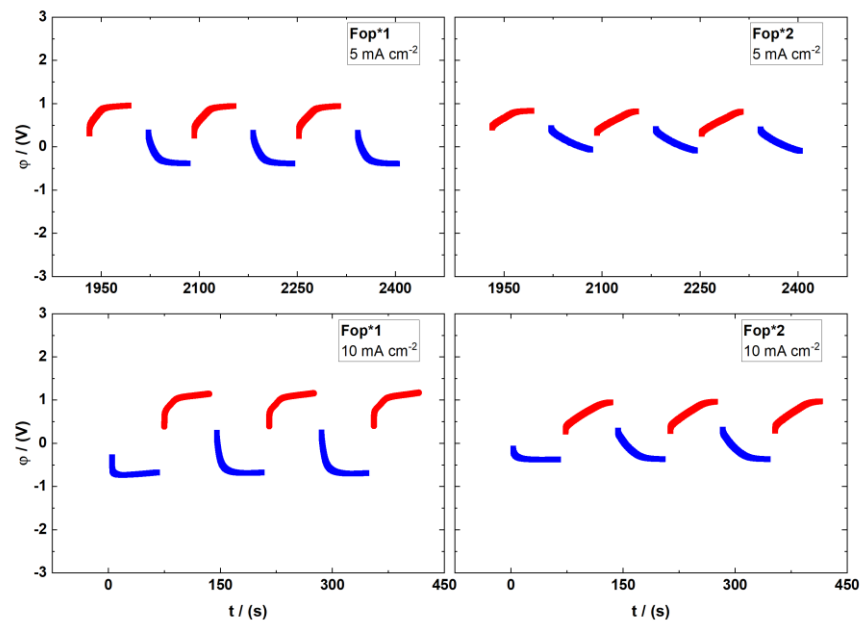
Appendix 20. Image of galvanostatic measurement raw data of Fop* samples.
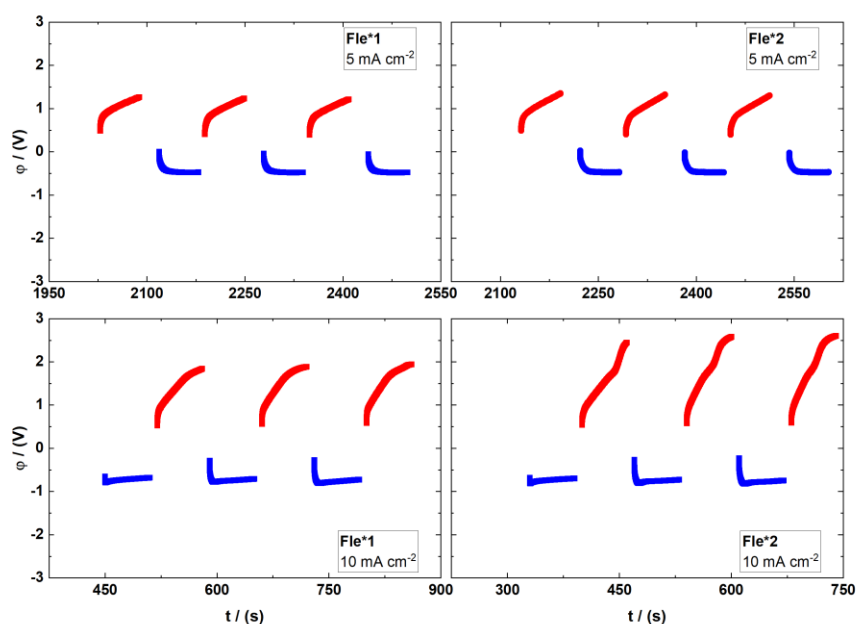
Appendix 21. Image of galvanostatic measurement raw data of Fle samples.*
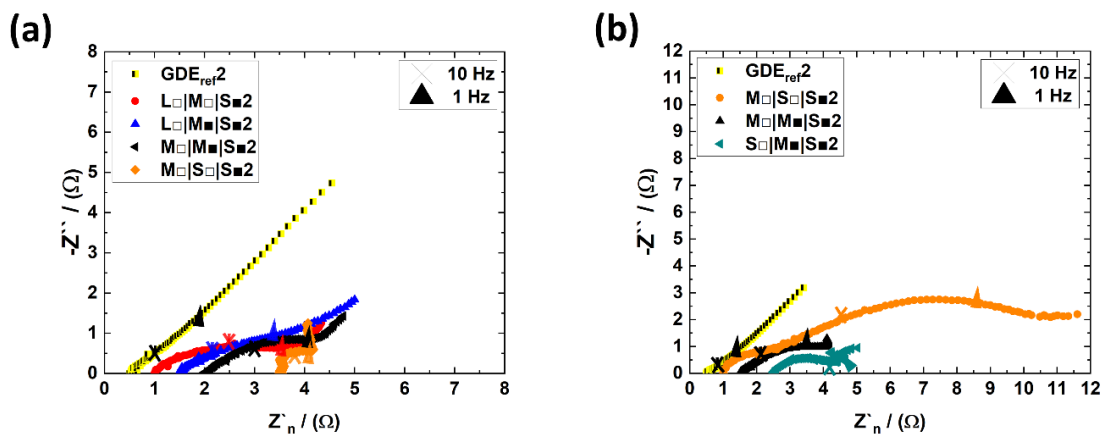
Appendix 22. Impedance spectroscopy measurement Nyquist plots of the second combined electrode bodies that were measured with gff (glass-fiber-fleece) (a) and measured without gff (b) at a frequency range of approx. 3 kHz – 0.1 Hz (last point) at φ_0 = 0.37 V vs. Hg/HgO 1 M NaOH. This sign "■" indicates the electrode body parts which were coated with PTFE and this "□" which is not coated with PTFE.
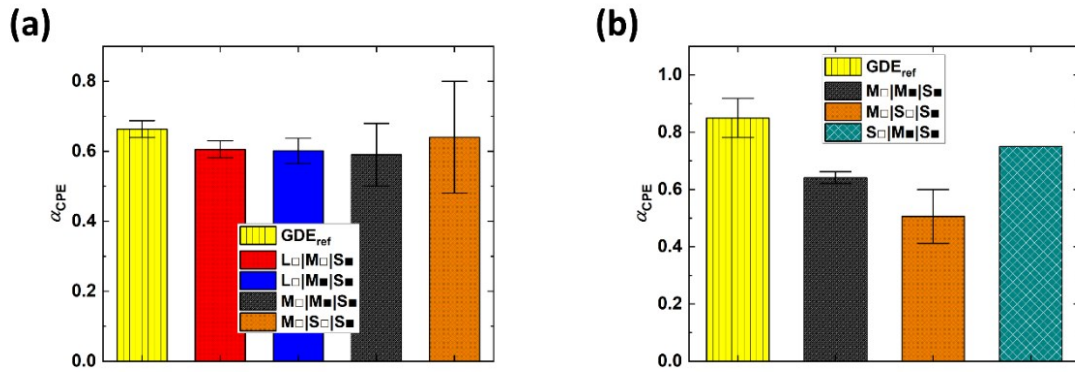
Appendix 23. Image of αCPE ((a) with glass fiber fleece and (b) without glass fiber fleece) at 0.37 V vs. Hg/HgO 1 M NaOH. Determined by the equivalent circuit fitting. This sign "■" indicates the electrode body parts which were coated with PTFE.
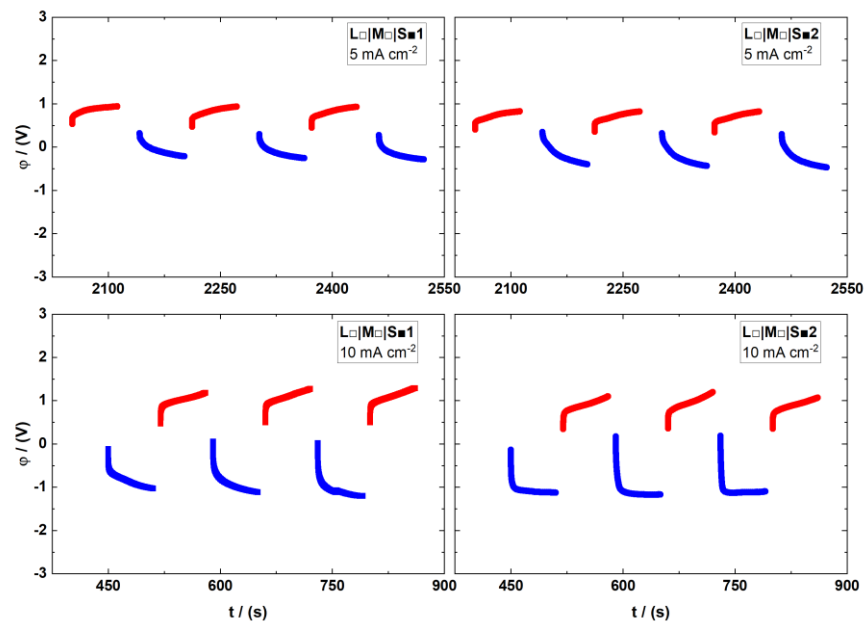
Appendix 24. Image of galvanostatic measurement raw data of L□|M□|S■ samples.
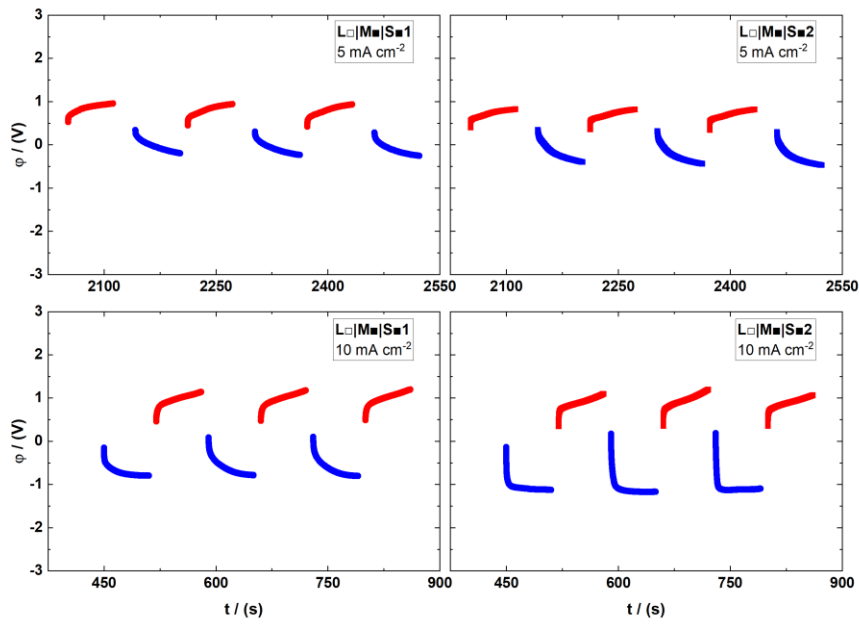
Appendix 25. Image of galvanostatic measurement raw data of L□|M■|S■ samples.
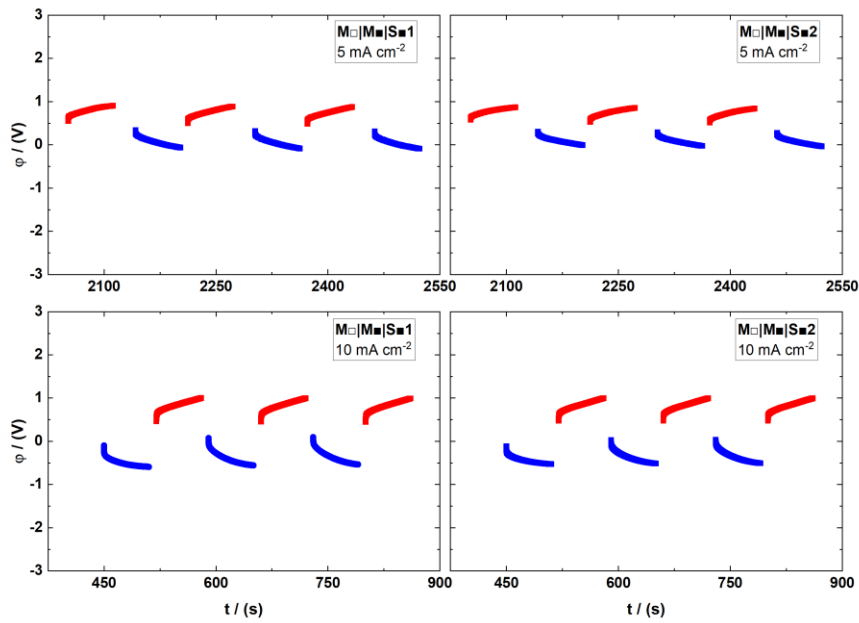
Appendix 26. Image of galvanostatic measurement raw data of M□|M■|S■ samples.
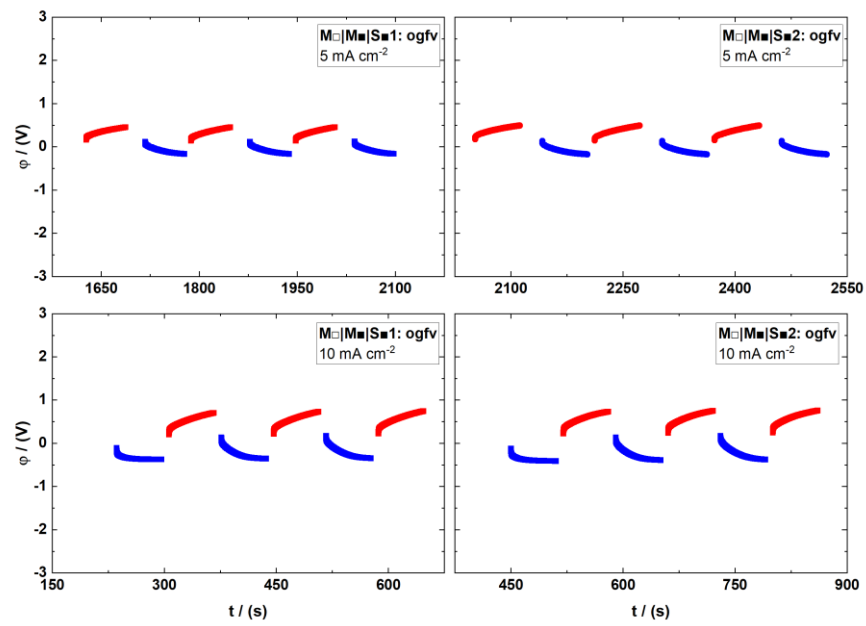
Appendix 27. Image of galvanostatic measurement raw data of M□|M■|S■ samples measured without glas fiber fleece.
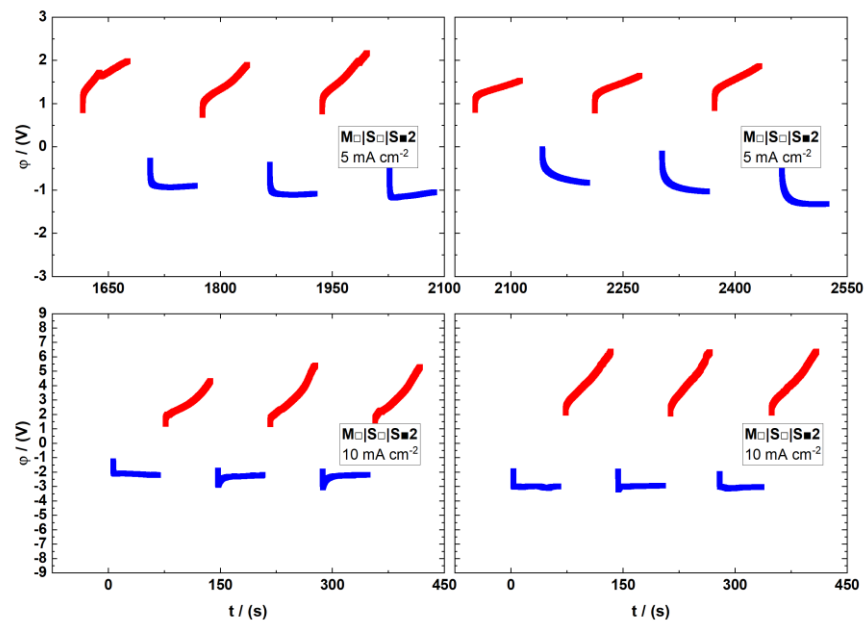
Appendix 28. Image of galvanostatic measurement raw data of M□|S□|S■ samples.
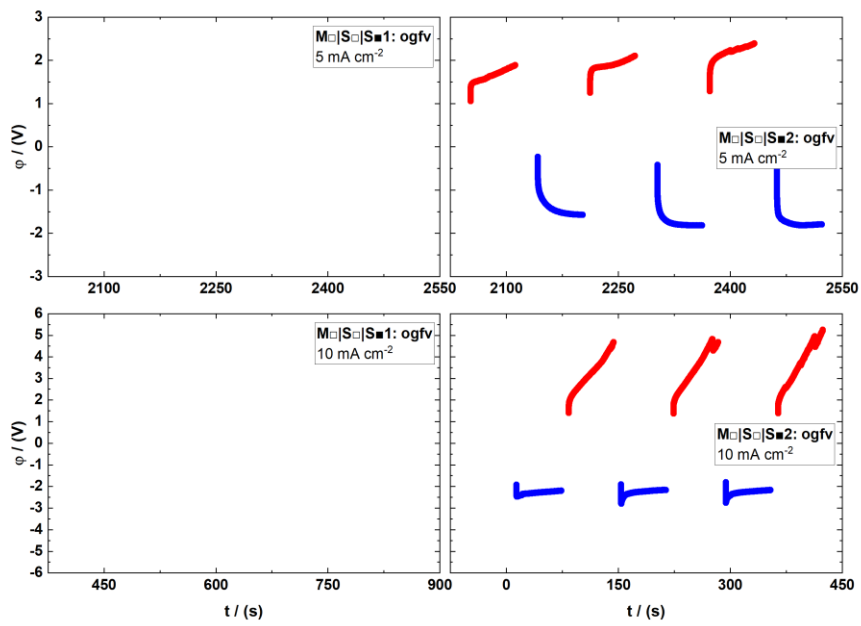
Appendix 29. Image of galvanostatic measurement raw data of M□|S□|S■ samples measured without glas fiber fleece.
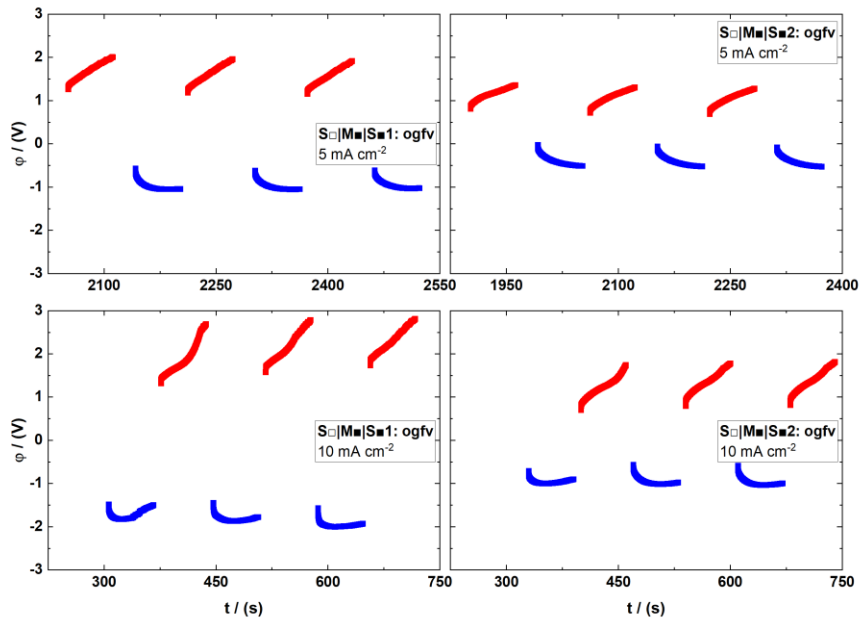
Appendix 30. Image of galvanostatic measurement raw data of S□|M■|S■ samples measured without glas fiber fleece.

(a)

(b)
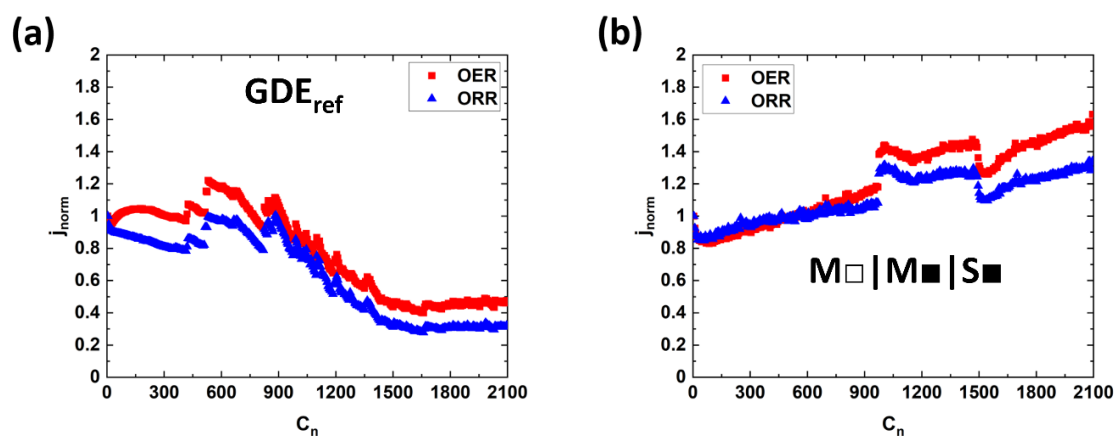
Appendix 31. Electrochemical long-term stability measurement of GDE_ref and HiFew second sample at 1.5 V and -0.75 V vs. Hg/HgO 1M NaOH for 2100 cycles and each working mode (OER and ORR) lasted 20 seconds.

11 Hypothesis

1. The deposited catalytically active Mn_xO_y sites are adjusted by the pH of the deposition solution and the applied electric potential.

2. The structure of the electrodeposited catalyst is set by the duration, the number of cycles, scan rate, and the combination of potentiostatic and potentiodynamic deposition methods.

3. The meniscus of the electrolyte film in the pores of the catalyst-coated substrate or GDE supplies dissolved O_2 to the catalytically active sites during ORR when the electrolyte film remains thin ($3 < x - 1000$ nm).

4. Transport resistance narrows the supply of reactants to the catalytic sites as the transport distance (e.g., thickness of the electrolyte film) increases, thereby increasing the ORR overpotential.

5. A hydrophilic electrolyte-filled macropore of a catalyst-coated substrate controls transport resistance through its size, which is reduced or increased by widening or narrowing the macropore or transport pathways to the catalytic site during OER.

6. The ORR overpotential depends on the size of the meniscus in the hydrophilic macropores of the catalyst-coated substrate, as it widens with larger macropores and increases the surface area of the electrolyte thin film ($x > 3 - 1000$ nm).

7. The hydrophobicity of the CF-GDEs exerts a repulsive force on the electrolyte in the wetted hydrophilic macropores of the catalyst coated-substrate, leading to an increase in the electrolyte thin film meniscus surface area within the CF-GDEs, which increases the ORR activity.

8. The electrolyte dams or fills the partially hydrophilic macropores of the catalyst-coated substrate until the repulsive force of hydrophobicity within the CF-GDE stops the electrolyte, and this extends the transport pathways to the catalytic site during OER, when the substrate pores are large ($200 - 600$ μm).

9. The combined advantage of fully filled large macropores in a hydrophilic porous layer and large menisci with large electrolyte thin film surface area in a hydrophobic porous layer leads to high OER and ORR activity in a layered CF-GDE.

12 Declaration of Authorship / Selbstständigkeitserklärung

I declare truthfully that I have prepared the present doctoral thesis independently and using only the specified sources and aids.

Hiermit erkläre ich, dass ich die vorliegende Promotionsarbeit selbstständig und unter Verwendung der angegebenen Hilfsmittel, persönlichen Mitteilungen und Quellen angefertigt habe.

Jena, den 16.11.2022

Artur Bekisch